Case and cd(_1-x)zn(_x)se single crystal photovoltaic devices

Abdullah.A.I. Al-Bassam

Al-Bassam, Abdullah.A.I. (1988) Case and cd(_1-x)zn(_x)se single crystal photovoltaic devices. Doctoral thesis, Durham University.

CdSe and $Cd_{1-x}Zn_xSe$ Single Crystal Photovoltaic Devices

by

Abdullah.A. I. Al-Bassam

Presented in Candidature for the Degree of

Doctor of Philosophy

in the

University of Durham

February, 1988

To My Parents

and my Wife

CONTENTS

Page

Acknowledgements

Abstract

CHAPTER 1 Photovoltaic conversion 1

1.1 Introduction 1

1.2 Solar radiation 2

1.3 The Solar Cell 3

1.4 The Junction Photovoltaic effect 4

1.5 The Present Work 6

References 8

CHAPTER 2 Materials Properties 10

2.1 Introduction 10

2.2 Structure of CdSe material 10

2.3 Electrical Properties of CdSe 11

2.4 Properties of $Cd_{1-x}Zn_xSe$ 12

2.5 Structure of Copper Selenide 15

2.6 Electrical Properties of Copper Selenide 16

2.7 Cadmium Selenide Solar Cells 17

References 20

CHAPTER 3 Background Theory 23

3.1 Introduction 23

3.2 Metal Semiconductor Barriers 23

3.2.1 The Schottky model 23

3.2.2 Schottky effect 25

3.2.3 Capacitance of Schottky diodes 26

3.2.4 Current-voltage relationship 28

3.2.5 Measurement of Barrier height 32

3.3 Surface States and rectification at a metal semiconductor contact 35

3.4 Theory of Heterojunctions 41

3.4.1 Anderson's model 41

3.5 Solar cell Parameters 43

3.5.1 Short-circuit Current 44

3.5.2 Open-circuit voltage 44

3.5.3 Cell efficiency 44

References 46

CHAPTER 4 Experimental Methods 48

4.1 Introduction 48

4.2 Crystal growth 48

4.2.1 The Clark-Woods or "Durham" method 49

4.2.2 The Piper-Polich Method 50

4.3 X-ray Diffractometry 51

4.4 Annealing in Selenium or Cadmium vapour 52

4.5 Copper dopping by evaporation 52

4.6 Contacts 53

4.6.1 Ohmic Contacts 53

4.6.2 Schottky diode fabrication 53

4.7 Reflection high energy electron diffraction (RHEED) 54

4.8 Scanning electron microscopuy 56

4.8.1 Scanning electron modes 56

4.8.2 Energy dispersive analyser X-ray (EDAX) 57

4.8.3 EBIC Measurements 58

4.9 Electrical Characteristics - 61

4.9.1 Measurements of current-voltage characteristics 61

4.9.2 Capacitance-voltage characteristic 61

4.9.3 Measurements of spectral response 62

References 63

CHAPTER 5 Physical properties of ZnCdSe 64

5.1 Introduction 64

5.2 Crystal growth 64

5.3 Composition measurements 66

5.4 X-ray diffraction measurements 70

5.4.1 Structure 70

5.4.2 Lattice Parameters 71

5.5 Band gap measurements 75

5.5.1 Photoconductivity 75

5.5.2 Optical absorption 76

5.5.3 Band gap measurements 77

5.6 Discussion 79

5.7 Conclusion 84

References 86

CHAPTER 6 Electrical Properties of $Zn_xCd_{1-x}Se$ 89

6.1 Introduction 89

6.2 Schottky barrier formation 89

6.2.1 Current-voltage characteristics 90

6.2.2 Capacitance-voltage characteristics 91

6.2.3 Photoelectric measurements 93

6.2.4 Dependence of Barrier Height on composition 94

6.3 Steady state photocapacitance 95

6.3.1 Undopped Au-$Cd_{1-x}Zn_xSe$ diodes 95

6.3.2 Steady state-infrared quenching of Photocapacitance (IRQ-PHCAP) 98

6.3.3 Dopped Au-$Cd_{1-x}Zn_xSe$ samples 98

6.4 Discussion 100

6.4.1 Electrical Characteristics 100

6.4.2 Barrier height in $Zn_{1-x}d_{1-x}Se$-Au diodes 102

6.4.3 Deep levels 104

6.5 Conclusions 106

References 108

CHAPTER 7 CdSe/Cu_2Se Heterojunction 110

7.1 Introduction 110

7.2 Structure of Polished and etched CdSe surfaces 111

7.3 Copper selenide Layer 112

7.3.1 Formation of Cu_xSe on CdSe 112

7.3.2 Thickness of the Cu_2Se layer 113

7.3.3 RHEED Studies 114

7.4 Properties of As-made devices 116

7.4.1 J-V Characteristics 116

7.4.2 Spectral response 117

7.4.3 Photocapacitance measurement 118

7.5 Heat treatment in air 118

7.5.1 J-V characteristics 118

7.5.2 Spectral response 121

7.5.3 Capacitance-voltage measurements 122

7.5.4 EBIC measurements 122

7.6 Heat treatment in Argon 123

7.6.1 J-V Characteristics 123

7.6.2 Spectral response 124

7.7 Discussion 124

7.7.1 Substrate preparation 124

7.7.2 Cu_xSe layer 125

7.7.3 As-made Cu_xSe/CdSe device 117

7.7.4 Heat treatment in air 129

7.7.5 Heat treatment in Argon 131

7.7.6 Analysis of CdSe/C_2Se Junction 131

7.8 Conclusion 132

References 134

CHAPTER 8 $Zn_xCd_{1-x}Se$ Photovoltaic cell 137

8.1 Introduction 137

8.2 Structure of Polished of $Zn_xCd_{1-x}Se$ surface 137

8.3 $Cd_{1-x}Zn_xSe/Cu_2Se$ Solar Cell 139

8.3.1 Preparation of the device 139

8.3.2 RHEED investigation 139

8.3.3 Current-voltage Characteristics 140

8.3.4 Spectral response 142

8.4 Photocapacitance Measurement 14

8.5 Capacitance Junction for $Zn_xCd_{1-x}Se/Cu_2Se$ 144

8.6 Barrier height measurements 146

8.7 Discussion 147

8.7.1 RHEED measurements 147

8.7.2 Current-voltage Characteristics 148

8.7.3 Spectral response 149

8.7.4 Deep levels 150

8.8 Conclusion 151

References 153

CHAPTER 9 Summary and Conclusions 155

9.1 Summary 155

9.2 Discussion and Conclusion 158

9.3 Suggestion for further work 159

ACKNOWLEDGEMENTS

I would like to thank my supervisor, Professor J. Woods, for his guidance and helpful encouragement. I am also grateful to Dr. A.W. Brinkman for many constructive discussions and assistance during the course of this work. I am grateful to Dr. G.J. Russell for his help in the use of electron microscopy studies.

I would like to thank Professor G.G. Roberts for the use of the departmental facilities, and the workshop staff headed by Mr. F. Spence for their skill and advice.

My thanks also extend to Mr. N.F. Thompson for growing the crystals, to Mr. T. Harcourt for cutting the crystals, to Mr. J.T. Mullins for proof reading this thesis, to Miss Kay Cummins and Ms. Julie Morgan for the drawing and photography for this thesis, and to Mrs. M.A. Chipchase for typing this thesis, and to other members of the group who rendered me their help during the course of this work in one way or another. In addition, I wish to acknowledge the assistance from Mr. R. Coult of the Chemistry Department and from Ron Hardy of Geology Department for providing the facilities of Atomic Absorption Spectorscopy and X-ray diffractometry. In addition, special thanks are due to all my brothers in Islam both here in the U.K. and at home in Saudi Arabia. My appreciation is also extended to the King Saud University for providing financial support over the years.

Finally I would like to express my gratitude to my parents, my wife, my brothers and my sisters for their many sacrifices and constant encouragement over the years.

ABSTRACT

With bandgap ranging from 1.74 to 2.67eV depending on composition, the ternary alloy (ZnCd)Se is an interesting system for optoelectronic applications. The main purpose of the work reported in this thesis was to characterise some of the electrical properties of crystals of $Zn_xCd_{1-x}Se$ and to assess the potential in $CdSe/Cu_2Se$ and $Zn_xCd_{1-x}Se/Cu_2Se$ photovoltaic cells.

Single crystals of this ternary compound have been grown from the vapour phase using two different methods. With each technique boules of graded composition were produced with the Cd/Zn ratio decreasing towards the end that was last to grow. The variation in composition was determined using atomic absorption spectroscopy and energy dispersive X-ray analysis. Lattice Parameters were determined using X-ray diffractometry and were found to vary linearly with composition over a wide range. This study showed that for $x < 0.5$ the crystal adopts the hexagonal Wurtzite structure, changing to the cubic sphalerite for higher values of x.

The variation is bandgap energy with composition was determined for single crystals of $Zn_xCd_{1-x}Se$ at 300K and 90K and shows that the bandgap changes quadratically in x for $x < 0.6$. The barrier heights of Au/$Zn_xCd_{1-x}Se$ $(x < 0.45)$ Schottky diodes were calculated from forward I-V characteristics, C-V and photoelectric measurements were also carried out. A good linear relationship with composition was obtained for barrier heights measured by the Photoelectric method. Deep levels were also investigated in these diodes using Photocapacitance, which revealed the presence of two dominant levels having activation energies of 0.4 - 0.5 eV and 0.9 - 1.0 eV (referred to the valence bandedge) that were independent of the composition.

The second part of the thesis described an investigation into $CdSe/Cu_2Se$ and $Zn_xCd_{1-x}Se/Cu_2Se$ $(x < 0.4)$ devices that had been prepared on orientated single crystal substrates by a chemiplating technique.

Reflection high energy diffraction (RHEED) showed that the structure of the Cu_2Se layer took the cubic modification. Cells formed on as-grown low resistivity substrates exhibited no rectification. However good Photovoltaic properties were produced by heating the devices in air or Argon at 200°C. However, for cells formed on higher resistivity CdSe, the resultant devices showed a Photovoltaic effect without any heat treatment.

The Photovoltaic output characteristics were measured under simulated AMI illumination. The properties of the Photovoltaic cells prepared on $Zn_xCd_{1-x}Se$ single crystals are

closely related to those of devices fabricated on CdSe substrates.

Cells formed on CdSe were found to have higher short circuit current densities (J_{SC}), but lower open circuit voltage (V_{OC}) than those produced on the mixed $Zn_xCd_{1-x}Se$ crystal substrates. Thus the open circuit voltage was increased with zinc content to 420 mV with a $Zn_{0.4}Cd_{0.6}Se$ based cell. However, there was a considerable decrease in the short circuit current.

The characterisation of these cells has revealed the main threshold in all the devices indicated a dominant level with an activation energy of between 1.0 and 1.1 eV with respect to the conduction band in both CdSe and $Zn_xCd_{1-x}Se$.

CHAPTER 1

Photovoltaic Conversion

1.1 Introduction

The photovoltaic effect was first discovered 148 years ago by Bequerel(1) in 1839, when he observed that a voltage was produced between two electrodes immersed in an electrolyte when they were illuminated. Adams and Day(2) demonstrated an analogous effect in solids using the element selenium in 1877, shortly after Smith (1873) had reported the observation of photoconductivity in selenium.

However, it was not until nearly a century after these discoveries that this laboratory phenomenon was considered a possible source of electrical energy. The modern history of photovoltaics began in 1954, when Chapin et al.(3) reported a solar conversion efficiency of 6% using a silicon single-crystal diffused p-n junction cell. In the same year a cadmium sulphide solar cell was developed by Reynolds et al.(4) also with an efficiency of about 6%. Since then there have been considerable developments and typical efficiencies for silicon solar cells are now in the range of 17-20%(5-9), while efficiencies close to 26% have been reported for GaAs solar cells(10-11). Other alternative devices include CdS/CdTe cells (efficiency 8.5%)(12) and CdSe MIS cells (efficiency 9-10%)(13,14).

1.2 Solar radiation

Each hour the top of the earth's atmosphere receives 172 x 10^{12} kW of radiation from the Sun, although not all of this energy reaches the surface of the earth(15). Approximately 25-50% of this energy is lost by scattering and absorption in passing through the Earth's atmosphere. These losses are not spread uniformly across the solar spectrum and as a result the spectrum is also substantially modified(16). The solar efficiency of a photovoltaic system depends critically on the spectral distribution of the energy coming from the sun(17).

The average solar irradiance in free space at the mean distance of the earth from the Sun is defined as the solar constant. Its measured value is 1.353 kW/m^2(16). The intensity and the spectral distribution of the radiation arriving at the earth's surface depend on the composition of the atmosphere(17), as well as the path length of the radiation through the atmosphere. The main losses arise from water-vapour absorption in the infrared, ozone absorption in the ultraviolet and scattering by airborne dust and aerosols(18).

The path length through the atmosphere is conveniently described in terms of an equivalent relative air mass which is actually the secant of the angle between the Sun and the zenith ($\sec\theta$). This is called the "air mass number" and is a measure of the atmospheric path length, relative to the minimum path length when the Sun is directly overhead(18) (i.e. $\sec\theta = 1$). As indicated above, it is not only the total magnitude of the irradiance which is affected by the path length (air mass number) but the spectrum as well. Figure 1.1. shows four spectra at different air mass numbers. The upper curve is the air mass zero condition (AMO) and corresponds to the solar spectrum in outer space at the top of the atmosphere. This condition can be approximated by a 5800K black body as shown by the dashed curve. The solar spectrum at the earth's surface when the Sun is at the zenith (i.e. $\sec\theta = 1$) is designated AM1, when the irradiance is about 925 W/m^2. The AM2 spectrum is for $\theta = 60^o$ and has an irradiance of about 691 W/m^2. Both AM1 and AM2 are defined for "a standard atmosphere" containing 2cm of precipitable water vapour and which is free of aerosol.

1.3 The Solar Cell

A solar cell is a photovoltaic device designed to convert sunlight into electrical power and to deliver this power into a suitable load in an efficient manner(19).

Solar cells at present furnish the most important long-duration power supply for satellites and space vehicles. Solar cells have also been successfully employed in small-scale terrestrial applications(18). The first photovoltaic cells to have a wide application were silicon single crystal homojunction cells developed for the space program, and have been used on a fairly large scale by the U.S. space program

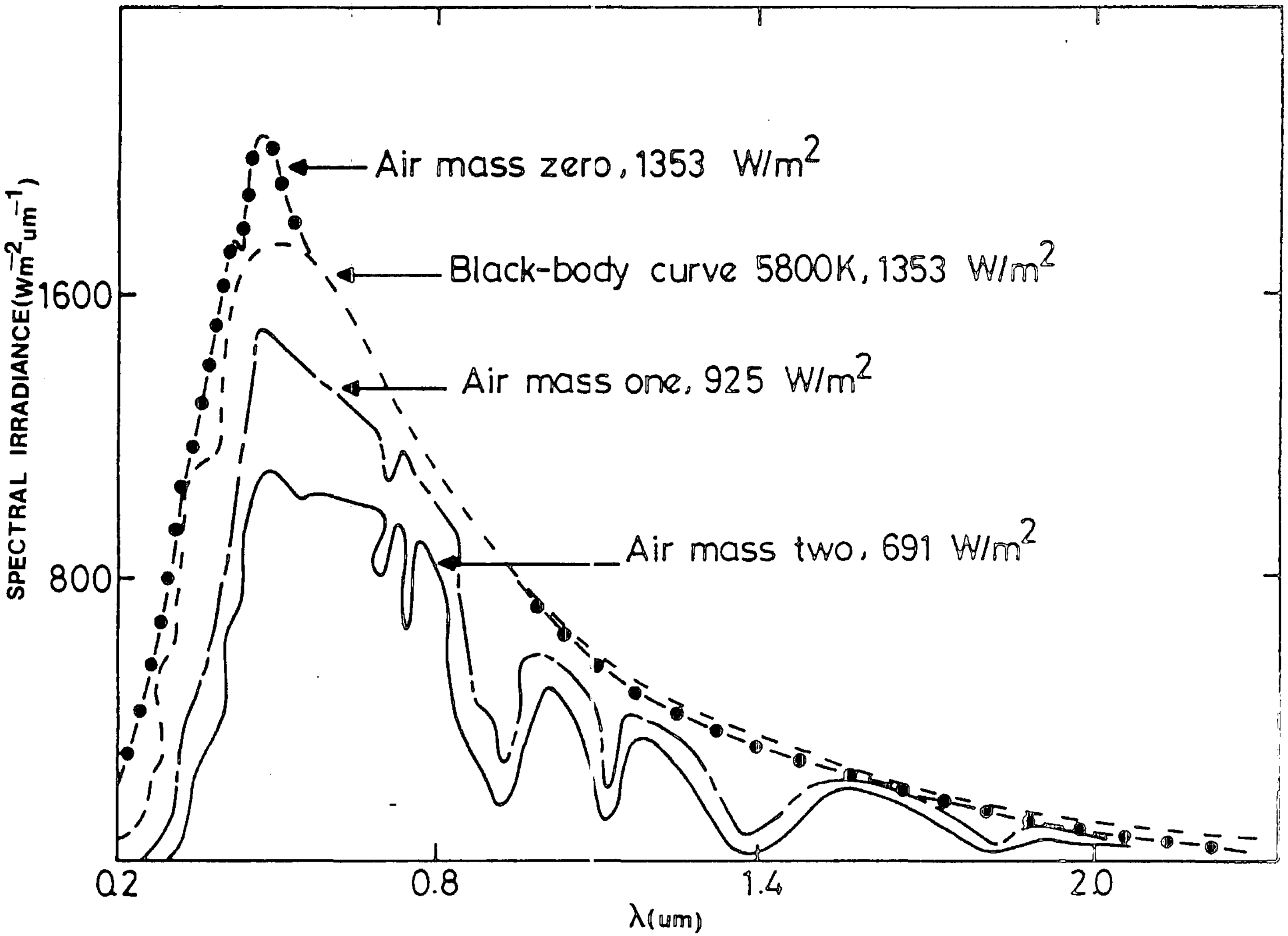

Figure 1.1 Four curves related to solar spectral irradiance.

in well over 1000(16) satellites of various types.

As useful as solar cells have been in the space program their potential importance for large-scale terrestrial power generation is even greater(19). Recently research and development of low cost, flat-panel solar cells, thin film devices, concentrator systems, etc. has been increasing and it is anticipated that in the near future small solar-power modular units and solar power plants will be economically feasible(18).

1.4 The Junction Photovoltaic effect

The generation of an e.m.f. by the absorption of light in a solar cell is termed the photovoltaic effect(1). The absorption of light in a semiconductor produces electron-hole pairs, and where these are generated near an internal electric potential barrier such as a p-n junction, they may become separated across the barrier. The charge imbalance leads to a reduction in the internal potential, and the difference from the thermal equilibrium value appears as a photovoltage, which can drive a photo-current through an external circuit.

The major elements of the junction-type device consist of:-

(a) The top contact which should be transparent in order to allow the light to reach the active region of the device,

(b) the top semiconductor layer or emitter, which should ideally also be non-absorbing,

(c) the base semiconductor, (of opposite conductivity type to the emitter) which forms the half of the p-n junction, and which should ideally be very absorbing,

(d) an ohmic back contact.

Solar cells may be classified in several ways, for example, cells may be classified in terms of the material structure;

(1) Single crystal or epitaxial materials, these types have the highest efficiencies,but are also the most expensive.

(2) Polycrystalline: primarily thin film devices, produced by sputtering, evaporation, screen printing, etc. Considerably less expensive than single crystal devices, they are also less efficient.

(3) Amorphous: primarily solar cells fabricated from amorphous silicon. The cost of the material and of solar cell fabrication procedures are low(20) as are the efficiencies compared to single crystal cells.

An alternative classification scheme is based on the method of junction formation (fig. 1.2):-

(i) The homojunction which is a p-n junction produced within the same semiconductor.

(ii) The heterojunction, where the junction is formed between p-type and n-type semiconductors of different species.

(iii) The Schottky (or metal-semiconductor) barrier where a rectifying contact is formed between a metal and a semiconductor.

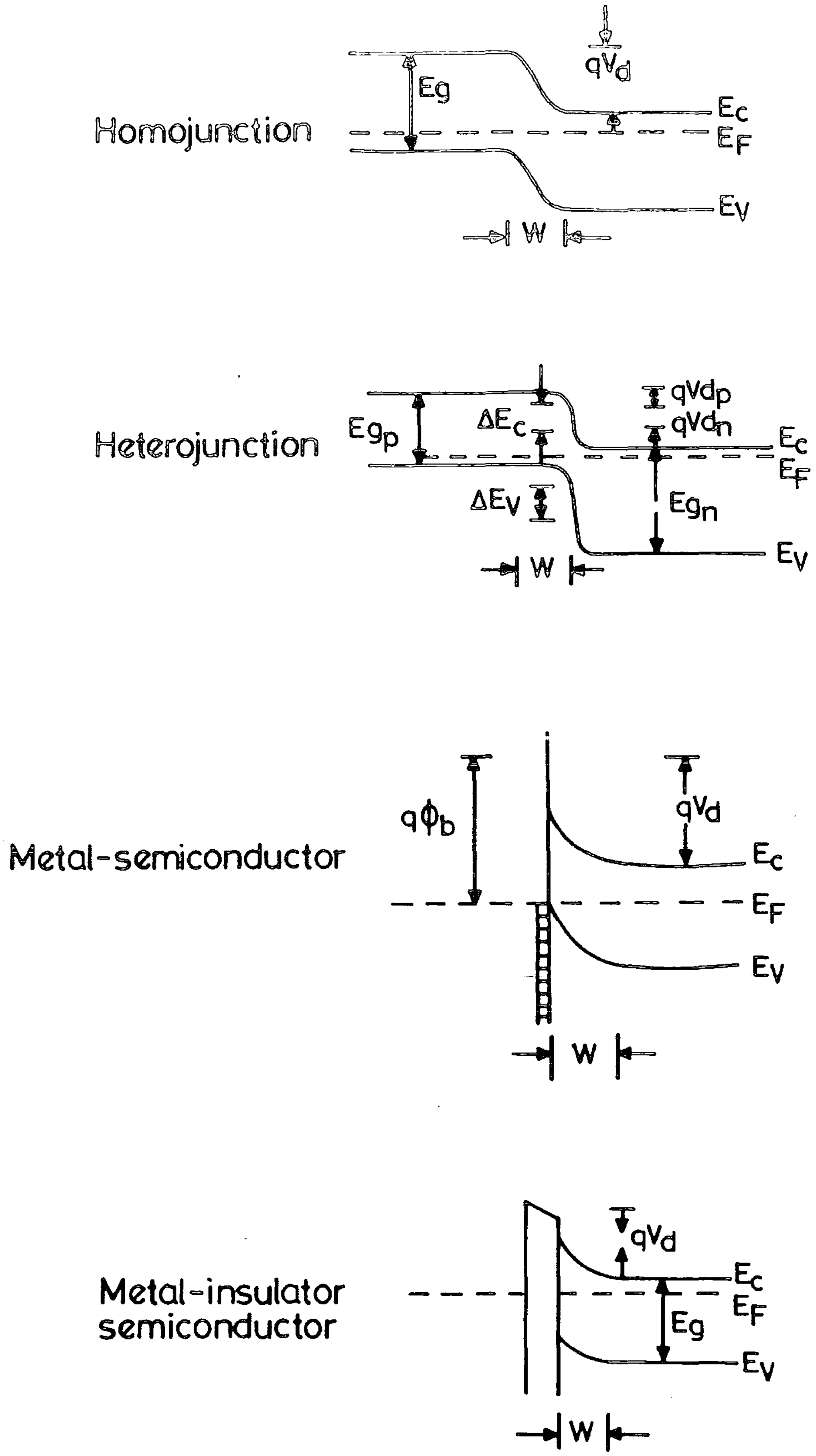

Figure 1.2 Illustrations of different types of solar cells.

(iv) The metal insulator-semiconductor (MIS) junction in which a thin insulating layer is used to separate the metal from the semiconductor.

1.5 The Present Work

The work reported in this thesis is mainly concerned with the material $Cd_{1-x}Zn_xSe$ and its use in the fabrication of $Au-Cd_{1-x}Zn_xSe$ metal semiconductor diodes, and in the $Cu_2Se/Cd_{1-x}Zn_xSe$ heterojunction. A general review of properties of CdSe, CdZnSe and $Cu_{2-x}Se$ compounds is given in Chapter 2. The theory underlying Schottky barriers and heterojunctions is discussed in Chapter 3.

Chapter 4 describes the experimental side of this work. Chapter 5 is concerned with the physical properties of the $Zn_xCd_{1-x}Se$ system, including the determination of the crystal structure, lattice parameters and the band gap energy (Eg) as a function of composition. Chapter 6 is concerned with some of the electrical properties of this crystal system including measurements made with the $Au-Cd_{1-x}Zn_xSe$ diode.

The formation of copper selenide on cadmium selenide is described in Chapter 7, together with a study of the structural phases of copper selenide and the effects of heat treating devices in air and in argon.

The photovoltaic properties of $Cu_{2-x}Se/CdSe$ cells are also discussed in this section.

The formation of copper selenide on $Zn_xCd_{1-x}Se$ single crystals is described in Chapter 8. These studies are similar to those made on CdSe/Cu_2Se cells and include an investigation of structural and electrical properties.

References

(1) Becquerel, E., (1839), Compt. Rend. 9, 561.

(2) Adams, W.G., Day, R.E., (1876), Roy. Soc. Proc. 24, 163.

(3) Chapin, D.M., Fuller, C.S. and Pearson, G.L., (1954), J. Appl. Phys. 25, 676.

(4) Reynolds, D.C., Leies, G., Ates, L.L. and Marburger, R.E., (1954), Phys. Rev. 96, 533.

(5) Rohatgi, A., (1985), Proc. 18th IEEE Photovoltaic Specialists Conf., Las Vegas, 7.

(6) Green, M.A., Blakers, A.W., Wenham, S.R., Narayanan, S., Willison, M.R., Toauk, M., and Szpitalak, T., (1985), Proc. 18th IEEE Photovoltaic Specialists Conf., Las Vegas, 39.

(7) Sah, C.T., (1986), Solar Cells, 17, 1.

(8) Rohatgi, A., and Rai-Choudhury, P., (1986), Solar Cells, 17, 119.

(9) Green, M.A., (1986), Proc. 7th E.C. Photovoltaic Solar energy Conference, Sevilla, Spain. 681.

(10) Fan, John C.C., (1985), Proc. 18th IEEE Photovoltaic Specialists Conf., Las Vegas, October, 28.

(11) Veizer, V.G. and Goldewski, M.P., (1987), Solar Cells, 20, 245.

(12) Matsumoto, H., Nakano, A., Kokatsu, Y., Uda, H., Kuribayashi, K. and Ikegami, S., (1976), Jpn. J. Appl. Phys. 15, 2281.

(13) Rickus, E., Bonnet, D., (1980), Proc. 3rd E.C. Photovoltaic Solar Energy Conf. Cannes, 871.

(14) Rickus, E., (1985), Proc. 5th E.C. Photovoltaic Solar energy Conf., London, 865.

(15) Neville, Richard C., (1978), Solar Energy Conversion, The Solar Cell, Elsevier.

(16) Frank, K. and Keider, J.F., (1978), Principles of Solar Engineering, McGraw.

(17) Fahrenbruch, A.L., Bube, R.H., (1983), Fundamentals of Solar Cells, Academic Press.

(18) Sze, S.M., (1981), Physics of Semiconductor devices, John Wiley & Son.

(19) Hovel, H.J., (1975), Semiconductors and Semimetals vol. 11, Solar Cells (Academic Press, New York).

(20) Fan, John C.C., Technology review, August/September, (1978), 14.

CHAPTER 2

Materials Properties

2.1 Introduction

In this chapter the structure and the electrical properties of CdSe are described. In addition some of the properties of CdZnSe and in particular the structure and electrical properties of copper selenide are discussed. Cadmium selenide solar cells are also reviewed.

2.2 Structure of CdSe material

Simple binary compounds formed from Cd or Zn and S, Se or Te all crystallise in the Wurtzite (hexagonal) or the zinc blende (cubic) structure.

The Wurtzite structure consists of two interpenetrating hexagonal close packed lattices (one on the cation the other on the anion) displaced with respect to each other by a distance 3c/8 along the c-axis (Figure 2.1). The nearest neighbour distance assuming ideal tetrahedral sites is $^{3c}/8$ or $\sqrt{3/8}$ a. Where a and c are the lattice parameters along the a and c axis respectively. The zinc blende structure is composed of two interpenetrating face-centred cubic lattices, (see Figure 2.2), translated with respect to each other by 1/4 of the body diagonal. The nearest neighbour separation in this instance is $\sqrt{3}/4$ a where a is the lattice parameter.

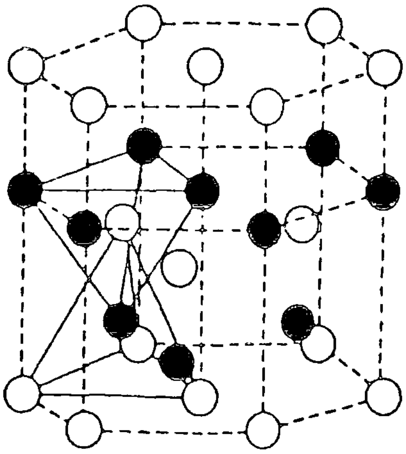

Figure 2.1 The Wurzite structure.

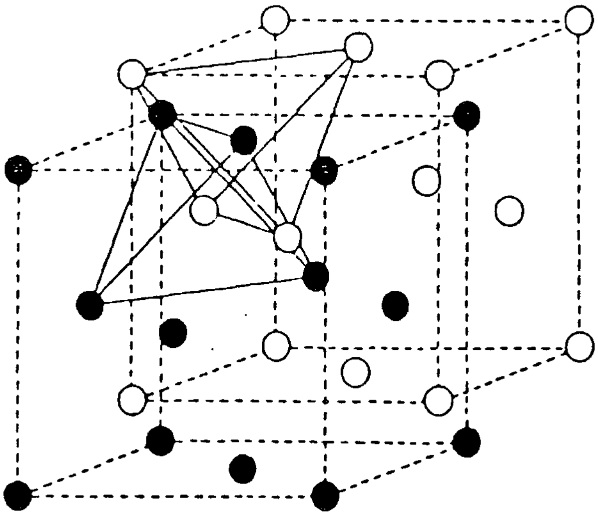

Figure 2.2 The zinc blende structure.

CdSe normally crystallises in the wurtzite modification at room temperature, in which case a = 4.298Å and c = 7.015Å.(1-4) However, under some conditions CdSe may be made to adopt the zinc blende structure, in which case a = 6.05Å.(1-4)

2.3 Electrical Properties of CdSe

Cadmium selenide, one of the photoconductive II-VI semiconductors, invariably displays n-type conduction with direct energy band gaps of about 1.74eV and 1.84eV at 300K and 90K respectively(5).

As prepared conductive cadmium selenide single crystals are often nearly degenerate n-type semiconductors. For example Masayuki and Hirou(6) found a value for the electron concentration of 3.6×10^{17}cm^{-3} and an effective mobility of 580cm^{2}/V.sec at room temperature in their crystals. Heat treatment in selenium vapor formed a surface layer that appeared to be different from the crystal interior. Measurements (I-V characteristics, barrier admittance, photoelectric effect and pulsed field effect) made on these treated surfaces suggested that a p-type layer had been formed on the n-type crystal. The hole mobility and surface trap density in the p-type layer were estimated to be ~ 50 cm^{2}/V.sec and ~ 10^{11}cm^{-2}, respectively. The electrical properties of n-CdSe were studied over the temperature range of 4.2 to 300K by Burmeister and Stevenson(7). Measurements were made in both as grown crystals and crystals annealed under controlled Cd pressure. Hall effect measurements on these low resistivity specimens indicated the presence of a donor level 0.014eV below the conduction band, with a concentration of typically $\approx 10^{16}cm^{-3}$. The electron effective mass has been obtained from a study of the Zeeman splitting of exciton lines by Wheeler and Dimmock(8). They have found values of the effective masses of electrons ($m^*/m = 0.13$).

2.4 Properties of $Cd_{1-x}Zn_xSe$

The ZnSe-CdSe system crystallises in the cubic zinc blende structure for Zn-rich compositions but undergoes a transition to a hexagonal structure for Cd rich compositions. Over the full range of compositions the band gap energy of the mixed crystal differs by 0.83eV (1.74eV for CdSe and 2.67eV for ZnSe) at room temperature which covers most of the visible spectrum and extends into the near infra-red. The full range of composition of this material was demonstrated as early as 1951(9). The growth of CdZnSe single crystals from the vapour phase was first reported by Reimers(10) in 1969, and again more recently by Burger and Roth(11) and by Al Bassam et al.(12). The lattice parameters of single crystals of $Zn_xCd_{1-x}Se$ were reported by Kolomiets and Chun-ming Lin(3), Budennaya et al.(13) and Al Bassam et, al.(12) based on X-ray diffraction studies. The lattice parameters of (Zn,Cd)Se appear to obey Vegard's Law and vary linearly with composition up to the hexagonal/cubic transition.

The energy band gap of the ternary CdZnSe system has been determined from photoelectric effect(3). The band gap was found to vary smoothly but not linearly with composition from 1.74eV (CdSe) to 2.67eV (ZnSe) at room temperature.

Generally the energy band gap E(x) of an alloy A_xB_{1-x} between two binary compounds A and B is given by(14) the empirical equation:

$$E(x) = E(B) + [E(A) - E(B) - b]x + bx^2 \tag{2.1}$$

where E(A) and E(B) are the band gaps of A and B respectively, and b is the so-called bowing parameter. The bowing parameter determines the degree of "bending" in the graph of energy band gap vs composition. Table 2.1 summarises some properties of CdSe and ZnSe materials.

	CdSe	ZnSe
Molecular weight	191.4	144.3
Density (g/cm^3)	5.8	5.4
Direct band gap at 300K	1.73eV	2.67eV
" " " at 90K	1.84eV	2.8eV
Lattice parameters wurtzite	a = 4.300A^o c = 7.002A^o	a = 4.01A^o c = 6.54A^o
" " Zincblende	a = 5.6056A^o	a = 5.669A^o
Effective mass of electrons (m_e^*)	0.13	0.13
Effective mass of holes (m_p^*)	0.45	0.7
Electron mobility (cm^2/v.s.)	650	530
Hole mobility (cm^2/vs)	75	28
Dielectric constant ε_s	9.4	8.1
Melting point (^{o}C)	1239	1520

* in direction Parallel to C axis

Table 2.1 Some properties of CdSe and ZnSe (1,5,15).

2.5 Structure of Copper Selenide

The compound $Cu_{2-x}Se$ has found interesting applications as the p-component of heterojunctions based on single crystals of CdSe(16), but it is only in recent years that Cu_2Se thin films have excited some interest for solar cell applications. The Cu_2Se system has been studied by several authors(16-22). P. Rahlfs(23) reported that $Cu_{2-x}Se$ has a face-centred cubic lattice and that its parameters vary in relation to the copper content. He reported that for Cu_2Se at 110^oC $a = 5.84A^o$, while for $Cu_{1.8}Se$ at room temperature, $a = 5.72A^o$. C.A. Efendiev(17) suggested that depending on the copper content, the lattice parameter of the phase $Cu_{2-x}Se$ varies over the range from $a = 5.65A^o$ to $a = 5.75A^o$ at room temperature. Epitaxial films(21) of the low temperature modification of Cu_2Se deposited onto NaCl single crystal substrates at 200^oC and 400^oC have been indexed on the basis of a hexagonal lattice with unit cell parameters $a = 7.07$ and $C = 6.68A^o$. These parameters are related to the parameters of the f.c.c. phase by the relations

$$a_h = (\sqrt{3}/\sqrt{2})a_c \text{ and}$$

$$c_h = (^2/\sqrt{3})a_c.$$

Shafizade et al.(22) found that during treatment in vacuum at temperatures below 350^oC, the compound Cu_2Se undergoes consecutive phase transformations:

$$\begin{array}{lllll} & & & & 300 \longrightarrow \text{room} \\ \text{CuSe} & \xrightarrow{100\text{-}300^{o}\text{C}} \text{Cu}_{2-x}\text{Se} & & \xrightarrow{3oo^{o}\text{C}} \text{Cu}_2\text{Se} & \xrightarrow{\text{temperature}} \text{Cu}_2\text{Se} \\ & \quad f_{cc} & & \quad f_{cc} & \text{Low temperature modifications} \\ & a = 5.68\text{-}5.75\text{A}^{o} & & a = 5.84\text{A}^{o} & \end{array}$$

They found the lattice parameter of the compound changed from 5.68 - 5.75A^{o} as the composition ranged from $Cu_{1.4}Se$ to $Cu_{1.75}Se$. At room temperature an ordered phase of Cu_2Se exists in the range $Cu_{1.75}Se$ to Cu_2Se. Above 350^{o}C Cu_2Se decomposes into two f.c.c. phases with a = 5.84A^{o} and a = 5.65A^{o}. On cooling to room temperature two phases coexist, a low temperature modification of Cu_2Se and an independent f.c.c. phase with a = 5.63A^{o}, corresponding to an approximate composition of $Cu_{1.15}Se$.

2.6 Electrical properties of Copper Selenide

Copper selenide is a p-type semiconductor. The energy band gap has been reported by Sorkine et al.(24), Komaschenko and Fedorus(25,26,27) to be 1.3eV, and by Ture et al.(28) to be 1.21eV. Copper selenide has a high carrier density in the range 10^{20}-10^{21} cm^{-3}. Thermoelectric power α , The electrical conductivity σ , and Hall coefficient R_H of copper selenide have been determined over a wide range of temperature from liquid nitrogen to 1000 K by Voskanyan et al.(29). The effective mass m^* increases with temperature in accordance with the law $m^* \propto T^{0.9}$ and at 550°K it amounts to $1.74m_o$, whereas at 950°K its value is $2.9m_o$. The rise in the density of states effective mass with temperature may be due to a number of factors: deviation of the quadratic dependence of the carrier energy, presence of valence subbands and changes in the lattice parameter with consequent changes in the energy band parameters.

The hole mobility, calculated from σ allowing for degeneracy, decreases with temperature in accordance with the law $u \propto T^{-2.2}$.

2.7 Cadmium selenide solar cells

Most studies of photovoltaic solar cell devices based on CdSe have been developed using the inherently simple MIS structures(30-35). Typically these have been fabricated by evaporating a thin CdSe layer onto a glass slide previously coated with a very thin chromium film. At a substrate temperature of 450°C and for deposition rates around 5A°/S, the CdSe films are polycrystalline but have their c-axis perpendicular to the substrate, indicating a high degree of preferred orientation. The films are highly stoichiometric with native doping levels around 10^{14} electrons per cm^3 and carrier mobilities of 10 to 30 cm^2/vs. A thin 40 to 50A° insulating layer of ZnSe or Sb_2Se_3 is evaporated onto the CdSe film. The properties of the device are improved by annealing the complete cells in N_2 at a temperature of around

200°C for cells where ZnSe is the insulator, and 150°C for cells where Sb_2Se_3 is the insulator. The CdSe MIS thin film solar cell has led to efficiencies of around 5 percent, with open circuit voltages ~ 650 mV and short-circuit current densities of over 20 mA/cm^2 at AM1 level of irradiance. The spectral response of these cells(32) is dominated by the wavelength - dependent reflection coefficient of the evaporated Schottky contact. The reflection coefficient of the gold layers used has a minimum at about 0.5um, causing a maximum in the spectral response of the cells at this wavelength.

The investigation of CdSe films(35) of different crystallographic structure has revealed a strong dependence of photovoltaic performance of the CdSe solar cell on the structure. The spectral response measurements on CdSe thin film solar cells at different bias voltages reveal a varying amount of photoconductivity, which it is thought may be correlated with microscopic disorder within the grain boundaries. This can give rise to high densities of interface states which finally limit the photovoltaic quality of polycrystalline CdSe films. Thus improvements the photovoltaic output of CdSe/ZnSe(35) layers should be achieved by detailed investigation of their doping conditions.

The investigation of the thin film CdSe/Cu_2Se heterojunction has been reported by several workers(25,27,36) and in particular by Komashchenk and Fedorus(25,26) and Ture et al.(28) for single crystal CdSe/Cu_2Se heterojunctions.

Photovoltaic cells have been fabricated by forming layers of p-type Cu_2Se onto n-type single crystal CdSe cells. Those produced on as-grown low resistivity CdSe crystal substrates exhibited no rectification. However good photovoltaic properties were produced by heating the cells in air at 200°C for 30 minutes, when values of V_{oc} of 200mV and of J_{sc} of 8mA cm^{-2} were obtained under AM1 illumination. Heterojunctions formed on higher resistivity CdSe prepared by heating as-grown crystals in selenium vapour produced cells which showed an optimum photovoltaic effect immediately, with V_{oc} = 200 mV and J_{sc} = 8mA cm^{-2}. The spectral response of devices formed on both types of CdSe substrates exhibited peaks at 1.21, 1.52 and 1.81eV.

References

(1) Goryunova, N.A., Frank-Kamenetskii, V.A., and Fedorova, N.N., (1955), Zhur. Tehk. Fiz. 25, 2419.

(2) Title, R.S., (1963), Phys. Rev. 130, 17.

(3) Kolomiets, B.T. and Chun-ming Lin, (1960), SOV. Phys: Solid State 2. 154.

(4) Pashinkin, A.S., and Sapozhnikov, R.A., (1962), Sov. Phys. Cryst., 7, 501.

(5) Ray, B., (1969), "II-IV Compounds", Pergamon Press, Oxford.

(6) Masayuki Itakura and Hirou Toyoda, (1965), Jap. J. of Applied Physics, 4, 560.

(7) Burmeister, R.A. Jr., and Stevenson, D.A., (1967), Phys. Stat. Sol. 24, 683.

(8) Wheeler, R.G. and Dimmock, J.C., (1962), Phys. Rev. 125, 1805.

(9) Forgue, S., Goodrich, R. and Cope, A., (1951), RCA Review 12, 325.

(10) Reimers, P., (1969), Phys. Stat. Sol. 35, 707.

(11) Burger, A., Roth, S.M., (1984), J. Crystal growth, 70, 386.

(12) Al-Bassam, A., Brinkman, A.W., Russell, G.J. and Woods, J.,(1985), British Assoc. Crystal Growth Conf. Brighton, 1985.

(13) Budennaya, L.D., Nizkova, A.I., Pekar, G.S. and Polisskii, G.N., ;(1982), Izvestiya Akademii Nauk. SSR, Neorgunicheskie Materily, V.18, No. 6, 908.

(14) Hill, R., (1974), J. Phys. C:Solid State Phys., vol. 7, 521.

(15) Hartman, H., Mach, R., Selle, B., (1982), Current Topics in Material Science, (North Holland) ed. E. Kaldis, 1.

(16) Idrichan, G.Z., and Sorkin, G.P., (1975), Izvakad Nauk SSR Neorgmater, 9, 1693.

(17) Efendiev, G.A. and Kazinets, M.M., (1960), Izv. Akad. Nauk. Azcrb, SSR, Ser. Fiz-Mat., Itekn. Nauk. No. 5, 91.

(18) Stevels, A.L.N. and Jellinek, F., (1971), Rec. Trav. Chim. Vol. 90, Part 3, 273.

(19) Konev, V.N. and Kudinova, V.A., (1973), Izv. Akad. Nauk. SSR, Neorg. Mater, Vol. 9, Part 7, 1132.

(20) Tonejc, A., Ogorelec, Z., and Estnik, B.M., (1975), J. Appl. Crystal, 8, 375.

(21) Shafizade, R.B., Ivanova, I.V. and Kazinets, M.M., (1976), Thin Solid Films, 35, 169.

(22) Shafizade, R.B., Ivanova, I.V., and Kazinets, M.M., (1978), Thin Solid Films, 55, 211.

(23) Rahlfs, P., (1936), Z. Physik, Chem. (B), 31, 157.

(24) Sorkin, G.P., Papshev, Yu.M., and Oush, P.T., (1965), FTT Soviet Physics-Solid State, vol. 7, 1810.

(25) Komashchenko, V.N. and Fedorus, G.A., (1968), Ukv. Fixz. Zh., 13, 688, (Ukr. Phys. J., 13, 486).

(26) Komashchenko, V.N. and Fedorus, G.A., (1967), Soviet Physics Semiconductors, I, 411.

(27) Komashchenko, V.N. and Fedorus, G.A., (1970), Soviet Physics Semiconductors, Vol. 3, No. 8, 1001.

(28) Ture, I.E., Russell, G.J. and Woods, J.,(1985), 6th. EEC Photovoltaic Conf., London, 861.

(29) Voskanyan, A.A., Inglizyan, P.N.,Lalykin, S.P., Plutto, I.A. and Shevchenko, Ya. M., (1978), Sov. Phys. Semicond. 12, 1251.

(30) Bonnet, D., (1978), Proc. Photovoltaic Solar Energy Conf., Dirdrecht, Boston, 630.

(31) Bonnet, D., (1979), Proc. 2nd Photovoltaic Solar Energy Conf., W. Berlin, 387.

(32) Rickus, E., Bonnet, D., (1980), Proc. 3rd E.C. Photovolt. Solar Energy Conf., Cannes, 871.

(33) Rickus, E., (1983), 5th E.C. Photovoltaic Solar Energy Conf., Athens,746.

(34) Rickus, E., Richter, H., (1985), 6th E. Photovoltaic Solar Energy Conf., London,856.

(35) Richter, H., Hewig, G.H., (1986), 7th E. Photovoltaic Solar Energy Conf., Sevilla, Spain,470.

(36) Komashchenko, V.N., Lukyanchikova, N.B., Fedorus, G.A. and Sheinkman, M.K. (1971), Proc. Intern. Conf. Phys. and Chem. Semiconductors, Heterojunction Layer Structure, Akademia Kiado, Budapest, 213.

CHAPTER 3

Background Theory

3.1 Introduction

This chapter reviews the theory used in the analysis of the results obtained from the Schottky diode and heterojunction structures. Three methods of determining the Schottky barrier height in metal-semiconductor junctions are described in this chapter. The effects of interfacial states on parameters such as barrier height are then considered.

3.2 Metal semiconductor Barriers

3.2.1 The Schottky model

When a metal with a work function Φ_m is brought in contact with a semiconductor having a work function Φ_s, which is less than that of the metal, electrons pass from the semiconductor into the metal until the Fermi levels are aligned and thermal equilibrium is established. The situation is illustrated in Figure 3.1 for an n-type semiconductor and shows that the region near the junction becomes depleted of charge carriers, in this case electrons. Thus a negative charge on the surface of the metal is balanced by a positive charge in the semiconductor. Since the latter is n-type, the positive charge will be provided by the uncompensated donor atoms left by the transfer of

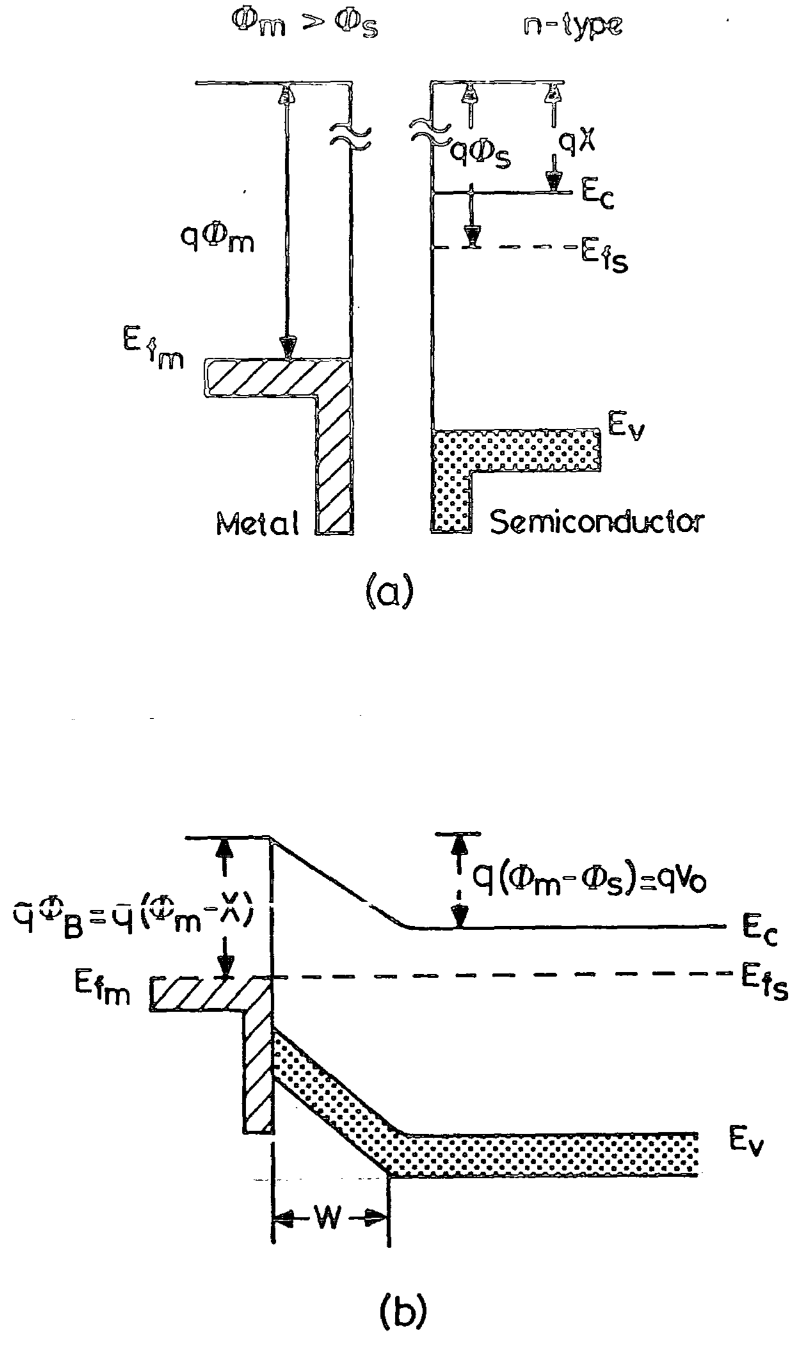

Figure 3.1 A Schottky barrier formed by contacting an n-type semiconductor with a metal having a larger work function:
(a) band diagrams for the metal and the semiconductor before joining;
(b) equilibrium band diagram for the junction.

electrons to the metal, and the bands are bent upwards as a result.

The equilibrium contact potential V_o, which prevents any further net electron diffusion from the semiconductor conduction band into the metal, is given by$^{(1-5)}$.

$$V_o = \Phi_m - \Phi_s \qquad (3.1)$$

and the potential barrier height Φ_{BN} for electron injection from the metal into semiconductor conduction band is given by

$$\Phi_{BN} = (\Phi_m - X_s) \qquad (3.2)$$

$$= V_o + (E_C - E_F) \qquad (3.3)$$

where $X_s = \Phi_s - (E_C - E_F)$ is called the electron affinity and is measured from the semiconductor conduction band edge to the vacuum level.

For an ideal contact between a metal and a p-type semiconductor, the barrier height Φ_{BP} is given by

$$\Phi_{BP} = E_g - (\Phi_m - X_s) \qquad (3.4)$$

For a given semiconductor and for any metal, the sum of the barrier heights on n-type and p-type substrates is thus expected to be equal to the band gap or

$$q(\Phi_{Bn} + \Phi_{BP}) = Eg \qquad (3.5)$$

3.2.2 Schottky effect

The Schottky effect is the image force induced lowering of the potential energy barrier for charge carrier emission when an electric field is applied. Thus electrons being emitted from a metal cathode into a vacuum see a barrier which depends upon the field strength at the cathode surface. The Schottky equation for this effect will be developed with respect to emission into vacuum and then transferred to the emission of electrons from a metal into a semiconductor.

The Fermi level of the metal will lie at an energy equal to the work function energy Φ'_{WF} below the vacuum level. When a charge-q is placed at a distance X from the metal, (Figure 3.2(a)) all the resulting field lines must be normal to the surface, since the metal is a good conductor. These field lines act as if an equal and opposite charge (the image charge) + q were situated at a distance - x (Figure 3.2(a)).

Hence the force acting on the electron at x is the same as if the metal surface were replaced by a charge + q at - x. From Coulomb's Law, the force attracting the electron to the metal is therefore

$$F = -q^2/4\pi\epsilon_0\ (2x)^2 \qquad (3.6)$$

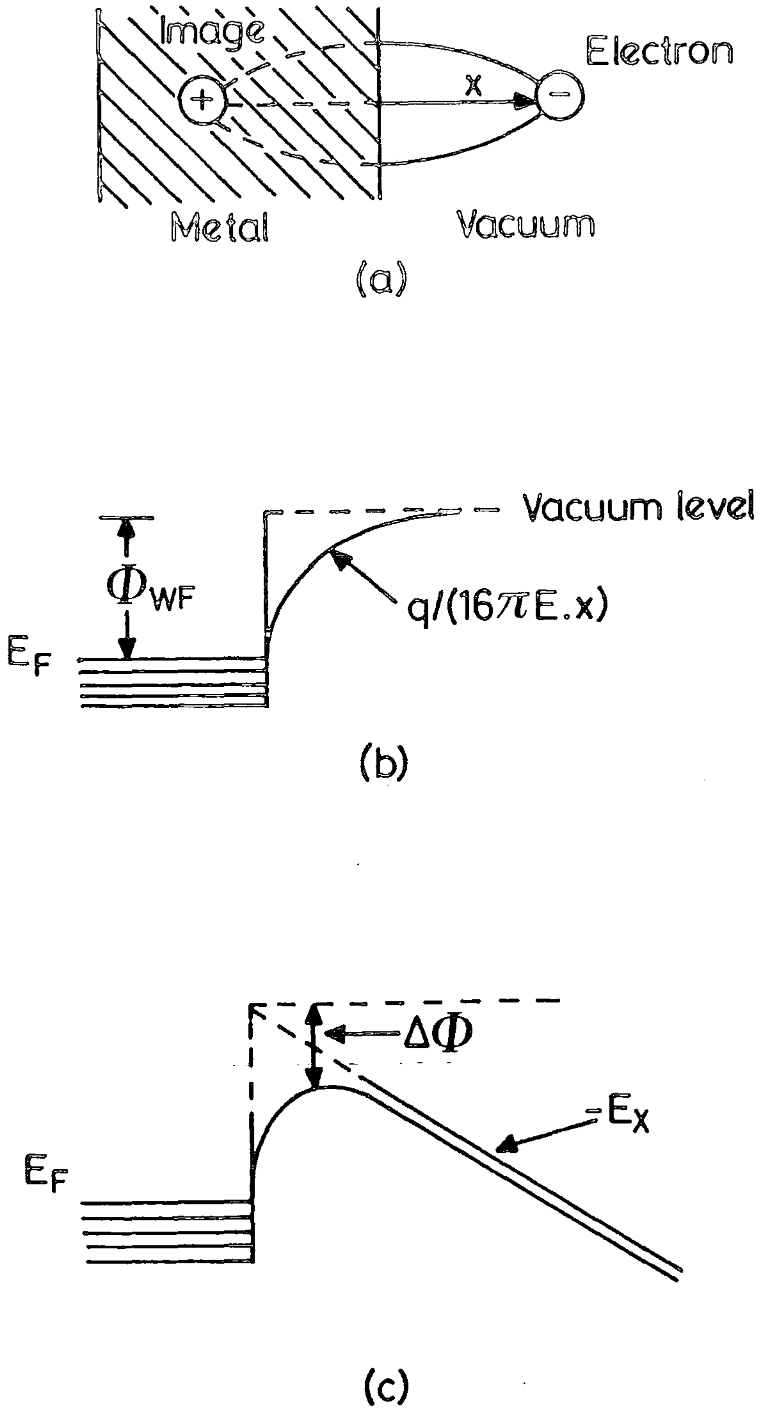

Figure 3.2 Barrier at a metal-vacuum interface.

(a) electron in vacuum with image charge in the metal.
(b) electron energy barrier in the absence of applied field.
(c) external applied field, E, reduces the barrier height by $\Delta\phi$.

where ϵ_0 is the dielectric constant of free space.

The potential energy of the electron at a distance X is therefore

$$E(x) = \int_{\infty}^{x} F.dx = - q^2/16\pi\epsilon_0 X \qquad (3.7)$$

and when an external field E is applied, the total potential energy PE as a function of distance is given by the sum

$$PE(x) = \frac{q^2}{16\pi\epsilon_0 x} + qE_x \qquad (3.8)$$

This has a maximum value at a value of x given by

$$X_m = \sqrt{\frac{q}{16\pi\epsilon_0 E}} \qquad (3.9)$$

Since this is not at the surface, there must be a reduction in the barrier by an amount $\Delta\phi$eV where

$$\Delta\phi = \sqrt{\frac{qE}{4\pi\epsilon_0}} = 2EX_m \qquad (3.10)$$

3.2.3 Capacitance of Schottky diodes:-

The differential capacitance can easily be expressed in terms of the diffusion voltage and donor density if the effect of the holes can be neglected.

The electric field at the interface will be due only to the uncompensated donors and is given by$^{(1)}$

$$E^2_{max} = \frac{2q}{\epsilon_s}\left\{N_d\left\{V_d - \frac{kT}{q}\right\} + \frac{kTN_d}{q}\exp\left\{-q\,V_d/kT\right\}\right\} \qquad (3.11)$$

where V_d is the diffusion voltage associated with the reverse bias V_r. If $qV_d > 3kT$ the last term in the bracket is negligible and

$$E^2_{max} = \frac{2qN_d}{\epsilon_s}\left(V_d - \frac{kT}{q}\right) \qquad (3.12)$$

From Gauss's theorem the charge due to uncompensated donors is given by

$$Q_d = \epsilon_s E_{max} = (2q\epsilon_s N_d)^{\frac{1}{2}}\left(V_d - \frac{kT}{q}\right)^{\frac{1}{2}} \qquad (3.13)$$

so that the capacitance is given by

$$C = \frac{dQ_d}{dV_r} = \frac{dQ_d}{dV_d} \qquad (3.14)$$

and also

$$C = \left(\frac{q\varepsilon_s N_d}{2}\right)^{\frac{1}{2}}\left(V_d - \frac{kT}{q}\right)^{-\frac{1}{2}} \qquad (3.15)$$

Since $V_d = V_{d_o} + V_r$, where V_{d_o} is the diffusion voltage at zero bias, equation (3.15) may be written

$$C = \left(\frac{q\varepsilon_s N_d}{2}\right)^{\frac{1}{2}} \left(V_{d_o} + V_r - \frac{kT}{q}\right)^{-\frac{1}{2}} \qquad (3.16)$$

or $$N_d = \frac{2}{q\varepsilon_s} \frac{V_d}{\left(C^{-2}\right)} \qquad (3.17)$$

If N_d is a constant throughout the depletion region then measuring the variation in the capacitance with reverse bias will give a straight line relationship when plotted in the form of $1/C^2$ versus V.

The barrier height $\phi_{b\ c-v}$ and the donor density N_d may then be estimated from the intercept on the voltage axis and the slope (equation 3.17) respectively.

3.2.4 Current-voltage relationship

Metal-semiconductor contacts are majority carrier devices, with little if any minority carrier injection being possible. There are four main current transport processes (Figure 3.3) in forward bias. For an n-type semiconductor these are:

(1) Emission of electrons from the semiconductor over the potential barrier into the metal.

(2) Quantum-mechanical tunnelling of electrons through the barrier.

(3) Recombination in the space charge region.

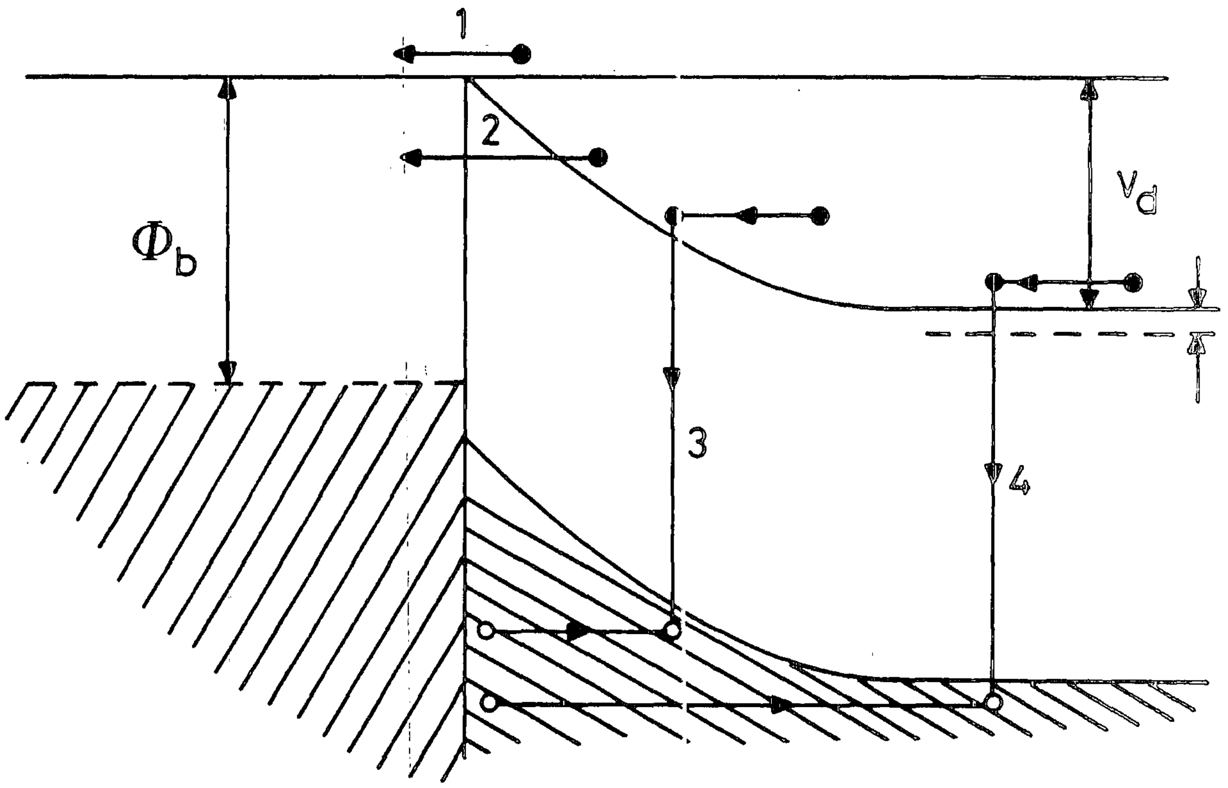

Figure 3.3 Transport processes in a forward-biased Schottky barrier.

(4) Hole injection from the metal to the semiconductor. Process (1) is the dominant mode and is utilised in practical Schottky diodes.

Processes 2,3 and 4 result from departures from the ideal behaviour . Before an electron can be emitted over the barrier into the metal, it must first be transported through the depletion region from the bulk of the semiconductor to the interface. This process is governed by the usual mechanisms of diffusion and drift(3). On arrival at the barrier, the electron must then have sufficient thermal energy to surmount the barrier into the metal.

The first theory of conduction in Schottky diodes (the diffusion theory) was developed by Wanger(6) and Schottky and Spenke(7) and assumed that the current was limited by diffusion and drift in the depletion region. Subsequently Bethe(8) developed a theory founded on the premise that it was thermionic-emission over the barrier that was limiting the current flow. In this case the current-voltage characteristics are given by:

$$J = J_s \left[\exp(qV/kT) - 1\right] \qquad (3.18)$$

where

$$J_s = A^{**}T^2 \exp\left[\frac{-q\phi_{bn}}{kT}\right] \qquad (3.19)$$

where J_s is the reverse saturation current and A^{**} is the modified Richardson constant, given by:-

$$A^{**} = 4\pi q m^* k^2/h^3 \simeq 120 \; m^*/m_o \; \text{amp/cm}^2.\text{K}^2 \qquad (3.20)$$

where m^* is the electron effective mass.

Thus $A^{**} = 15.6$ amp/cm^2 K^2 for CdSe and ZnSe since $m^*/m_o = 0.13$ for CdSe and ZnSe$^{(9,10)}$. On the other hand the diffusion theory leads to the following expression. If the space charge region is greater than the diffusion length:

$$J = qN_c \, \mu_e \, E_{max} \exp\left[\frac{-q\phi_B}{kT}\right]\left[\exp\left[\frac{qV}{kT}\right]-1\right] \qquad (3.21)$$

Here E_{max} is the maximum electric field at the junction, μ_e the electron mobility and N_c is the effective density of states in the conduction band

$$N_c = 2\left(\frac{2\pi m^* kT}{h^2}\right)^{3/2} \qquad (3.22)$$

A number of authors have combined the thermionic emission and the diffusion theories by assuming the two mechanisms to be in series and then effectively finding the position of the quasi-Fermi level at the interface. The complete theory is that worked out by Crowell and Sze$^{(11)}$ who found that the current density is given by

$$J = \frac{qN_C \upsilon_r \{\exp(-q\phi_m/kT)\,[\exp(qV/kT)-1]\}}{1+\frac{\upsilon_r}{\upsilon_d}} \qquad (3.23)$$

where υ_d is the effective velocity due to drift and diffusion of electrons at the top of the barrier, and υ_r is the effective recombination velocity and is given by

$$\upsilon_r = (kT/2m^*\pi) = A^{**}\,T^2/qN_C \qquad (3.24)$$

The experimental forward characteristic can be written in the form

$$J = J_o\,[\exp(qV/nkT)-1] \qquad (3.25)$$

n is often called the ideality factor. If $d\phi_b/dV$ is constant, n is also constant. For values of V greater than 3kT/q the J-V relationship according to thermionic emission theory is given by(3)

$$J = J_o\,\mathrm{EXP}\,(qV/nkT) \qquad (3.26)$$

Thus a plot of lnJ against V should result in a straight line, with a slope given by q/nkT. The intercept of the straight line on the vertical axis gives the value of J_o.

3.2.5 Measurement of Barrier height

Three methods have been used to determine the barrier height ϕ_b of a metal semiconductor contact. These are: the determination of ϕ_{bn} from the saturation current density J_s-V, the measurement of threshold V_{ph} for the photoexcitation of carriers over the barrier, and the measurement of the depletion capacitance as a function of bias voltage[9-17].

(a) Current Voltage Measurement.

The barrier height of a Schottky diode can be determined from the forward bias I-V characteristics. According to the thermionic emission theory, the forward biased current density is:-

$$J = J_o \exp (qV/nkT) \{1-\exp(-qV/kT)\} \qquad (3.27)$$

where n is approximately independent of V and is greater than unity. For values of V greater than 3kT/q, equation 3.27 can be written in the approximate form:

$$J = J_o \exp (qV/nkT) \qquad (3.28)$$

and a plot of lnJ against V in the forward direction should give a straight line.

Thus the ideality factor is given from Equation (3.28)

$$n = \left\{\frac{d\,\{\ln J\}}{dV}\right\}^{-1} \frac{q}{kT} \qquad (3.29)$$

and the barrier height can be obtained from the equation

$$\phi_{bn} = \frac{kT}{q} \ln \left\{ \frac{A^{**}T^2}{J_s} \right\} \qquad (3.30)$$

where J_s the saturation current density.

(b) Capacitance-Voltage Measurement.

The barrier height can also be determined by capacitance measurements. The differential capacitance associated with the depletion region of a schottky barrier is given by equation (3.16). Thus if N_d is constant in the depletion region, a plot of $1/C^2$ against V should give a straight line with slope of $2/q\epsilon_s N_d$ and negative intercept $(-V_I)$ on the V_r axis equal to $-V_{do} + kT/q$.

Then:

$$V_{do} = V_I + kT/q \qquad (3.31)$$

The barrier height is given by:

$$\phi b_{c-v} = V + (E_c - E_f) \qquad (3.32)$$

where $E_c - E_f$ is difference between the Fermi energy and the conduction band edge, and is given by

$$E_c - E_f = \frac{kT}{q} \ln \frac{N_c}{N_D} \tag{3.33}$$

(c) Photoelectric Measurements

The barrier height may also be obtained from photoelectric measurements. This provides an accurate and direct method of determining the barrier height.

When monochromatic radiation with quantum energy exceeding $(\phi_b - \Delta\phi_{bi})$ is incident on the metal surface electrons are excited from the Fermi level of the metal into the semiconductor, generating a photocurrent in an external circuit.

According to Fowler(118) the photocurrent per absorbed photon of energy $h\upsilon$ is given by

$$R \simeq B[\pi^2/6 + x^2/2 - (e^{-x} - e^{-2x}/4 + e^{-3x}/9 \ldots]$$

$$\text{for } x > 0 \tag{3.34}$$

$$\text{where } B = T^2/\sqrt{E_s - h\upsilon} \tag{3.35}$$

Where $h\upsilon_o$ is the barrier height $(q\phi_{bn})$, E_s the sum of $h\upsilon_o$ and the Fermi energy (measured from the bottom of the metal conduction band) and

$$x = h(\nu - \nu_o)/kT \qquad (3.36)$$

Under the condition that $E_s \gg h\upsilon$, and $x > 3$ the equation reduces to:

$$R \simeq C\,(h\nu - h\nu_o)^2 \text{ where C is a constant} \qquad (3.37)$$

$$\text{for } h(\nu - \nu o) > 3kT$$

Thus a plot of the square root of the photoresponse against photon energy should give a straight line, with an extrapolated intercept on the energy axis equal to the effective barrier height.

3.3 Surface states and Rectification at a metal semiconductor contact

In 1947 Bardeen$^{(19)}$ proposed a theory to explain the rectification characteristics of a metal-semiconductor junction. He showed that if the density of surface states with energies in the forbidden band is sufficiently high ($> 10^{12}/cm^2$), then there will be a dipole layer at the free surface of the semiconductor formed from the charge localised in the surface states and an induced space charge of opposite sign. This dipole layer tends to make the work function independent of the position of the Fermi level in the interior of the semiconductor.

Suppose that the metal and the semiconductor remain separated by a thin insulating layer as illustrated in Figure 3.4, then in the absence of surface states, the negative charge Q_m on the surface of the metal must be equal and opposite to the positive charge Q_d due to the uncompensated donors. However, if there is a continuous distribution of surface states, characterised by some neutrality level ϕ_o, then the neutrality condition becomes

$$Q_m + Q_d + Q_{ss} = 0 \qquad (3.38)$$

where Q_{ss} is the charge in the surface states up to the neutrality level.

The occupancy of the surface states is determined by the Fermi level, and for most purposes it is good enough to use the absolute zero of temperature approximation, where the states are assumed to be filled up to the Fermi level and empty above it. Thus if the neutrality level ϕ_o happens to lie above the Fermi level E_f then the surface states will contain a net positive charge and Q_d must therefore be less than if the surface states were absent. This suggests that the width W of the depletion region and the associated band bending will be correspondingly reduced. As a result the barrier height ϕ_b will be reduced. On the other hand, if ϕ_o happens to lie below E_f, Q_{ss} is negative and Q_d must be larger than if surface states were absent. Hence both W and

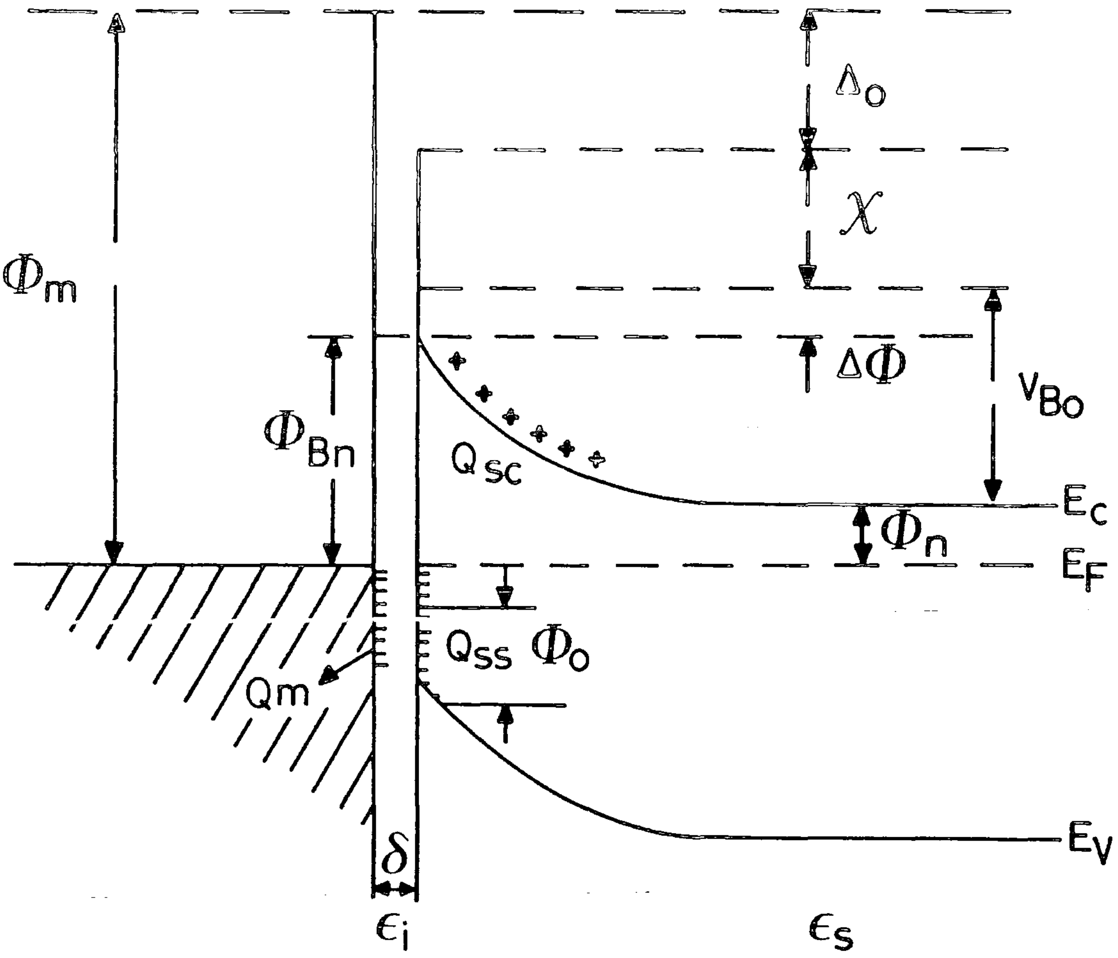

Figure 3.4 Energy band diagram of a metal n-type semiconductor contact with an interfacial layer. (After Cowley and Sze[(20)]

ϕ_b will be increased such that ϕ_o is raised towards the Fermi level, E_f.

If the density of surface states is very large and $\phi_o \simeq E_f$. Then the barrier height will be given by

$$\phi_b \simeq E_g - \phi_o \tag{3.39}$$

The interfacial layer is assumed to have a thickness of a few Angstroms and so may be assumed to be transparent to an electron whose energy is greater than the potential barrier. We first consider a semiconductor with a uniform density of acceptor surface states D_s ($cm^{-2}eV^{-1}$), in the energy range from $q\phi_o$ to the Fermi level. The surface-state charge density on the semiconductor Q_{ss} is then given by

$$Q_{ss} = - q\, D_s \left(E_g - q\phi_o - q\phi_{Bn} - q\Delta\phi\right) \tag{3.40}$$

where $q\Delta\phi$ is the schottky-barrier lowering. The quantity in parenthesis is simply the difference between the Fermi level at the surface and $q\phi_o$. Multiplied by D_s, this quantity yields the actual number of surface states above $q\phi_o$ that are full.

The space charge in the depletion layer of the semiconductor at thermal equilibrium is given by $^{(20)}$

$$Q_{sc} = 2q\varepsilon_s\, N_D \left(\phi_{Bn} - V_n + \Delta\phi - kT/q\right) \tag{3.41}$$

The potential across the interfacial layer can be obtained by application of Gauss's Law to the surface charge on the metal and the semiconductor

$$\mathbb{L} = - \delta \frac{Q_m}{\varepsilon_i} \tag{3.42}$$

where ε_i is the dielectric constant of the interfacial layer and δ its thickness.

Another relation for Δ can be determined by inspection of the energy band diagram (Figure 3.4).

$$\Delta = Q_m - (X + \phi_{BN} + \Delta\phi) \tag{3.43}$$

Since at equilibrium the Fermi level must be constant through the metal-interfacial layer - semiconductor system, if Δ is eliminated from equations (3.42) and (3.43) and equation 3.38 is used to substitute for Q_m, then:-

$$(Q_m - X) - (\phi_{Bn} + \Delta\phi) = \sqrt{\frac{2q\varepsilon_s N_D \delta^2}{\varepsilon_i^2}}$$

$$\sqrt{\left(\phi_{BN} + \Delta\phi - Vn - \frac{kT}{q}\right)} - \frac{qD_s\delta}{\varepsilon_i}\left\{Eg - q\phi_0 - q\phi_{BN} - q\Delta\phi\right\}$$

(3.44)

which may be solved for ϕ_{BN}. Introducing the quantities

$$C_1 = \frac{2q\epsilon_s N_d \delta^2}{\epsilon_i^{\,2}} \tag{3.45a}$$

$$C_2 = \frac{\epsilon_i}{\epsilon_i + q^2 \delta D_s} \tag{3.45b}$$

gives for the barrier height:-

$$\phi_{BN} = \Big(C_2(\phi_m - X) + (1 - C_2)(E_g/q - \phi_o) - \Delta\phi\Big)$$

$$+ \left[\frac{C_2^{\,2} C_1}{2} - C_2^{\,3/2}\left[C_1(\phi_m - X) + (1 - C_2)\right.\right.$$

$$\left.\left.(E_g/q - \phi_o)\frac{C_1}{C_2} - \frac{C_1}{C_2}(V_n + kT/q) + \frac{C_2\, C_1^{\,2}}{4}\right]^{\frac{1}{2}}\right] \tag{3.46}$$

The dielectric constant of such a thin layer may be approximated by the free space value, $\varepsilon_1 = \varepsilon_o$, (since this approximation represents a lower limit for ε_i, it leads to an overestimation of C_2) and setting $\varepsilon_s \simeq 10\ \varepsilon_o$ $N_d < 10^{18}$ cm^{-3}, C_1 is small of the order 0.01V, and there the term in the curly brackets in equation (3.46) may be neglected to give:

$$\phi_{BN} = C_2\ (\phi_m - X) + (1 - C_2)\ (E_g/q - \phi_o)\ - \Delta\phi$$

$$= C_2\, \phi_m + C_3 \tag{3.47}$$

If C_2 and C_3 can be determined experimentally and if χ is known, then

$$\phi_o = E_g/q - \frac{C_2\chi + C_3 + \Delta\phi}{1 - C_2} \qquad (3.48)$$

and from equation (3.45b)

$$D_s = \frac{(1 - C_2)\,\varepsilon_i}{C_2 \delta q} \qquad (3.49)$$

By using the previous assumptions for δ and ε_i we obtain

$$D_s \approx 1.1 \times 10^{13}\ (1 - C_2)/C_2 \qquad (3.50)$$

There are two limiting cases which may be considered from Equation (3.47).

(1) When $D_s \rightarrow \infty$, then $C_2 \rightarrow 0$

and $q\phi_{BN} = (E_g - q\phi_o) - q\Delta\phi$ (3.51)

The Fermi level at the interface in this case is pinned by the surface states at the value $q\phi_o$ above the valence band. The barrier height is independent of the metal work function and is determined entirely by the doping and surface properties of the semiconductor. This is often referred to as the Bardeen limit.

(2) When $D_S \rightarrow 0$, the $C_2 \rightarrow 1$

$$\text{and } q\phi_{Bn} = q\,(\phi_m - \chi) - q\Delta\phi \qquad (3.52)$$

This is the equation for the barrier height of an ideal Schottky barrier (equation 3.2) and is sometimes referred to as the Schottky limit. Most Schottky barrier diodes are not intimate metal semiconductor (M-S) contracts but include an interfacial layer (eg. surface oxide layer and are thus metal-interfacial layer-semiconductor (MIS) structures$^{(20)}$.

The effects of an interfacial layer on I-V characteristics have been studied by Card and Rhoderick$^{(21)}$, and on the C-V characteristics by Cowley$^{(15)}$, Crowell and Roberts$^{(22)}$ and by Fonash$^{(20)}$.

3.4 Theory of Heterojunctions

3.4.1 Anderson's Model

A heterojunction is a junction formed between two different semiconductors. When the two semiconductors have the same type of conductivity (n-n), the junction is called an isotype heterojunction. When the conductivity types differ (n-p), the junction is called an anisotype heterojunction. The absorber generator is usually a small band gap semiconductor and the collector converter will generally be a large band gap material. The energy band model of a semiconductor heterojunction was first described by Anderson in 1960$^{(24)}$. In Figure 3.5(a) the two semiconductors are assumed to have different band gap energies (Eg), different electron affinities, different work functions Φ, and different dielectric constants. The difference in energy of the conduction-band edges in the two semiconductors is represented by ΔE_C and that in the valence-band edges by ΔE_V. Figure (3.5a) shows that $\Delta E_C = (\chi_1 - \chi_2)$. When a junction is formed between these semiconductors, the energy band profile at equilibrium is as shown in Figure (3.5b) for an n-p heterojunction. Since the Fermi level must coincide on both sides in equilibrium and the vacuum level is everywhere parallel to the band edges and is continuous, the discontinuity in conduction band edges (ΔE_C) and valence band edges (ΔE_V) is invariant with doping in those cases where Eg and are not functions of doping (i.e. nondegenerate semiconductors). Then the difference in the work functions of the two materials is the total built-in voltage (Vd). Vd is equal to the same or the partial built-in voltages ($Vd_1 + Vd_2$) where Vd_1 and Vd_2 are the electrostatic potentials supported at equilibrium by semiconductor 1 and 2 respectively.

The depletion widths and capacitance can be obtained by solving Poisson's equation for the step junction on either side of the interface in the presence of an applied voltage V_a. The total width W of the transition region is just the

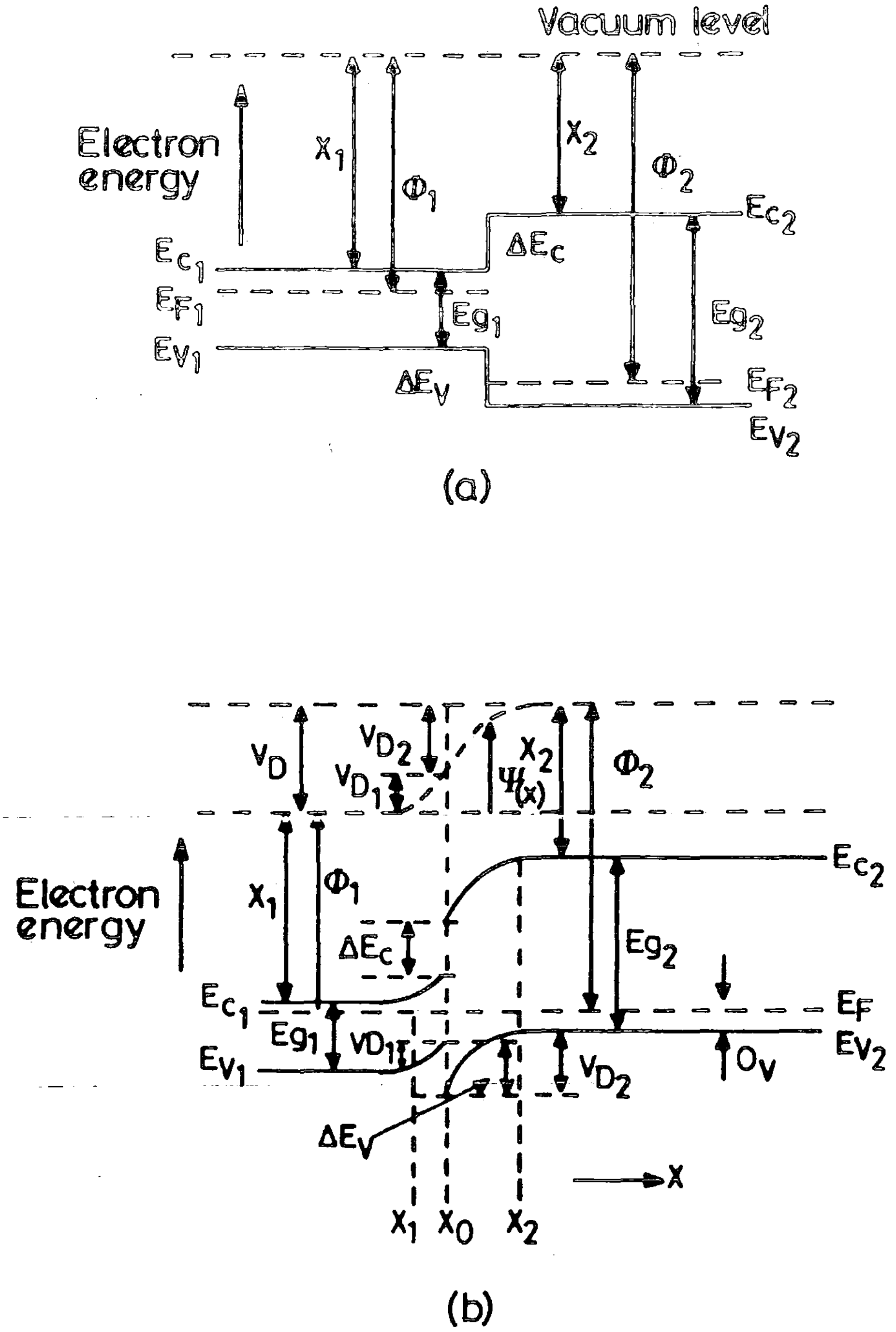

Figure 3.5 Energy band diagrams for (a) two isolated semiconductors in which space-charge neutrality is assumed to exist in every region, and (b) for a n-p heterojunction at equilibrium (after Anderson, ref. 24).

sum of the depletion regions in the p, (X_1), and n, (X_2) sides of the junctions, i.e.

$$W = X_2 + X_1 = \left[\frac{2\epsilon_1\epsilon_2 (V_d - V_a)(N_{a2}+N_{d1})^2}{q(\epsilon_1 N_{d1}+\epsilon_2 N_{a2})N_{d1}N_{a2}}\right]^{1/2} \qquad (3.53)$$

The capacitance is then:

$$C = \left[\frac{qN_{d1}N_{a2}\epsilon_1\epsilon_2}{2(\epsilon_1 N_{d1}+\epsilon_2 N_{a2})} \frac{1}{(V_d - V_a)}\right]^{1/2} \qquad (3.54)$$

The relative voltages supported in each of the semiconductors are

$$(V_{d1}-V_1)/(V_{d2}-V_2) = N_{a2}\, E_2/N_{d1}\, E_1 \qquad (3.55)$$

where V_1 and V_2 are the portions of the applied voltage V_a supported by material 1 and 2 respectively.

3.5 Solar Cell Parameters

The I-V characteristics of a solar cell are used to calculate the cell power output and conversion efficiency and hence, some of the photovoltaic parameters are defined here.

3.5.1 Short-circuit current

The short circuit current I_{sc} is the current that flows through the junction under illumination with zero applied bias and in the ideal case (if Series R_s and Shunt R_{sh} resistance effects are not present) is equal to the light-generated current I_L, and is proportional to the incident number of photons.

3.5.2.1 Open-circuit voltage

The open-circuit voltage V_{oc} at zero current through the device is given by$^{(25)}$

$$V_{oc} = (1/A)\ [(^{Isc}/I_o) + 1] \qquad (3.56)$$

where $A = q/nkT$ and I_o is the reverse saturation current..

3.5.3 Cell efficiency

Figure 3.5 shows typical current-voltage characteristics for a solar cell in the dark and under illumination. It is only that part of the characteristic which lies in the positive voltage, negative current quadrant (i.e. 4th quadrant) from which power may be extracted.

The maximum of the current-voltage product along this part of the curve corresponds to the maximum power operating point J_m, V_m. The corresponding area of the shaded rectangle represents the maximum output power of the cell, i.e.

$$P_{max} = I_m \times V_m \qquad (3.57)$$

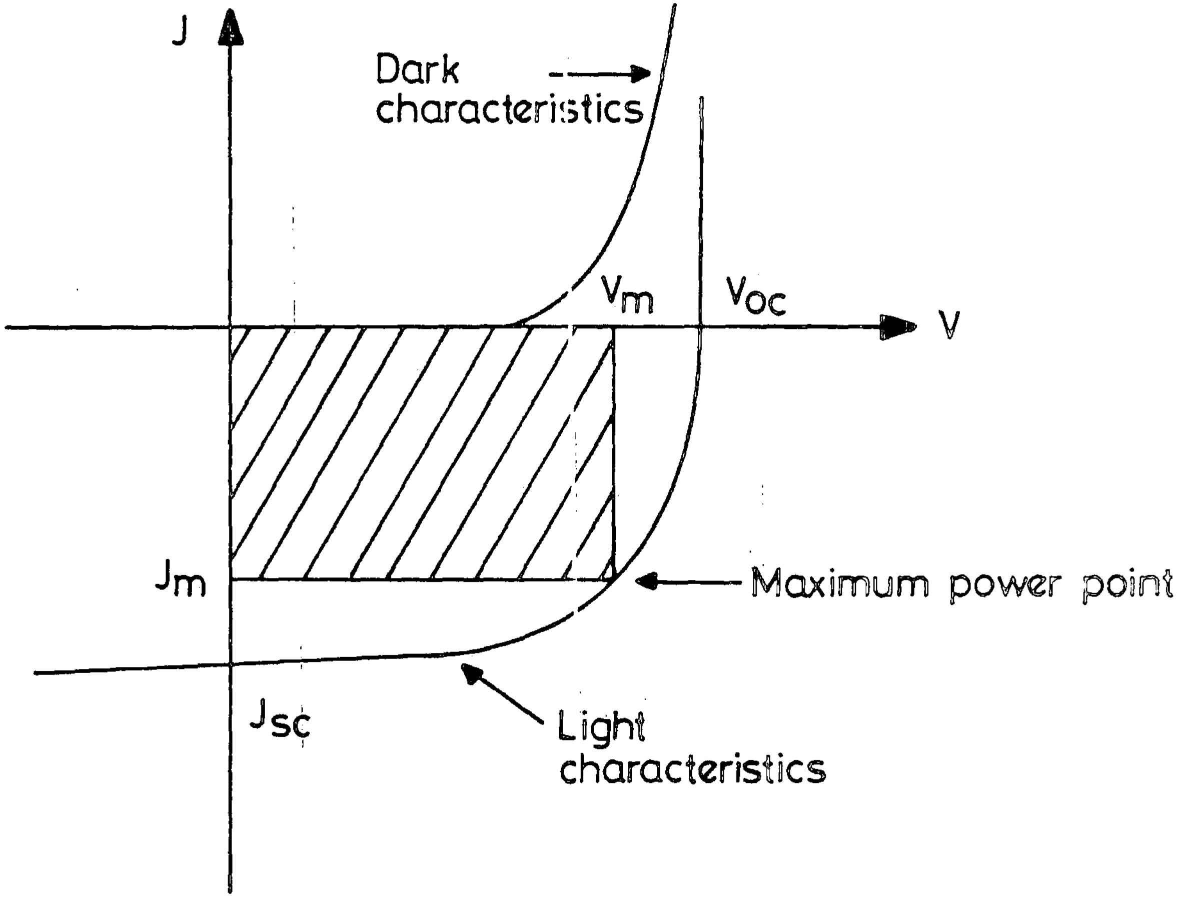

Figure 3.6 Typical dark and light J-V characteristics of solar Cell.

The ratio of $(I_m V_m)$ to $(I_{sc} V_{oc})$ is defined as the fill factor FF

$$FF = \frac{(I_m V_m)}{(I_{sc} V_{oc})} \tag{3.58}$$

The cell efficiency is computed at the maximum power point of the illuminated I-V characteristics and is given by:

$$\eta = \frac{(V_m I_m)}{P_{in}} = \frac{P_{max}}{P_{in}}$$

$$= \frac{FF\,[V_{oc} I_{sc}]}{P_{IN}} \tag{3.59}$$

where P_{in} is the incident optical power(26).

References

(1) Rhoderick, E.H., (1978), Metal-semiconductors (Oxford University Press, London.

(2) Streetman, Ben G., (1980), Solid State Electronics Devices. Prentice Hall, International editions.

(3) Sze, S.M., (1981), Physics of Semiconductor devices, John Wiley and Sons, New York.

(4) Rhoderick, E.H., (1982), IEE Proc., vol. 129, 1.

(5) Yang, Edward S., (1978), Fundamentals of Semiconductor Devices, McGraw-Hill Book Company.

(6) Wagner, C., (1931), Phys. Z., 32, 641.

(7) Schottky, W. and Spenke, E., (1939), Veroff a.d. Siemens-Werken, 18, 225.

(8) Bethe, H.A., (1942), M.I.T. Rad. Lab. Rep. 43;12.

(9) Wheeler, R.G. and Dimmock, J.O., (1962), Phys. Rev. 125, 1805.

(10) Hartmann, H., Mach, R., Selle, B., (1982), Current Topics in Material Science, (N. Holland Pub.), ed. E. Kaldis.

(11) Crowell, C.R. and Sze, S.M., (1966), Sol. Stat. Elec. 9, 1035.

(12) Goodman, A.M., (1963), J. Appl. Phys. 34, 329.

(13) White, H.G. and Logan, R.A., (1963), J. Appl. Phys. 34, 1990.

(14) Spitzer, W.G. and Mead, C.A., (1963), J. Appl. Phys. 34, 3061.

(15) Cowley, A.M., (1966), J. Appl. Phys. 37, 3024.

(16) Mead, C.A., (1966), Solid State Electronics, 9, 1023.

(17) Rideout, V.L., (1978), Thin Solid Films, 48, 261.

(18) Fowler, R.H., (1931), Phys. Rev. 38, 45.

(19) Bardeen, J., (1947), Phys. Rev. 71, 717.

(20) Cowley, A.M. and Sze, S.M., (1965), J. Appl. Phys. 26, 3212.

(21) Fonash, S.J., (1983), J. Appl. Phys. 54, 1966.

(22) Card, H.C. and Rhoderick, E.H., (1971), J. Phys. D:Appl. Phys. 4, 1589.

(23) Crowell, C.R. and Roberts, G.I., (1969), J. Appl. Phys. 40, 3726.

(24) Anderson, R.L., (1962), Solid State Electron, 5, 341.

(25) Chopra, K.L. and Das, S.R., (1983), Thin Solid Film Solar Cells, Plenum Press.

(26) Ashok, S. and Pande, K.P., (1985), Solar Cells, 14, 61.

CHAPTER 4

Experimental Methods

4.1 Introduction

This chapter is devoted to a description of the techniques employed in the fabrication of the various device structures investigated, and in their characterisation. In the first section a brief summary is given of the crystal growth procedures, together with the methods used for determining lattice parameters and controlling resistivity. This is followed by a description of the formation of ohmic contacts to the devices. The next sections review the principles of scanning electron microscopy (SEM), reflection electron diffraction (RHEED), and energy dispersive X-ray analysis (EDAX). The final part of the chapter is concerned with the techniques for device characterisation, i.e. J-V, C-V, photocapacitance and spectral response measurements.

4.2 Crystal Growth

The single crystals (Cd,Zn)Se reported in this study, were all grown from the vapour phase. The source materials used were ZnSe (polycrystalline lump grade) supplied by Merck, and CdSe which had been synthesised from the elements (6 nines purity) in this laboratory. In the case of the ternary crystals, appropriate quantities of the two binary compounds were weighed out and thoroughly mixed before being loaded into the crystal growth capsules.

The crystal growth procedures used during the course of this study have been in regular use at Durham for the growth of a wide range of the II-VI compounds, and full details have been published elsewhere$^{(1)}$. Briefly two techniques were used, a closed tube method developed at Durham by Clark and Woods$^{(2)}$ (and referred to in this thesis as the Durham method), and the technique developed by Piper-Polich$^{(3)}$. Both techniques were capable of yielding crystal boules 1cm in diameter and 4cm in length, containing just a few large grains of good quality.

4.2.1 The Clark-Woods or "Durham" Method

The technique used for the growth of single crystal (Cd,Zn)Se was developed by Clark and Woods$^{(2)}$. This method employs a specially designed, evacuated and sealed silica capsule as shown in Figure 4.1. A few pieces of high purity selenium or cadmium as required were held in the long tail of the reservoir tube, which is connected to the growth ampoule via a narrow orifice. The polycrystalline charge of CdSe and ZnSe is then added and the tube evacuated and sealed by a specially designed growth tip. The sealed capsule is suspended vertically in a double zone furnace, such that the growth tip is located at the hottest point of the main furnace, while the tail, containing a reservoir of cadmium or selenium, is maintained at the appropriate temperature for optimum growth, by the lower furnace. The tube is then

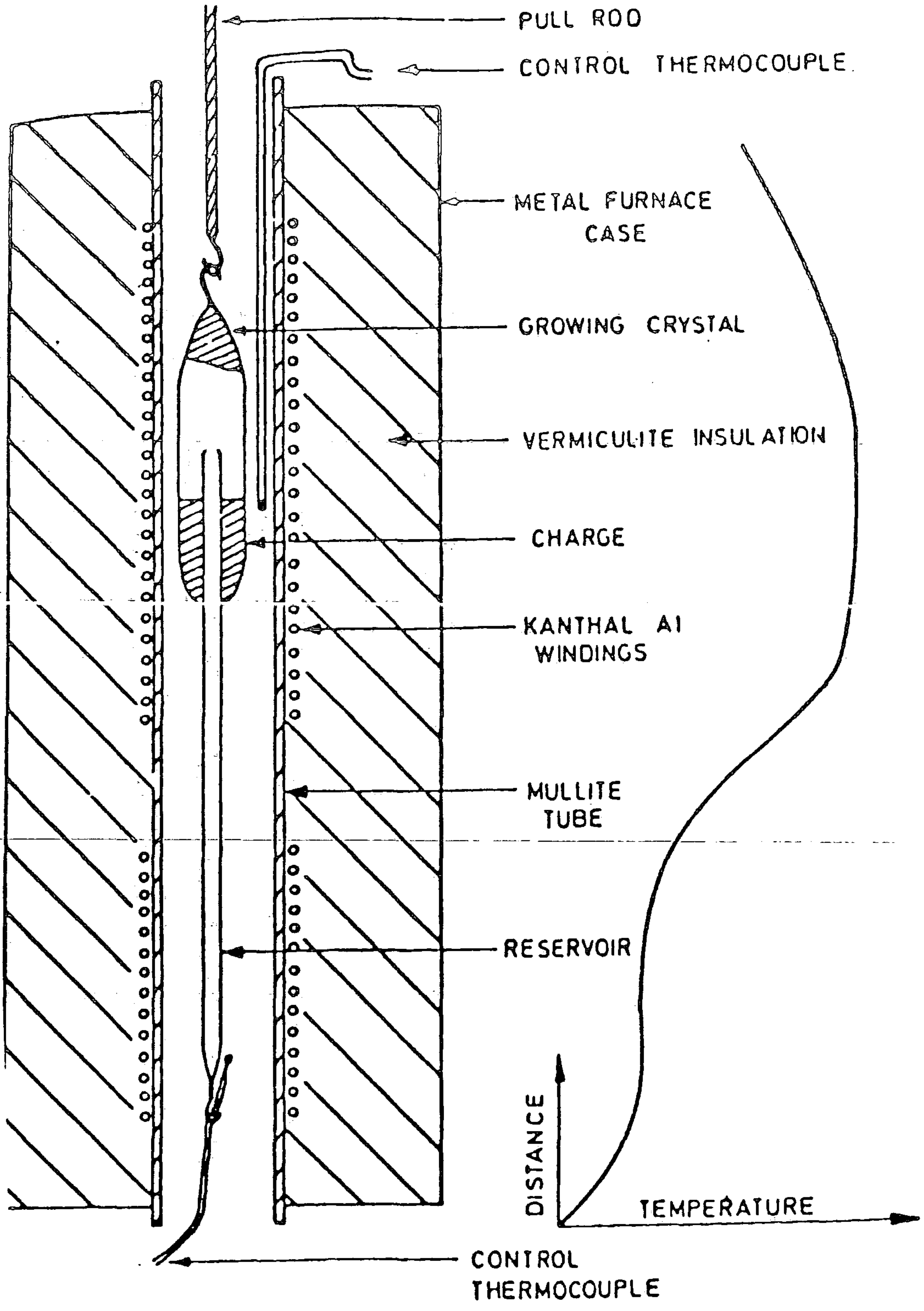

Figure 4.1 The Clark-Woods method.

raised slowly (1.5mm h^{-1}) through the temperature profile and mass transfer from the charge to the growth tip commences when a suitable temperature difference is established between the tip and the charge. As the capsule is pulled through the temperature gradient, the tip-charge temperature difference gradually increases until it reaches 40^{o} - $50^{o}C$, when the pull is switched off and the crystals are then left to grow for a further few days. Finally, the crystals are cooled slowly to room temperature in a controlled manner over a period of three days.

4.2.2 The Piper-Polich Method

This is a self-sealing method of crystal growth which is a modification of the technique developed by Piper and Polich(3). A typical arrangement for the growth system is shown in Figure 4.2. In this method the design of the silica growth capsule is much simpler. The tube is sealed at one end, and the other is pulled out into a long thin tube, and two or three constrictions are made in it. The capsule is loaded with the charge and placed in a horizontal furnace such that a temperature difference of $40^{o}C$ to $50^{o}C$ exists across the capsule, with the charge end at the hottest zone of the furnace. Vapour phase transport occurs from the charge to the constrictions in the narrow bore silica tubing at the neck of the capsule. These become blocked and the capsule is thus effectively sealed off in an ambient of argon at about atmospheric pressure. Nucleation and growth proceed at the cooler end of the main body of the capsule,

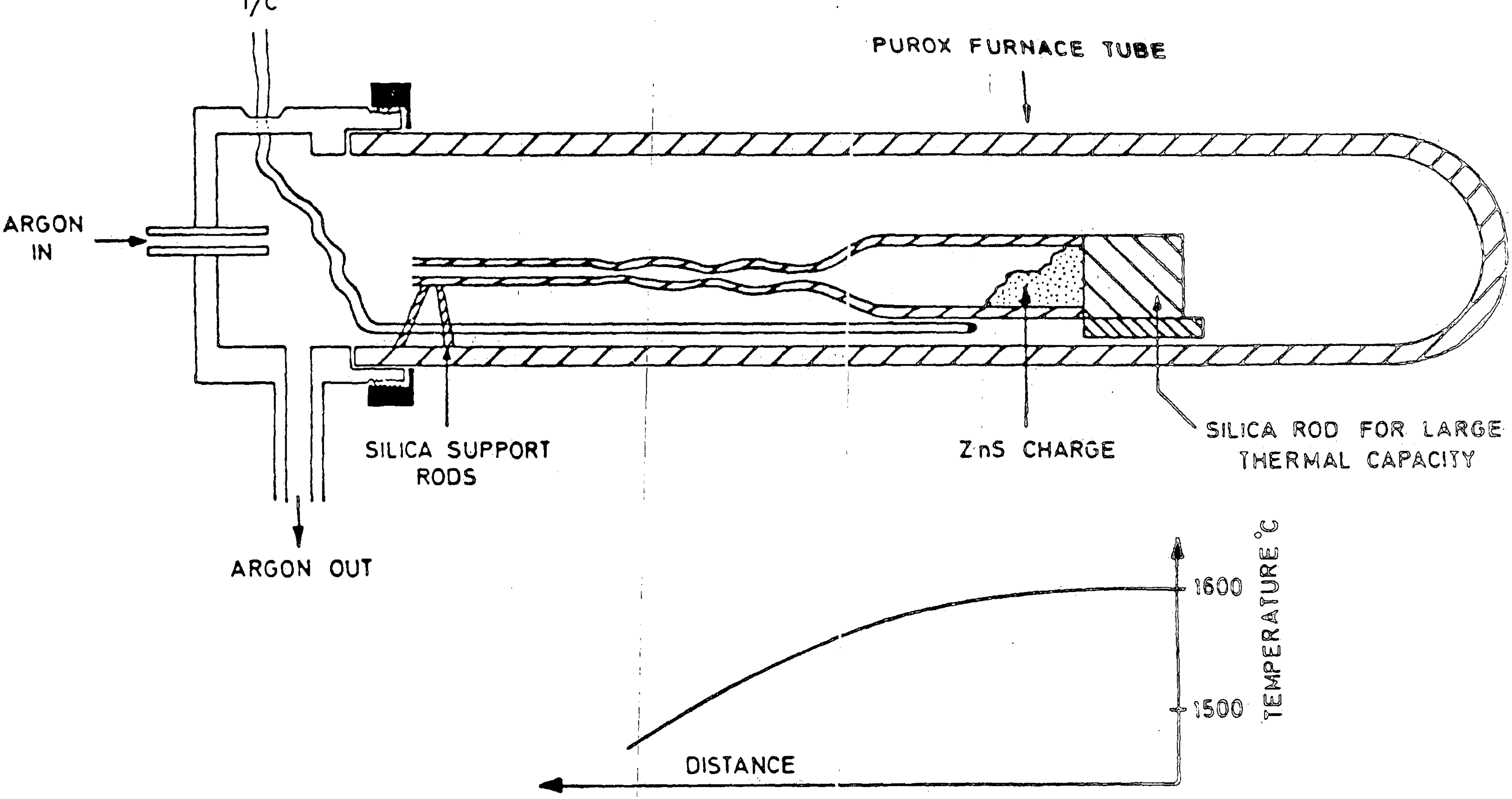

Figure 4.2 The Piper-Polich method.

and transport is complete in about three days.

4.3 X-ray Diffractometry

X-ray powder photography was used to determine the lattice parameters and the structure of the (Cd,Zn)Se mixed crystals. This was done using a Philips PW 1130 diffractometer with cobalt Kα radiation of average wavelength 1.7902Å. It was operated with target voltage and current of 40kV and 20mA respectively.

The films were deposited on glass substrates which were then mounted in the sample chamber of the diffractometer. X-ray diffraction scans were recorded from $2\theta = 20^{o}$ to $2\theta = 80^{o}$ and the interplanar spacing d_{hkl} was found from Bragg's Law(4).

$$\lambda = 2d_{hkl}\sin\theta \qquad (4.1)$$

where θ is the diffraction angle. Then for hexagonal crystals (characterised by two variable parameters a and c). The interplanar spacing(4) is related to a and c by:

$$\frac{1}{d_{hkl}^2} = \frac{4(h^2 + hk + k^2)}{3a^2} + \frac{l^2}{c^2} \qquad (4.2)$$

4.4 Annealing in Selenium or Cadmium vapour

As grown single crystals of $Cd_{1-x}Zn_xSe$ were normally very conductive ($\rho = 10^{-2}$ Ωcm) for Cd rich compositions, but the resistivity increased with increasing Zn composition. To obtain a suitable resistivity for Schottky diode fabrications, for compositions $x \leq 0.1$ the samples had first to be annealed in Se vapour to raise the resistivity. On the other hand samples with composition $X > 0.1$ had to be annealed in Cadmium vapour to lower their resistivity. This was carried out in 6mm diameter in silica tubes 300 mm long (Figure 4.3) which had been divided into two parts by a small constriction. A specimen was placed in one half with selenium or cadmium at the bottom of the tube. After evacuating the tube it was sealed off and inserted in a vertical (two zone) furnace. The Se treatment was carried out with the sample maintained at a temperature of 550°C and the Se or Cd reservoir held at 450°C for several days. Annealing in cadmium vapour(5) was done at a temperature of 650 °C.

4.5 Copper doping by evaporation

Since copper acts as an acceptor impurity in CdSe, it will increase the resistivity of n-type CdSe. The crystals, were doped by evaporating copper onto one side, and then annealing them for several hours at 650°C in a sealed silica tube filled with argon, in order to obtain a homogeneous

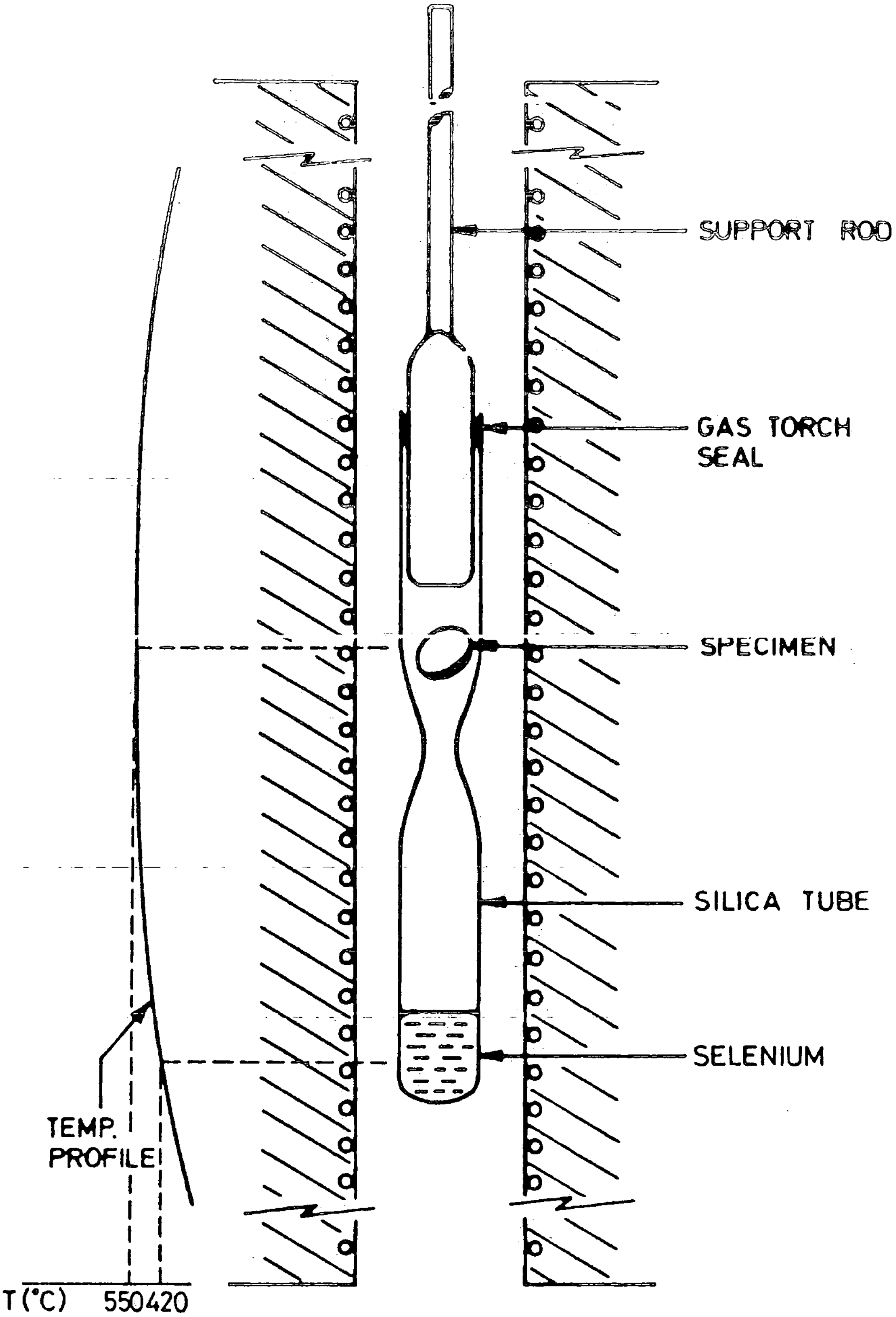

Figure 4.3 Experimental arrangement for annealing in Selenium vapour.

distribution of copper.

4.6 Contacts

4.6.1 Ohmic contacts

These were generally formed using high purity In wire. The crystal surfaces were first cleaned and etched to minimise contamination, before the In was applied. This was done in one of two ways(5).

In the first method a 1mm pellet of indium wire was pressed out on the prepared surface and then annealed in an argon atmosphere at 200°C for a few minutes to melt and diffuse into the surface. In the second method, indium wire was applied to the samples directly, using a special soldering iron.

4.6.2 Schottky diode fabrication

Schottky diodes were formed on material that had been previously annealed (see Section 4.4) to control the resistivity. The samples, in the form of dice, $4 \times 4 \times 2\ mm^3$ were mechanically polished with alumina powder down to a grit size of 1μm and etched, first in a 2% solution of bromine in methanol for 3 min., and then in concentrated HCl for 2 min. before being finally rinsed in methanol.

Au-CdZnSe Schottky barriers were then formed on these dice by the vacuum evaporation of gold dots (2mm diameter) onto the etched and cleaned surface. An In ohmic contact was made on the reverse face as discussed previously (Section 4.6.1).

4.7 Reflection high energy electron diffraction (RHEED)

The reflection electron diffraction studies were carried out in a JEM 120 transmission electron microscope (TEM). The technique provides information about the structure of the crystal surface. In particular, it provides a rapid assessment of the effects of polishing and etching, and enables the phase of the Cu_xSe layers produced on single crystal substrates to be determined.

In the RHEED technique, an electron beam with energy in the range 10-100 keV, is used to obtain diffraction from the atomic planes at the surface of a crystalline specimen. As for X-ray diffraction (section 4.3), the requirement for Bragg diffraction is that

$$\lambda = 2d_{hkl}\sin\theta \qquad (4.3)$$

where the wavelength (λ), depends on the accelerating voltage, and varies from 0.12 to 0.04 Å over the energy range from 10 to 100 keV. Since the interplanar spacing is of the order of 2Å, grazing incidence (1.5° - 0.5°) will give a diffraction pattern. Consequently in the RHEED technique, only those crystal planes that are inclined at less than a few degrees to the surface of a specimen will diffract an electron beam, as illustrated in Figure 4.4.

Each plane (hkl) in real space produces a reciprocal

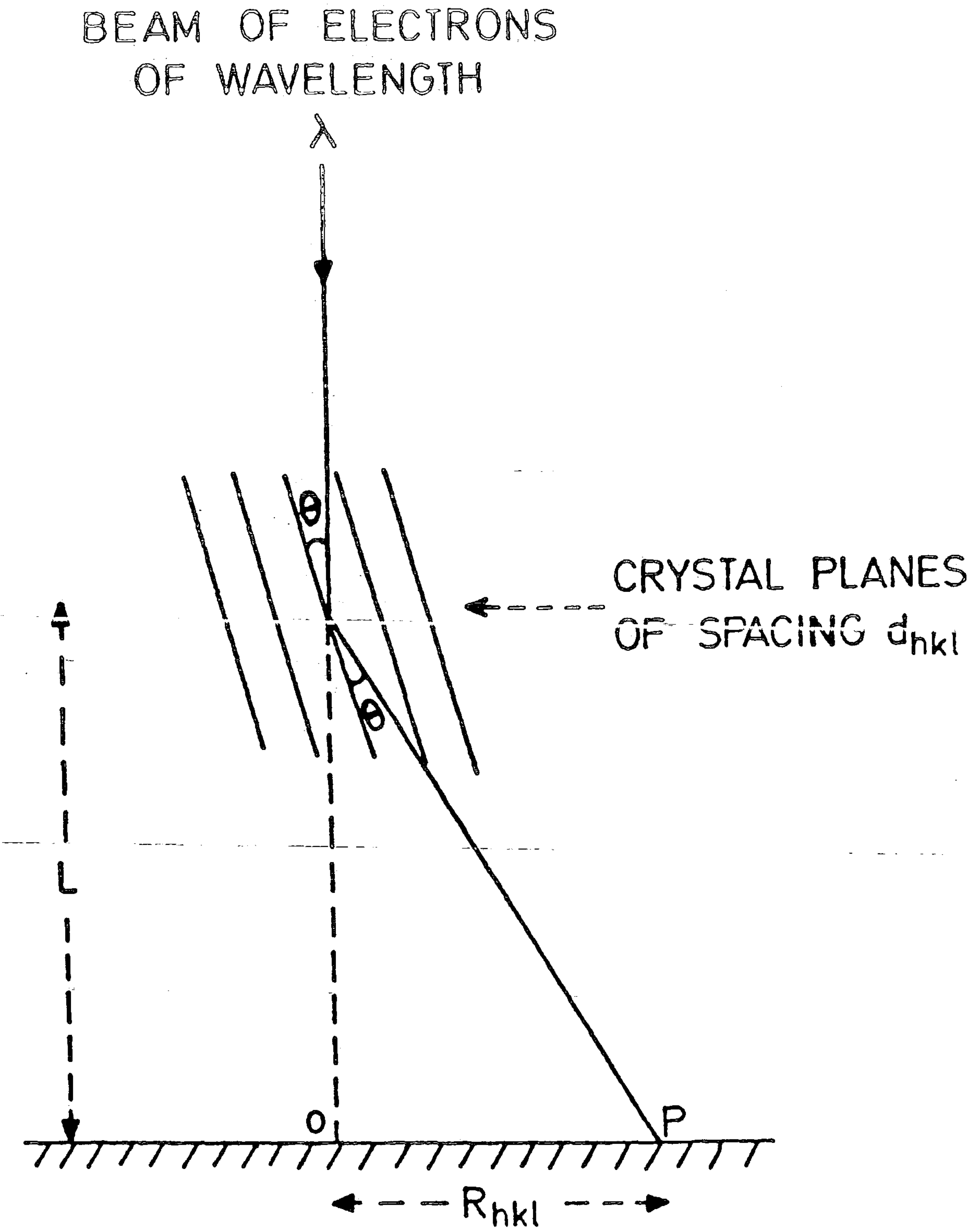

Figure 4.4 Schematic diagram of Reflected electron diffraction.

lattice point which lies on a line which passes through the origin of reciprocal space, and which is perpendicular to its corresponding plane in real space. If the incident beam strikes the crystal plane (hkl) at the Bragg angle (θ), then a diffraction spot is formed on the fluorescent screen placed at a distance, L, from the sample. In three dimensions the Bragg reflection condition can be determined using a geometrical model known as the Ewald sphere construction (see Figure 4.5). In this graphical representation of Bragg's Law of diffraction, constructive interference occurs only when the reflection sphere intersects points in the reciprocal lattice. As the radius of this sphere is $1/\lambda$ it is very large compared with the reciprocal lattice distances of $1/d_{hkl}$, for the diffraction of a beam of high energy electrons. For small values of the Bragg angle, the relationship

$$\lambda L = R_{hkl}\, d_{hkl} \qquad (4.4)$$

can be derived from the Bragg condition for constructive interference (see Figure 4.4).

This is the camera equation for the electron microscope, and may be used to calculate the interplanar spacings (d_{hkl}) from the observed diffraction pattern. The advantages of RHEED compared with X-ray techniques can be summarised as follows(6):

(1) In forming a diffraction pattern, the electron beam samples a much smaller volume of material in the form of a

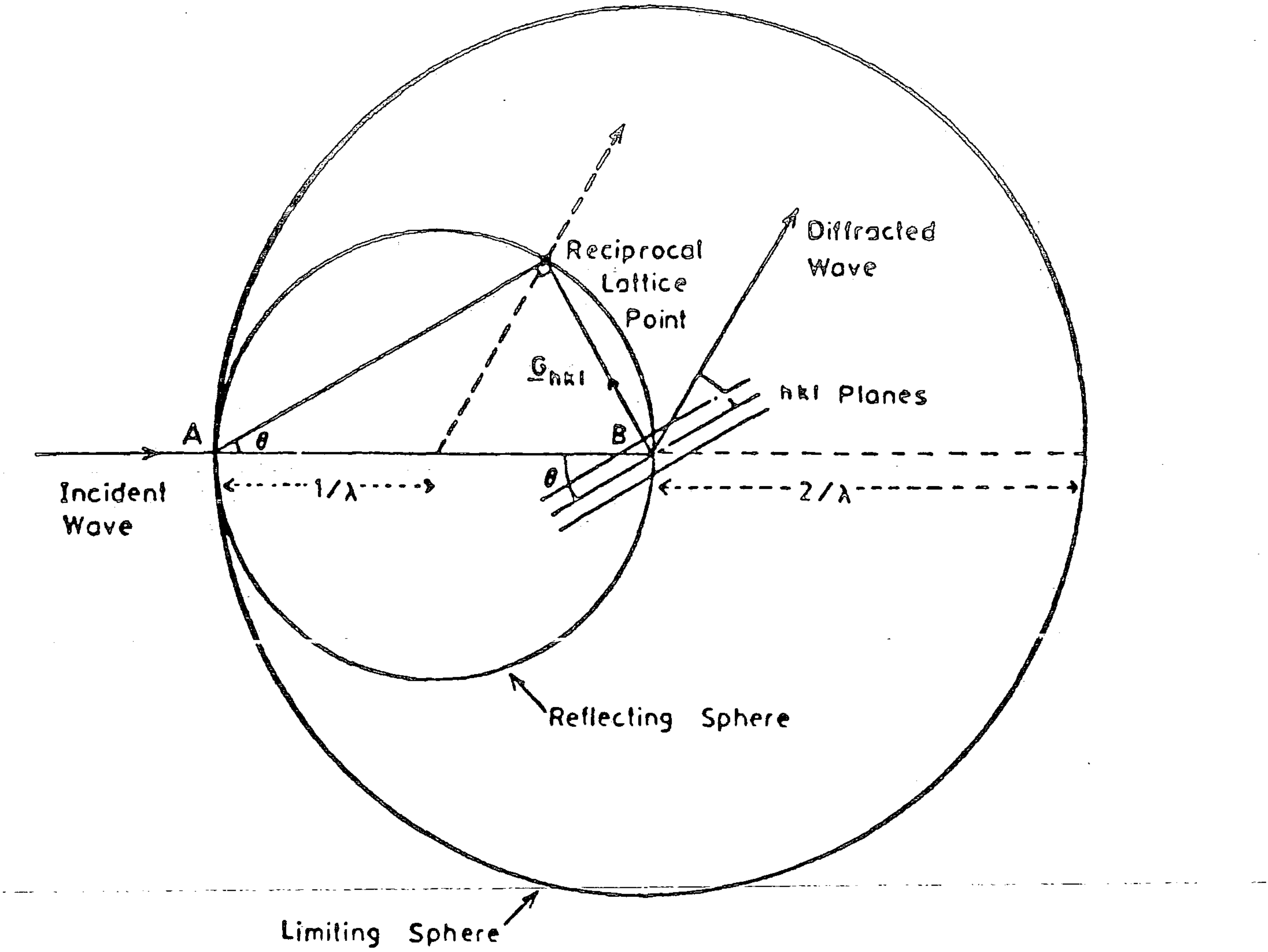

Figure 4.5 Ewald's Sphere Construction.

very thin surface layer. In contrast X-ray diffraction samples the whole volume. In this respect the two techniques are complementary.

(2) As the angle for Bragg diffraction of electrons by crystal planes is typically less than 2 degrees, a diffraction pattern covering a large number of reflections in reciprocal space can be recorded on a flat photographic film or plate. With X-ray diffraction and Low Energy Electron Diffraction a large angular spread of the patterns has to be covered.

(3) Changes in the complete diffraction pattern may be clearly observed on a fluorescent screen as the crystal orientation and diffraction conditions are changed. No such facility is possible with X-ray diffraction.

(4) Photographic exposure times are generally much less for electron diffraction than they are for X-ray diffraction.

(5) The transformation from real to reciprocal space is much more easy to visualise than it is for X-ray diffraction because of the necessary condition that the crystal planes should lie approximately parallel to the incident beam.

4.8 Scanning electron microscopy

4.8.1 Scanning electron modes

The surface topographies of single crystals and the electrical properties of CdSe/Cu_2Se and $Cd_xZn_{1-x}Se/Cu_2Se$ heterojunctions were investigated using a Cambridge stereoscan 600 scanning electron microscope (SEM). A schematic diagram of an SEM is shown in Figure 4.6. The basic components of the SEM are the lens system, electron gun, electron collector, visual and recording cathode ray tubes (CRTs), and associated electronics.

The SEM may be used in several different modes by imaging the signals derived from the different interactions that occur between the electron beam and the specimen(7). These are illustrated in Figure 4.7. Most commonly used in scanning electron microscopes, is the scintillator-photomultiplier system developed into its current configuration by Everhart and Thornly(8). Generally, scintillators require electron energies of 10-15 keV for efficient light production(8). However, the secondary electrons emitted from the sample surface are not sufficiently energetic to activate the scintillator and in order to improve the collection of secondary electrons, an additional positive potential of several hundred volts is applied to the detector system, by a Faraday cage arrangement.

4.8.2 Energy dispersive analyser X-ray (EDAX)

In addition to the secondary electrons emitted when the electron beam strikes the sample surface, X-rays are emitted as well. These may be spectrum or energy analysed to obtain an elemental analysis of the surface. This technique is known as the energy dispersive analysis of X-rays (EDAX) and was employed in the present study using a Link Systems 860-series 2 Analyser. A schematic diagram of an energy

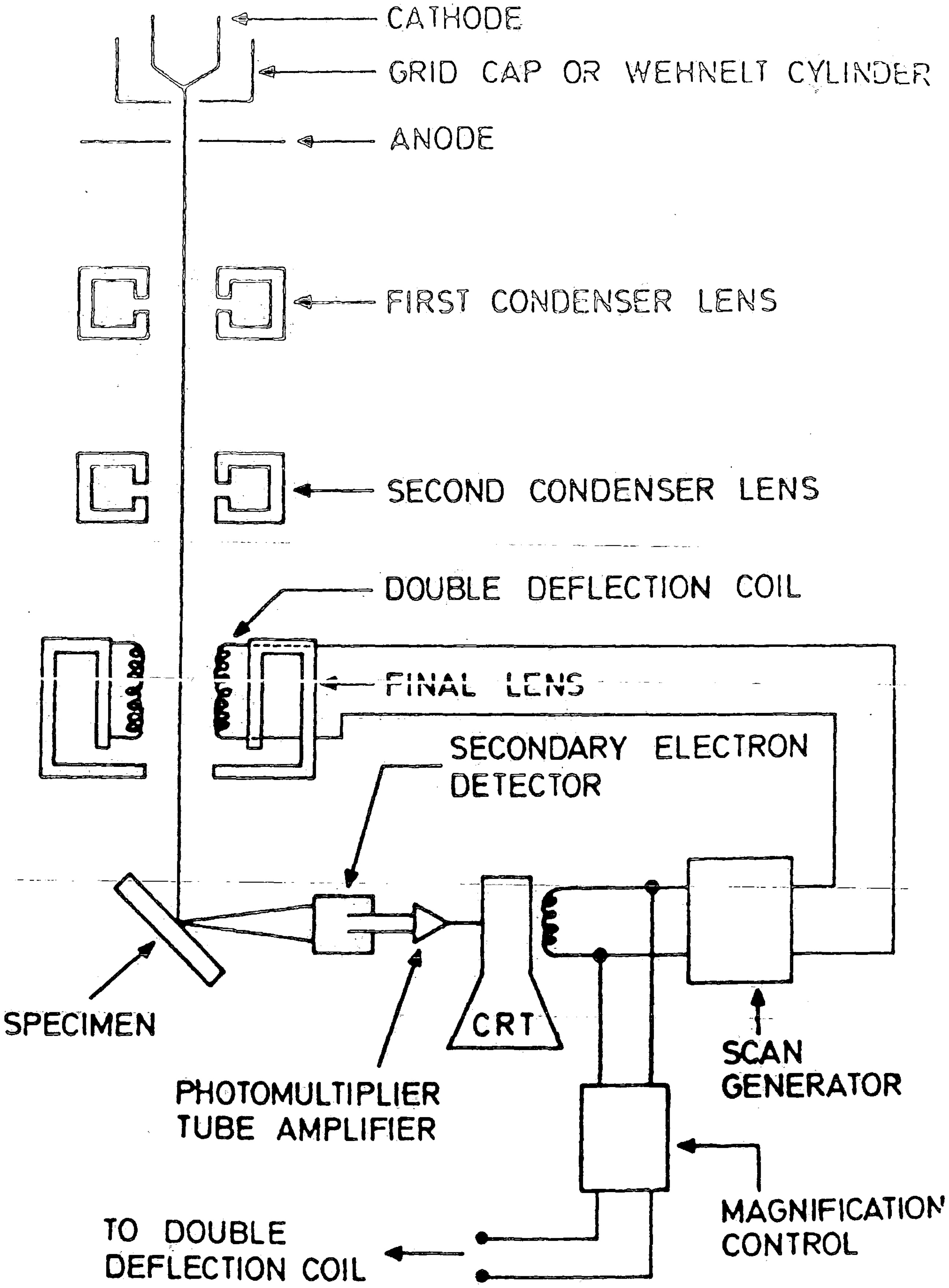

Figure 4.6 Schematic diagram of the SEM.

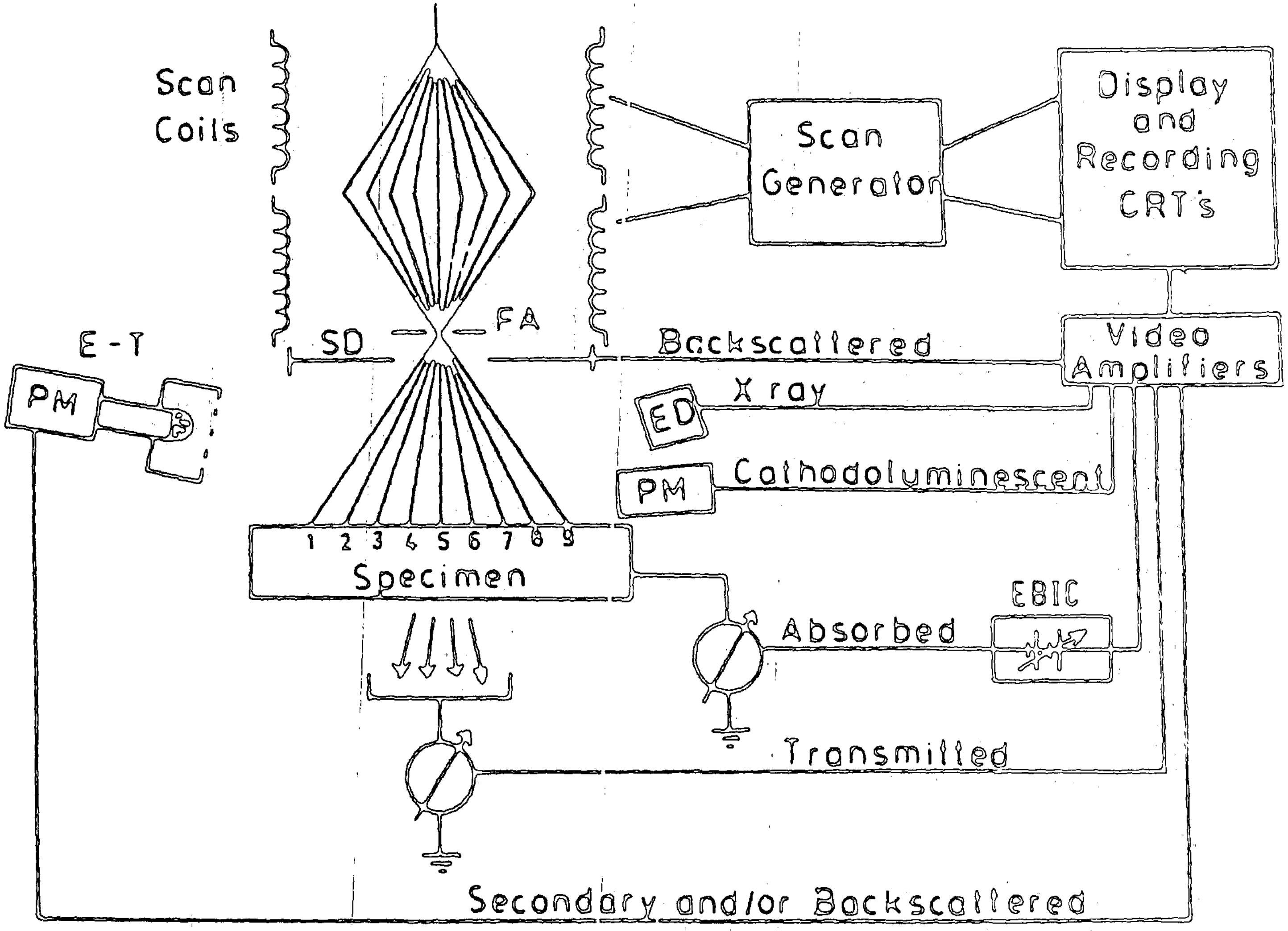

Figure 4.7 Schematic diagram showing the various modes of operation of the SEM.

dispersive analyser is given in Figure 4.8.

The X-rays emitted from the sample pass through a thin beryllium window into a cooled, reverse-bias p-n Si(Li) detector$^{(8)}$. This leads to the ejection of a photoelectron which gives up most of its energy to the formation of several electron-hole pairs. These are swept away by the applied bias to form a charge pulse, which in turn is converted to a voltage pulse by a charge-sensitive preamplifier. The amplitude of this voltage pulse is proportional to the magnitude of the charge released by the photoelectron which in turn is proportional to the energy of the incident X-ray photon. Thus an energy spectrum of the incident X-rays can be built-up by sorting and summing the voltage pulses according to pulse-height in a multi-channel analyser (MCA).

The resulting spectrum is then (in the Link system) displayed on a cathode ray tube and may be "screen-dumped" to a matrix printer for permanent record. The contents of the MCA memory can be further processed to obtain, for example, peak identification by comparison with the known position of the characteristic X-ray lines.

4.8.3 EBIC measurements

In the electron beam induced current (EBIC) mode of the SEM (see Figure 4.7), the current produced by absorption of the incident electron beam is imaged.

In this study, the EBIC current generated and collected at metal-semiconductor junctions and p-n heterojunctions were recorded and measured as a function of beam distance from the

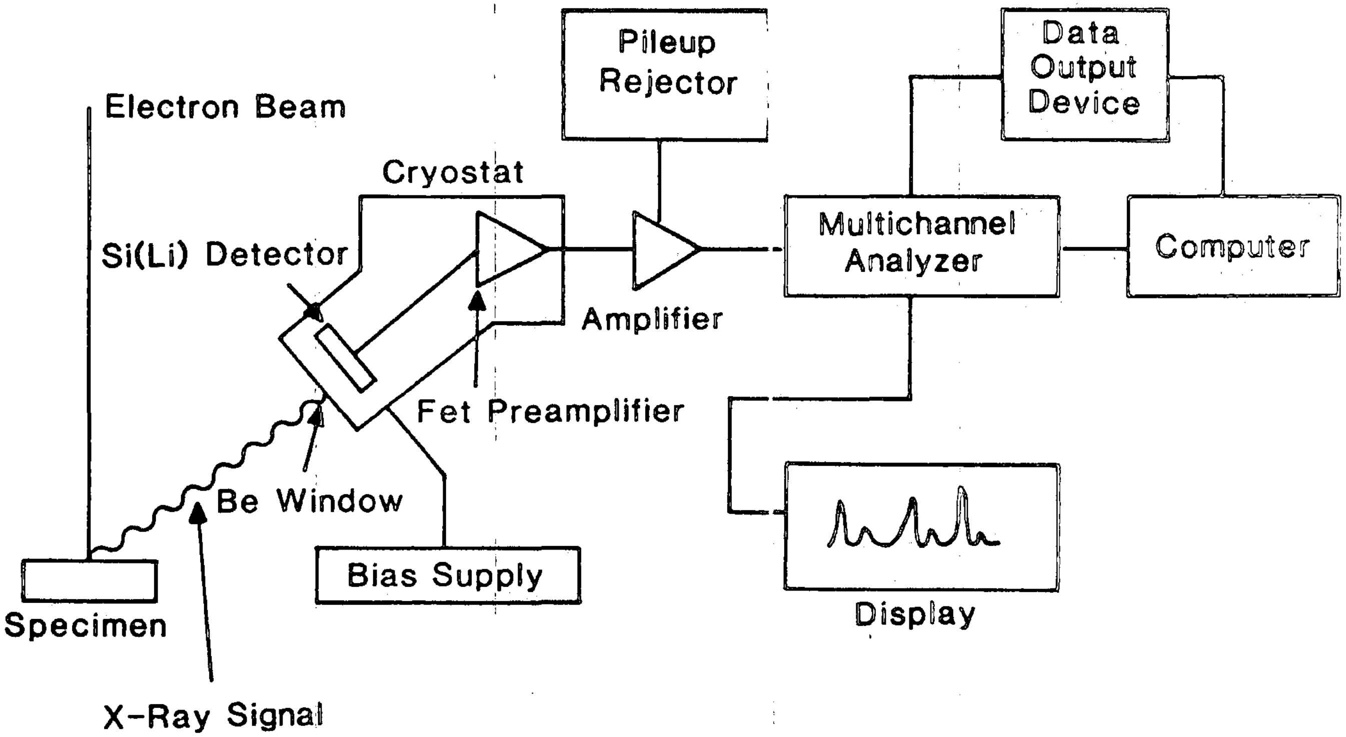

Figure 4.8 Energy dispersive X-ray analyser.

junction, on both sides, as a means of determining diffusion lengths. This was first done by Kyser and Wittry(9). If it may be assumed that there is no electric field in the material except at the junction, the continuity equation for the excess minority carrier density (n) in a semiconductor material(10) reduces to:

$$D\nabla^2 n - n/\tau + g(r) = 0 \qquad (4.5)$$

where

D = minority carrier diffusion coefficient

τ = minority carrier lifetime

$g(r)$ = generation rate. Since this is zero, except directly under the incident beam, where it is approximately constant, and using:

$$L^2 = D\tau_n \qquad (4.6)$$

where L = minority carrier diffusion length, equation (4.5) becomes:

$$\nabla^2 n - n/L^2 = 0 \qquad (4.7)$$

Assuming the electron beam generates a point source of carriers with an isotropic (spherically symmetric) distribution the solution of the continuity equation is:

$$n = \frac{Ae^{-r/L}}{r} \qquad (4.8)$$

Where A is a constant relating to the beam intensity and absorption properties of the semiconductor. The number of minority carriers that reach the junction is $-D\,\partial n/\partial r$ evaluated at the junction, this gives the EBIC current as:

$$I(r) = 2\pi ADe^{-r/L} \qquad (4.9)$$

where A is the junction area. The pre-exponential term, $2\pi AD$ corresponds to the incident beam current I(0) when all surface and interface states are neglected(11). For a semi-infinite junction collector the EBIC current (equation 4.6) can be expressed in terms of the distance x from the junction by(12)

$$I_{(x)} = I_o \exp(-x/L_D) \qquad (4.10)$$

where I_o is the value of $I_{(x)}$ at the junction plane (X = 0) and L_D is the minority carrier diffusion length on the side of the junction where the beam is located.

In the present study EBIC measurements were made to determine the minority carrier diffusion length of samples fabricated on CdSe/Cu_2Se single crystals.

4.9 Electrical characteristics

4.9.1 Measurements of current-voltage characteristics

Current-voltage characteristics were recorded in the dark at different temperatures, and under AMI illumination at room temperature. Simulation of AMI illumination was accomplished using a 1.5kW quartz halogen lamp with a parabolic reflector housing. A 2cm deep tray of flowing water was placed between the source and the sample platform to simulate water vapour absorption.

Measurements of the current-voltage characteristics were carried out point by point using a high impedance Bradley digital voltmeter (type 173B) and low impedance Hewlett-Packard digital multimeter (type 3465B). A calibrated voltage source (Time Electronics type 2003) was used to bias the samples. An automatic current-voltage characteristics tracer was also available for more rapid but less detailed measurements.

4.9.2 Capacitance-voltage characteristic

The capacitance measurements were made using a Boonton 72B capacitance meter. C-V characteristics were recorded point-by-point using the calibrated voltage source to provide the bias. The spectral dependence of photocapacitance (PHCAP) measurements were made using a tungsten light source and a Barr and Stroud double prism monchromator model VL2 The output of the capacitance meter was connected to a

Honeywell chart recorder. A schematic diagram of the arrangement for these photocapacitance measurements is shown in Figure 4.9. PHCAP measurements were made at room temperature and at liquid nitrogen temperature.

4.9.3 Measurements of spectral response

The spectral response of the devices was measured using a Barr and Stroud double prism monochromator type VL2 with a 250 Watt quartz halogen lamp as source. The energy distribution of this light at the exit slit was measured using a Hilger and Watts Schwartz thermopile FT 16301. Relatively large monochromator slit widths of 1mm were employed.

The photocurrent and voltage were measured using a Keithley electrometer model 602 which has a high input impedance for voltage measurement and very low input impedance for current measurements. The open circuit voltage and short circuit current were plotted on a Honeywell potentiometric (Model 196) chart recorder. A schematic diagram of measurement system is shown in Figure 4.10.

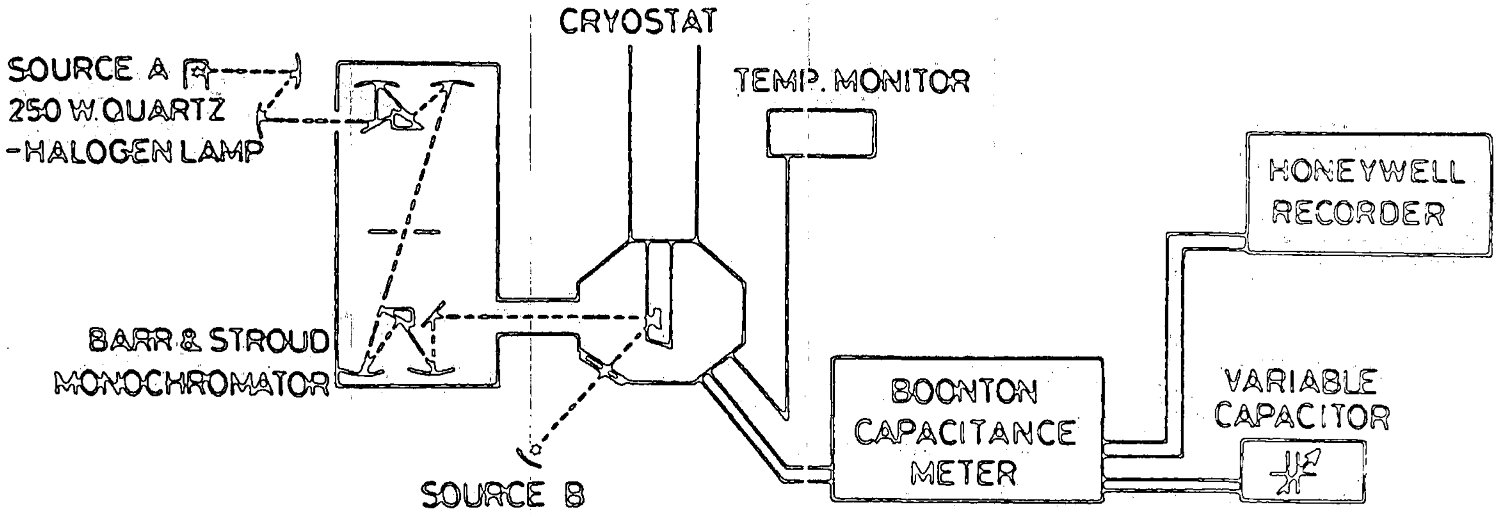

Figure 4.9 Experimental system used for photocapacitance measurements.

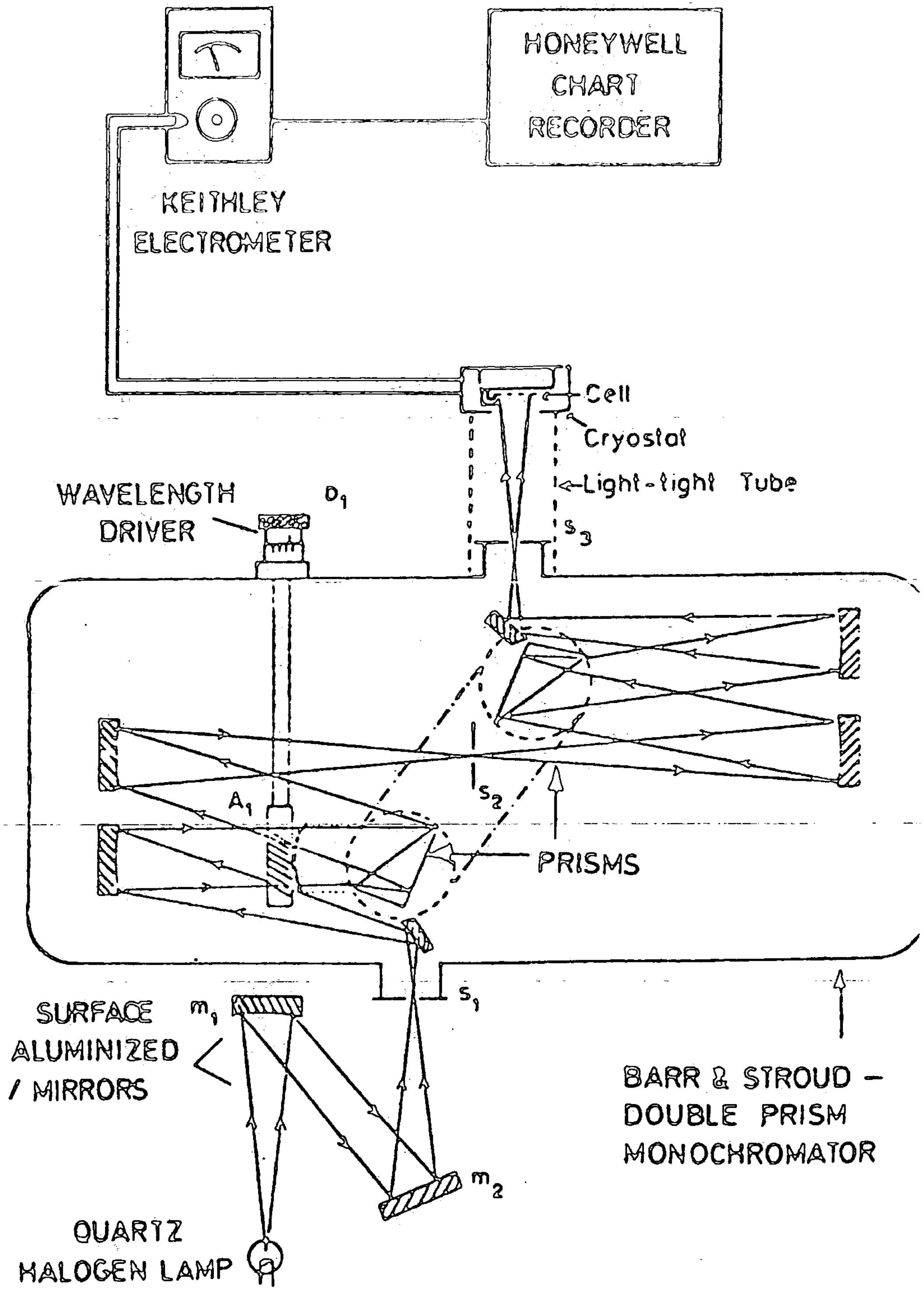

Figure 4.10 Experimental arrangement used for spectral response measurements.

References

(1) Russell, G.J., Thompson, N.F. and Woods, J., 1985, J. Crystal growth, 71, 621.

(2) Clark, L., and Woods, J., 19689, J. Cryst. Growth, 3, 126.

(3) Piper, W.W. and Polich, S.J., 1961, J. Appl. Phys., 32, 1278.

(4) Cullity, B.D., 1967, "Elements of X-ray diffrraction", Addison-Wesley.

(5) Ture, E., Ph.D. Thesis, 1984, University of Durham.

(6) Russell, G.J., 1982, Prog. Crystal Growth and Characterisation, 5, 291.

(7) Goldstein, J.I. (ed.) and Yokowitz, H. (ed.), 1975, Practical Scanning electron Microscopy, (Plenum Press, New York).

(8) Goldstein, J.I., Newbury, D.E., Echlin, P., Joy, D.C., Fiori, C. and Lifshin, E., 1981, "Scanning electron Microscopy and X-ray Microanalysis", Plenum press, New York.

(9) Wittry, D.B., and Kyser, D.F., 1964, J. Appl. Phys. 35, No. 8, 2439.

(10) Holt, D.B., Muir, M.D., Grant, P.R. and Boswarva, I.M., (1974) Quantitative scanning electron micscopy (Academic Press, London).

(11) Oktik, S., Ph.D. Thesis, 1982, University of Durham.

(12) Oakes, J.J., Greenfield, I.G. and Partain, L.D., 1977, J. Appl. Phys., 48, 2548.

CHAPTER 5

Physical properties of ZnCdSe

5.1 Introduction

The results to be described in the present chapter relate to the physical properties of ZnCdSe crystals which have been prepared in the course of this study. The growth of single crystals of $Zn_xCd_{1-x}Se$ over the full range of composition (1 > x > 0) is reported, together with the results of a study of a number of their characteristics. The mixed crystals were grown from the vapour phase, using both the Durham(1) and the Piper-Polich(2) techniques. The composition of the crystals was determined using atomic absorption spectroscopy and energy dispersive X-ray analysis and the structure and lattice parameters were determined using X-ray diffractometry. Finally the band gap for this ternary was measured as a function of composition by two different methods, photoconductivity and optical absorption.

5.2 Crystal growth

The single crystals of $Zn_xCd_{1-x}Se$ used in this study were grown from the vapour phase as described in Section 4.2. The starting material was a mixture of the two binary compounds, ZnSe of polycrystalline lump grade supplied by Merck, and CdSe which had been synthesised from the elements

(6 nines purity) in this laboratory. The two binary compounds were weighed out in varying proportions and were thoroughly mixed before being loaded into the crystal growth capsules. These were evacuated sealed and loaded into the furnace (section 4.3). Growth took place over 10 days at a temperature of 1165°C with the Durham method and for 3 days at 1165°C using the Piper-Polich technique[(3)]

A nominal value of the composition was recorded from the weight of CdSe and ZnSe starting material incorporated in the growth tube to produce a partial mixed crystal. The nominal and the actual values of the composition are listed in Table 5.1.

Boule Number	Nominal value	Actual value (x)
858) 855)	14g ZnSe 6g CdSe ($x \approx 0.7$)	0.57 - 0.1
857	18g ZnSe 2g CdSe ($x \approx 0.9$)	0.93 - 0.86

Table 5.1 Composition of mixed alloy crystals.

These techniques produced 1cm diameter crystal boules of a few centimetres in length. Although Cd-rich crystals were relatively uniform in composition, high x material tended to show a gradation of composition along the length. Radial uniformity was however good and variation in composition across the diameter of the boules was below what could be detected by EDAX (< 2%). Many boules showed a gradation of colour along their length indicating a progressive change in composition during growth. Crystals with a composition of about 80% Zinc and 20% Cadmium were yellow in colour. This changed to a dark red colour as the composition changed to 45% zinc and 55% cadmium, turning to black when close to CdSe.

5.3 Composition measurements

The composition of the ternary CdZnSe crystals was determined by atomic absorption spectroscopy (AAS) and by energy dispersive analysis of x-rays (EDAX). The latter was of particular interest since, in principle, it provides a simple, rapid and non-destructive way of determining composition, and it is also independent of sample shape and size. However the use of the AAS technique to measure composition was deployed after all other measurements on the samples had been completed because of the destructive nature of this technique. Samples were prepared for AAS by dissolving them in solution of 0.5ml concentrated HCl, and 0.5ml concentrated HNO_3, with deionised water added to make up the solution to 50ml. The dissolved samples were scanned for Cd and Zn. The AAS analysis was carried out using a Perkin Elmer 5000 absorption spectrophotometer. Normally EDAX determinations would be carried out using calibration curves of net intensity against concentration derived from standards. This becomes inappropriate in a situation where the sample size, shape, take-off angle etc. differ radically from those of the standards. Consequently, it was decided to adopt a procedure developed by E.P. Bertin$^{(4)}$ for binary systems.

This procedure derives from the basic relationship between emitted intensity I and concentration C:-

$$I_a = K_a\, C_a^{n_a} \quad (A) \qquad (5.1)$$

$$I_b = K_b\, C_b^{n_b} \quad (B)$$

where a and b refer to the two elements constituting the binary compounds and K_a, K_b, n_a and n_b are constants. Thus taking the logarithm of the ratio I_a/I_b and rearranging gives:-

$$\text{Log}\frac{I_a}{I_b} = \text{Log}\frac{K_a}{K_b} + n_a \text{ Log } C_a - n_b \text{ Log } c_b$$

$$\text{Log}\frac{I_a}{I_b} = \text{Log } K + n_a \text{Log}\frac{C_a}{C_b} + (n_a - n_b)\text{Log } C_b \qquad (5.2)$$

if $n_a \approx n_b = n$ then the third term in equation (5.2) may be neglected and the expression may be rewritten as:-

$$\text{Log}\frac{I_a}{I_b} = \text{Log } K + n \text{ Log}\frac{C_a}{C_b} \qquad (5.3)$$

Thus if $n_a \approx n_b$ a Log-Log plot of the intensity ratios of the two elements in a binary compound vs the actual concentration ratio will yield a straight line that is essentially independent of sample shape and size etc. This technique may be extended to ternary compounds providing that the third element does not preferentially absorb any of the x-ray fluorescence from either of the other two components.

The as-grown boules were normally cut into slices and routinely assessed by EDAX for compositional uniformity, the best crystals were of uniform composition throughout their length as is demonstrated by the two EDAX traces shown in the Figure 5.1. These were obtained from slices number 6 and 9 of the same boule, which was of composition 25%Zn and 75%Cd. However, in general crystals exhibited a compositional gradient along their length, although radial uniformity was usually good.

The EDAX $^{Cd}/Zn$ intensity ratios and the $^{Cd}/Zn$ concentration ratios as measured by atomic absorption spectroscopy for samples of different composition are given in table 5.2, and are plotted on logarithmic axes as shown in Figure 5.2.

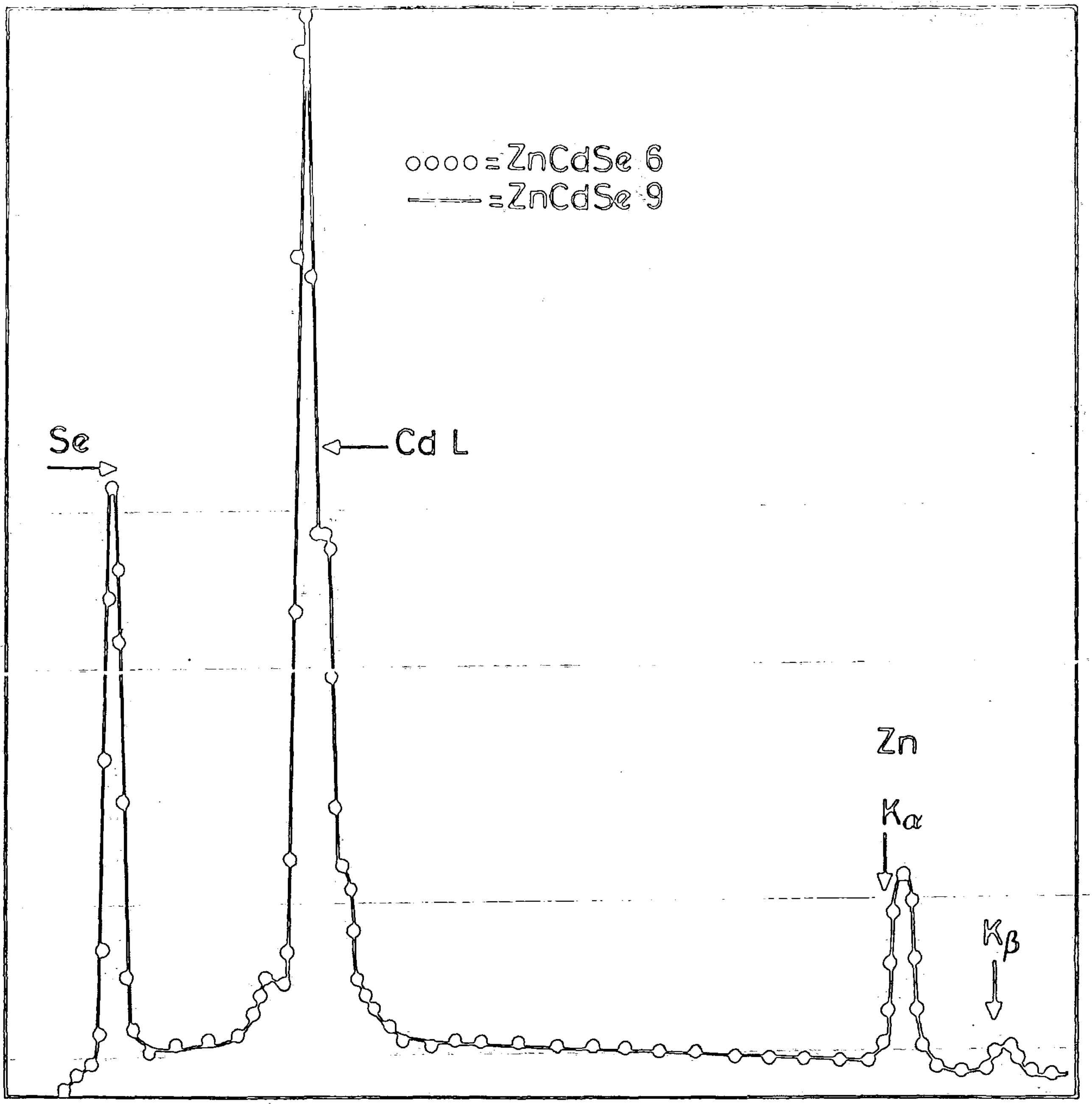

Figure 5.1 Typical EDAX spectra from two slices taken from a single boule of $Zn_{.25}Cd_{.75}Se$.

AAS			EDAX		
%Cd	%Zn	Cd/Zn	I(Cd)	I(Zn)	I(Cd/Zn)
74.58	25.41	2.94	18.1	3.3	5.48
69.46	30.42	2.28	17.8	3.3	5.39
66.77	33.23	2.01	17.9	5.0	3.58
64.10	35.90	1.79	18.1	4.3	4.21
55.90	44.10	1.27	17.4	9.9	1.76
52.35	47.60	1.10	17.8	8.8	2.0
44.47	55.52	0.80	16.7	15.0	1.11
34.56	65.44	0.53	13.7	17.6	0.78
13.24	86.76	0.15	5.3	18.1	0.29
12.33	87.70	0.14	3.2	16.8	0.19
11.74	88.26	0.13	4.1	18.3	0.22
9.62	90.40	0.11	2.3	18.2	0.13

Table 5.2. The composition of the $Cd_{1-x}Zn_xSe$ from EDAX and AAS.

It was found that these points lay along a good straight line and that equation (5.3) was therefore applicable i.e.:-

$$\log \frac{I(Cd)}{I(Zn)} = \log K + n \log \frac{C(Cd)}{C(Zn)} \qquad (5.4)$$

where

I(Cd) is the intensity for CdL line

I(Zn) is the intensity for Zn kα line

C(Cd) is the fractional concentration of Cd

C(Zn) is the fractional concentration of Zn

A least squares analysis gave values of $n = 1.078$ which was close to unity, and of $\log k = 0.2466$. The approximation made in the derivation of equation 5.2 will clearly hold less well for zinc rich compositions where C(Cd)/C(Zn) is small but is satisfactory over the rest of the compositional range.

The graph, (Figure 5.2) therefore, gives a quick and non-destructive means of estimating composition. However, the final absolute determination of the composition of a given sample was always made by AAS after all other measurements had been completed.

5.4 X-ray diffraction measurements

X-ray powder photography was used to determine both the structure and the variation in lattice parameter with composition. Samples of each composition were lightly crushed to a fine powder in an agate pestle and mortar, and the fine powder was then smeared on to a glass slide using acetone.

5.4.1 Structure

The two binary compounds, from which the ternary alloy is formed, have different crystal structures; CdSe normally crystallizes in the hexagonal wurtzite modification, ZnSe in ~~the cubic sphalerite, as discussed in chapter 2. In an X-ray~~ diffractometry study it is important to find the transition point. Analysis of the x-ray diffractometry data covering the full compositional range showed that samples with compositions close to CdSe were hexagonal, while those near to the ZnSe end of the spectrum were cubic. The phase transition point appeared to occur approximately at the 50/50 composition. The results of this investigation are presented in the table 5.3. Two samples with x = 0.45 displayed the hexagonal structure, while a sample with x = 0.57 was found

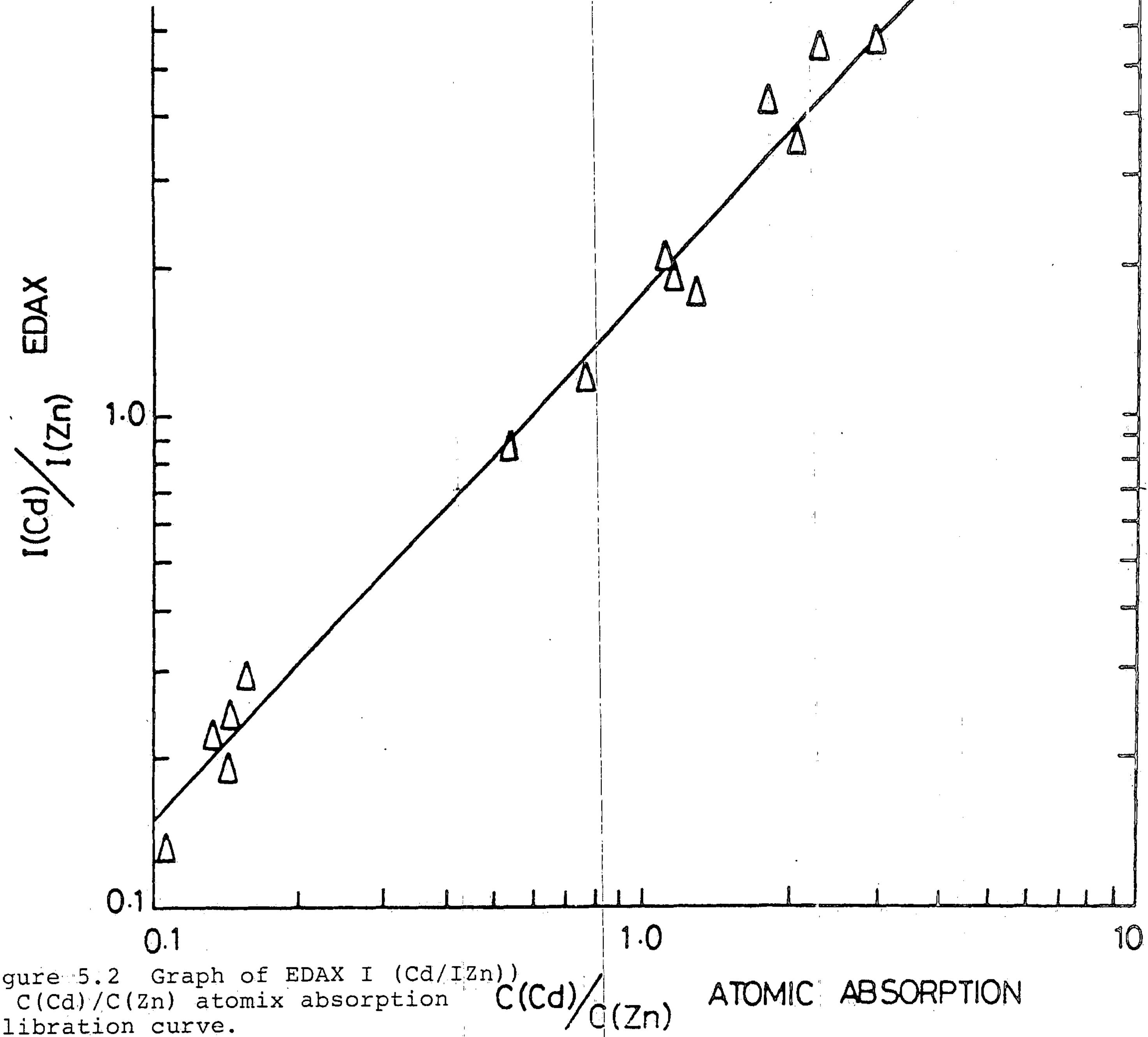

Figure 5.2 Graph of EDAX I (Cd/IZn))
vs C(Cd)/C(Zn) atomix absorption
calibration curve.

to be cubic. However, there was a region in the middle (30%–70%Zn) where both structures occurred (section 5.4.2). Although samples with $x \approx 0.45$ were hexagonal, they often contained included grains of cubic material, while the reverse was observed for material with $x \approx 0.55$.

5.4.2 Lattice parameters

The lattice parameters were calculated by using the $(11\bar{2}2)$ and $(20\bar{2}1)$ reflections for hexagonal material, and the (111), (220) and (311) lines for cubic samples. The hexagonal crystals are characterised by two lattice parameters a and c and the interplanar spacing$^{(5)}$ is given by:-

$$\frac{1}{d_{hkl}{}^2} = \frac{4}{3}\,\frac{h^2 + hk + k^2}{a^2} + \frac{l^2}{c^2} \qquad (5.5)$$

where (hkl) are the Miller Indices of the plane in question. Equation (5.5) reduces to:

$a = 4d_{hkl}$ for the (220) reflection

and $c = 2d_{hkl}$ for the (002) reflection

Cubic crystals are characterised by one parameter a, and the interplanar spacing is given by:

$$\frac{1}{d^2_{hkl}} = \frac{h^2 + k^2 + l^2}{a^2} \qquad (5.6)$$

which reduces to

$a = 3d_{hkl}$ for (111) reflections.

The interplanar spacings d_{hkl} are obtained from the Bragg angle (equation 4.1) positions of the diffraction lines and then these are used to calculate the lattice parameters from equations (5.5) or (5.6) as appropriate. The measured variation in a and (where appropriate) c with composition is given in Table 5.3, together with the type of structure.

The variation in a with composition (x) is shown in Figure 5.3, where the squares and triangles refer to the hexagonal and cubic phase material respectively.

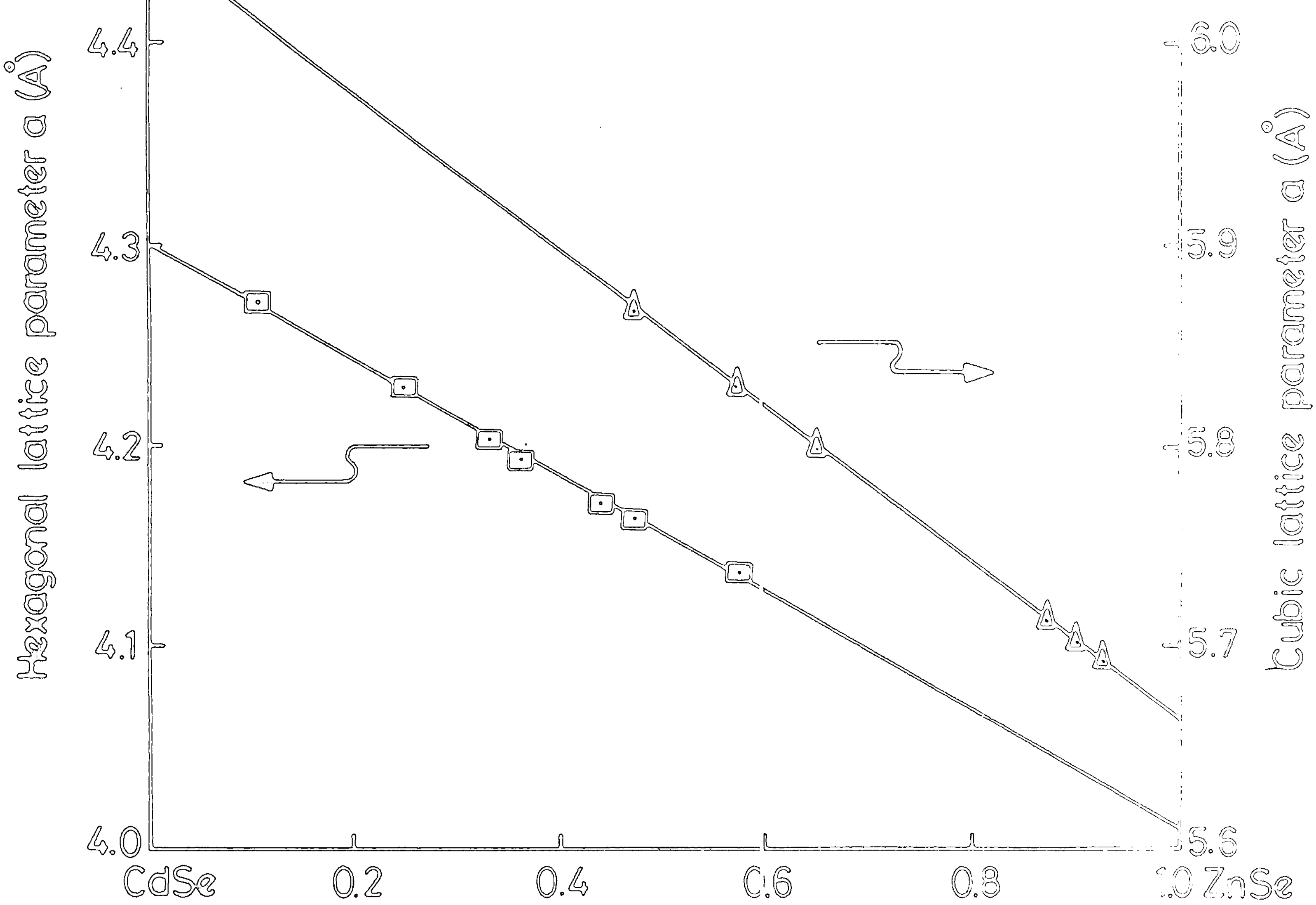

Figure 5.3 Lattice parameter a as a function of composition.

Composition x	Structure		Lattice Constant (Å)		$\frac{c}{a}$
	Sphalerite	Wurtzite	a	c	
1.00	"		5.669	-	-
0.93	"		5.693	-	-
0.90	"		5.698	-	-
0.88	"		5.712	-	-
0.65	"		5.800	-	-
0.57	"		5.832	-	-
0.57		"	4.138	6.740	1.629
0.48	"		5.870	-	-
0.48		"	4.162	6.780	1.629
0.44		"	4.170	6.806	1.632
0.36		"	4.192	6.830	1.629
0.33		"	4.203	6.849	1.630
0.25		"	4.228	6.900	1.632
0.11		"	4.269	6.97	1.633
0.00		"	4.298	7.010	1.631
0.00*	"		6.084	-	-

Table 5.3 Variation of Lattice parameters with composition.
* value quoted by ref. (6).

The measured values of a for the wurtzite material appear to lie on a straight line between the the value for hexagonal

CdSe (4.298Å) and that of hexagonal ZnSe at (4.013Å). Similarly the values of a for cubic CdZnSe lie close to the line between the value for ZnSe, (5.666Å) and cubic CdSe of (6.050Å).

Figure 5.4 shows the variation in c parameter for hexagonal material ($x < 0.45$). These points also lie along the line between the values of 7.01Å for CdSe and 6.54Å for hexagonal ZnSe. Interestingly, samples in the middle of the composition range, sometimes had additional lines, arising from included grains of the other modification. This is illustrated in the figures 5.5 and 5.6 which show x-ray diffractometer traces from two different samples. The trace in Figure 5.5 was taken from a sample with composition 25% zinc, 75% cadmium, and was completely hexagonal as attested by the presence of the ($10\bar{1}0$), (0002) and ($10\bar{1}1$) lines. The trace in Figure 5.6 was from a sample of composition 57% zinc, 43% cadmium and is predominantly cubic but has additional lines, which can be indexed as arising from the hexagonal modification, suggesting the presence of some included grains of this phase. The reverse situation of a sample with a predominantly hexagonal structure and included grains of cubic phase material was also observed. The dependence of the lattice parameters of a and c on composition can be expressed as:-

(1) $a = 4.298 - 0.28x$

$c = 7.01 - 0.48x$

for hexagonal material with $x < 0.5$, where x is the mole

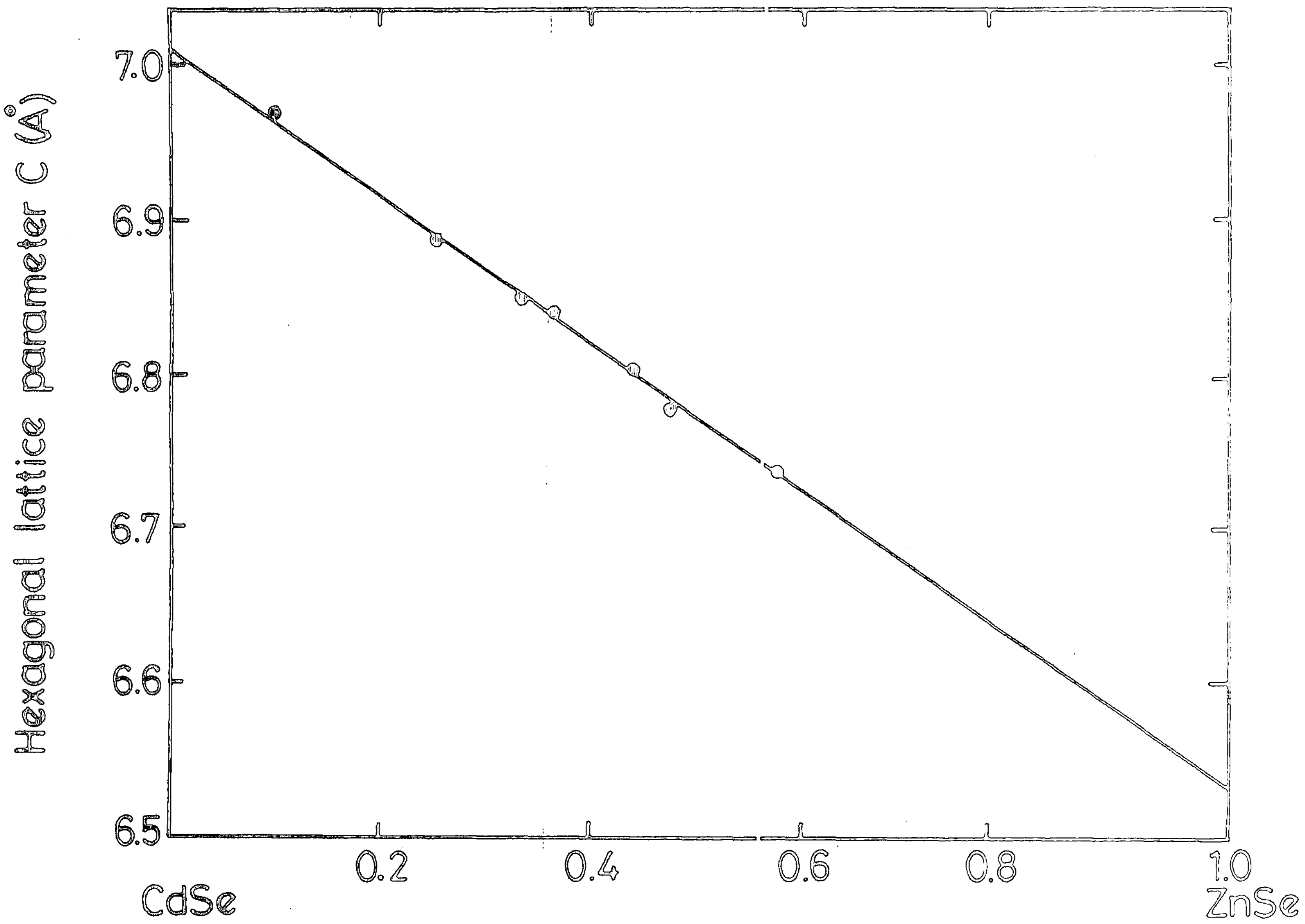

Figure 5.4 Lattice parameter c as a function of composition.

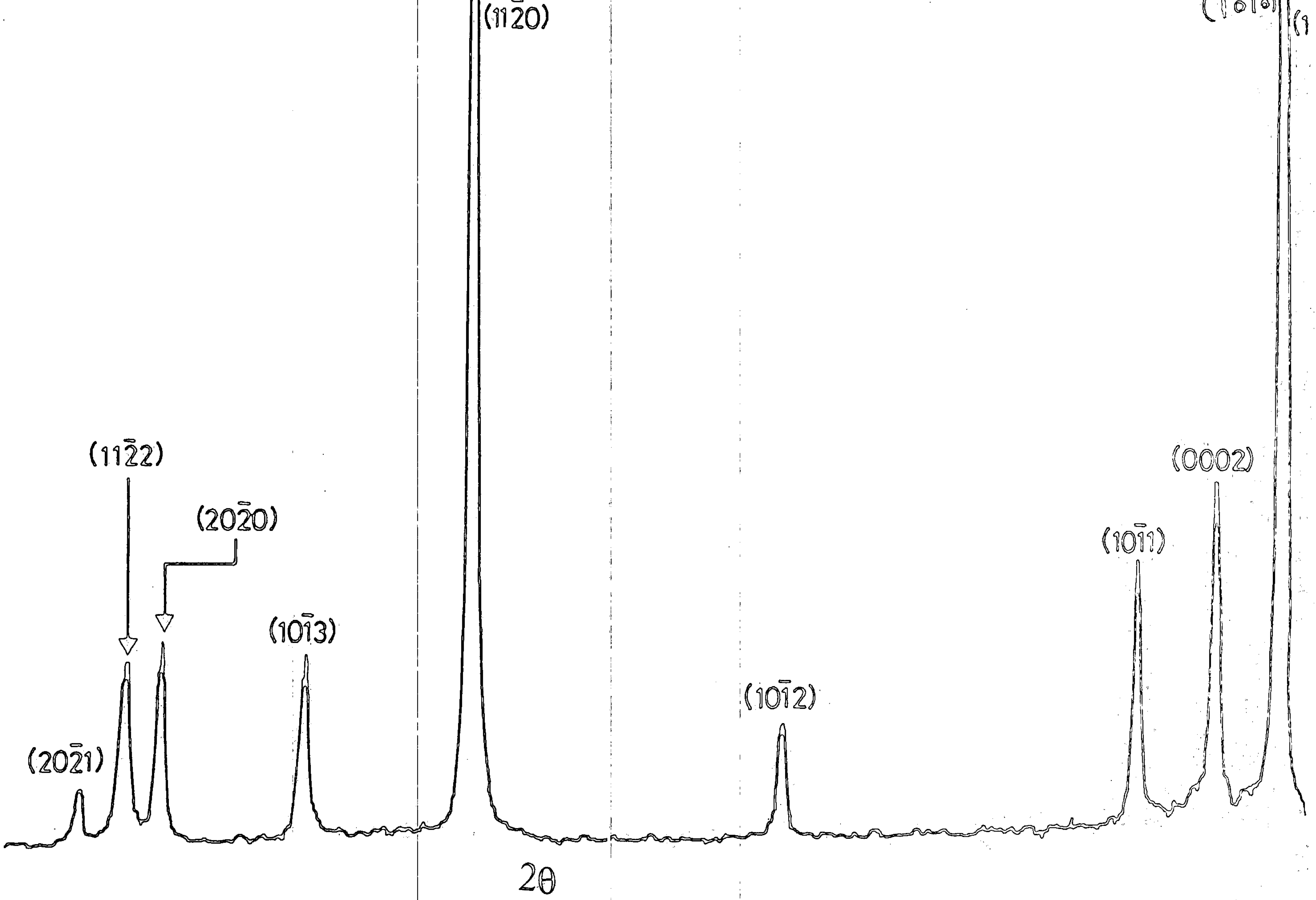

Figure 5.5 Diffraction pattern from a Cd$_{.25}$Zn$_{.75}$Se showing only the hexagonal phase.

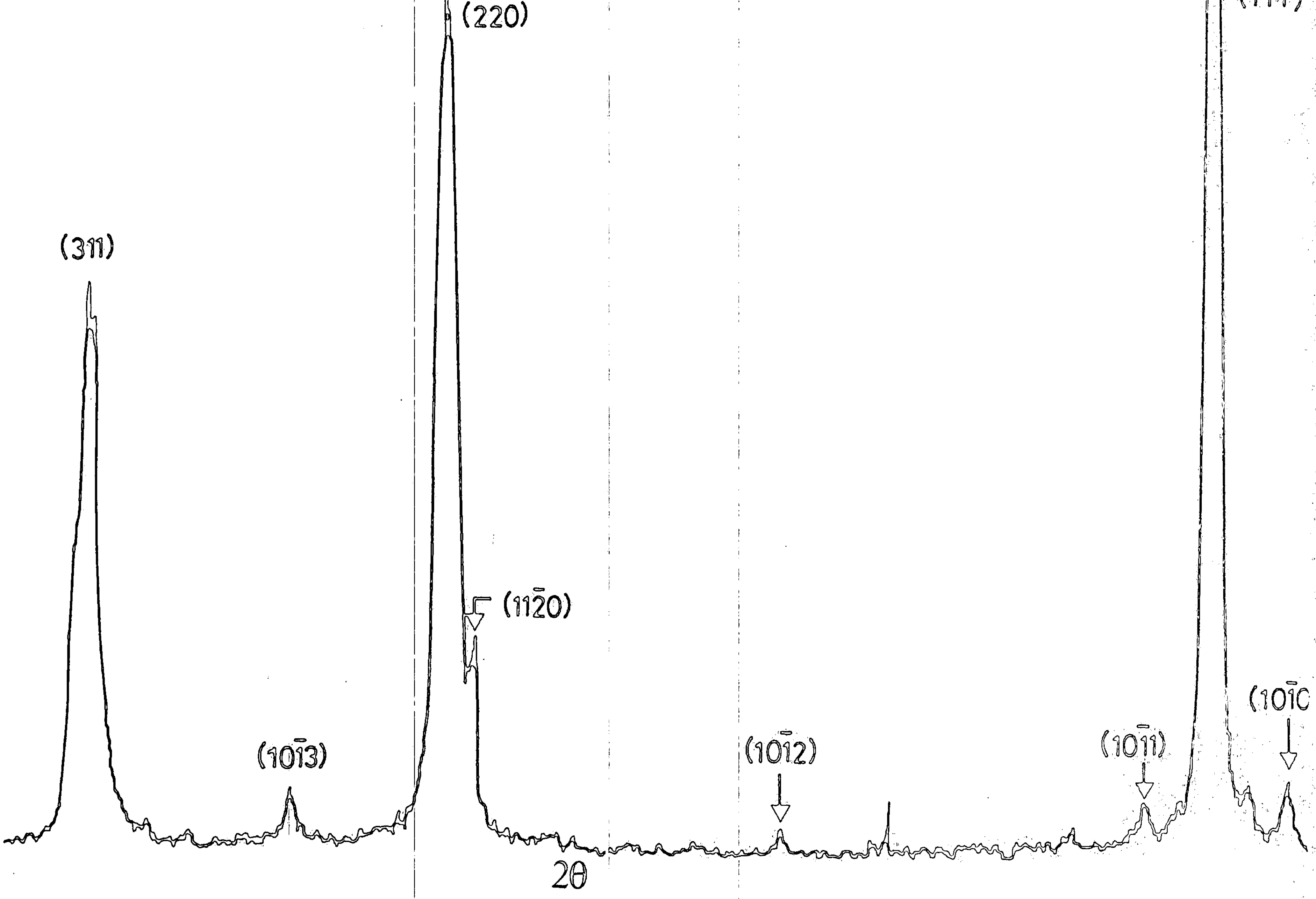

Figure 5.6 Diffraction pattern from $Cd_{.43}Zn_{.57}Se$ showing a predominantly cubic structure with additional lines from included grains to hexagonal phase material.

fraction of zinc in $Cd_{1-x}Zn_xSe$.

(2) $a = 5.831 - 0.16x$

for cubic crystals with $x > 0.5$.

5.5 Band gap measurements.

5.5.1 Photoconductivity

The increase in conductivity of a material under illumination is known as photoconductivity and was first observed by W. Smith 1873$^{(7)}$, although it has not been until the last thirty years or so that the effect has found wide application, in the detection of light. The general background to photoconductivity has been developed in several articles by Bube$^{(8-9)}$ and Moss$^{(10)}$, and will be described only briefly here. The absorption of light, by the material, leads to the creation of free electrons and holes and hence to an increase in the conductivity of the sample, which for an n-type material is given by

$$\sigma = nq\mu e \qquad (5.7)$$

where n is the density of free electrons and μe is the electron mobility. A change in conductivity, $\Delta\sigma$, due to illumination of the material, can be expressed as:-

$$\Delta\sigma = q(\Delta n\ \mu e + n\Delta\mu e) \qquad (5.8)$$

Since the number of free carriers is related to the excitation rate of electrons, and the free carrier life time by

$$n = f\tau$$

$$\Delta\sigma = \Delta f\tau + f\Delta\tau \tag{5.9}$$

then substitution of equation 5.9 in equation 5.8 gives

$$\Delta\sigma = f \quad \tau_n \quad q \quad \mu_n \quad + \quad n \quad q\Delta\mu_e \tag{5.10}$$

A quantity that is widely used to express the performance of a photoconductor, is the photoconductivity gain, which is defined as the ratio of the number of free charge carriers passing between the electrodes per unit time to the number of photons absorbed per unit time.

For a single carrier system this is given by

$$G = \frac{\tau}{T_R} \tag{5.11}$$

where T_R is the transit time between electrodes.

5.5.2 Optical absorption

Optical absorption is an important process yielding a measurement of the band gap energy of a semiconductor. Only photons with energies greater than the band gap energy are absorbed, while photons with energies less than the band gap are not. Thus the transmitted intensity in this experiment gives an accurate indication of the band gap energy. The ratio of transmitted to incident light intensity depends on the wavelength and the thickness of the sample. Assume that a sample of thickness d is illuminated by light of intensity I_o (photons cm^{-2} s^{-1}) and that the intensity at a distance x from the surface is I(x).

If the probability of absorption per unit distance in the sample is α, the absorption coefficient then(11)

$$\frac{dI(x)}{d(x)} = -\alpha I(x) \qquad (5.12)$$

and hence

$$I(x) = I_o e^{-\alpha x} \qquad (5.13)$$

and the intensity of light transmitted through the sample thickness d is

$$I_t = I_o e^{-\alpha d} \qquad (5.14)$$

The absorption coefficient α is a function of the wavelength and in particular increases dramatically as the wavelength of the incident light is reduced below that corresponding to the band-gap energy. This leads to an abrupt reduction in the transmission at the wavelength corresponding to the band-gap energy and hence allows a determination of it.

5.5.3 Band gap measurements

The variation of energy gap with composition was determined from the spectral dependence of the photoconductivity and from optical absorption. Samples were prepared for photoconductivity as described in section 4.5.1, and the spectral dependence of photoconductivity was recorded as outlined in section 4.8. Photoconductivity measurements were made at room temperature and at liquid nitrogen temperature, and in general measurements were taken over the wavelength range 4600A^o to 7800A^o. The electrical resistivity of all the samples varied between 1-10^{10} ohm.cm.

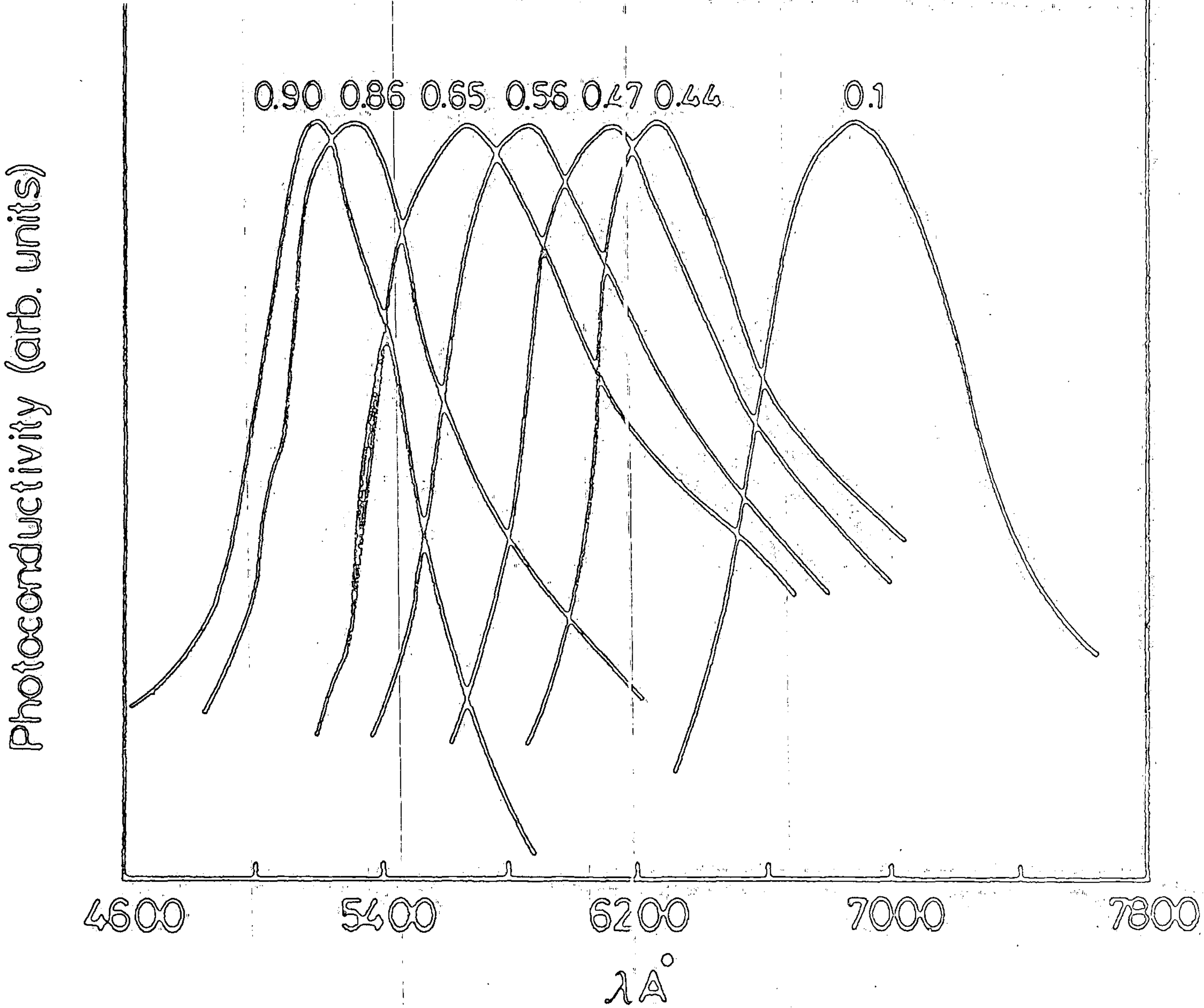

Figure 5.7 Photoconductivity response spectra at room temperature for $Zn_xCd_{1-x}Se$.

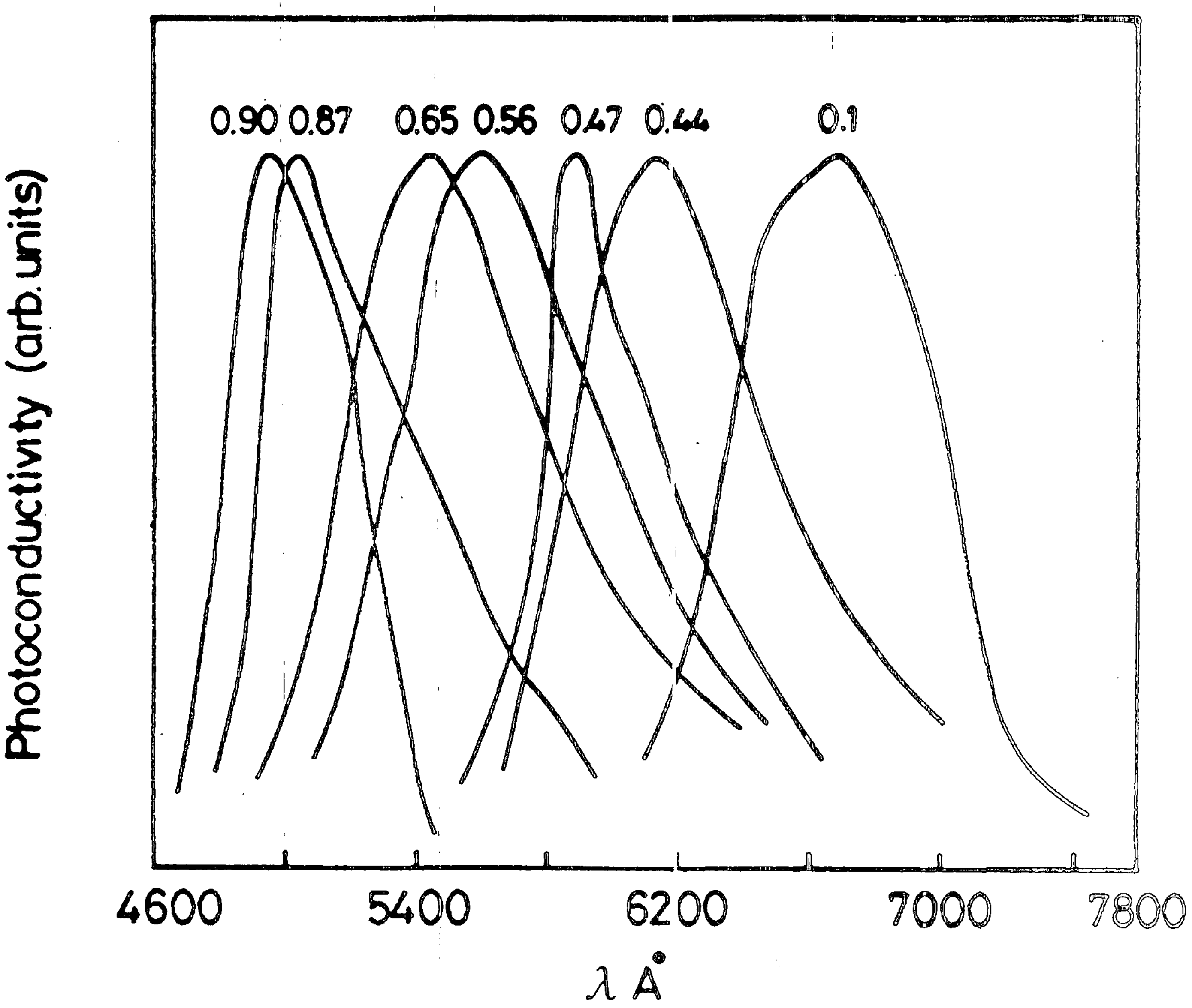

Figure 5.8 Photoconductivity response spectra at liquid nitrogen for $Z_{nx}Cd_{1-x}Se$

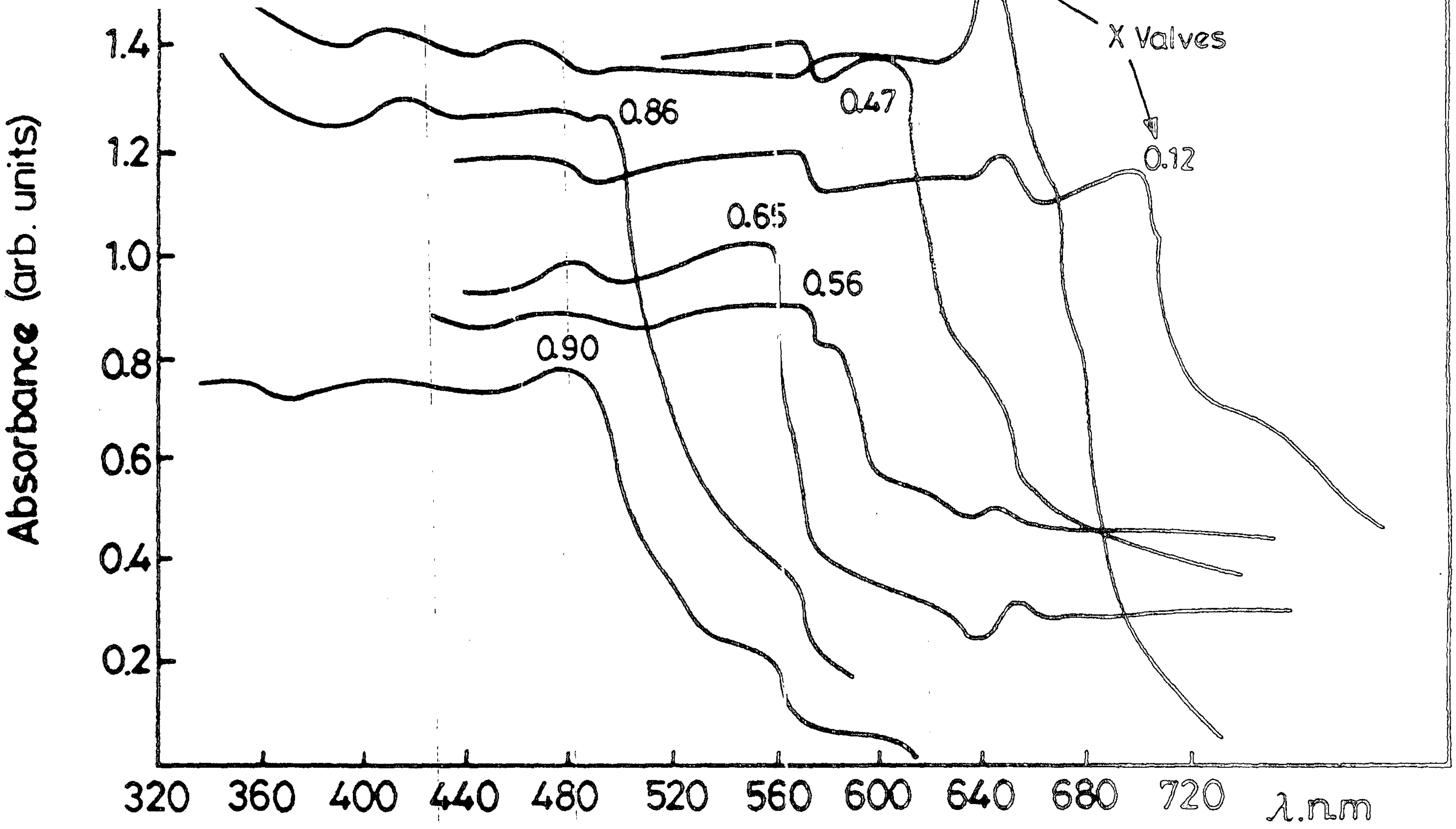

Figure 5.9 Optical absorption spectra for $Zn_xCd_{1-x}Se$ samples with the different x values shown.

The spectral dependence of photoconductivity at room and liquid nitrogen temperatures is shown in Figures 5.7 and 5.8 respectively, for a range of samples. The curves have been corrected for the variations in the incident light intensity with wavelength, and are given in arbitrary units. These show a gradual shift in the peak response to shorter wavelengths as the proportion of zinc is increased. These curves were used to determine the forbidden energy gap (Eg) as a function of composition, and the results are summarized in table (5.4).

Composition (x)	Eg(eV) 300K	Eg(eV) 90K
0.10	1.79	1.86
0.44	1.98	2.06
0.47	2.02	2.11
0.56	2.11	2.20
0.65	2.18	2.28
0.87	2.35	2.48
0.90	2.38	2.51

Table 5.4 Variation in the energy gap of $Zn_xCd_{1-x}Se$ with composition.

The optical absorption spectra were recorded using a Cary 2300 spectrophotometer at room temperature. Usually the spectral measurements were made over the wavelength range from 400nm to 720nm. The variation in the absorbance with wavelength is shown in Figure 5.9 for several samples with different compositions. As expected the principal absorption edge moves to higher energies with increasing Zn content in the alloy. The results are given in Table 5.5 and are summarized in Figure 5.10, which presents the variation in the band gap with x, the mole fraction of Zn.

Composition (x)	Wavelength (n.m)	Eg(eV)
0.12	700	1.77
0.33	676	1.86
0.47	624	1.99
0.56	595	2.06
0.65	575	2.14
0.86	520	2.38
0.90	512	2.42

Table 5.5 Variation in the energy gap of $Zn_xCd_{1-x}Se$ with composition measured from optical absorption.

5.6 Discussion

Bulk crystals of $Zn_xCd_{1-x}Se$ were grown over the full compositional range by two methods; the Durham closed tube and the Piper-Polich self sealing methods. Generally the more controlled Durham method produced crystals that were both larger and of better quality than the Piper-Polich method, but of course with a 2-3 week growth cycle, the Durham method takes much longer.

Bulk crystals grown from the vapour phase have been reported before by Reimers in 1969(12) and more recently by Burger and Roth (13) and by Lewis et al.(14). Budennaya et al.(15) have reported the growth of single crystals from the

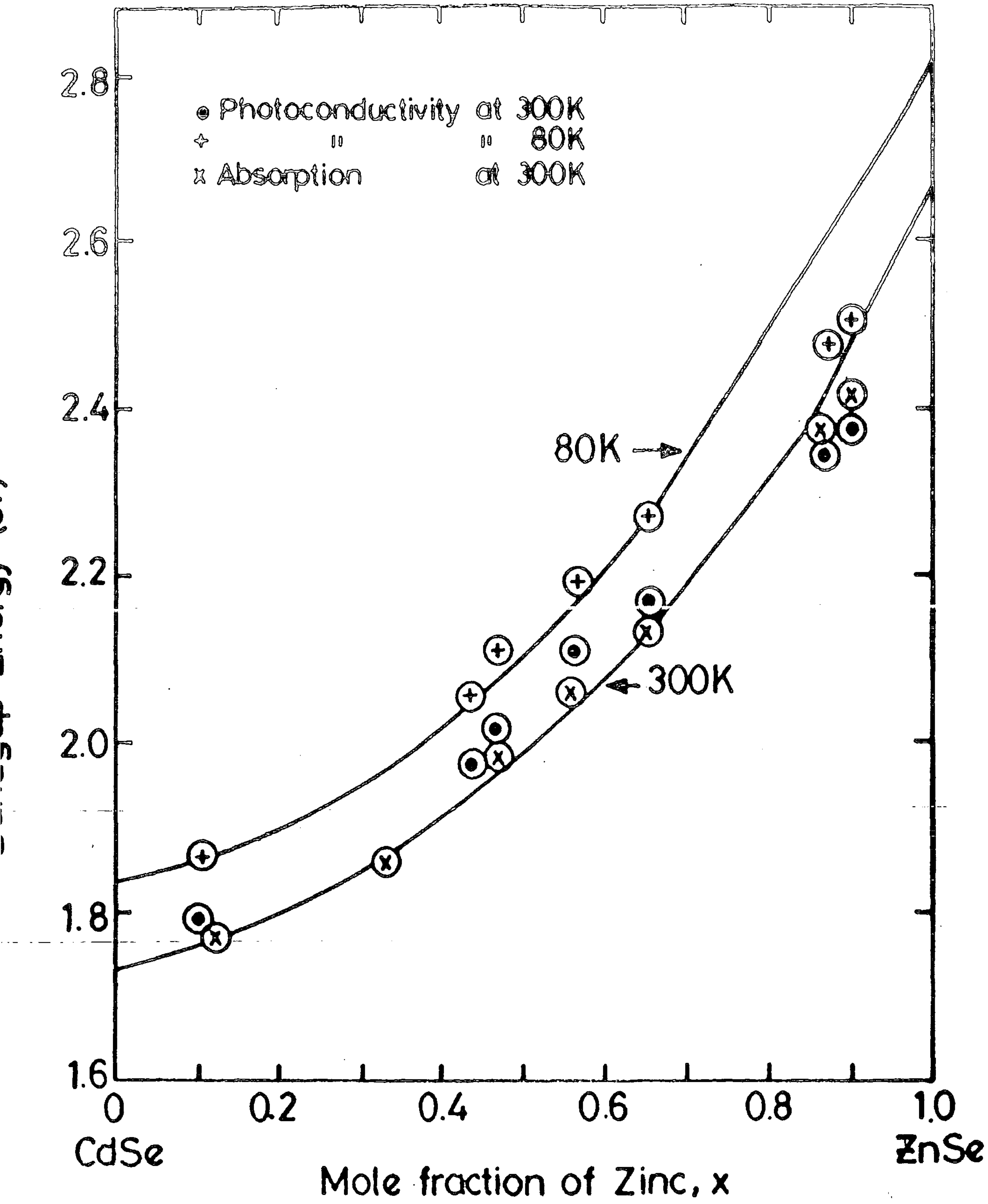

Figure 5.10 Variation in band gap energy of $Zn_xCd_{1-x}Se$ with composition.

gas phase by the "free growth" method. A particular difficulty in the growth of $Zn_xCd_{1-x}Se$ is the large difference in melting point temperatures of the CdSe and ZnSe starting materials. An additional problem occurs because the vapour pressure of CdSe is much greater than that of ZnSe(15). Nevertheless, good crystals of the ternary alloy were grown, although it was more difficult to grow good crystals with compositions in the middle of the range, possibly because one modification is not so strongly preferred over the other.

The composition of the crystals was determined by atomic absorption spectroscopy AAS and by EDAX. EDAX was of particular interest since, in principle, it provided a simple, rapid and non-destructive way of determining the composition, that was also independent of the structure or of the electrical properties of the material. However, there were substantial difficulties in using EDAX which arose from its inherent non-linearities, its dependence on sample detection geometry etc. However a Log-Log plot of the intensity ratio of the two elements in a ternary compound vs the actual concentration ratio as determined by AAS should yield a straight line over at least a significant portion of the range. Since "take off" angles, surface morphology etc. effects will affect all the x-ray emissions equally, then a technique based on ratios will be essentially independent of sample shape and size etc.

A straight line was obtained (Figure 5.2) over the observed range with a scatter in the points, indicating an uncertainty in the composition of about 5%. It may be inferred from this relationship that selective absorption of the zinc or cadmium fluourescence by the selenium did not appear to be significant.

Measurements made on $Zn_xCd_{1-x}S$(16) have been found to show a similar relationship between the ratio of the CdL and ZnKα lines with the concentration ratio of ZnS and CdS. X-ray diffraction analysis covering the full range of ZnCdSe composition concentration from CdSe-ZnSe showed that samples with compositions close to CdSe were hexagonal while those near to the ZnSe end of the composition were cubic. (Table 5.3). The transition from the wurtzite to the sphalerite occurred at $x \approx 0.5$ and the present investigations(17) suggest that for compositions with less than about 50%, the mixed crystal tended to be hexagonal, but was cubic for zinc concentrations greater than 50%. However, there was a region in the middle (30% - 70% zinc) where both crystal phases were observed to occur, two samples with 45% zinc, 55% cadmium were hexagonal, while a sample with 57% zinc, 43% cadmium was cubic. This accords with results reported by Goryunova et al. and Kolomiets and Chun-ming Lin(19) who found that, for a CdSe fraction of up to 45 mole %, solid solutions of CdSe in ZnSe exist with the sphalerite structure, while for CdSe contents of over 45-50%, solid solutions of ZnSe in CdSe occurred with the wurtzite structure. Budennaya et al.(15) reported that $Zn_xCd_{1-x}Se$ solid solutions with $1 > x > 0.6$ had the sphalerite structure, while those with $0.5 > x > 0$ had the wurtzite structure. The fact that the transition from the hexagonal to the cubic started at a lower concentration of Zn, may be connected with the fact that ZnSe possesses a considerably larger heat of formation and a considerably higher melting point than CdSe(18).

The measurements presented here show that the lattice parameters varied linearly with composition except of course, at the transition between the two structures. The variation in lattice parameters with the composition therefore would appear to obey Vegard's Law. The c/a ratios were calculated (Table 5.3) and lay in the range 1.629 - 1.633. In the case of ZnSe and CdSe the c/a ratios are 1.627 and 1.631, respectively. Since the lattice parameters of the hexagonal modification of ZnSe were not obtained in this study, then the corresponding lattice parameter values of the hexagonal ZnSe were estimated from the relationships between the a and c lattice parameters of the hexagonal and the parameter of the cubic structure giving (6):

$$a_{hex} = \frac{1}{2}\sqrt{2}\ a\ cub$$

$$c_{hex} = \frac{2}{3}\sqrt{3}\ a\ cub$$

Taking the value of a = 5.832Å for x = 0.57 (see Table 5.3), then the corresponding values of a and c for the hexagonal phase for this composition would be

a = 4.124Å and c = 6.734Å

Similar results for the lattice parameters have been found by

Goryunova et al.,(18), Kolomiets and Chun-ming Lin(19) and Budennaya et al.(15). The latter suggested that the distinctness of the reflections constituted evidence for the homogeneity of the single crystals obtained.

Two methods, photoconductivity and optical absorption were employed to investigate the dependence of the band gap on composition. The results are summarised in Figure 5.10 which presents the variation in the band gap with x. This shows that the band gap varied smoothly and monotonically, but not linearly over the composition range. The band gap energy Eg(x) in ternary alloys of the form $A_xB_{1-x}C$ is often found to follow a quadratic relationship of the form:-(20)

$$Eg(x) = Eg(A) + (Eg(B) - Eg(A)-b)\,x + bx^2 \qquad (5.15)$$

where Eg(A) and Eg(B) are the band gap of the binary compounds AC and BC respectively and b is the bowing parameter. The band gap range for $Zn_xCd_{1-x}Se$ is 1.74 - 2.67 eV at room temperature and was found to follow a relationship of the form of equation 5.15 for $x < 0.6$, fitting equation 5.15 for the data gave a value for b of 0.82.

Thus at room temperature(21)

$$E_g(x) = 1.74 + 0.11x + 0.82x^2.$$

At liquid nitrogen temperature (90K) the band gap range for $Zn_xCd_{1-x}Se$ is 1.84 - 2.84eV and the bowing parameter was found to be 0.87, giving

$$Eg(x) = 1.84 + 0.13x + 0.87x^2.$$

However, this expression (equation 5.15) seriously overestimates the value of Eg near the ZnSe end of the compositional range. This is in contrast to $Zn_xCd_{1-x}S$ where the quadratic (b = 0.61)(20) relationship holds for all x. Kolomiets and Chun-ming Lin(19) have published some data on the variation of Eg with composition although they did not attempt to determine any empirical relationships. However, their values are in general agreement with those presented here, and show for example that at Cd rich compositions Eg varies more slowly with x, than at the ZnSe end of the spectrum. The increase in b with temperature is expected, since both CdSe and ZnSe experience different temperature coefficients for Eg.

5.7 Conclusion

Using atomic absorption spectroscopy it has been demonstrated that EDAX may be used as a rapid and non-destructive technique for the determination of the composition of mixed crystals of $Zn_xCd_{1-x}Se$ grown from the vapour phase over the full range of composition. The absolute composition was determined by atomic absorption spectroscopy and this was used to calibrate the EDAX system. X-ray diffractometry has shown that the transition from sphalerite to wurtzite occurs at a composition of about $Zn_{0.5}Cd_{0.5}Se$. The lattice parameters (both a and c) of the hexagonal and cubic crystals were found to show a linear dependence with zinc composition over a wide range. The energy gaps were determined at 90K and 300K, using photoconductivity measurements, and also by optical absorption (at room temperature). The band gap was found to vary monotonically but not linearly with x, with bowing parameters of 0.82 and 0.87 at 300K and 90K respectively. The energy gap Eg has been found to obey an empirical relationship of the form:

$$Eg(x) = 1.74 + 0.11x + 0.82x^2 \text{ at } 300K$$

and $$Eg(x) = 1.84 + 0.13x + 0.87x^2 \text{ at } 90K.$$

References

1. Clark, L. and Woods, J., J. Crystal Growth 3/4 (1968), 126.
2. Piper, W.W. and Polich, S.J., J. Appl. Phys., 32 (1961), 1278.
3. Russell, G.J., Thompson, N.F. and Woods, J., J. Crystal growth, 71 (1985), 621.
4. Bertin, E.P., Anal. Chem. 36 (1964), 827.
5. Cullity, B.D., : "Elements of x-ray diffraction", (Addison-Wesley, 1967).
6. Aven, M. and Prener, J.S., "Physics and Chemistry of II-VI Compounds", North Holland, Amsterdam (1967).
7. Smith, W., Nature 7 (1873), 303.
8. Bube, R.H., Photoconductivity of Solids, J. Wiley, New York, (1960).
9. Bube, R.H., Photoelectronic Materials and Devices, (S. Larach ed. van Nostrand, 1965).
10. Moss, T.S., Photoconductivity in the element, Academic Press, New York, (1952).
11. Streetman, Ben G., Solid State electronic devices, Prentice Hall International, Englewood, 1980.
12. Reimers, P., (1969), Phys. Status Solid: 35, 707.
13. Burger, A. and Roth, M., J. Crystal Growth, 70, (1984), 386.
14. Lewis, J.E., Ture, I.E., Brinkman, A.W. and Woods, J., Semicond. Sci. Technol. 1. (1986), 213.
15. Budennaya, L.D., Nizkova, A.I., Pekar, G.S., and Polisskii, G.N., Institute of Semiconductors, Academy of Science of Ukranian SSR. Translated from Izvestiya Akademii Nauk. SSR, , June, (1982), 908.
16. Saidin, K., Ph.D. Thesis, University of Durham, 1987.
17. Al-Bassam, A., Brinkman, A.W., Russell, G.J. and Woods, J., (1985), British Assoc. Crystal Growth Conf. Brighton, (1985).

18. Goryunova, N.A., Frank - Kamenetskii, V.A. and Fedorova, N.N., Zhur, Tech. Fix. 25, (1955), 2419.

19. Kolomiets, B.T. and Chun-ming Lin, Soviet Physics: Solid State 2 (1960-1), 154.

20. Hartman, H., Mach, R. and Selle, B., Current Topics in Materials Science 9, ed. E. Kaldis (Amsterdam: North Holland).

21. Al-Bassam, A, Brinkman, A.W., Russell, G.J. and Woods, J., J. Crystal Growth, 86(1988)667.

CHAPTER 6

Electrical Properties of $Zn_xCd_{1-x}Se$

6.1 Introduction

In this chapter results are presented for Au-$Zn_xCd_{1-x}Se$ Schottky diodes which have been prepared on single crystal substrates. The primary aim is to see how the parameters of the Schottky diodes change with composition.

The principal measurements were of the current voltage characteristics and the capacitance voltage characteristics, and were taken immediately after fabrication of the Schottky devices. These measurements were used to provide estimates for the uncompensated donor density and the barrier height at the metal-semiconductor interface. The barrier was also determined from short circuit photocurrent measurements. In addition, photocapacitance studies were carried out to provide a preliminary survey of some of the deep levels in the material.

6.2 Schottky barrier formation

As grown single crystals of $Zn_xCd_{1-x}Se$ ($x < 0.1$) are normally too conductive ($\rho = 10^{-2}$ Ωcm) for the fabrication of Schottky barrier structures, conversely when the Zn fraction exceeds ~10% the material becomes too resistive. Consequently, various annealing procedures had to be used to obtain samples of suitable resistivity (1-100 Ωcm) for Schottky barrier formation. The annealing procedures are described in detail in Section 4. These entailed heating the sample for several hours in selenium vapour, to increase, or in cadmium vapour, to decrease.

6.2.1 Current-voltage characteristics

The current-voltage (I-V) characteristics for Au-$Zn_x Cd_{1-x}Se$ Schottky diodes were measured immediately after fabrication, and were found to give good rectifying characteristics with little reverse bias leakage, as shown in in Figure 6.1. However, rectifying characteristics could only be obtained for x <0.45. Figure 6.2. shows the forward I-V characteristics for a number of compositions. The corresponding values of the ideality factor n, saturation current and the barrier height calculated are from the characteristics (Section 3.2.5) and summarized in table 6.1,

Composition (x)	Js(Amp)	Ideality factor n	ϕ(eV) I-
0.10	5.8×10^{-7}	1.18	0.74
0.24	2.0×10^{-7}	1.12	0.70
0.30	4.0×10^{-4}	2.07	0.57
0.36	2.3×10^{-4}	1.04	0.58
0.40	1.0×10^{-5}	1.12	0.66
0.44	3.0×10^{-6}	1.01	0.71
0.47	2.4×10^{-4}	1.11	0.58

Table 6.1 Barrier heights and ideality of factor for Au-CdZnSe

The ideality factors ranged from 1.01 to 2.07.

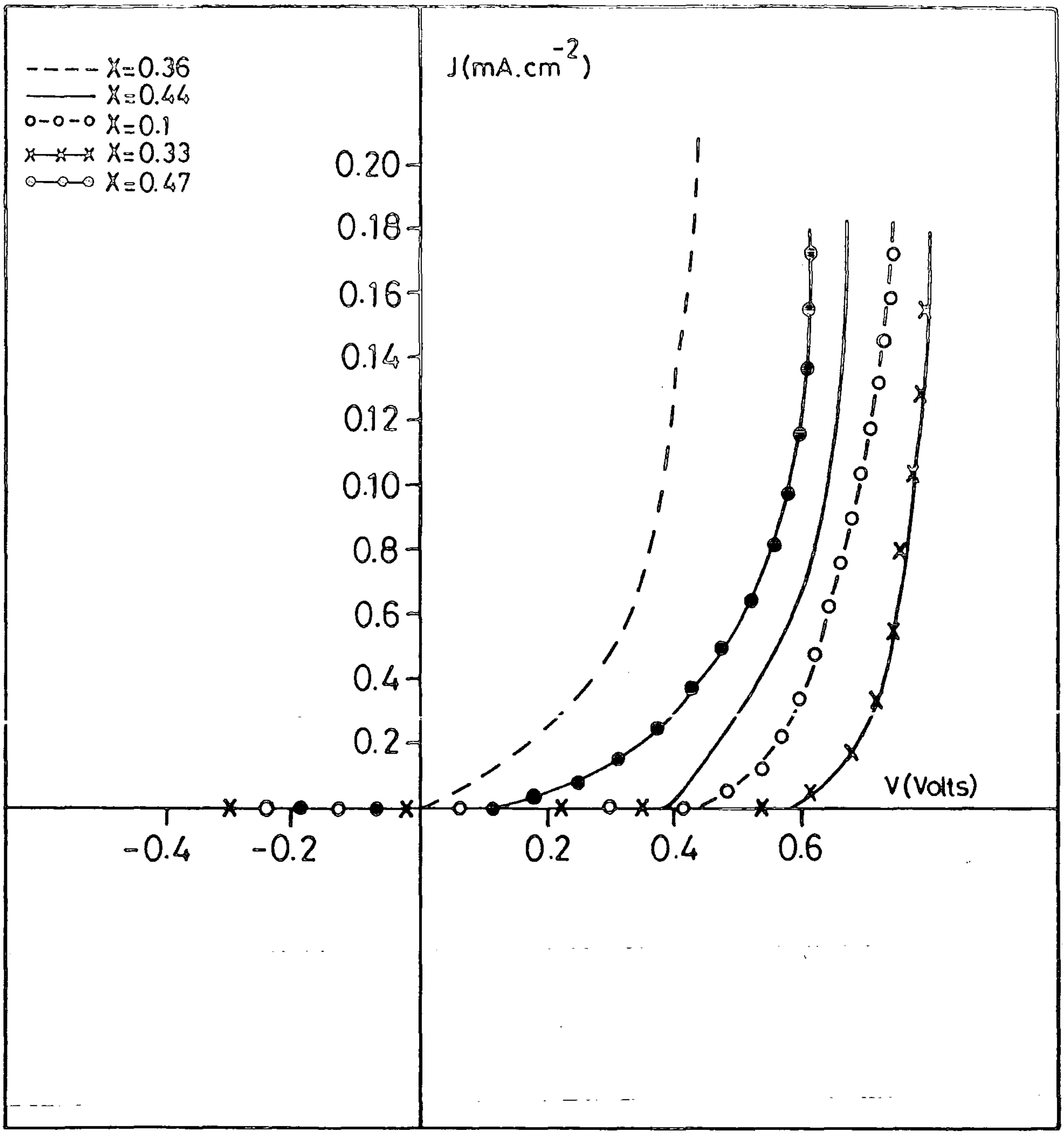

Figure 6.1 Current voltage characteristics of Au-$Cd_{1-x}Zn_xSe$ diodes

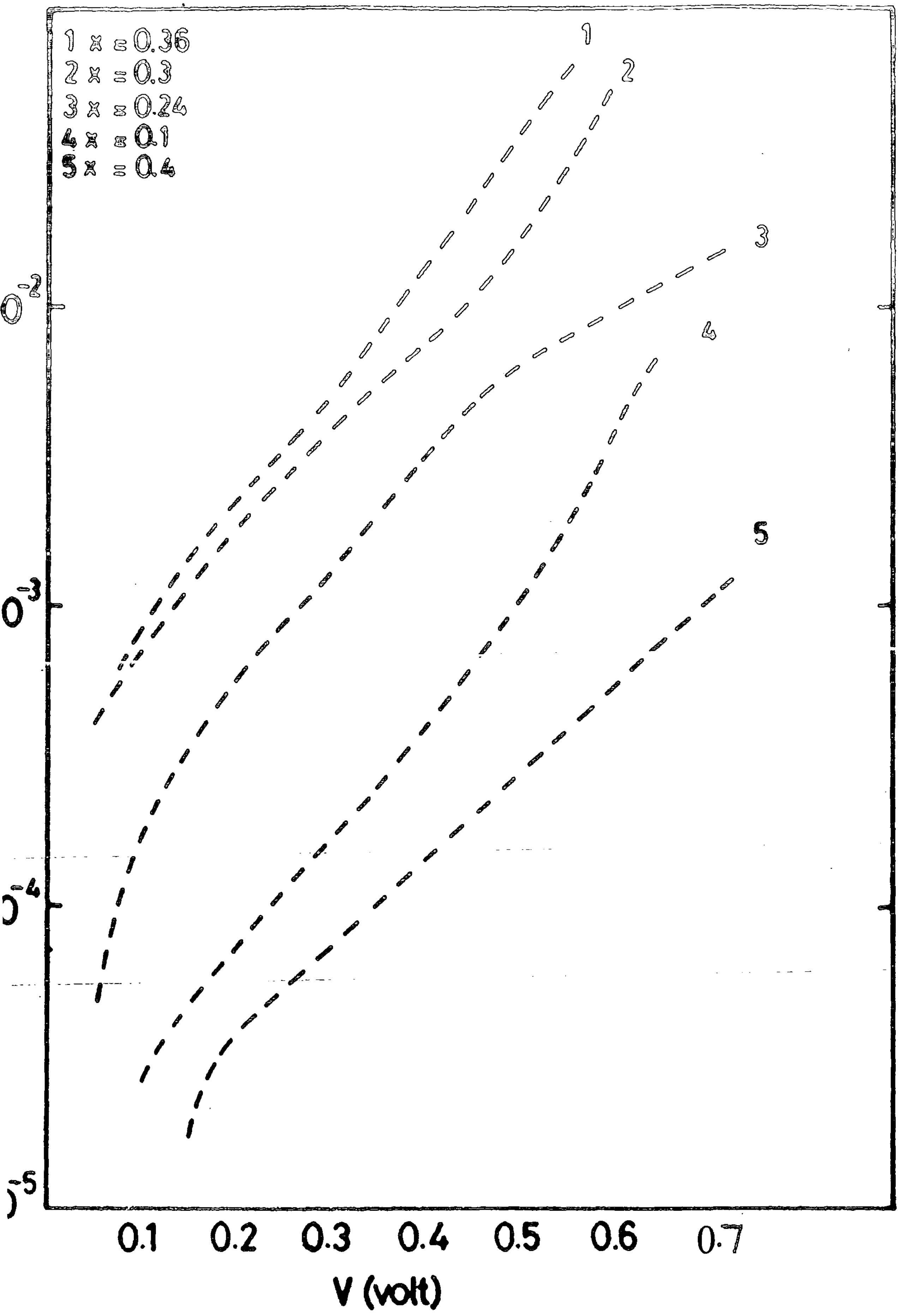

Figure 6.2 Typical forward bias current-voltage (I-V) characteristics of $Cd_{1-x}Zn_xSe$.

6.2.2 Capacitance-voltage characteristics

Capacitance measurements were made at 1 MHz with a Boonton 72B capacitance meter. Detailed C-V characteristics were measured point-by-point using a calibrated voltage source type 2003. These measurements help to provide information on the uncompensated donor density and estimates for the barrier height at the gold-semiconductor interface. The C-V characteristics for diodes of different compositions $(x < 0.47)$ were measured.

In general, the characteristics were good straight lines, as illustrated in Figure 6.3, which shows the capacitance-voltage results in the form of C^{-2}-V plots for a number of typical diodes, with different composition. Analysis of the C-V plots led to estimates for the diffusion potential (V_d), donor density (N_d), Fermi energy (E_c-E_f), barrier height, ϕ_{C-V} and the width of depletion region W_{C-V} using the equations as discussed in Section 3.2.5.

It was assumed that ϵ_s varied linearly with x, and so estimated values of ϵ_s for particular $Zn_xCd_{1-x}Se$ compositions were obtained by linear interpolation between the relative permittivity values of CdSe (9.4) and ZnSe (8.1).(1,2)

The values of N_d, (E_c-E_f) etc. have been calculated and are summarized in Table 6.2.

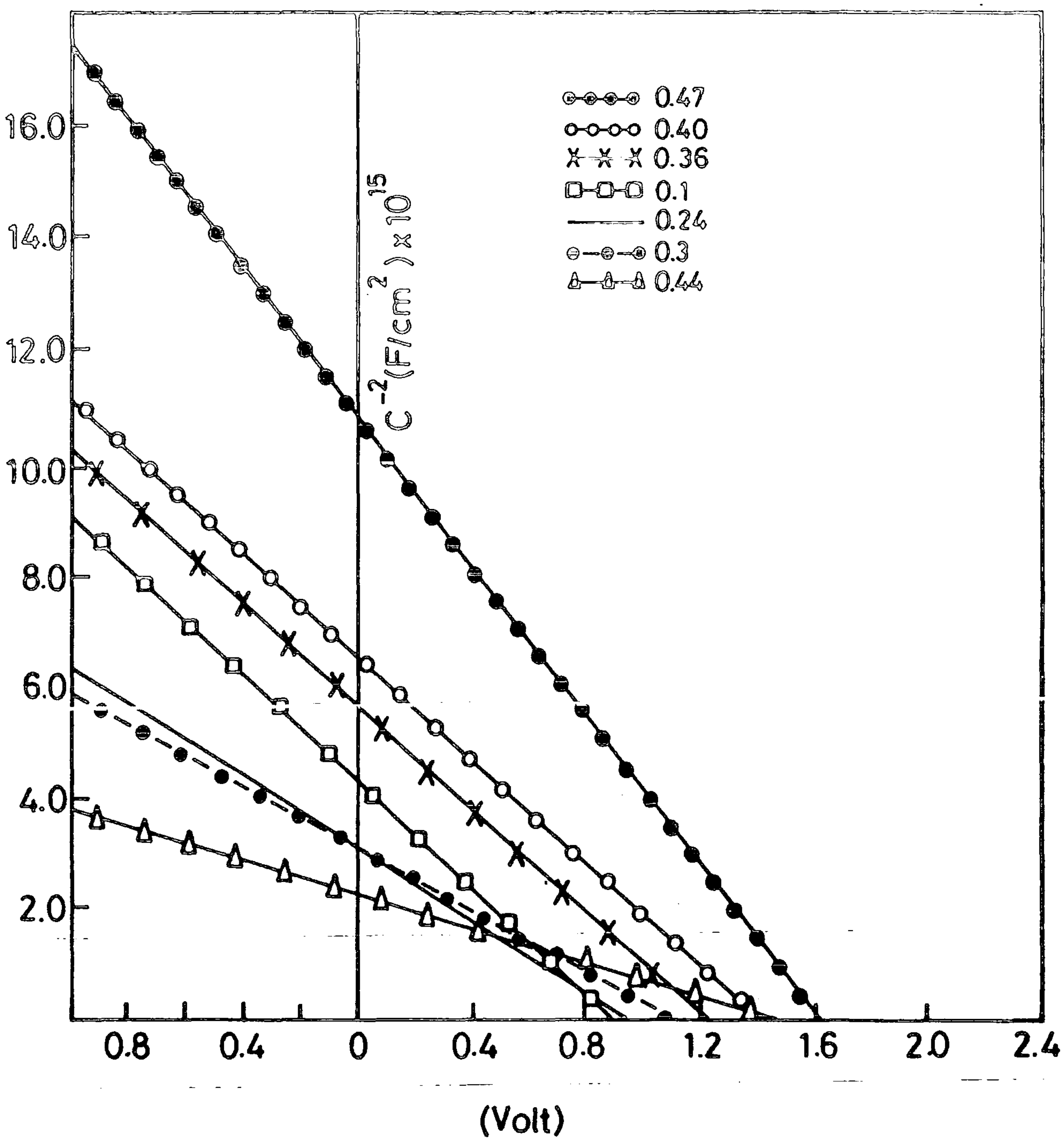

Figure 6.3 C^{-2}-V characteristics for Au-$Zn_xCd_{1-x}Se$.

Composition	$N_d x10^{16} cm^{-3}$	E_c-E_f(eV)	Vd(eV)	Φ_{c-v}(eV)	Wμ.m.
0.10	4.57	0.079	0.9	0.98	0.14
0.24	4.50	0.079	0.96	1.04	0.14
0.30	4.40	0.080	1.16	1.24	0.15
0.36	4.04	0.082	1.25	1.33	0.21
0.40	3.46	0.086	1.27	1.36	0.20
0.44	1.12	0.116	1.31	1.43	0.41
0.47	0.71	0.128	1.34	1.47	0.43

Table 6.2 Barrier heights and carrier densities for Zn_xCd_{1-x} Se.

Thus the calculated values of N_d (from the slopes of the C^{-2}-V plots) obtained from samples of different compositions varied between 4.6 x 10^{16}cm^{-3}for x = 0.1 and 0.71 x 10^{16} cm^{-3} for x = 0.47.

The curve plotted in figure 6.4 shows that N_d was approximately constant for x < 0.25 but started decreasing steeply at higher values of x. The corresponding Fermi energy (E_c - E_f) values were calculated and found to increase with increasing x, from 0.079 eV at x = 0.1 to 0.128 eV at x = 0.47 (Figure 6.5). The width of the depletion region at zero bias W_{C-V} were determined and was found to range between 0.14 um at x = 0.1,and 0.43 μ.m. at x = 0.47 (Figure 6.6).

The diffusion voltage Vd was inferred from the voltage intercepts in the C^{-2} vs V plots and varied between 0.9eV and 1.34eV as x was increased from 0.1 to 0.47. The barrier height Φ_b, was calculated (the sum of the diffusion potential and the fermi energy) and varied between 0.98 and 1.467 eV for compositions from x = 0.1 to x = 0.47 respectively

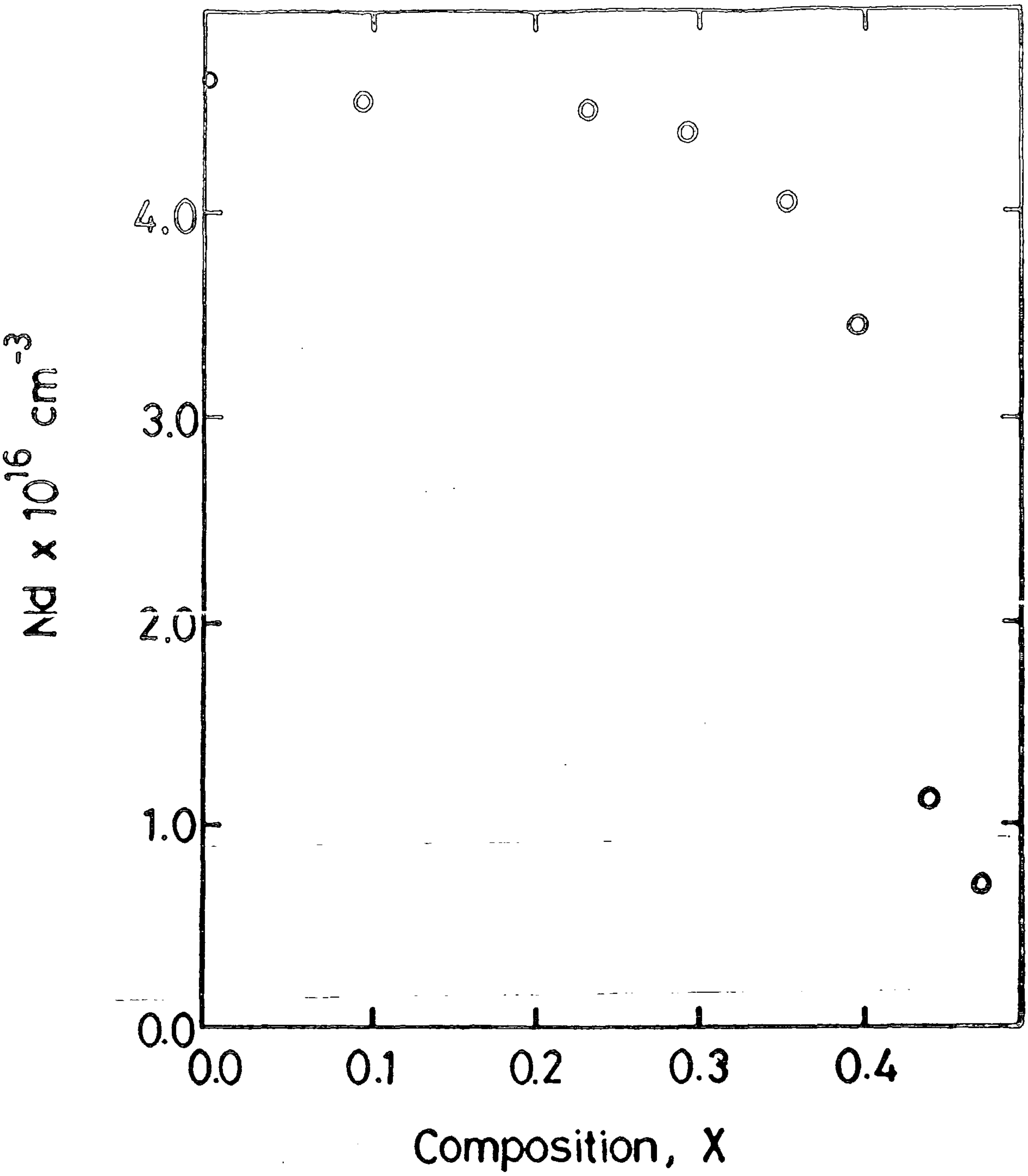

Figure 6.4 Variation in N_d with composition.

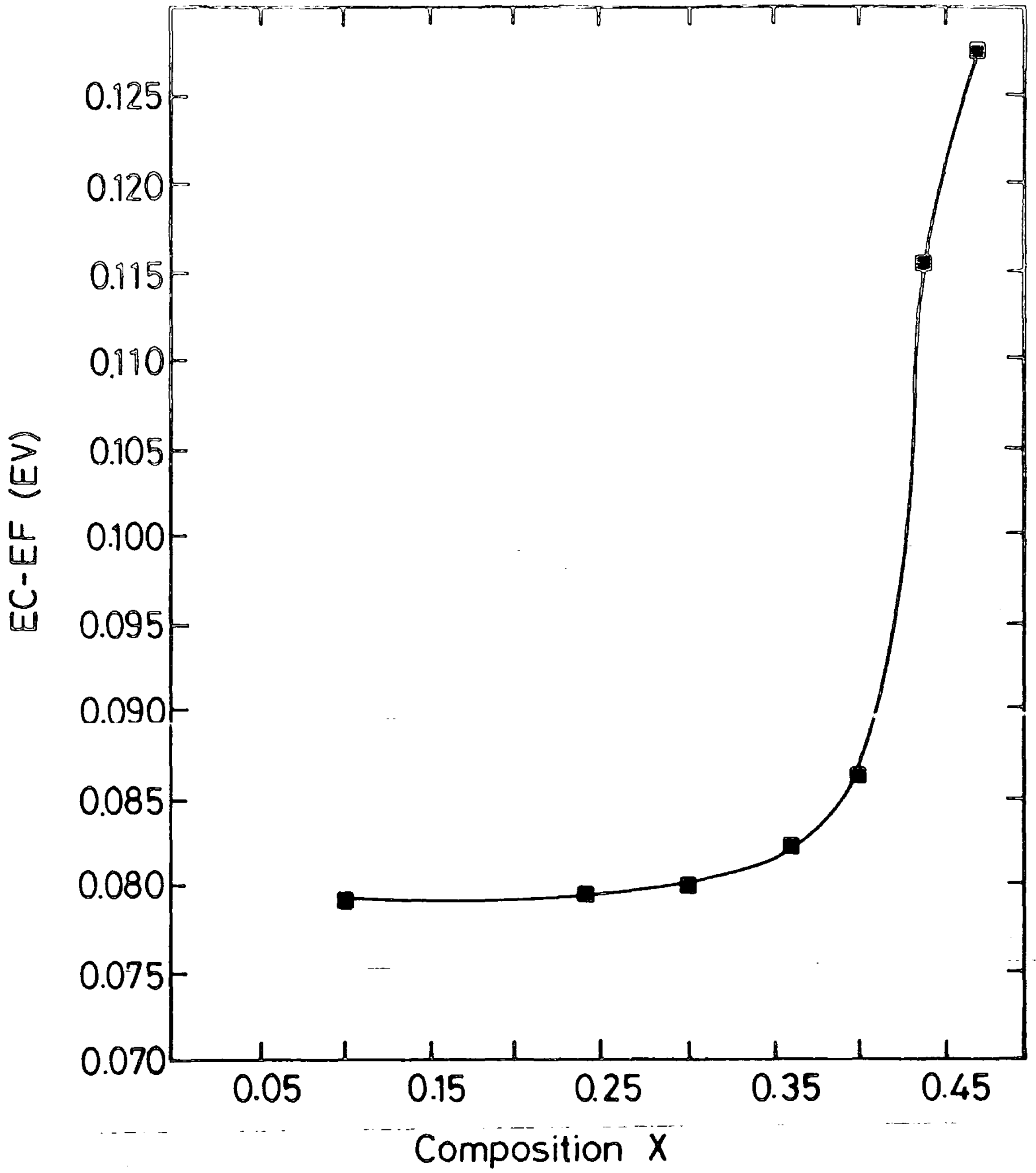

Figure 6.5 Fermi energy (E_c-E_f) Vs composition.

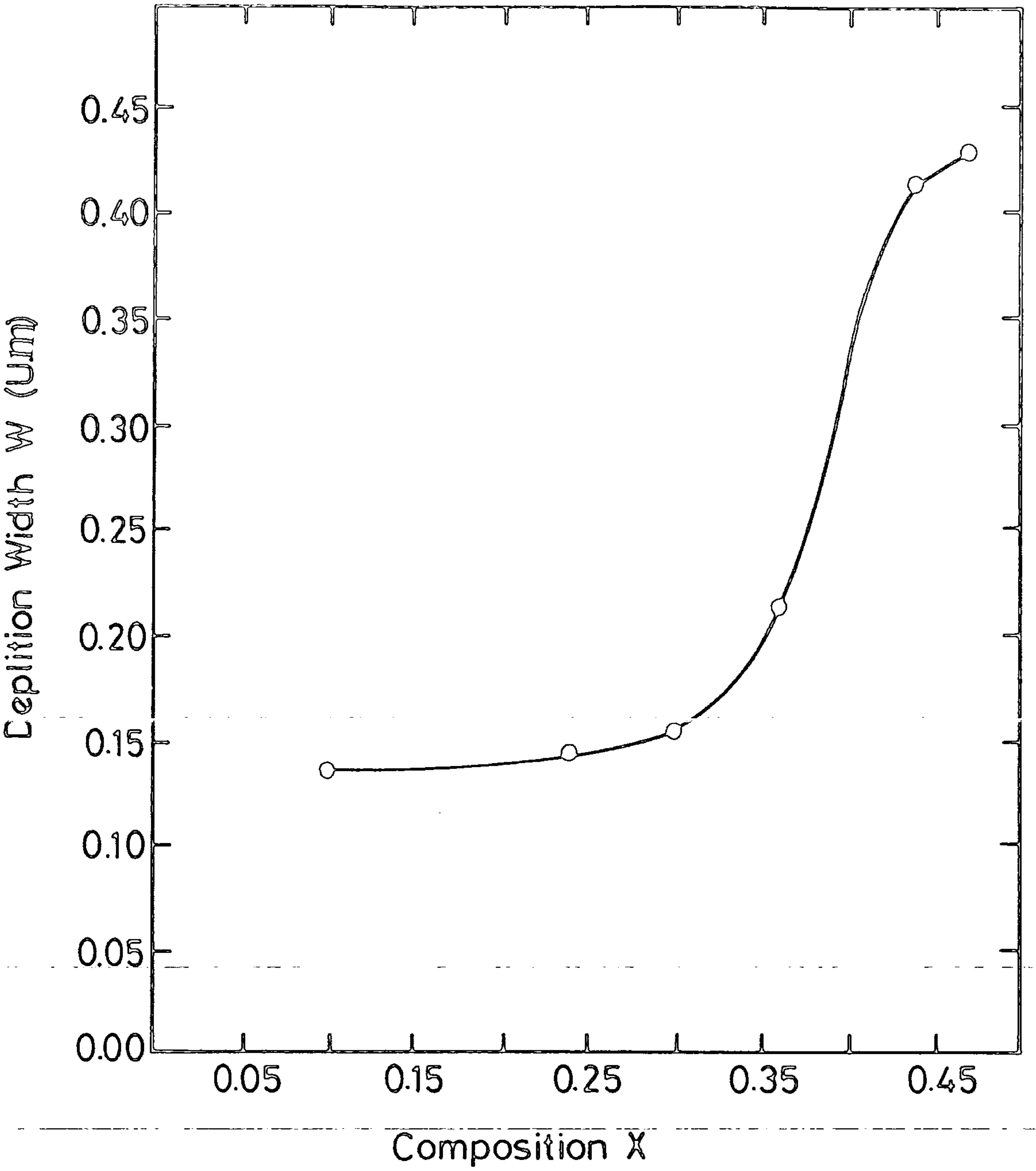

Figure 6.6 Width of depletion region vs composition.

(section 6.2.4).

6.2.3 Photoelectric measurements

The photoelectric measurements provide an accurate and direct method of determining the barrier height. When a metal surface is illuminated by light of sufficient energy, some of the electrons are excited from the Fermi level, into the semiconductor where they contribute to the Short Circuit Photo current. Figure 6.7 shows the spectral response of three typical Au-$Zn_xCd_{1-x}Se$ diodes of different composition ($x = 0.24, 0.4, 0.47$). Of interest here is the low energy threshold which corresponds to the onset of electron excitation from the metal over the barrier into the semiconductor. The peak response and high energy tail-off are the result of electron-hole pair generation in the semiconductor and the effect of surface recombination, respectively. As discussed in Section 3, the low energy tail of the response is approximately proportional to $(h\nu - h\nu_0)^2$ where $h\nu_0$ is the threshold photon energy and equivalent to the barrier height.$^{(3,4)}$ Thus plotting the square root of the response against $h\nu$ should give a straight line, which when extrapolated back to the energy axis, will give the threshold energy (i.e. barrier height).

Figure 6.8 shows a graph of the square root of the photoresponse (Fowler plot) at zero bias as a function of photon energy in the near infrared region for Au-$Zn_xCd_{1-x}Se$ ($x = 0.10, 0.30, 0.36, 0.44, 0.47$) diodes. Extrapolated values of barrier height (i.e. the intercepts on the energy

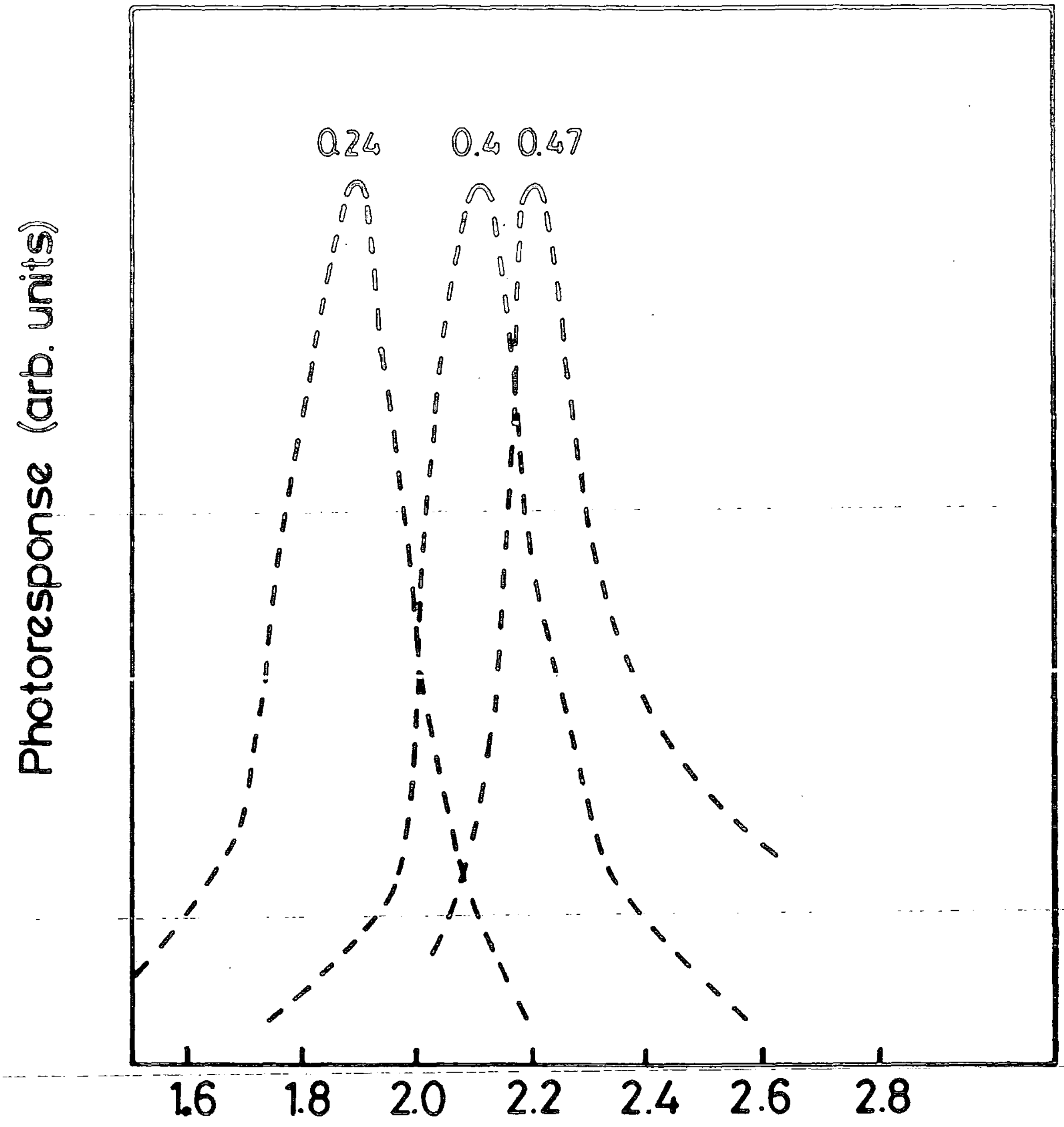

Photon Energy (eV)

Figure 6.7 Photoresponse spectra for Au-$Zn_xCd_{1-x}Se$.

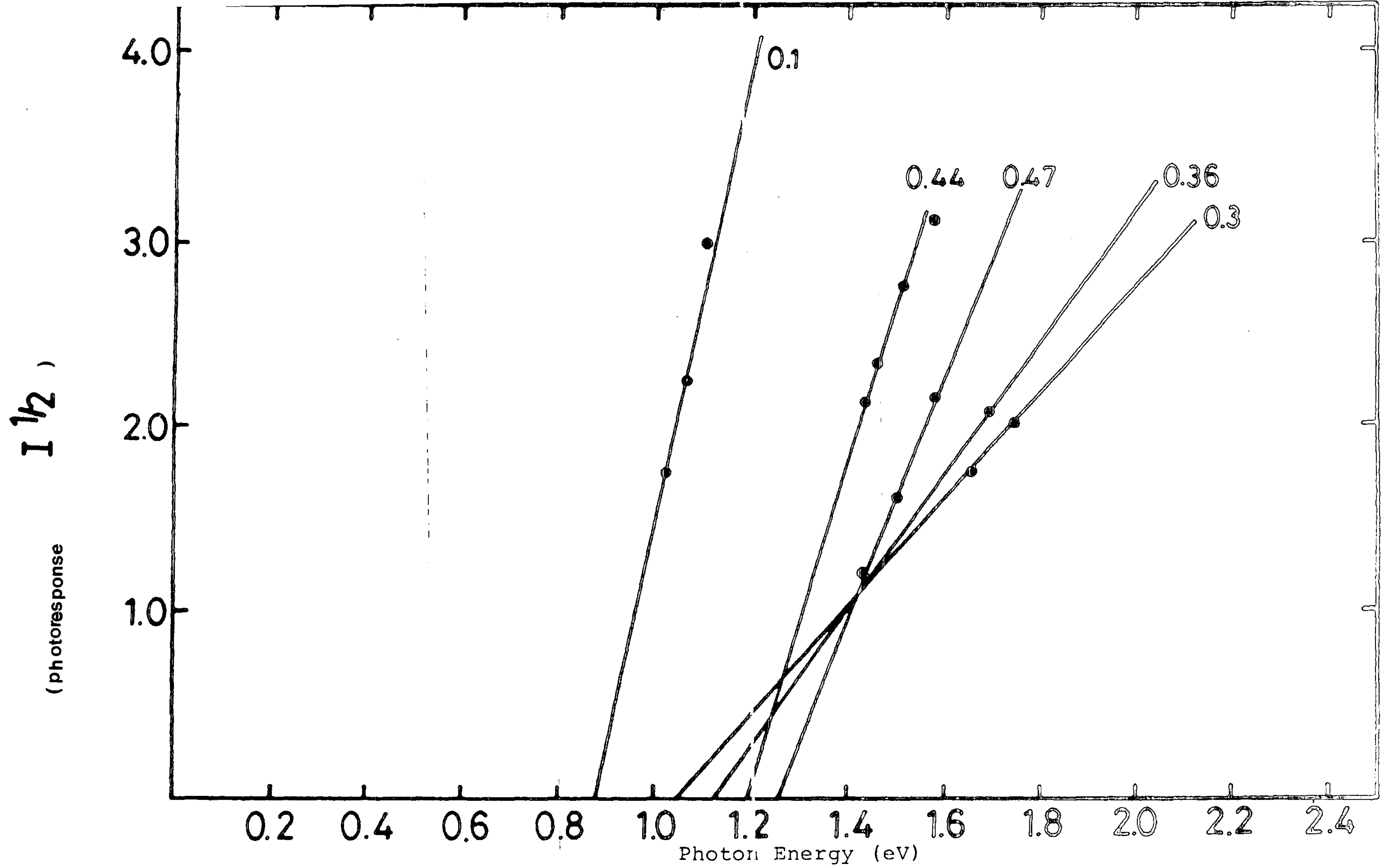

Figure 6.8 Fowler plots of Au-Zn_xCdSe diodes for several different compositions.

axis), are summarized in Table 6.3.

Composition (x)	(Photoresponse) Φ_{ph}
0.10	0.88
0.30	1.04
0.36	1.12
0.44	1.19
0.47	1.26

Table 6.3 Barrier heights from Photoresponse measurements for Au-$Zn_xCd_{1-x}Se$ diodes.

The barrier height measured by this method for CdSe was found to be 0.64 at room temperature$^{(5)}$. With x > 0, the barrier heights were found to increase quite linearly up to the limiting concentration of zinc, x = 0.47, for diode fabrication. A least squares analysis gives an empirical relationship for the dependence of barrier height on composition as:

$$\Phi_{PH} = 0.64 + 1.32 \; x \; eV \qquad (6.1)$$

6.2.4 Dependence of Barrier Height on Composition

The dependence of the barrier height on the composition for Au-$Zn_xCd_{1-x}Se$ devices (x < 0.5) is shown in Figure 6.9. This presents the barrier height measurements as determined from both the photoelectric data (Section 6.2.3) and from the C-V characteristics (Section 6.2.2) as a function of the Zn mole fraction, x. The variation of the band gap Eg(x) (Section 5.5.3) has also been plotted on the same graph for

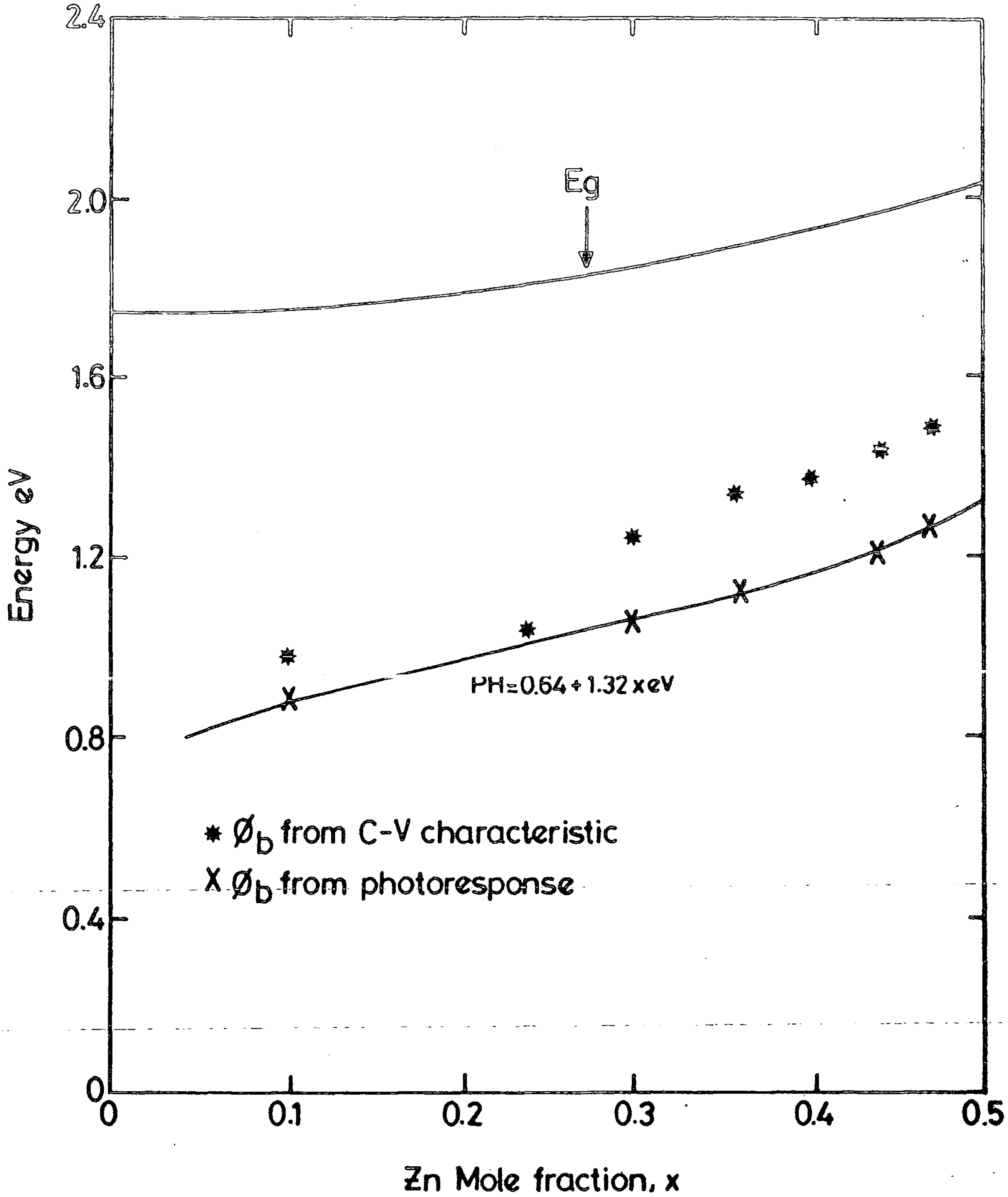

Figure 6.9 Variation in Au-$Zn_xCd_{1-x}Se$ Barrier Height with composition.

reference. These results indicate that the barrier height increased with increasing x in line with the direct energy gap. The estimates for the barrier height obtained from the capacitance measurements, appear to give consistently higher values than those derived from the photoelectric results. This probably indicates that the metal-semiconductor interface contained a significant density of interface states. This is highly likely as the contacts were not formed on cleaved surfaces in conditions of ultra-high vacuum but on polished and etched surfaces which inevitably would have been contaminated.

6.3 Steady State Photocapacitance.

The experimental details for determining the spectral dependence of photocapacitance (PHCAP) are given in chapter 4. These measurements were also carried out on Au-$Zn_xCd_{1-x}Se$ ($x < 0.45$) diodes (Section 4.9) at room and liquid nitrogen temperatures, with the intention of identifying the most important deep levels.

6.3.1 Undoped Au-$Cd_{1-x}Zn_xSe$ diodes

(a) Au-CdSe

The photocapacitance spectra for Au-CdSe diodes are shown in Figure 6.10. This shows that the main room temperature threshold occurred at 1.04eV indicating a level 0.7eV above the valence band. Two additional features were observed in the room temperature spectrum at photon energies of 1.22eV and 1.38eV implying that there were at least two

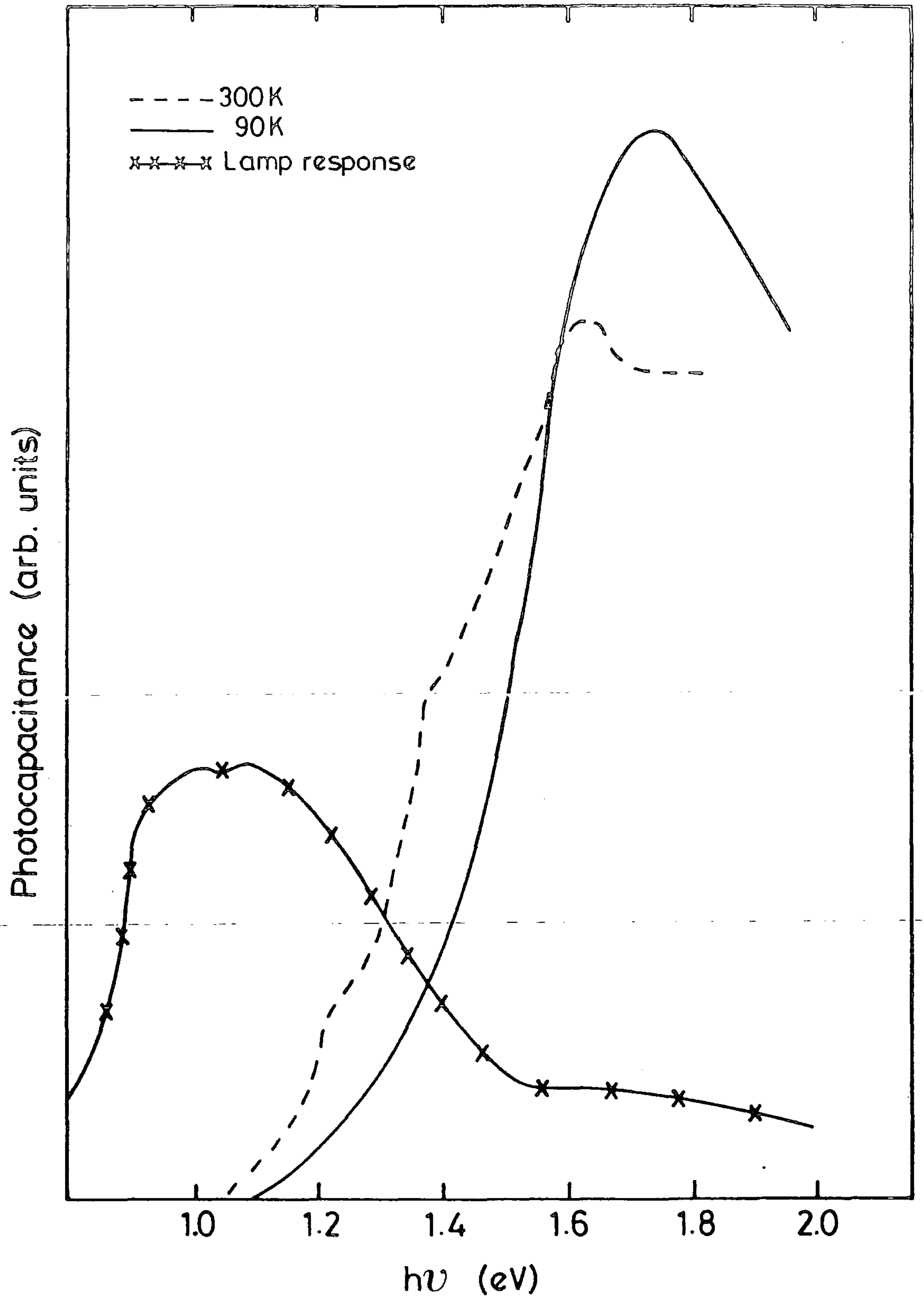

Figure 6.10 Photocapacitance spectra of undoped CdSe at 300K and 90K.

more deep levels with activation energies of 0.52 and 0.36eV with respect to the valence band edge.

At 90K the principal threshold occurred at a photon energy of 1.07eV corresponding to an activation energy of 0.77eV above the valence band. However, there was no evidence for the presence of the other two levels observed in the room temperature spectrum. The maximum PHCAP signal occurred when the energy of the incident light was 1.63eV at 300K and 1.74eV at 90K which was less than the band-gap energy in both cases and provides some evidence for the existence of a donor-like level with an activation energy (referred to as the conduction band) of 0.11 and 0.1 eV respectively.

(b) Au-$Zn_{0.1}Cd_{0.9}Se$

Figure 6.11 shows PHCAP spectra taken from Au-$Zn_{0.1}Cd_{0.9}Se$ diodes at 300K and 90K.

In the room temperature case, the principal threshold occurred at photon energy of 0.8eV corresponding to an activation energy of 0.96eV referred to the valence band. The room temperature curve showed an additional level of 1.34eV indicating a second deep level with an activation energy of 0.42eV relative to the valence band. The band gap energy for this composition was expected to be 1.76eV at 300K.

At low temperature the principal threshold occurred at a photon energy of 0.86eV corresponding to a deep level with an activation energy of 1.0eV with respect to the valence band. There was an additional level at a photon energy of 1.38eV, implying a possible acceptor level at an energy of 0.48eV

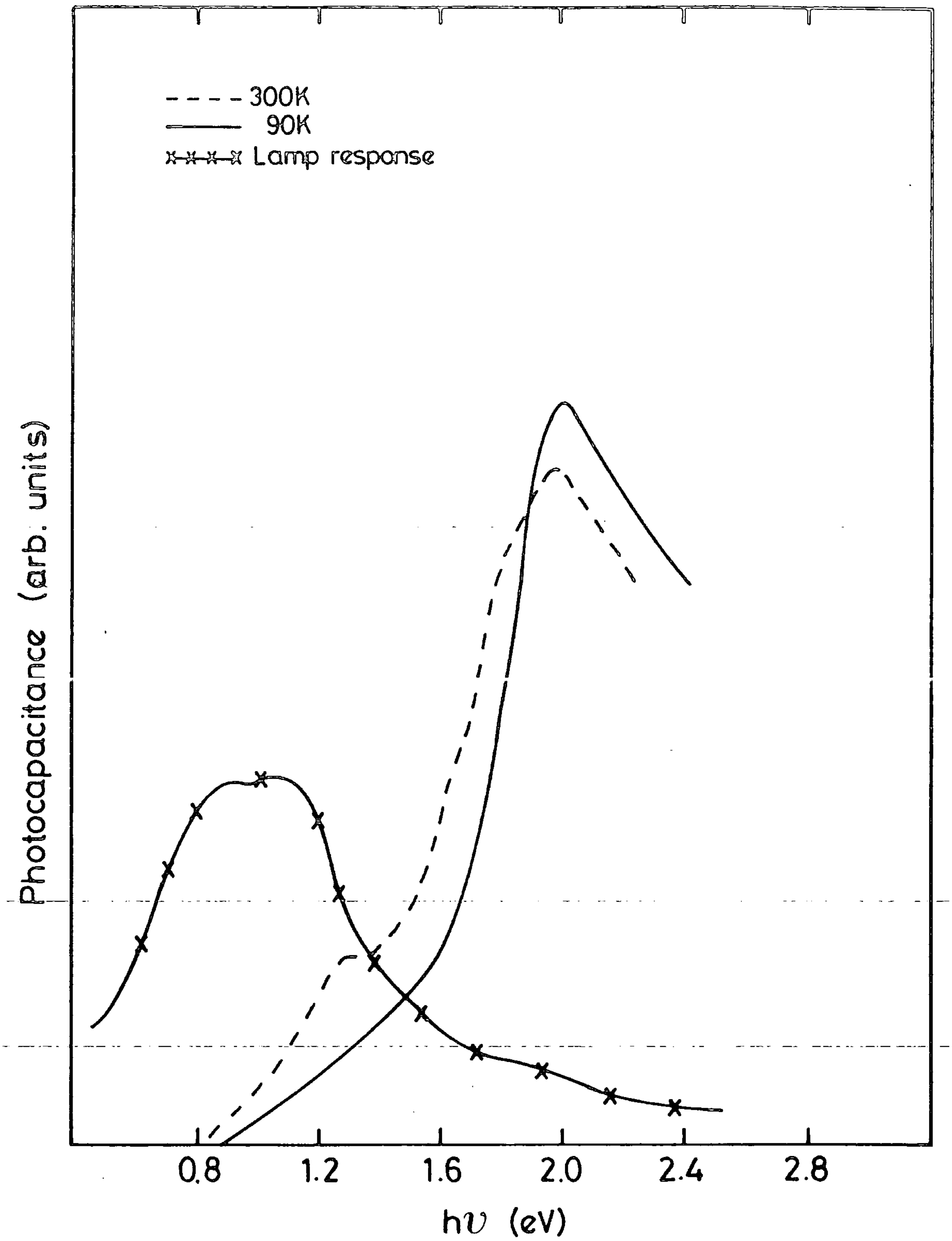

Figure 6.11 Photocapacitance spectra of as-grown $Zn_{0.1}Cd_{0.9}Se$ at 300K and 90K.

with respect to the valence band edge. The band gap has been taken for this composition to be 1.86eV at 90K.

(c) Au-$Cd_{0.64}Zn_{0.36}Se$

Figure 6.12 show the PHCAP spectrum for Au-$Cd_{0.64}Zn_{0.36}Se$ single crystals at room and liquid nitrogen temperatures.

In the room temperature spectrum the principal threshold was observed at 0.9eV corresponding to a value of 1.0eV for the activation energy of the level relative to the valence band. The band gap has been taken to be 1.9eV at 300K. Other positive-going thresholds were observed in the spectrum at photon energies of 1.5eV and 1.67eV implying that there were possible levels at energies of 0.40 and 0.23eV both with respect to the valence band edge. The main threshold at liquid nitrogen temperature was observed at 1.0eV giving a value of 1.0eV for the energy of the corresponding level relative to the valence band edge. An additional threshold was observed in the 90K spectrum at a photon energy of 1.54eV corresponding to level with an energy of 0.46eV relative to the valence band. The band gap has been taken to be 2.0eV.

(d) Au-$Zn_{0.47}Cd_{0.53}Se$

Figure 6.13 shows the typical steady state PHCAP spectra taken from an Au-$Zn_{0.47}Cd_{0.53}Se$ diode at 300K and 90K. There was a negative going threshold in the PHCAP section at room temperature at 1.06eV indicating a level 0.92eV with respect to the conduction band. This was followed by a positive going threshold at 1.58eV, corresponding to a level with an energy of 0.4eV referred to the valence band. In the low

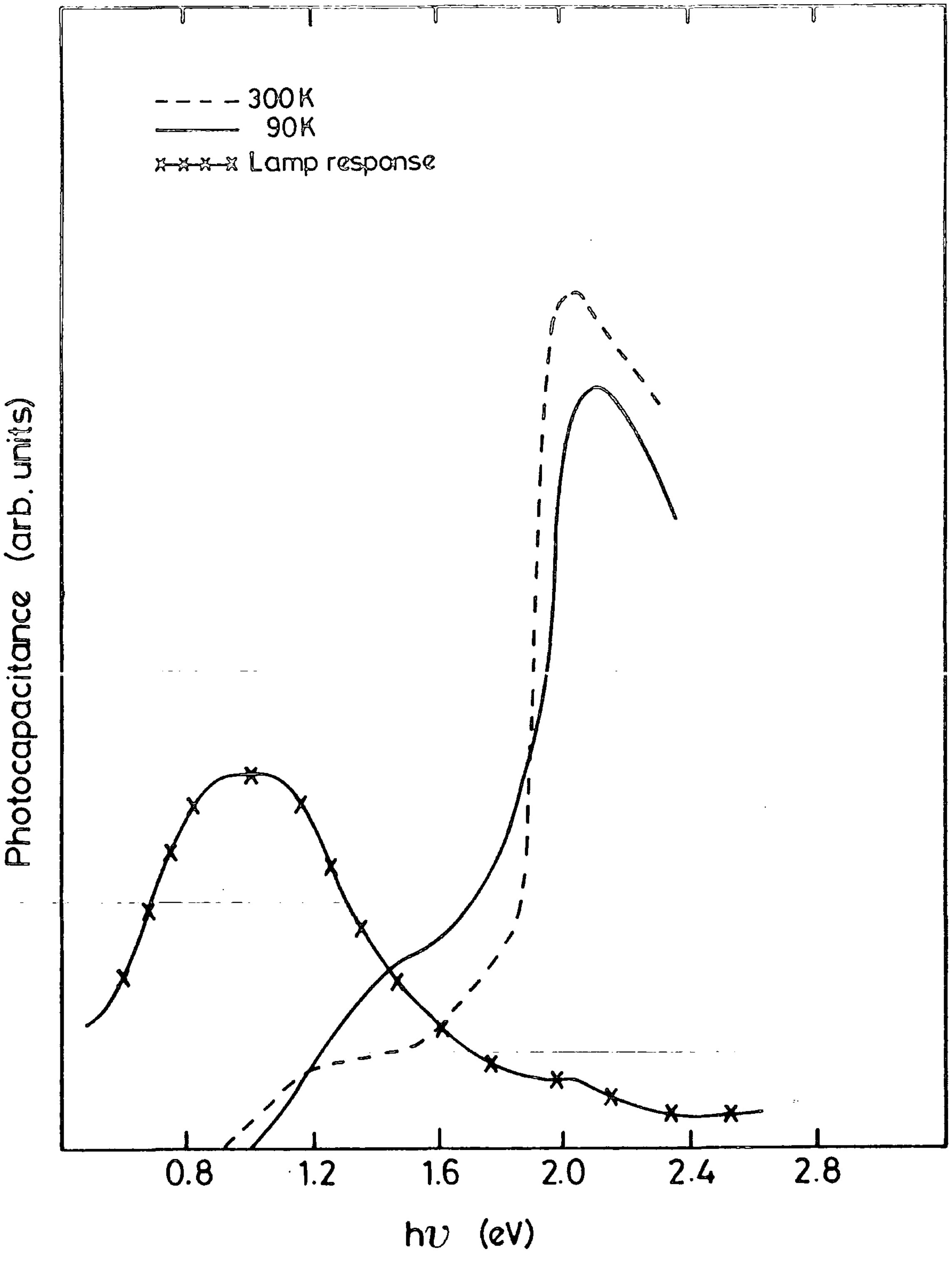

Figure 6.12 Photocapacitance spectra of as-grown $Zn_{0.36}Cd_{0.64}Se$ at 300K and 90K.

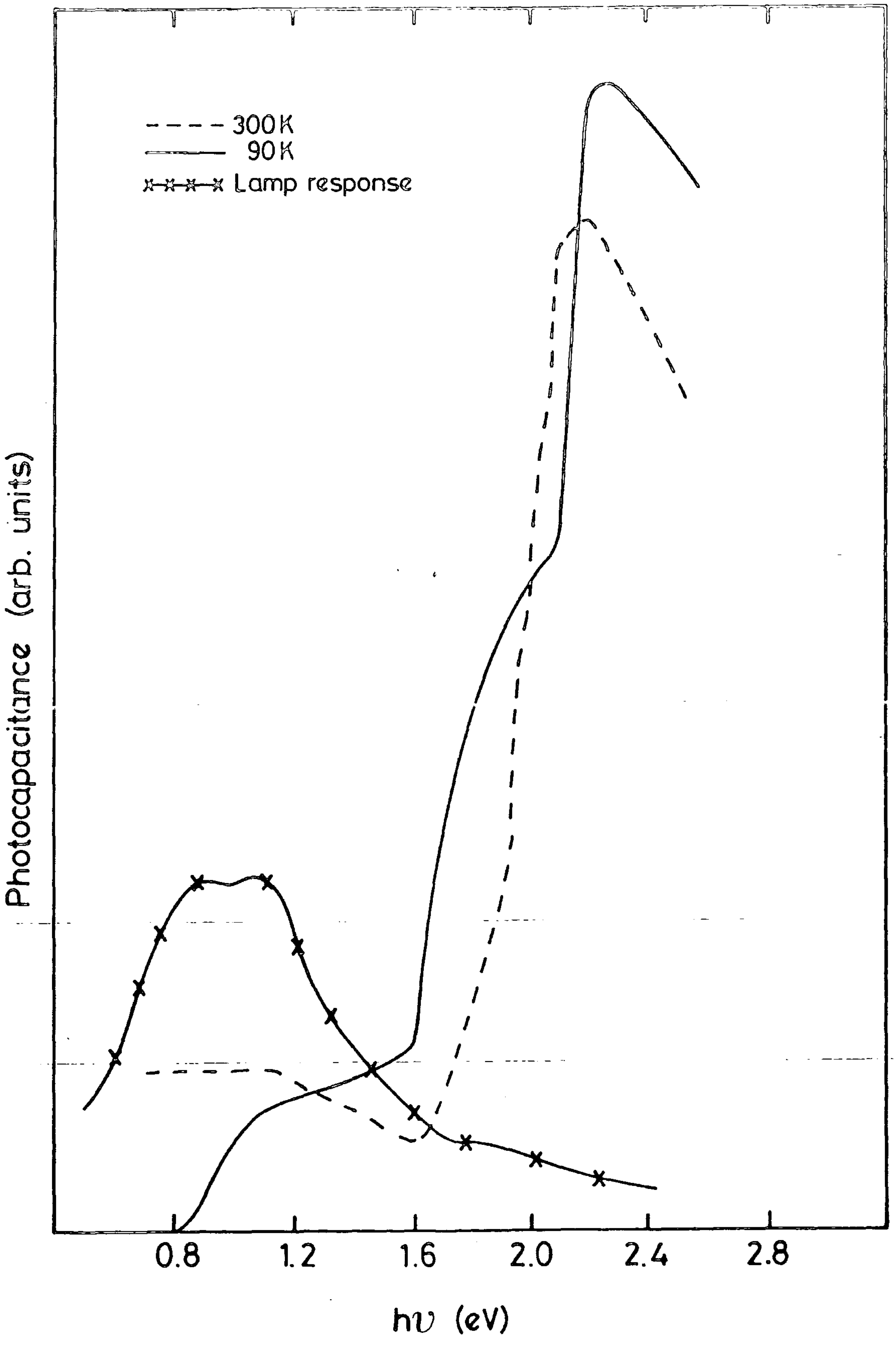

Figure 6.13 Photocapacitance spectra of as-grown $Zn_{0.47}Cd_{0.53}Se$ at 300K and 90K.

temperature spectrum, there was no negative going threshold and the principal (positive going) threshold occurred at 1.1eV indicating a level with an energy of 1.0eV relative to the valence band. Additional levels at 1.6eV (corresponding to an activation energy of 0.5eV relative to the valence band) and at 1.91eV (corresponding to an activation energy of 0.19 eV with respect to the valence band) were also observed.

6.3.2 Steady State-Infrared Quenching of Photocapacitance (IRQ-PHCAP)

The system used for the photocapacitance measurements was adapted by the addition of second light source and used to measure the infrared Quenching of photocapacitance. The spectrum of the secondary light source was filtered to limit the spectrum between 4800Å to 7000Å. The spectral dependence of infrared quenching of photocapacitance for an Au-$Zn_{0.47}Cd_{0.53}Se$ diode is shown in Figure 6.14 at 90K. The principal quenching threshold was observed at 1.15eV indicating the presence of a deep level with an active energy of 1.1eV relative to the valence band. Other features were observed at 1.59eV and 1.9eV suggesting levels with energies of 0.66 and 0.35eV with respect to the valence band.

6.3.3 Doped Au-$Cd_{1-x}Zn_xSe$ samples

Photocapacitance spectra for a CdSe:Cu diode are shown in Figure 6.15. The principal threshold of PHCAP at room temperature occurred at 0.8eV, indicating a level at 0.94 referred to the valence band. At 90K the threshold occurred at a photon energy of 0.89eV corresponding to an energy of

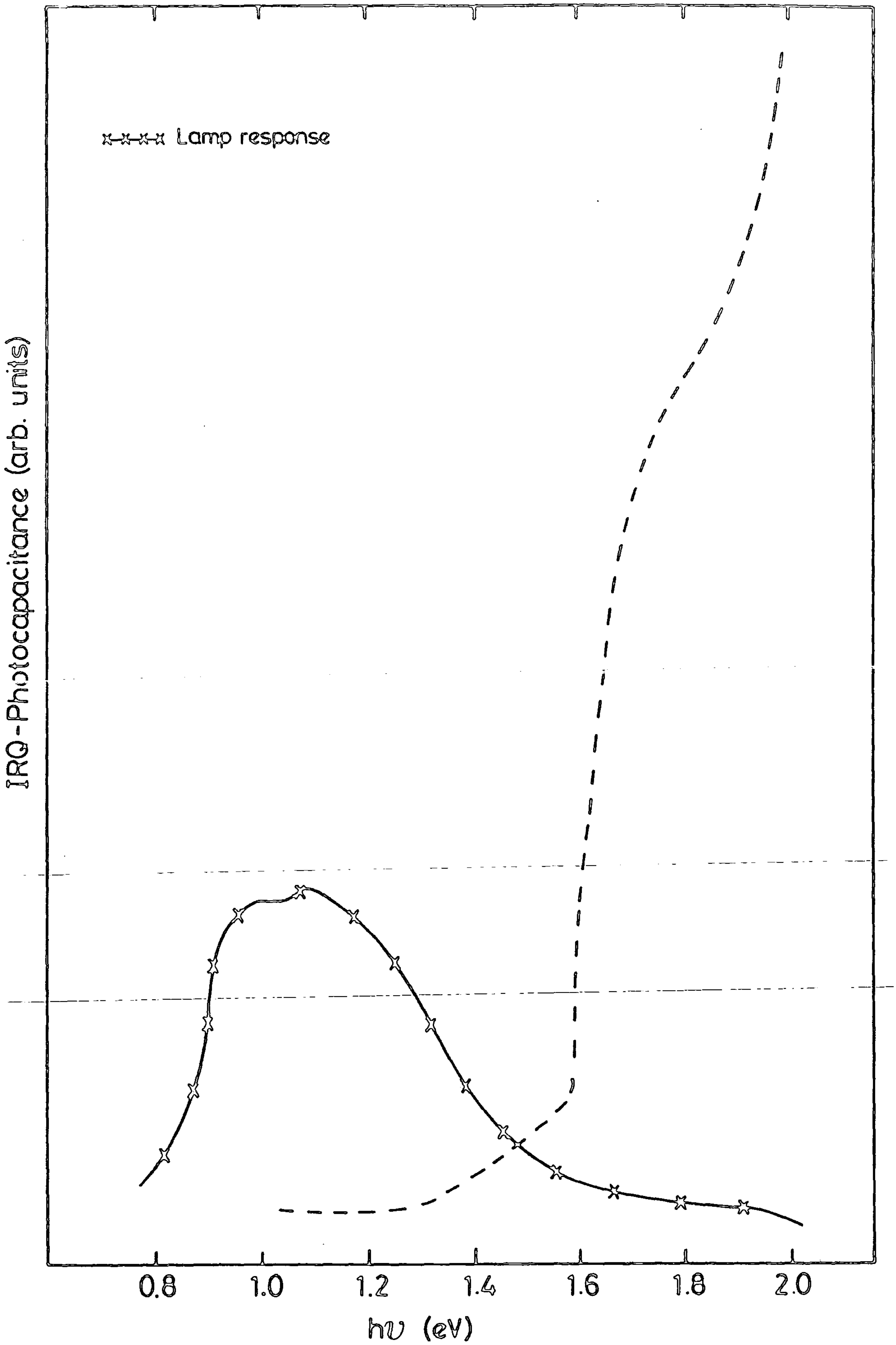

Figure 6.14 Steady-state IRQ-PHCAP measurements for $Zn_{0.47}Cd_{0.53}Se$.

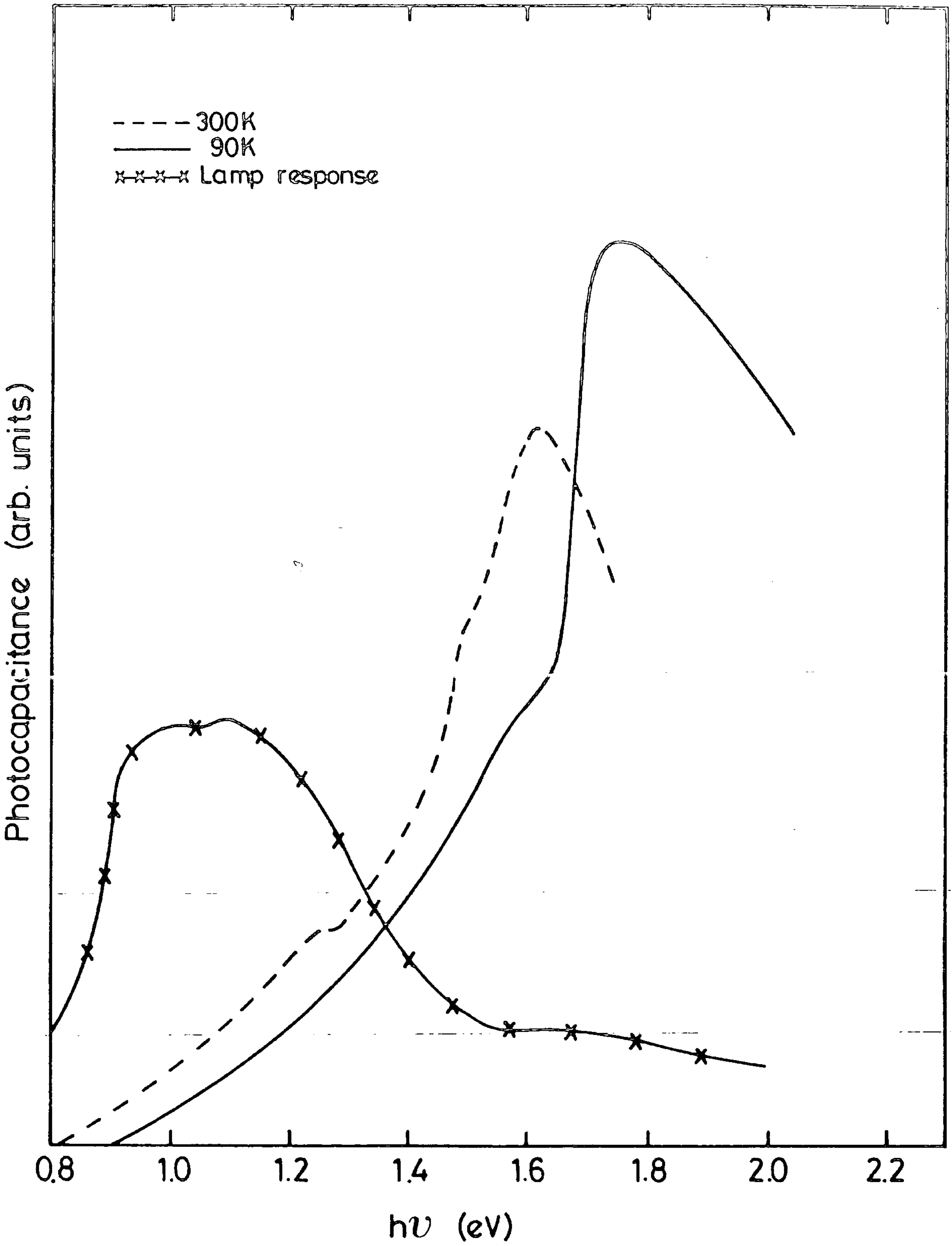

Figure 6.15 Photocapacitance spectra of copper doped CdSe at 300K and 90K.

0.95eV with respect to the valence band. The room temperature spectrum showed additional thresholds corresponding to levels at 0.51 and 0.24eV with respect to the valence band. The maximum PHCAP signal occurred when the energy of the incident light was 1.61eV at 300K and 1.74eV at 90K which is less than the band gap energy and therefore suggests a donor like energy level at 0.13 and 0.1eV with respect to the conduction band at the two temperatures.

The PHCAP spectrum for Au-$Cd_{0.7}Zn_{0.3}Se$:Cu is shown in Figure 6.16. The band gap has been taken to be 1.85 and 1.96eV at 300K and 90K respectively. The principal threshold of PHCAP at room temperature occurred at 1.1eV, indicating a level 0.96eV above the valence band. The room temperature curve showed an additional threshold at a level 0.16eV above the valence band.

At 300K the magnitude of the PHCAP response started to decrease when the photon energy of the incident light was increased above 1.8eV suggesting a donor like level with an activation energy of 0.26eV relative to the conduction band . In the low temperature spectrum, the principal threshold occurred at a photon energy of 1.22eV which implied that there was an acceptor like state with an energy of 0.92eV.

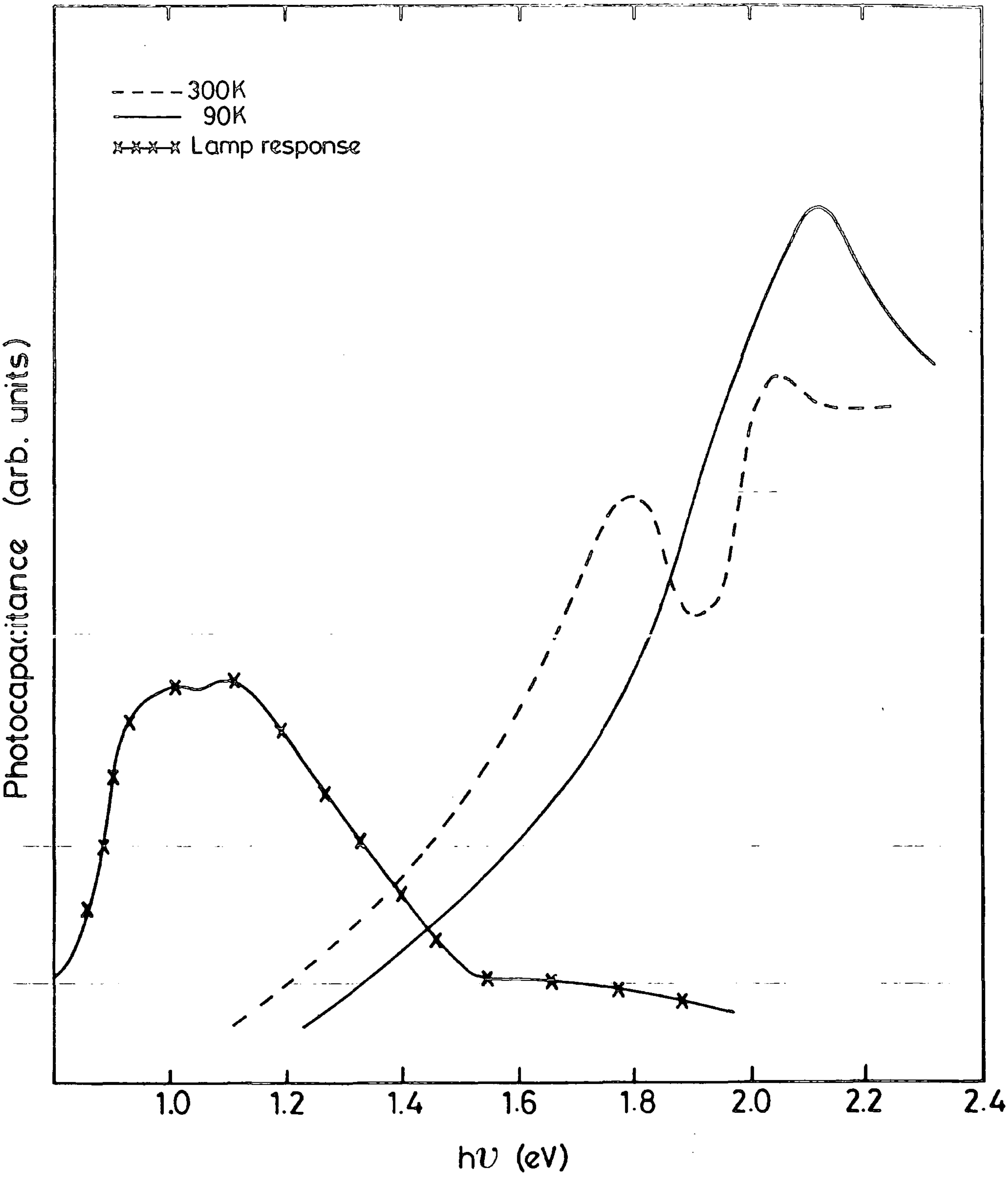

Figure 6.16 Photocapacitance spectra of copper doped $Zn_{0.3}Cd_{0.7}Se$ at 300K and 90K.

6.4 Discussion

6.4.1 Electrical characteristics

The electrical properties of Au-$Cd_{1-x}Zn_xSe$ ($0 < x < 0.5$) have been investigated. The current-voltage characteristics for Au-$Cd_{1-x}Zn_xSe$ were measured immediately after forming the Schottky device and gave good rectifying characteristics with small reverse bias leakage currents (see Figure 6.1). This in a good agreement with other results reported by Lewis et al.(6) and by Ture et al.(5) on Schottky diodes in single crystal CdSe which has been annealed in Se vapour for several days to(7,8) suppress the selenium vacancies and increase the resistivity. Such Au-CdSe Schottky diodes were not rectifying until they had been heated in air at 100°C for several hours. The common feature of all the Schottky devices was the reduction of reverse bias leakage current after heating in air(7). This is believed to be due to oxygen absorption and diffusion(9). Heating in air or ageing produced changes in the surface structure. They were then considered to approximate to MIS rather than MS(7) structures. Ture et al.(5) demonstrated that the same degree of improvement as that which was produced by 2 months of ageing could also be achieved by heating in air at 100°C for 16h.

The present measurements of the forward J-V characteristics samples of different composition gave ideality factors that ranged from 1.01 to 2.07. Deviation from the ideal situation (n = 1) can be due to many reasons(10,11) such as the presence of surface states and an oxide layer(12). According to Card and Rhoderick(11), the ideality factor increases from 1.03 where thin insulating layers 10Å thick are present on the surface of a semiconductor, to 1.5 when the insulating layers are 22Å thick, and this suggests that insulating layers of different thickness were present after chemical etching and can yield non-ideal Schottky barriers.

High conductivity samples normally give rise to thin barriers and tunnelling through the barrier can then occur.(13) Thus the dependence of the ideality factor on conductivity has also been investigated on Au-Si Schottky diodes with high conductivity samples and these also gave high n values(14).

The C^{-2}-V characteristics for the diodes (with $x < 0.47$) are given in Figure 6.3, and in general displayed good straight lines. There is a systematic increase in the extrapolated voltage intercept with increasing x, suggesting a corresponding increase in the Au-$Zn_xCd_{1-x}Se$ barrier height. There was also a variation with composition in the uncompensated donor density N_d calculated from the slopes of the C^{-2}-V characteristics. This is recorded in Figure 6.4 and shows that for $x < 0.28$,N was constant at about $4.5 \times 10^{16} cm^{-3}$ but that it fell rapidly as the proportion of Zn was increased beyond this. The behaviour of Nd with x for nominally undoped material is similar to that observed in

$Zn_xCd_{1-x}S$ (15), and in that material it is also coupled with a large reduction in the carrier mobility, due possibly to alloy scattering, and resulting in a very large increase in the resistivity. Although Hall effect measurements were not made during the course of the present study, it is probable that a similar situation would apply, and might explain why it was not possible to fabricate diodes from crystals with x > 0.5.

6.4.2 Barrier height in $Zn_xCd_{1-x}Se$-Au diode

The barrier heights of Au-$Zn_xCd_{1-x}Se$ diodes were determined from the forward I-V characteristics, the C-V characteristics and by the photoelectric method.

The barrier height in a metal-semiconductor junction depends on the work function of the metal Φ_m, the electron affinity of the semiconductor ϵ_s, and the concentration and distribution of surfaces states at the interface(16). The variation in the Au-$Zn_xCd_{1-x}Se$ barrier height with composition has not been previously reported, so far as the author is aware. The barrier height is significantly larger, even at low x, than values normally observed in CdSe (5). The latter should in principal have a very low value for the barrier height due to the large electron affinity of CdSe. However measured values are generally much higher, due to surface effects(5). Thus the observation of yet larger values in the mixed crystals even at x = 0.1, would suggest that these devices were also strongly affected by surface state activity. The fact that the barrier height values obtained from C^{-2} -V measurements were consistently higher than those determined from the photoelectric measurements lends additional support to this. The barrier height from photoelectric measurements probably gives the most accurate measure of the barrier height(10). These values (Table 6.3) lie between 0.49eV and 1.36eV for CdSe and ZnSe respectively(12). The barrier heights observed from the current-voltage characteristics were sometimes in disagreement with those determined from capacitance-voltage and photoelectric measurements. The disparity between these estimates of barrier height can be attributed to the presence of an interfacial layer between the gold contact and the semi conductor(18,19). However, the $Zn_xCd_{1-x}Se$ diodes did not show the reverse bias leakage problems experienced with Au-CdSe devices prepared in the same way.

According to the simple Schottky-Mott theory, the barrier height is given by:-

$$\Phi_b(x) = \Phi_{Au} - \chi_x \qquad (6.2)$$

where $\Phi_b(x)$ is the barrier height for gold on a mixed crystal with an electron affinity χ_x.

The barrier height for Au-CdSe and Au-ZnSe should be 0.63 and 1.64eV respectively(20,21), and thus the results suggest that the electron affinity of $Zn_xCd_{1-x}Se$ decreases as the zinc composition increases (see Figure 6.17). A similar situation has been found with Au-$Zn_xCd_{1-x}S$ structures(22).

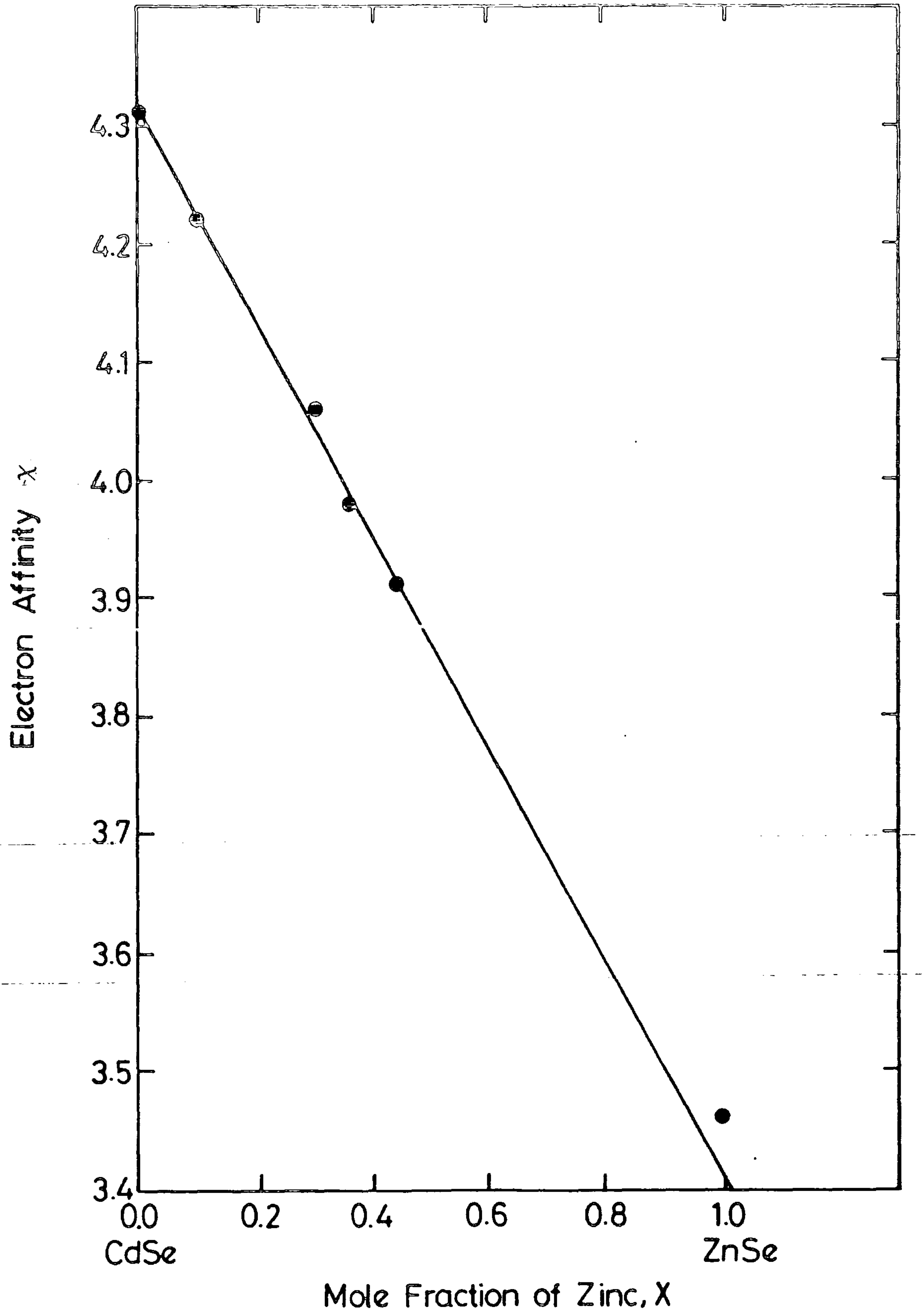

Figure 6.17 Variation in electron affinity χ with composition.

6.4.3 Deep levels

Deep levels have been reported in a $Zn_{0.3}Cd_{0.7}Se$ crystal by Burger and Roth(23) and by Lewis et al.(6) for $Zn_{0.25}Cd_{0.75}Se$. Burger and Roth identified a level located about 0.49eV below the conduction band, from a detailed analysis of space charge limited currents in their devices. They suggested that it might be associated with a Cu interstitial-Cd vacancy pair by analogy with a similar level in CdSe. Lewis et al. reported observing two electron traps, with activation energies (referred to the conduction band) of 0.54 and 1.04eV, and three hole traps with activation energies referred to the valence band) of 0.2, 0.55 and 0.85eV. These results were derived from a combination of photocapacitance, and thermal and optical DLTS studies on Durham grown crystals. Consequently, it is probable that the 0.55eV level reported by Lewis et al. corresponds with the centre observed in all the samples investigated in the present study(24) with about the same activation energy. (The results are summarised in table 6.4). Lewis et al.(16) pointed out that the activation energy of this level is close to that of a widely reported centre in CdSe of 0.62eV which has been associated with doubly ionised Cd vacancies(25).

The other principal centre observed here(24) at 0.9-1.0eV is more difficult to interpret as it is situated in the middle of the band gap. However, this may be related to the trap reported by Lewis et al. with an activation energy of 1.04 with respect to the conduction band. They suggested that this level would behave primarily as an electron trap. The uniformity in the activation energies for the two main levels observed in the photocapacitance spectra when these are referred to the valence band implies that these levels were pinned to the valence band. This lends additional support to the suggestion that the 0.5eV level might be related to a Cd-vacancy, since that might be expected to behave in this way.

Table 6.4. Summary of deep levels observed in $Zn_xCd_{1-x}Se$.
(a) undoped samples - (b) doped samples

Composition x	Temperature (K)	Energy gap Eg eV	Threshold	Activation Energies (eV)		
0	300	1.74	0.7(v.b)	0.52(v.b)	0.36(v.b)	0.1(c)
0	90	1.84	0.77(v.b)	-	-	0.11(c)
0.1	300	1.76	0.96(v.b)	0.42(v.b)	-	-
0.1	90	1.86	1.0(v.b)	0.48(v.b)	-	-
0.36	300	1.9	1.0(v.b)	0.4(v.b)	-	0.23(v)
0.36	90	2.0	1.0(v.b)	0.46(v.b)	-	-
0.47	300	1.98	0.92(c.b)	0.4(v.b)	-	-
0.47	90	2.1	1.0(v.b)	0.5(v.b)	-	0.19(v)

(a) undoped samples

Composition x	Temperature (K)	Energy gap Eg eV	Threshold	Activation energies (eV)		
0	300	1.74	0.94	0.51	0.24	0.13
0	90	1.84	0.95	-	-	0.1
0.3	300	1.85	0.96	-	0.26	0.16
0.3	90	1.96	0.92	-	-	-

(b) doped samples

The PHCAP measurements on the copper doped material indicate that the acceptor level at 0.96 eV above the valence band is related to the copper impurity(25,26). This is close to the value of 1.05 eV found by Robinson and Bube(25) and 1.0eV observed by Ture et al.(26,27) for the main copper impurity centre in CdSe.

6.5 Conclusion

Schottky diodes of Au-$Zn_xCd_{1-x}Se$ $(0 < x < 0.45)$ were fabricated from dice cut from the various crystals and these have allowed measurements of some of the electrical characteristics to be made. The current-voltage characteristics were generally rectifying with ideality factors which varied from 1.01 to about 2.07. The values of the saturation current density decreased as the zinc content increased.

Capacitance-voltage characteristics were also determined and these gave estimates for the barrier heights and donor densities. The latter were found to decrease as the zinc composition increased. Barrier height was also measured using the photoelectric technique and showed that the barrier height increased nearly linearly with x $(x < 0.45)$.

The spectral dependence of steady-state photocapacitance and infrared quenching of photocapacitance were also measured over the same composition range in both doped and undoped

$Zn_xCd_{1-x}Se$ crystals. This revealed two main levels with activation energies (referred to the valence band) of 0.4 - 0.5eV and 0.9-1.0eV that were seemingly independent of the composition.

References

1. Sze, S.M., Physics of Semiconductor Devices, John Wiley and Sons, New York (1969).

2. Wheeler, R.G. and Dimmock, J.U., Phys. Rev. 125 (1962), 1805.

3. Rhoderick, E.H., Metal Semiconductor Contacts, Clarendon Press, Oxford (1980).

4. Fowler, R.H., Phys. Rev. 38 (1931), 45.

5. Ture, I.E., Brinkman, A.W., Russell, G.J. and Woods, J., Phys. Stat. Sol. (a) 100 (1987), 681.

6. Lewis, J.E., Ture, I.E., Brinkman, A.W. and Woods, J., Semi cond. Sci. Technol. 1 (1986), 213.

7. Ture, I.E., Russell, G.J. and Woods, J., Journal of Crystal Growth, 59 (1982), 223.

8. Ture, I.E., Poulin, F., Brinkman, A.W. and Woods, J., Phys. State Sol. (a) 77, (1983), 535.

9. Rickus, E., Bonnet, D., Proc. 3rd E.C. Photovolt. Solar Energy Conf. Cannes, (1980), 871.

10. Rideout, V.L., Thin Solid Films, 48(1978), 261.

11. Card, H.C. and Rhoderick., E., J. Phys. D:Appl. Phys, 14 (1971), 1589.

12. Cowley, A.M., J. Appl. Phys., 37 (1966), 3024.

13. Saidin, K., Ph.D. Thesis, Durham University, 1987.

14. Khang, D., Sol. State Electron, 6 (1963), 281.

15. Hartman, H., Mach, R., and Selle, B., Current Toopics in Materials Science, ed. E. Kaldis (Amsterdam:North Holland).

16. Spitzer, W. and Mead, C.A., J. Appl. Phys. Vol. 34(10), (1963), 3061.

17. Mead, C.A., Solid State Electron, (1966), vol. 9, 1023.

18. Goodman, A.M., J. Appl. Phys. 34, (1963), 329.

19. Cowley, M. and Heffiner, H., J. Appl. Phys. 35, (1964), 255.

20. Ture, I.E., Ph.D. Thesis, Durham University, (1984).

21. Jones, A.P.C., Ph.D. Thesis, Durham University, (1987).

22. Burton, L.C., Solar cells, (1979/80) 1, 159.

23. Burger, A. and Roth, M., J. Crystal growth 70, (1984), 386.

24. Al Bassam, A., Brinkman, A.W., Russell, G.J. and Woods, J., J. , Crystal Growth, 86(1988)667.

25. Robinson, A.L. and Bube, R.H., J. Appl. Phys. 42, (1971) 5280.

26. Ture, I.E., Claybourn, M., Brinkman, A.W. and Woods, J., J. Crystal Growth, (1985), 72, 189.

27. Ture, I.E., Claybourn, M., Brinkman, A.W., and Woods, J., J. Appl. Phys. 60 (5), (1986), 1670.

CHAPTER 7

CdSe/Cu_2Se Heterojunction

7.1 Introduction

The results to be described in this chapter relate to the properties of CdSe/Cu_2Se photovoltaic cells which have been prepared by forming layers of p-type Cu_2Se on n-type single crystals of CdSe.

Most of the research carried out on solar cells based on CdSe has been concerned with MIS devices (1,2,3). The only reported solar cell investigations of the CdSe-Cu_2Se heterojunction are those of Komaschenko et al.(4) who formed Cu_2Se on thin films and Sorokin et al.(5) and Ture et al.(6) who used single crystal CdSe substrates.

In the present study the structure of the Cu_2Se layers was examined using reflection high energy electron diffraction (RHEED) to determine the phase of the $Cu_{2-x}Se$ film. The Current-voltage and photovoltaic characteristics of the devices were measured in the dark and under 100 mW/cm^2 (simulated AM1) illumination. The characteristics of all the cells were measured immediately after fabrication and after baking in air or Argon at 200°C for different periods of time. In Section 7.5.1 a study of the current-voltage characteristics of CdSe/Cu_2Se at several temperatures is presented. The spectral responses of V_{oc}, I_{sc} and photocapacitance for the devices have also been measured at room and liquid nitrogen temperatures.

In addition the minority carrier diffusion lengths in both the CdSe and the Cu_2Se were measured for the CdSe/Cu_2Se solar cell using EBIC.

7.2 Structure of polished and etched CdSe Surfaces

The samples used were prepared on CdSe substrates with dimensions of 4 x 4 x 2 mm^3 cut from larger single crystal boules of cadmium selenide grown in this laboratory as described in Section 4.2. The single crystal boules were first oriented using X-ray back reflection techniques and then the dice were cut with their large area faces parallel to the basal plane of the hexagonal crystal. Some of substrates were mechanically polished by hand on a polishing pad, and others were polished on a lapping machine. The normal practice was to start the polishing with alumina powder of 5 μm particle size and then to reduce the grain size in stages to 1μm.

After polishing, the resulting surface (regardless of the orientation of the underlying crystal) gave rise to RHEED patterns similar to that shown in Figure 7.1. The diffraction rings in this pattern indicate that the surface layer on this sample was entirely polycrystalline. The radii of the first three rings increase in the sequence $\sqrt{3}$, $\sqrt{8}$, $\sqrt{11}$, and are indexed as the (111), (220) and (311) reflections of the cubic sphalerite phase of CdSe.(7,8)

It was therefore necessary to remove the damaged polycrystalline surface by etching the sample in Conc. Hcl. This left a good single crystal surface as indicated by diffraction patterns such as that shown in Figure 7.2.

7.3 The Copper Selenide Layer

7.3.1 Formation of Cu_xSe on CdSe

Prior to the topotaxial growth of Cu_xSe it was necessary to form the back contact to the substrate. This was done by pressing a 1mm pellet of indium wire (0.5mm thick) onto the freshly etched, and cleaned cadmium face of a dice, and then heating it in an argon atmosphere at 200°C for 10 minutes. The samples were then maintained in the Argon atmosphere while they were cooled to room temperature. The dice were bonded to a microscope slide with the Indium contact face down and the copper selenide was grown selectively on the selenium face by masking off all other faces with an acid resistant lacquer.

Before the CuCl was added to the plating bath, it was first washed in a 10% solution of HCl to remove any Cu^+ions. The powder was then rinsed in acetone and finally dried in vacuum.

The chemiplating technique used for forming the Cu_xSe layer can be summarised as follows:-(9,10)

1. 75ml of deionized water was heated in a closed reaction vessel, and then oxygen free nitrogen gas was bubbled through the water to remove any dissolved oxygen.

(2) 12ml of concentrated HCl acid was added to the water, while the heating, and nitrogen gas flow was continued.

(3) 7ml of hydrazine hydrate solution was added to the solution to produce a pH value between 2 and 3, as measured by narrow pH paper.

(4) 1gm of the treated cuprous chloride was added to the plating solution, and the pH value checked.

(5) The temperature of the solution was raised to 95°C, and the pH value was measured again and corrected to 2.5 using small amounts of hydrochloric acid or hydrazine hydrate as required. The plating solution was now ready for use. The prepared device was immersed in the hot plating solution for periods of up to 300 seconds to produce the thin topotaxial layer of Cu_xSe. The dice were then washed with deionized water and dried in a stream of nitrogen.

The Cu_xSe is formed by a displacement reaction

$$CdSe + 2CuCl \rightarrow Cu_2Se + CdCl_2$$

which produces a topotaxial layer of Cu_2Se on the surface of the CdSe. The $CdCl_2$ goes into solution.

A circular gold dot, 2mm in diameter was deposited onto the copper selenide layer by thermal evaporation to complete the fabrication of the device.

7.3.2 Thickness of the Cu_2Se layer

The relationship between the thickness of the layers and the dipping time was investigated by a sequence of experiments in which the dipping time was systematically increased from 30sec to 300sec. The thickness of these topotaxial layers was measured directly from scanning electron micrographs recorded from sections through the heterojunction.

Figure 7.3 shows some typical cross-sections for Cu_2Se layers formed on the selenium plane of the etched CdSe for periods of 40, 60 and 120 seconds. The average thickness of each Cu_2Se layer was determined and these are given in table 7.1.

Table 7.1: Thickness of Cu_2Se on the Se plane of etched CdSe as a function of the chemiplating period.

Chemiplating period seconds	Average thickness of Cu_2Se layer μm
300	51.0
200	39.0
180	36.0
120	26.0
60	10.5
40	5.5
30	4.5

The average thickness of the Cu_2Se layers with plating time is approximately described by a parabolic relationship as shown in Figure 7.4, where the thickness is plotted as a function of the dipping time, t (curve 1), and $t^{1/2}$ (curve 2). The good straight line in the latter case indicates that the rate of copper selenide growth on an etched surface of CdSe follows a simple parabolic law ($d \propto \sqrt{t}$)$^{(11)}$ for chemiplating periods in the range 30s to 300s.

7.3.3 RHEED Studies

There are several phases of Cu_xSe and it was therefore important to identify which phase had been formed on the

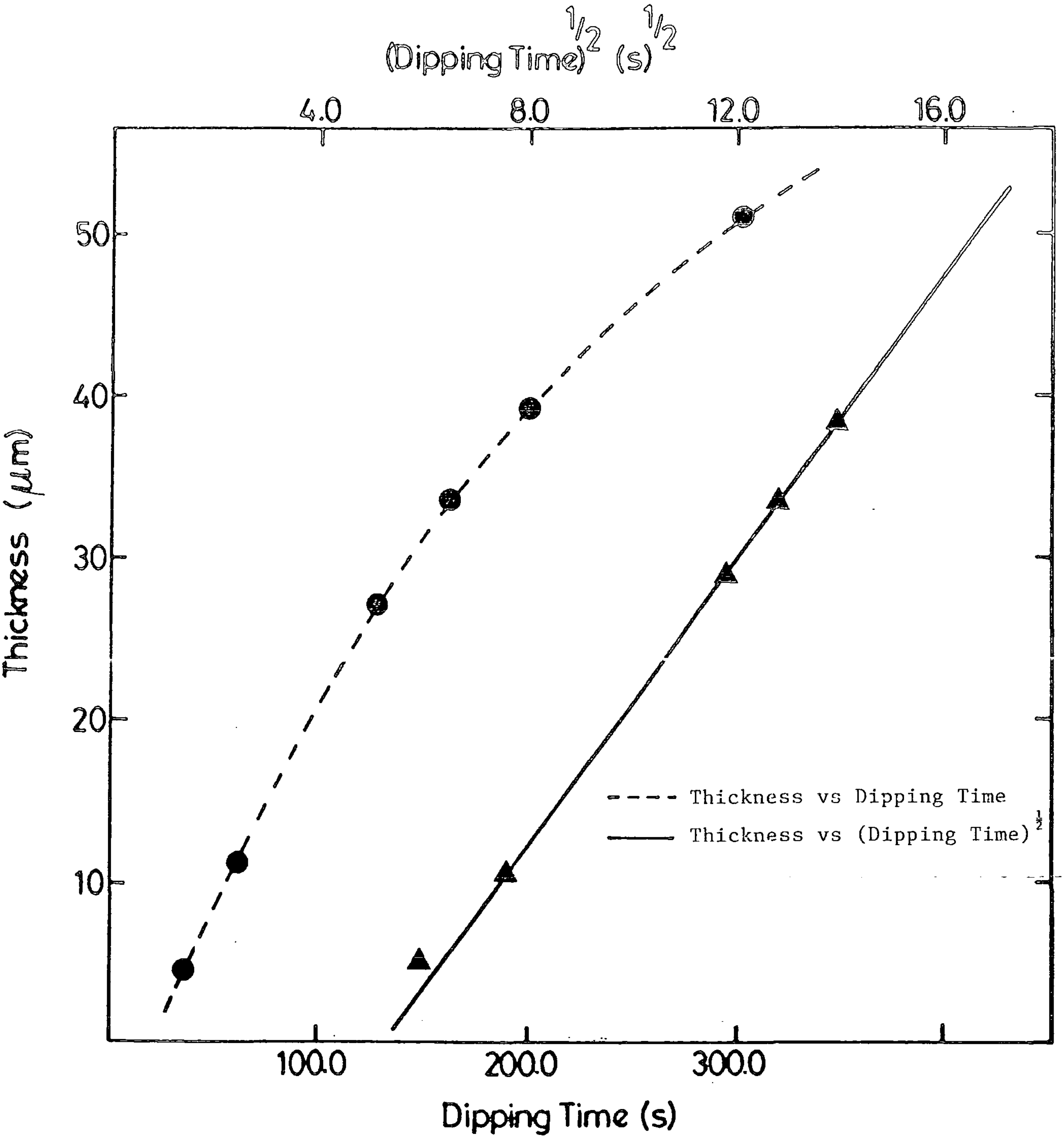

Figure 7.4 The thickness of Cu_2Se layer as a function of dipping time.

CdSe single crystals. This was done by examination of the structure of the layer by reflection high energy electron diffraction (RHEED).

Typical RHEED patterns obtained from as-prepared layers of copper selenide formed on the selenium $(000\bar{1})$ plane are shown in Figures 7.5 and 7.6. Where the electron beam was incident along the $[10\bar{1}0]$ and $[11\bar{2}0]$ directions in the CdSe respectively. There are polycrystalline rings which pass through some of the more intense spots. The analysis of the diffraction patterns enables the lattice parameters of the samples to be measured and the phase of the Cu_xSe determined. The relative diameters of the rings indicates that they are derived from a f.c.c. structure with lattice parameter as given in table 7.2.

Table 7.2 Lattice parameters of Cu_xSe from the experimental patterns and corresponding value from the ASTM index.

	a (A^o)	
hkl	Experimental	ASTM
(111)	5.82	5.85
(220)	5.81	5.86
(311)	5.81	5.85

The phases of Cu_xSe layers grown on the CdSe single crystals have also been studied after post growth air bakes at 200^oC for 2 min, as shown in Figure 7.7. This shows that some of the spots in Figures 7.5 and 7.6 disappear following the heat treatment at 200^oC. The resulting patterns are typical of that expected from a <110> zone axis of a twinned cubic structure(6).

7.4 Properties of As-made Devices

7.4.1 J-V Characteristics

CdSe/Cu_2Se heterojunction devices were fabricated by evaporating gold dots, 2mm in diameter on the Cu_2Se to form the second electrical contact.

The current-voltage (J-V) characteristics of such devices were measured in the dark, and under 100 mW cm^{-2} (simulated AM1) illumination. Figure 7.8 shows the typical current-voltage characteristics for a cell formed on the high resistivity 2Ωcm substrates (Type A), measured in the dark and under AM1 illumination. The cell showed good diode behaviour with little leakage current in reverse bias. The photovoltaic response gave an open-circuit voltage V_{oc} of 0.2V, a short circuit current of $3.8mA/cm^2$, with a fill factor of 0.33 and an efficiency of 0.25% under simulated AM1 illumination.

The dark current-voltage characteristics of the CdSe/Cu_2Se at room temperature are presented in Figure 7.9 on semi-logarithmic axes. The forward current increases exponentially with applied forward voltage V, in agreement with the usual relationship:

$$J = Jo \exp (qV/nkT) \qquad (7.1)$$

for values of V greater than 3kT/q.

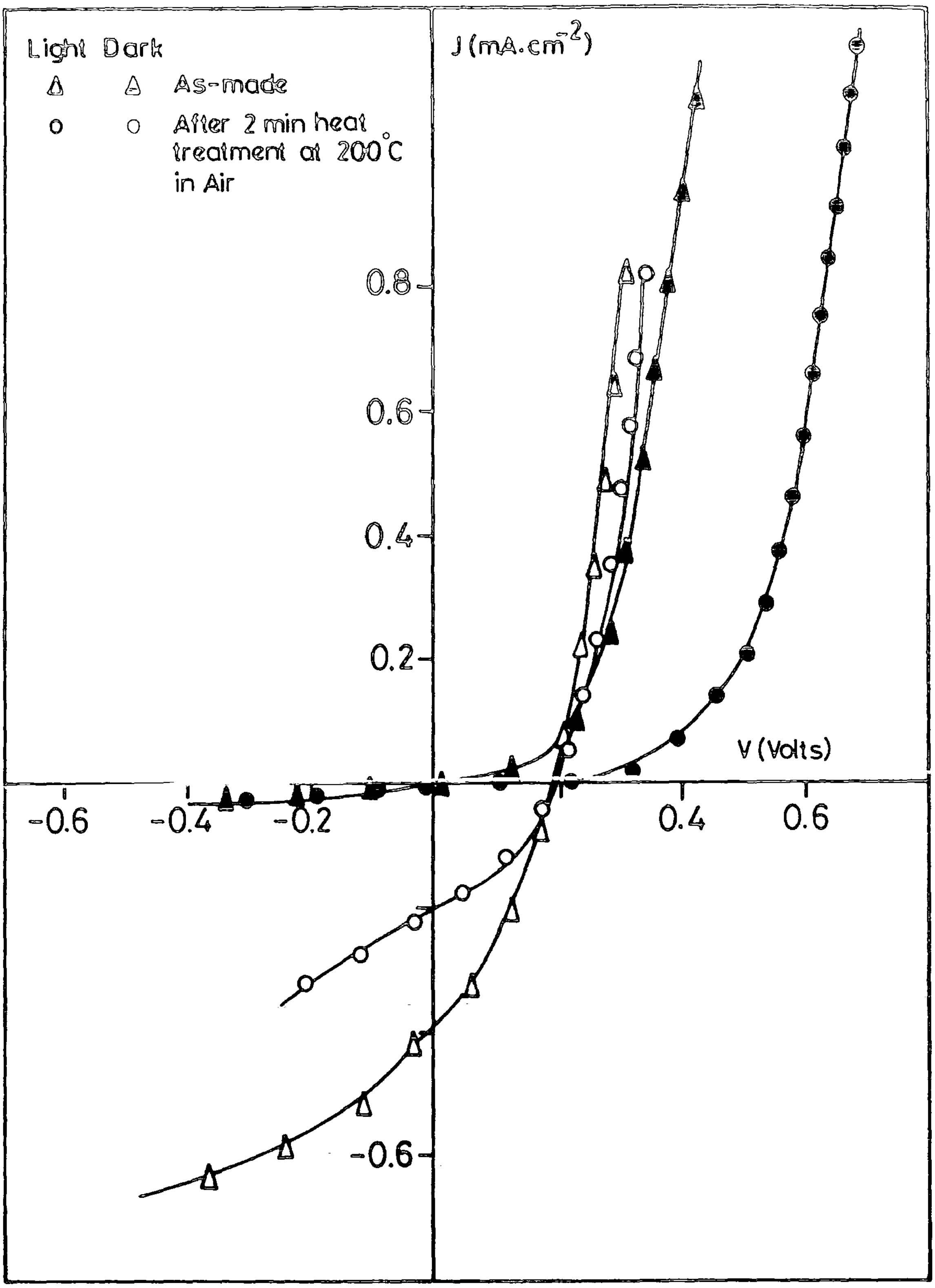

Figure 7.8 Photovoltaic characteristics for a Type A cell as-made and after 2 min. heat treatment in air at 200°C.

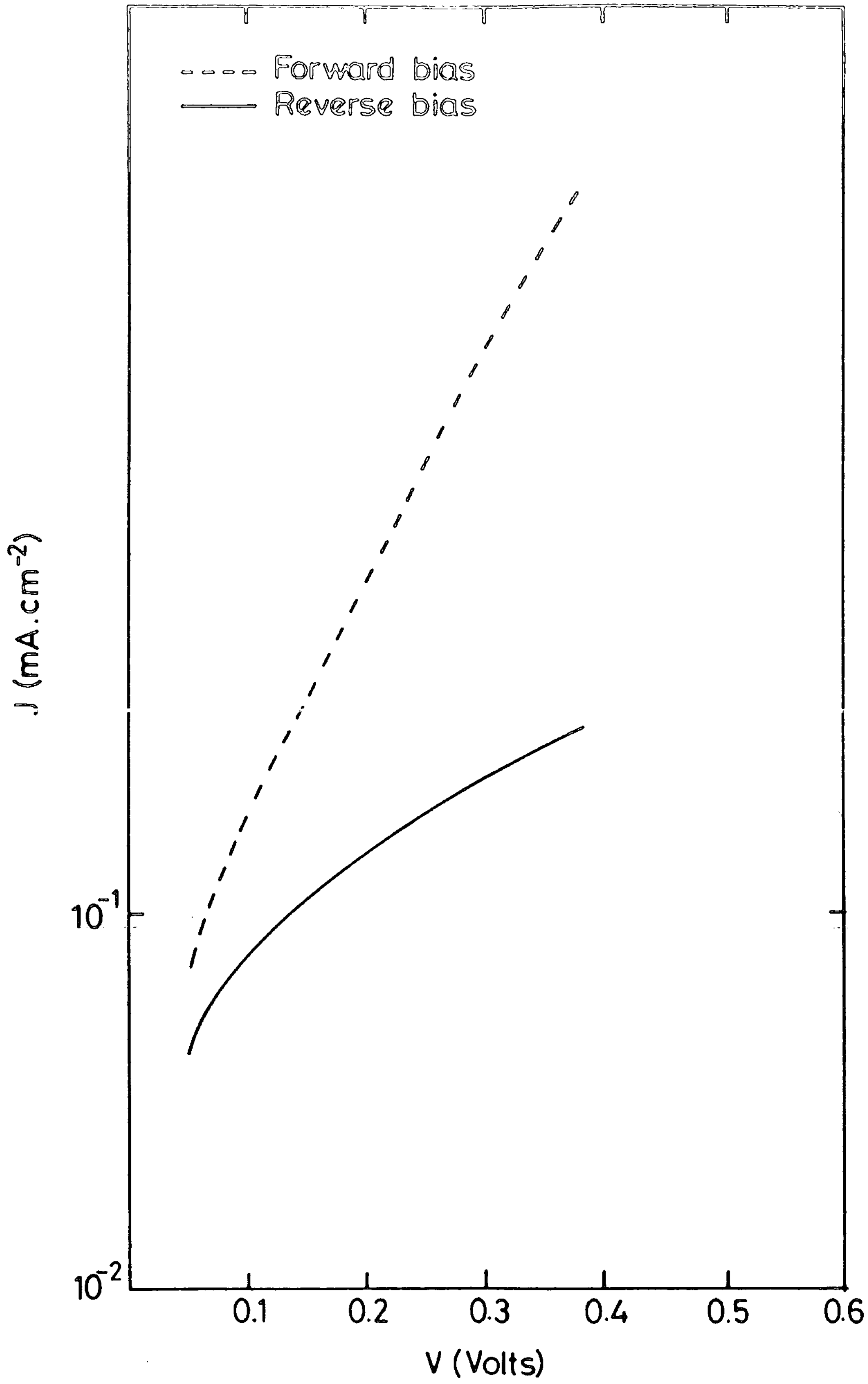

Figure 7.9 Dark current-voltage characteristics for as-made Type A cell at room temperature.

The value of the diode factor n, calculated from the slope of the straight line is 1.1. The saturation current density, obtained by extrapolating the straight line to zero bias is 4.5×10^{-2}mA/cm^2 and the calculation for the barrier height using the intercepts of this plot gave $\varnothing b_{I-V} = 0.63$eV.

7.4.2 Spectral Response

The spectral response of the open circuit-voltage V_{OC} of each device was measured using a Barr and Stroud prism monochromator (see chapter 4, section 9) and the open circuit voltage responses of a typical high resistivity cell (type A) at room, and at liquid nitrogen temperatures are shown in Figure 7.10.

The room temperature curve (A) shows three peaks at wave lengths of 1.04, 0.8and 0.68µm. The major response was at 1.04µm corresponding to the band gap which in Cu_2Se is at about 1.2eV. The second largest response was at 0.68µm and is probably associated with the band gap of CdSe. Curve B shows the open circuit voltage response for the same cell at liquid nitrogen temperature and shows three peaks at 1.04, 0.82 and 0.65µm. The maximum response was again at 1.04µm, and was larger than at room temperature. There was a small shift in the peak at 0.65µm at low temperature consistent with this being associated with absorption in CdSe. (The band gap of CdSe increases from 1.8 eV to 1.9eV at liquid nitrogen temperature). The response at 0.82µm (~ 1.51eV) may be associated with the excitation to the conduction band of electrons from copper levels 0.2eV above the valence band of CdSe(6). Figure 7.11 shows the spectral distribution of

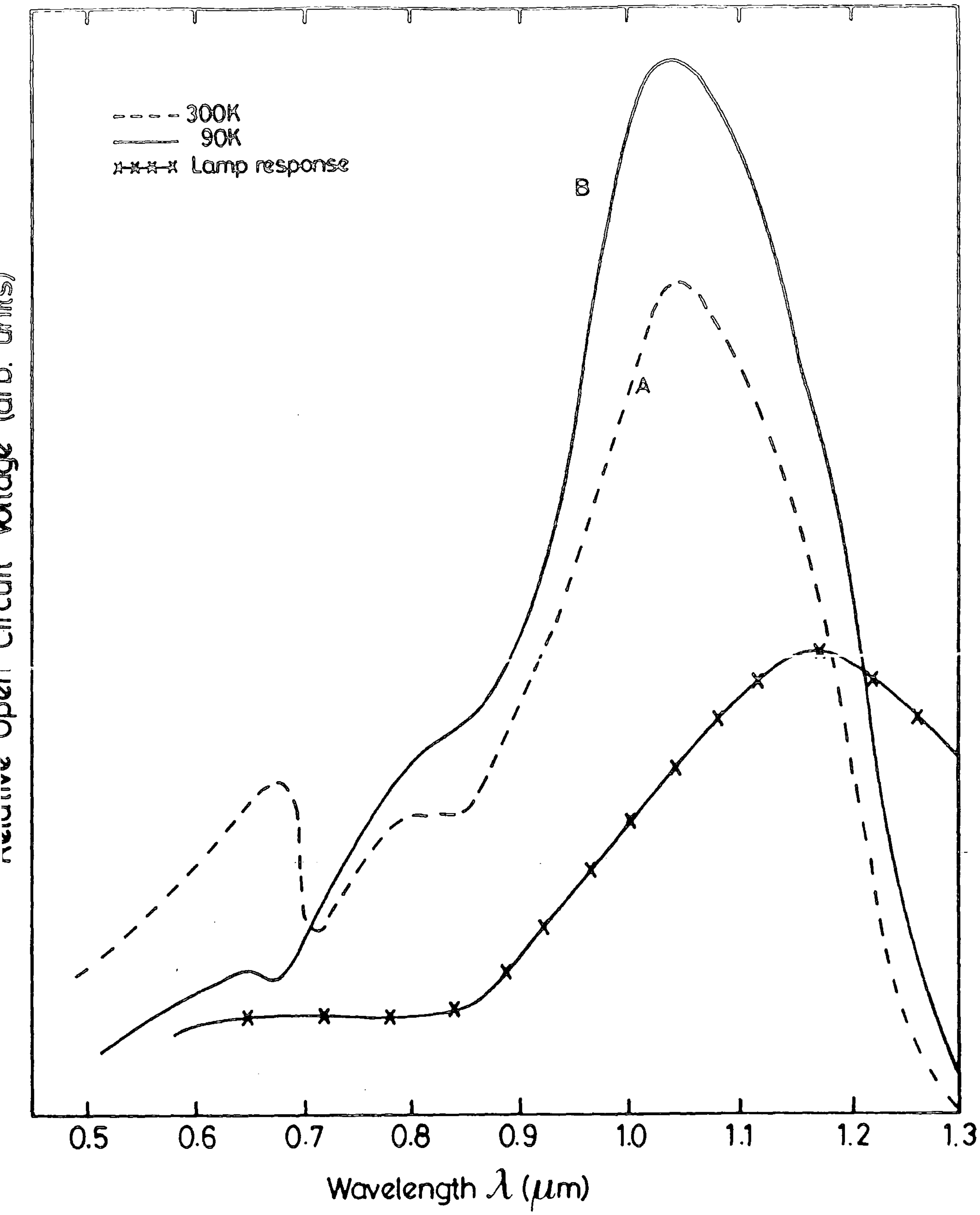

Figure 7.10 Spectral response of V_{OC} for a typical as-made, Type A cell at room and liquid nitrogen temperatures.

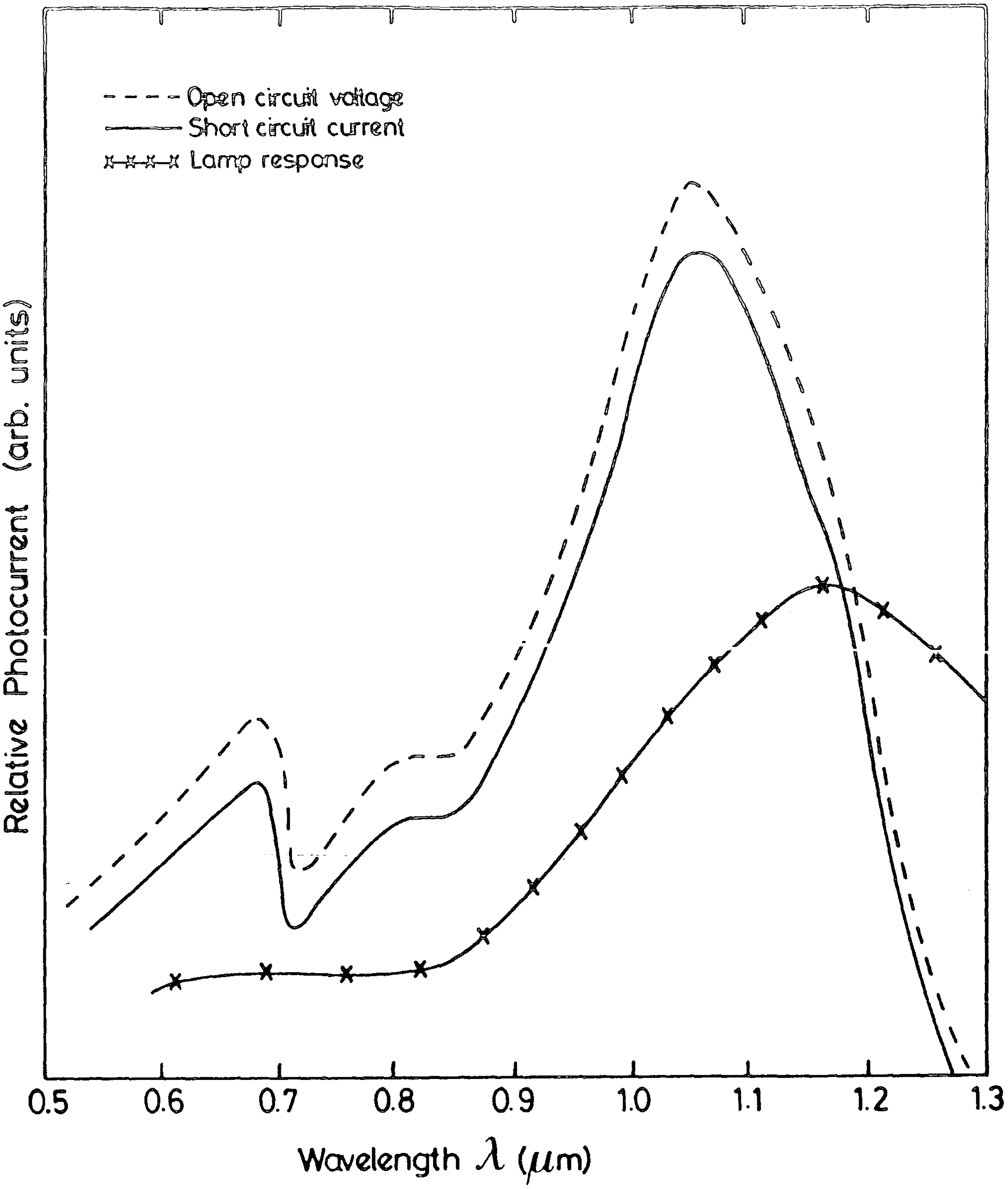

Figure 7.11 Spectral response of V_{OC} and I_{SC} at room temperature for a typical as-made type A cell.

both V_{OC} and I_{SC} and indicates that the spectra were very similar.

7.4.3 Photocapacitance measurement

Steady state photocapacitance curves were obtained for a type A device at room, and liquid nitrogen temperatures, and are shown in Figure 7.12. A negative going threshold in the PHCAP at room temperature occurred at 0.79eV, suggesting a donor level 0.95eV below the conduction band. The room temperature PHCAP also showed an additional positive going threshold at 0.96eV corresponding to a level 0.78eV above the valence band, so that the 300K spectra also revealed a relatively shallow acceptor level 0.21eV above the valence band, corresponding to a photon energy of 1.53eV.

The principal threshold of the PHCAP spectrum at low temperature was observed at an incident photon energy of 0.85eV indicating an electron emission process to the conduction band and therefore the change in the threshold from 0.79eV (at room temperature) to 0.85eV (at liquid nitrogen) implies that the level is pinned to the valence band, i.e. the centre is located at $\simeq$ 1.0eV above the valence band edge.

7.5 Heat treatment in air

7.5.1 J-Vcharacteristics

The characteristics shown in Figure 7.8 also included those which were obtained from a type A cell which had been subjected to a post barrier bake in air at $200^{o}C$. This

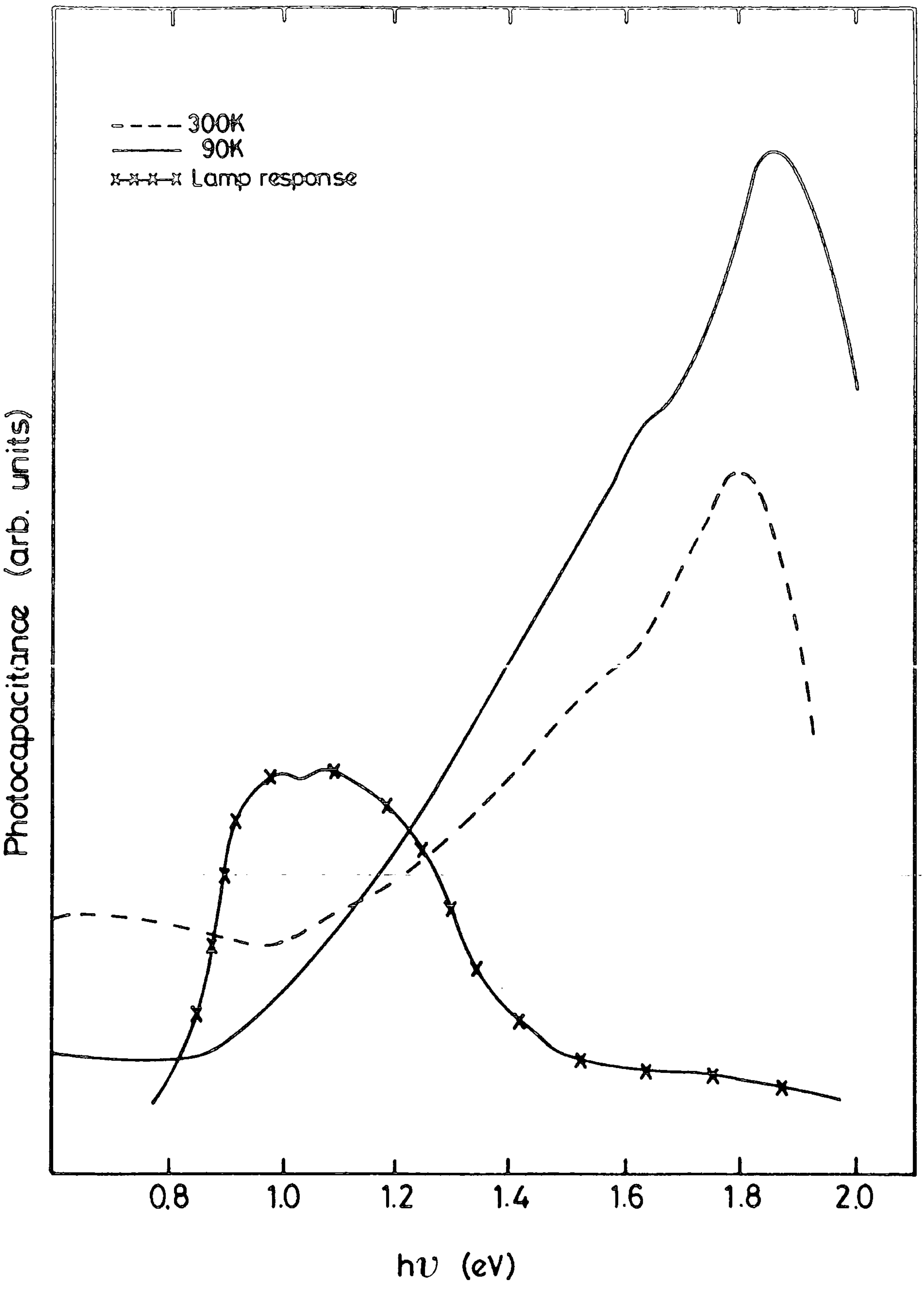

Figure 7.12 Photocapacitance spectra of a typical CdSe/Cu_2Se Type A cell at room and liquid nitrogen temperatures.

clearly demonstrates that the conventional 2 mins post barrier air bake led to a very small increase in V_{OC} and considerable reduction in J_{SC}. The photovoltaic response gave an open circuit voltage V_{OC} of 0.21V, a short circuit current of 2.1mA/cm^2, with a fill factor 0.33 and an efficiency of 0.15% under simulated AM1 illumination. Heating for 2 min led to a fall in J_{SC} from 3.8mA /cm^2 in the as-made cell to 2.1 mA/cm^2. After heating, the open circuit voltage V_{OC} increased from 0.2 to 0.21V. The fill factor for the same device was not much affected by heating in air, however the cell efficiency (AM1) decreased from 0.25% to 0.15%. Typical forward current-voltage characteristics of the same device have been measured in the dark at room temperature after 2min heating in air and are shown in Figure 7.13. The current also increased from 4.5 x 10^{-2}mA/cm^2 to 5 x 10^{-2} mA/cm^2 and the barrier height from 0.63eV to 0.65eV. The current-voltage characteristics of devices fabricated on low resistivity CdSe $\rho < 0.2$ Ωcm (type B) were also recorded after different periods of heat treatment in air at 200°C. The J-V and photovoltaic characteristics of a typical device are shown in Figure 7.14 for dark and AM1 conditions. The as-made cell never exhibited any rectifying behaviour or any photovoltaic effect. However, after heating in air at 200°C for 2 min both rectification and a photovoltaic response were observed (V_{OC} = 0.12V, J_{SC} = 1.3mA cm^{-2}, F.F = 0.635, η = 0.1%. In order to determine the optimum annealing time the current-voltage curves of type B devices were measured after

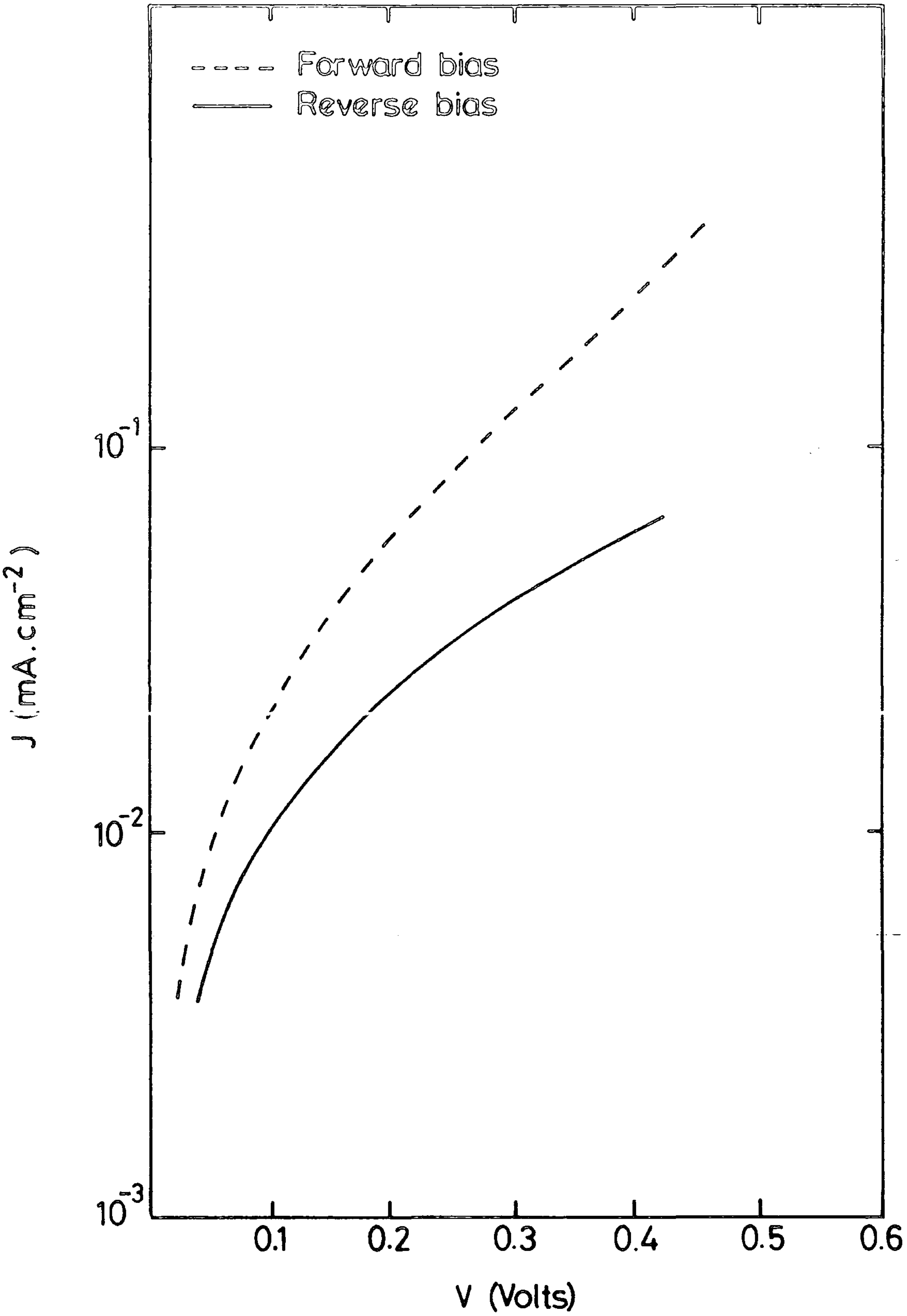

Figure 7.13 Dark (J-V) characteristic after 2 min. heat treatment in air at 200°C for type A cell.

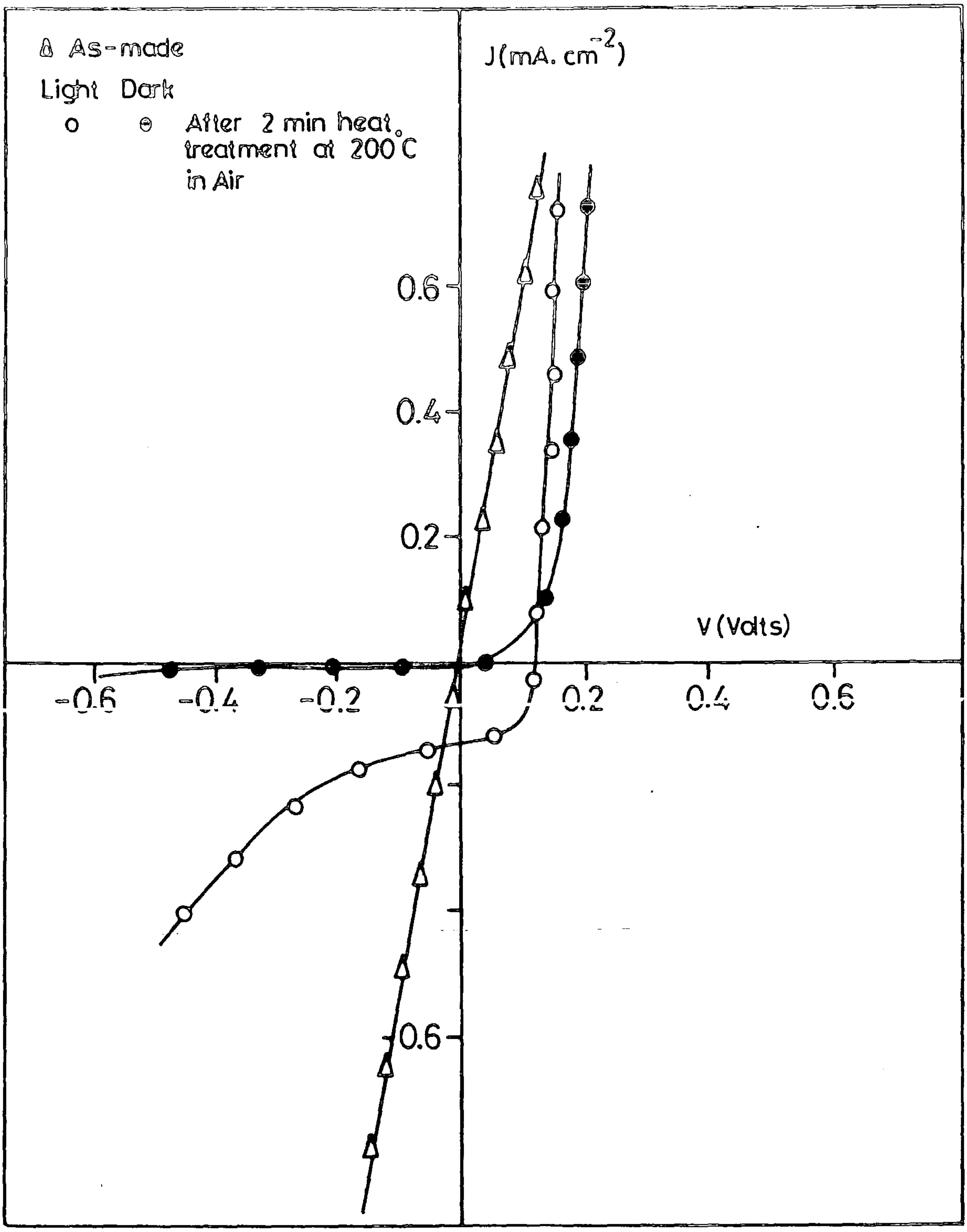

Figure 7.14 Current-voltage characteristics for type B cell as-made and after 2 min. heat treatment in air at 200°C.

different periods of heat treatment in air at 200°C. These results are summarised in Figures 7.15 and 7.16. They show that rectification effects began to appear after 25 sec., but full rectification did not occur until after 120 sec. of heating. There was a parallel improvement in the photovoltaic response and in general the optimum appeared to be achieved after about 2 min heating in air. The dark current-voltage characteristics of a typical type B $CdSe/Cu_2Se$ device after 2 min. heat treatment shown in Figure 7.17, were taken at several temperatures between 300K and 122K. The forward current increased exponentially with applied forward voltage V for voltages greater than 3kT/q. At small bias the forward log J-V characteristics show a linear relationship but as J_f increasesthe diode behaviour of the junction becomes more apparent. The values of the diode factor n, saturatiuon current density J_o, the slopes and barrier height measured at different temperatures are recorded in table 7.3.

Temperature (K)	diode factor (n)	$J_o(mA/cm^2)$	$\phi_b(eV)$
300	1.01	2.4×10^{-2}	0.64
223	1.25	2.4×10^{-4}	0.55
173	1.75	3.5×10^{-5}	0.45
123	1.98	1.3×10^{-5}	0.32

Table 7.3 Dark diode parameters measured at different temperatures, for a type B cell.

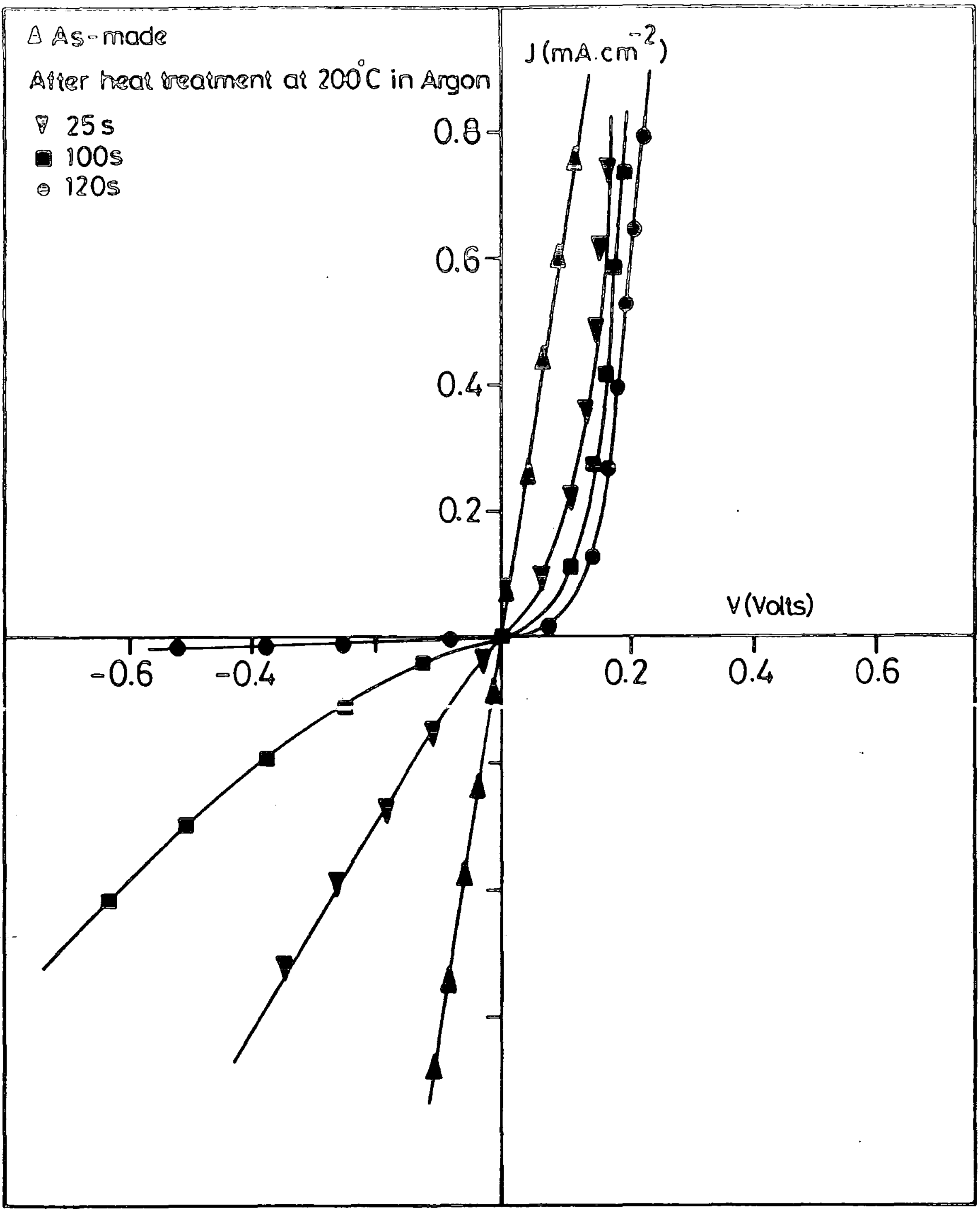

Figure 7.15 Dark J-V characteristics of a type B cell, as-made and after 25s, 100s and 120s heat treatment in air at 200°C.

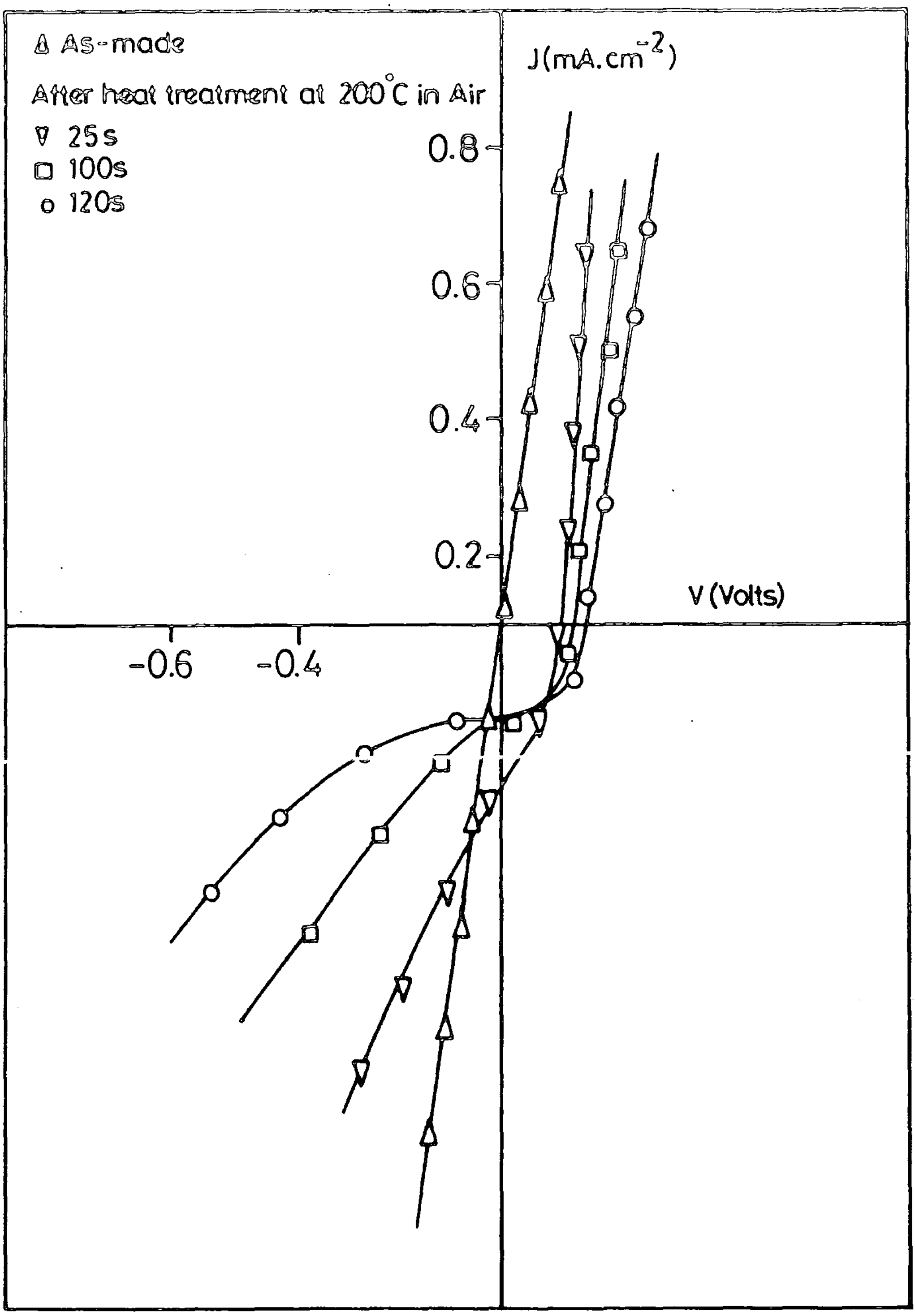

Figure 7.16 AMI illumination, as-made and after 25s, 100s and 120s heat treatment in air at 200°C.

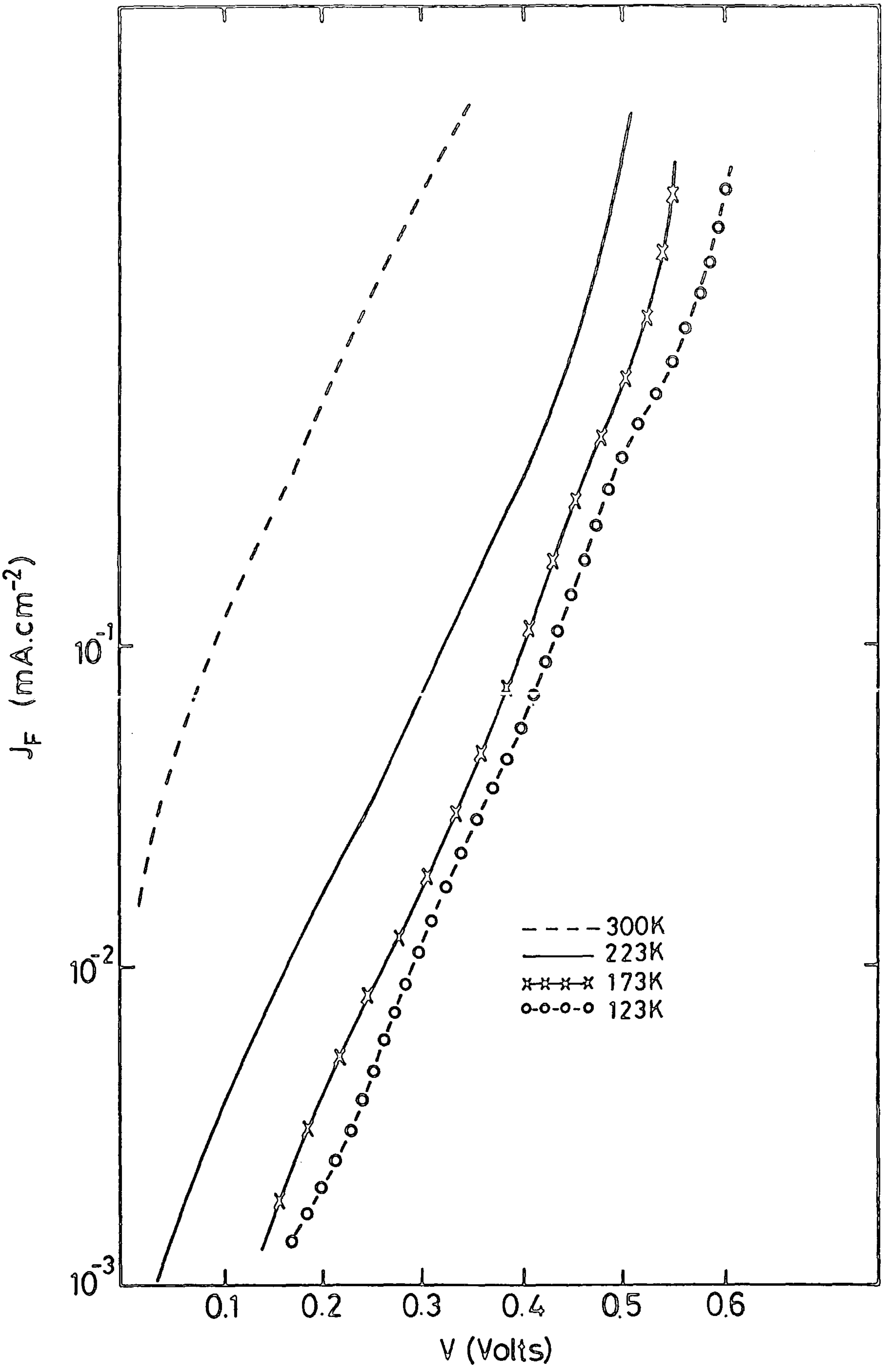

Figure 7.17 Dark current-voltage characteristics as a function of temperature for Type B cell.

As the temperature was reduced J_o decreased from 2.4×10^{-2} to 1.3×10^{-5}mA cm^{-2} and the apparent barrier height also decreased from 0.64 to 0.32eV.

7.5.2 Spectral response

The spectral responses of a heat treated type A device at 300K and 90K are given in Figure 7.18 and show the major response was at wave lengths of 0.65µm (90K) and 0.68um (300K), the second largest response occurred at wavelengths of 0.78µm (300K) and 0.73um (90K) but there was no response evident at 1.04 µm. This is in contrast to the results obtained for as-made devices where the maximum response was at 1.04µm; cooling the device to 90K resulted in an increased response of 0.73 µm but a reduced peak at 0.68 µm, compared to room temperature.

The spectral responses of the open circuit voltage of a type B device are shown in Figure 7.19 for a typical cell after heat treatment at 200°C in air for 1 min and for 2 min. No photo response had been detected in the as-made cell. After 1 min. heat treatment three peaks were apparent at wavelengths of 1.04, 0.8 and 0.7µm, with the maximum response in the open circuit voltage occurring at 1.04µm. The second largest response occurred at 0.8µm, while there was only a small peak in the response at 0.7µm. After 2 min heat treatment V_{oc} clearly increased in magnitude at all wavelengths, and although the maximum response still occurred at 1.04µm, the relative response at 0.7µm had increased dramatically and was now greater than that at 0.8µm. The

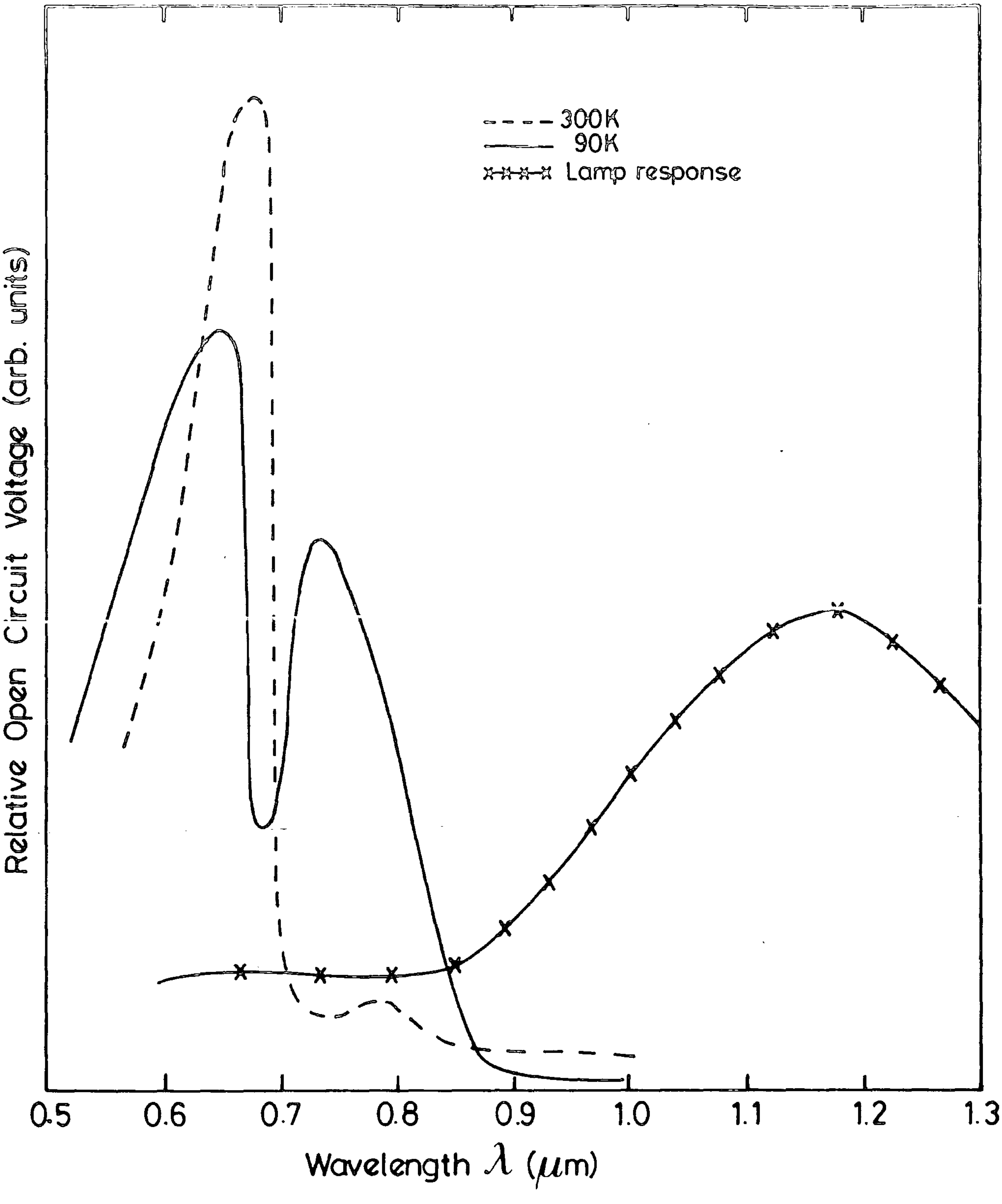

Figure 7.18 Spectral response of V_{OC} after 2 min. heat treatment in air at 200°C for Type A cell at 300K and 90K.

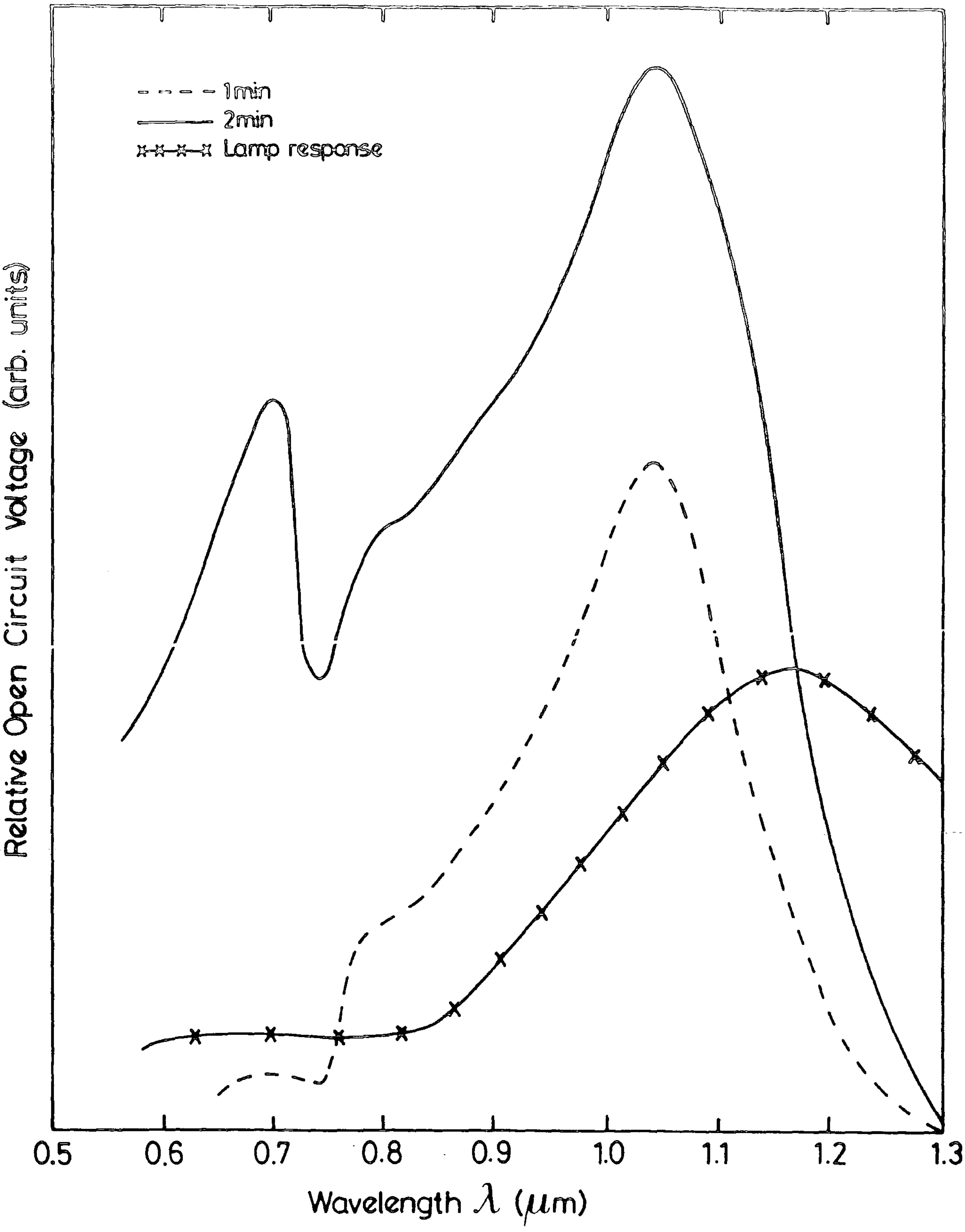

Figure 7.19 Spectral response of V_{OC} for a Type B cell after 1 and 2 min. heat treatment in air at 200°C.

response at 0.7µm (1.77eV) is probably related to the band gap of CdSe.

7.5.3 Capacitance-voltage measurements

The capacitance of $CdSe/Cu_2Se$ heterojunctions was also measured in devices that had been heat treated in air at 200°C. The capacitance measurements were made at 1MHz. Typical C-V characteristics in the form $1/C_2$ vs V, are given in figure 7.20 for an as-made cell and for a cell after 2 min heat treatment in air at 200°C. Both characteristics give straight lines which are analysed for N_d and Vd. The results are summarised in table 7.4.

Table 7.4 Barrier height and carrier densities for $CdSe/Cu_2Se$

Para-meter	$N_d \times 10^{15}$ cm^{-3}	(E_c-E_f) ev	Vd(eV)	$\varnothing_{c-v}$ (eV)	W_{c-v} µ.m.
as-made	0.7	0.19	0.37	0.56	0.80
2min. heat treat-ment in air	0.4	0.20	0.55	0.75	1.76

This shows that the donor density decreased from 0.7×10^{15} cm^{-3} in the as-made to 0.4×10^{15} cm^{-3} after 2 min. heat treatment and the barrier height increased from 0.56eV to 0.75eV.

7.5.4 EBIC measurements

Devices were cleaved through the contact and viewed in

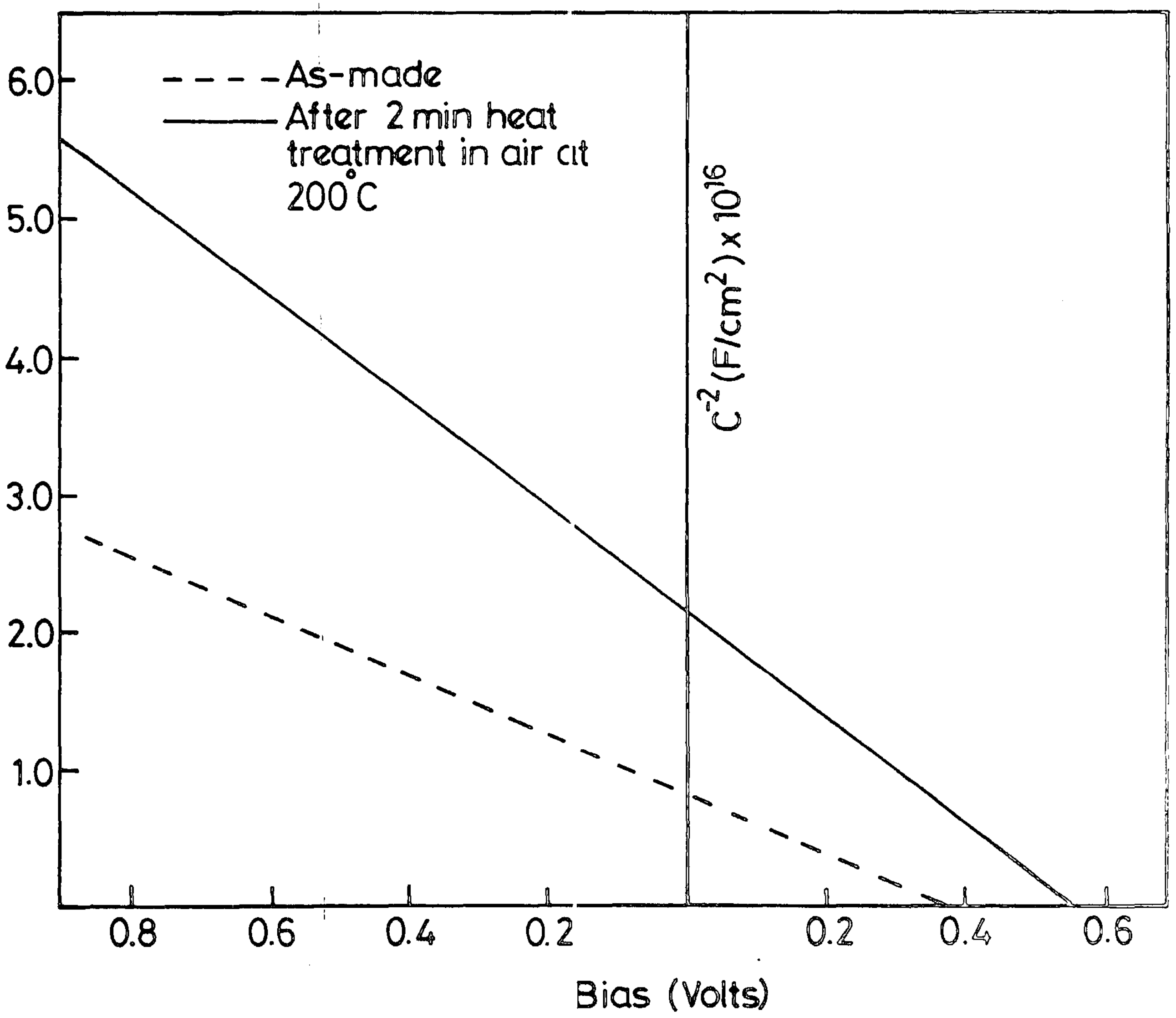

Figure 7.20 C^{-2}-V characteristics of a Type A device measured before and after heating in air.

cross section (i.e. electron beam parallel to the junction plane) in the EBIC mode of the SEM. A line scan recorded across the junction provided a trace of the EBIC current as a function of position. A typical example is shown in Figures 7.21 and 7.22 which show the SE image of the junction and the corresponding EBIC line scan, respectively. The measurements of the minority carrier diffusion lengths (Lp, Ln) were all taken with a beam energy of 7.5kV. Using equation 4.6 the values of (Lp, Ln) can be readily and accurately determined from the slope of a semi-log plot of the EBIC signal (Log I_x/I_o) versus beam position (x). The graph corresponding to this scan is shown in Figure 7.23. The values of the diffusion length determined from the slopes of the lines are

Ln(CuxSe) = 0.45um

Lp(CdSe) = 0.48um

7.6 Heat treatment in Argon

7.6.1 J-V characteristics

The current-voltage (J-V) characteristics of a typical Type B cell measured in the dark and under AM1 illumination are shown in Figures 7.24 and 7.25 respectively after different periods of heat treatment in Argon at 200^{o}C. Both sets of characteristics show an improvement with heating time. Heating in Argon for 30 minutes produced good rectifying characteristics with very little leakage current in reverse bias, and a corresponding improvement in the

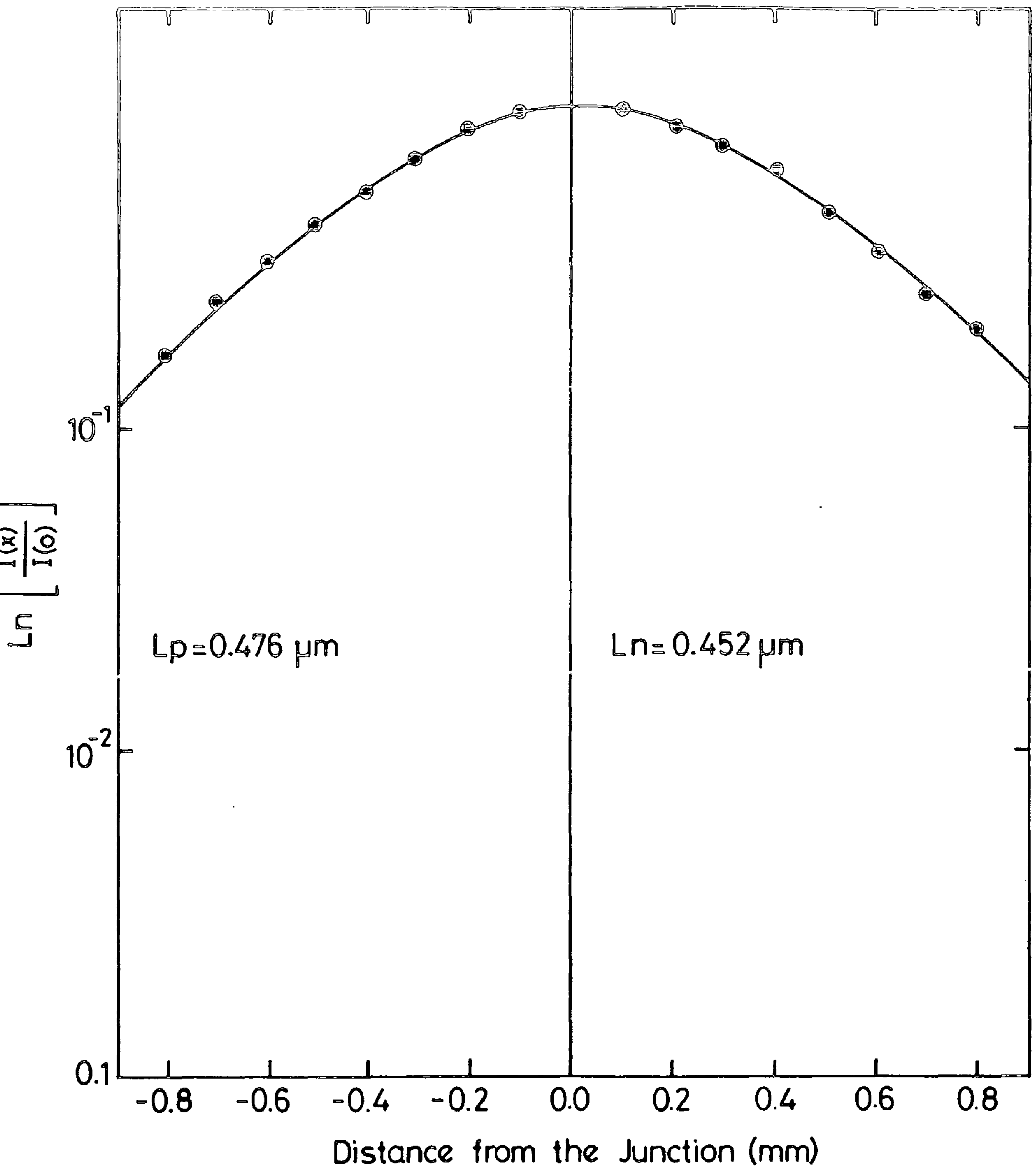

Figure 7.23 A plot of Log(I(X)/I(O)) vs distance from the junction for the line scan shown in Figure 7.22.

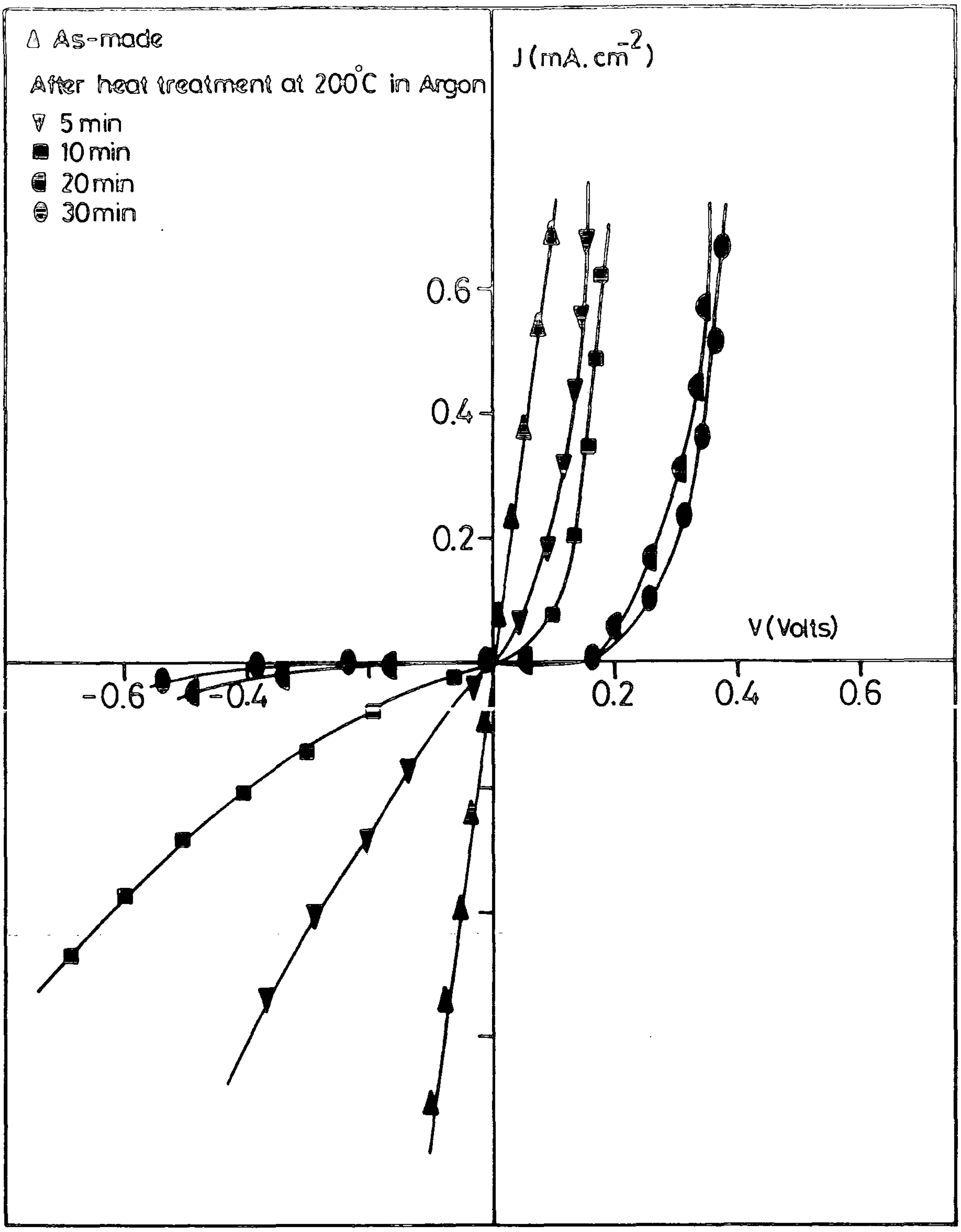

Figure 7.24 Dark current-voltage characteristics of type B devices after varying periods of heat treatment (200°C) in Argon.

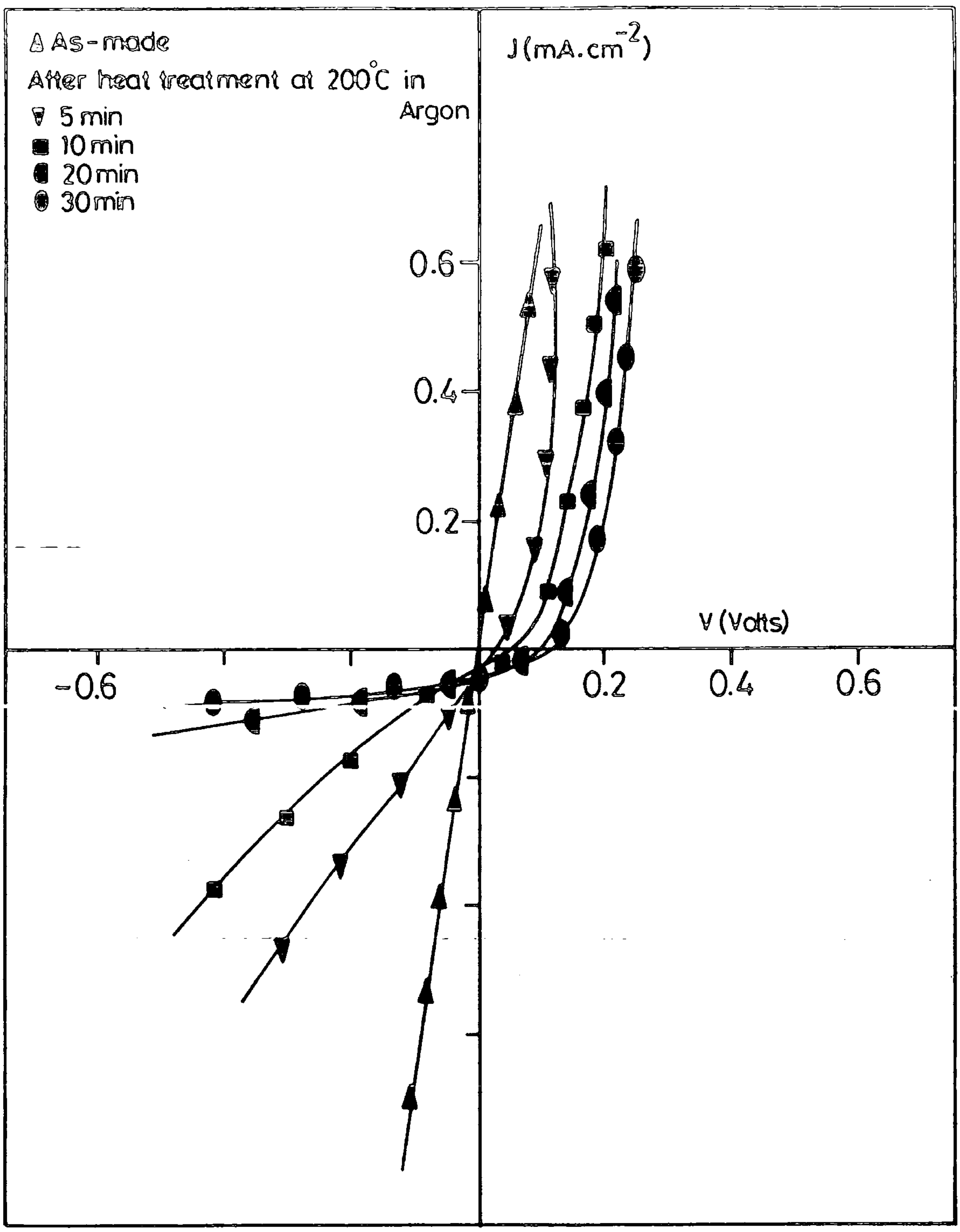

Figure 7.25 Current-voltage characteristics of type B cells under AMI illumination after varying periods of heat treatment in Argon.

photovoltaic properties of the junction. However, comparison with results presented in Figure 7.14 for heating in air show similar improvements after only two minutes of heat treatment. The value of V_{oc} of 100mV, J_{sc} of 0.5 mA/cm^2 and a fill factor 0.7 were measured.

7.6.2 Spectral response

Figures 7.26 and 7.27 show the spectral response of open circuit voltage at room and liquid nitrogen temperatures of a type B cell after heating in Argon for 20 min. and 30 min. respectively. Three peaks are apparent in the room temperature spectrum of Figure 7.26 at 1.06, 0.8 and 0.71μm as was observed in the spectral response of cells heat treatmed in air (Figure 7.19). The maximum response occurred at 1.06μm. At low temperature, there is a peak at 1.06μm and a shoulder at 0.82μm corresponding to similar features in the room temperature spectrum but there is no evidence for a third peak at ~ 0.65μm.

The responses for the same device after 30min heat treatment in Argon (Figure 7.27) are very similar to those obtained after 20 minutes heat treatment, except that they are larger at all wavelengths.

7.7 Discussion

7.7.1 Substrate preparation

When a single crystal of CdSe was mechanically polished a polycrystalline diffraction pattern (Figure 7.1) was obtained. This can be indexed as arising from a sphalerite

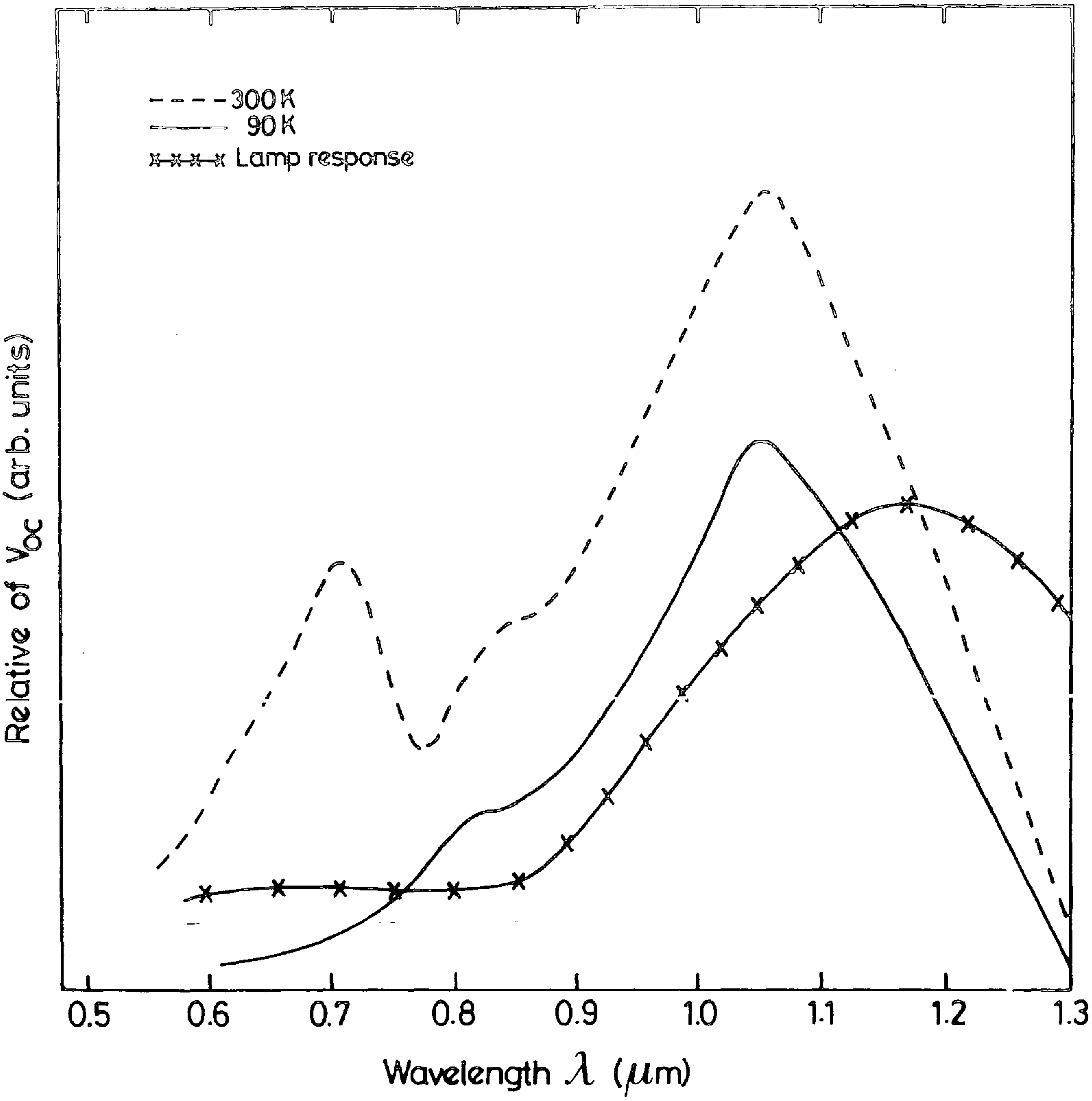

Figure 7.26 Spectral response of V_{OC} for Type B device after 20 min. heat treatment in Argon at 200°C.

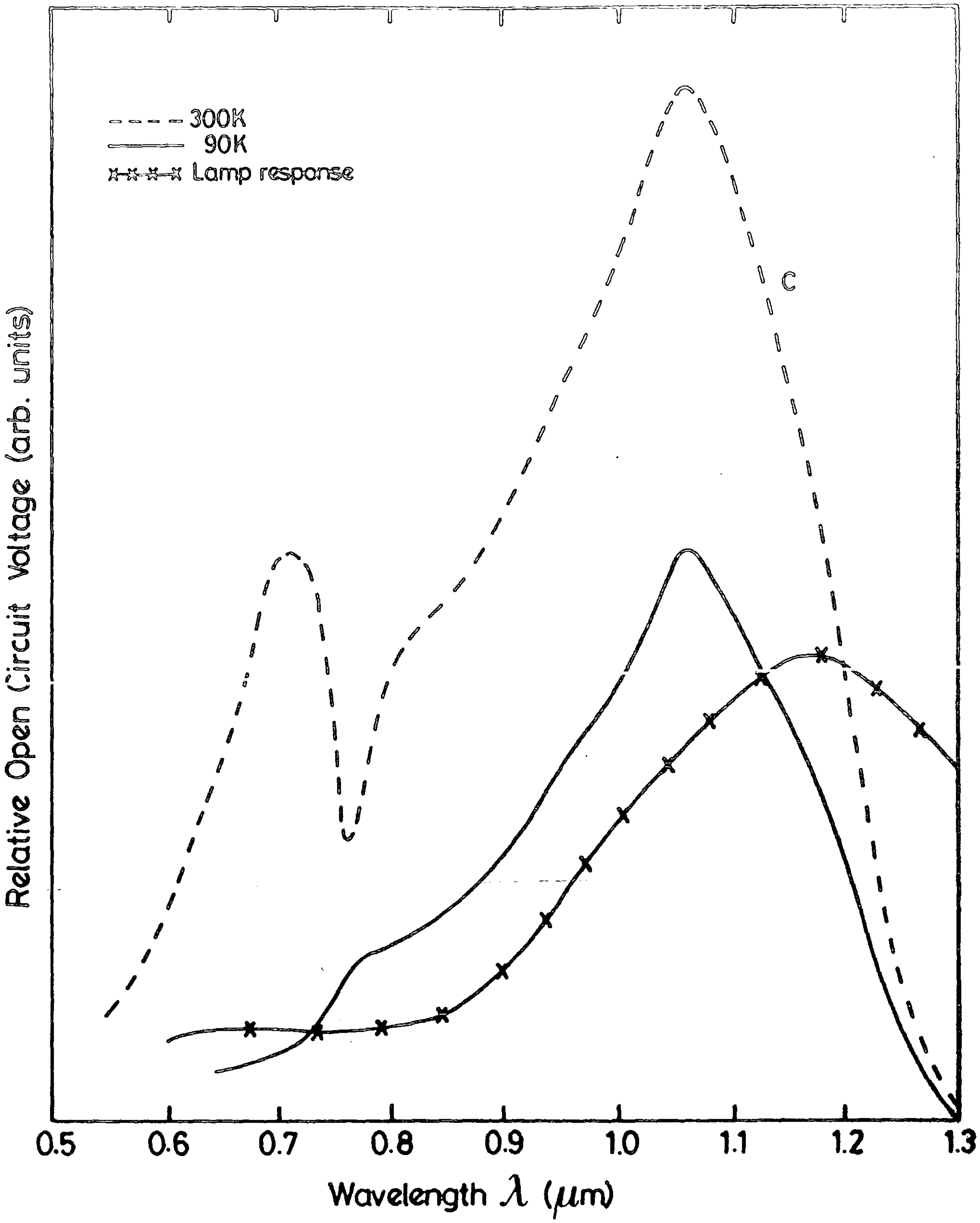

Figure 7.27 Spectral response of V_{OC} for Type B cell after 30 min. heat treatment in Argon at 200°C.

structure, with a lattice constant of $6.06A^{o}$ in close agreement with the estimate of $6.05A^{o}$ by Stuckes and Farrell(12) and by Durose et al.(8)– implying that the polishing producesan initial phase change from the hexagonal to the sphalerite phase of CdSe(13). However, more recent work with ball milled CdSe(8) has shown the conversion of a hexagonal structure to cubic must presumably depend upon the introduction of an appropriate stacking disorder through the movement of dislocations.

The next stage in sample preparation is to remove the polycrystalline layer by etching in concentrated HCl.

7.7.2 Cu_xSe Layer

Photovoltaic cells composed of a layer of Cu_xSe on CdSe have been formed by the immersion of CdSe substrate in cuprous chloride solution. The rate of copper selenide formation on an etched $(000\bar{1})$ surface of CdSe was found to follow a simple parabolic law $(d \propto \sqrt{t})$(11) for chemiplating periods ranging from 30s to 300s in duration (Figure 7.4). However the resulting straight line did not go through the origin indicating that the initial conversion process cannot be described by the same parabolic law. Similar results have been produced on single crystal CdS(11). There are conflicting results on the growth rate of Cu_xS on CdS single crystals. Shiozowa et al.(14) and Lindquist and Bube(15) found that thickness of the cuprous sulphide layer increased linearly with immersion time, whereas Singer and Faeth(16), Buckley and Woods(17), and Russell et al.(11) found that the rate of growth of the copper selenide layer followed a parabolic law. The present results are clearly in agremeent with the second group of workers. Typical RHEED patterns obtained from freshly prepared layers of copper selenide Figures 7.5 and 7.6 contain polycrystalline rings which pass through some of the more intense spots. This confirms that the rings are associated with a polycrystalline deposit of the same ordered material which gave rise to the spot pattern(6). Thus the interplanar spacings measured from the relative diameters of the rings indicated that they are derived from a f.c.c. structure with a lattice parameter of 5.82Å. This is in agreement with the value of 5.85Å for Cu_2Se from the ASTM index. This also accords with other results reported by Idrichan and Sorokin(18) from a study of X-ray diffraction patterns of $Cu_{2-x}Se$. These showed that $Cu_{2-x}Se$ had an f.c.c. lattice and that the lattice parameter increased monotonically from 5.78 to 5.66Å as x increased ($0 < x < 0.20$), similar results have been reported from transmission electron diffraction studies of Cu_2Se by R.H. Hyding(19), G.A. Efendiev and M.M. Kazinets(20), and Shafizade et al.(21,22), and by Ture et al.(6) from RHEED studies.

The arrangement of two rows of pairs of spots in Figure 7.6 between rows of single spots is similar to a <110> zone axis pattern from a twinned cubic structure, but differs from it in that there are twice as many reflections. The reason for this may be attributable to a double diffraction effect.

The RHEED patterns were also studied after heating an as-made device at 200°C for 2 min. Figure 7.7 shows that some of the spots disappear after heat treatment, and the diffraction patterns are precisely those to be expected from the <110> zone axis of a twinned cubic structure. It is concluded therefore that the f.c.c. modification of Cu_2Se grows topotaxially as grains in twin oriented positions on the basal planes of CdSe with the orientational relationship <111> Cu_2Se parallel to (0001) CdSe and [110] Cu_2Se parallel to $[10\bar{1}0]$ CdSe.

7.8.3 As-made Cu_xSe/CdSe devices

The results reported here show that Cu_2Se/CdSe single crystal cells can be fabricated with optimum efficiency without a post barrier air bake provided that they are prepared on type A substrates with suitable bulk resistivity ($\simeq 2\ \Omega$ cm). Thus when the chemical junction between Cu_2Se and CdSe was first formed on this cell, the current-voltage characteristics exhibited good rectifying behaviour, with some photovoltaic performance and small leakage current in reverse bias. This is probably because of the wider depletion region in CdSe. Current-voltage characteristics for the devices formed on low resistivity CdSe (type B), showed no rectification in the as-made condition. This would be expected from a situation where the heterojunction was formed between two highly conducting degenerate semiconductors. The implication is that the depletion-layer thickness in both the Cu_2Se and the CdSe was too narrow and carriers were able to tunnel easily through the barrier.

A similar effect has been reported in discussing higher resistivity CdSe prepared by heating as-grown crystals in selenium vapour, (which would have increased the bulk resistivity)(6). The resultant devices showed some photovoltaic effect, while cells formed on the as-grown low resistivity crystals exhibited no rectification. A comparable effect has been reported on single crystal CdS/Cu$_2$S devices by Lindquist and Bube(23), and by Oktik et al.(24). A type A device which had good rectification characteristics and a relatively large photovoltaic effect for as-made cells showed three peaks at 1.04, 0.8 and 0.68μm at room temperature. The major response occurred at 1.04μm which corresponds to the band gap of Cu$_2$Se at about (1.2eV). This indicates that the most of the incident light is absorbed in the Cu$_2$Se. However, there is some uncertainty in the band gap energy of Cu$_2$Se. Most recently Ture et al.(6) found this to be 1.21eV, but Sorokin et al.(5) and Komaschenko and Fedorus(4,25,26) have reported a value of 1.3eV, in which case absorption in Cu$_2$Se would occur at 0.95μm. The second largest response at 0.68μm corresponds to an energy of ~ 1.8eV and is probably associated with the band gap absorption of CdSe indicating that a considerable fraction of the incident light reaches the CdSe through the Cu$_2$Se. The peak at 0.8μm (~ 1.52eV) may be associated with the excitation to the conduction band of electrons from copper levels ~ 0.2eV above the valence band of CdSe. Such a copper related centre at 0.21eV above the valence band was reported by Ture et al.(28,29) from photocapacitance measurements. The measurements of steady state photocapacitance indicated that the principal threshold at room temperature occurred at 0.79eV suggesting a donor level 0.95eV below the conduction band (Figure 7.20). This level is probably associated with copper. Robinson and Bube(27) have found the principal level for the copper centre to be at 1.05eV, from photoconductivity measurements. A level between 0.94 and 1.0eV above the valence band which was only observed in crystals doped with copper has also been reported by Ture et al.(28,29).

7.7.4 Heat treatment in air

The 2min heat treatment in air had a deleterious effect on the current-voltage characteristics of type A cells as copper diffusion led to the formation of an insulating region in the CdSe(6). On the other hand the heat treatment improved the characteristics of type B cells. This is probably because these cells are formed on near degenerate CdSe and an increase in the resistivity due to copper diffusion and probably oxygen absorption at the interface(6) is helpful. It is well known that copper can readily diffuse into CdSe where it forms acceptors even at temperatures as low as 200°C. Thus the heat treatment was designed to induce the adsorption of oxygen at the interface, which would also introduce acceptor states(6,30), with a consequent increase in the resistivity. This is consistent with Ture et al.(6) who have reported that cells formed on as-grown CdSe exhibited no rectification. However, good photovoltaic properties were produced by heating the device in air at

200°C for 30 min. They also found that the heat treatment had a deleterious effect on devices which had good characteristics in the as-made state. Also a similar effect has been reported for cells formed on high and low resistivity CdS(31) substrates. It was found that when a Cu_2S/CdS cell was baked in air the diffusion of copper from the copper sulphide into the CdS produced a copper compensated layer in the CdS at the junction(31-33).

After heating in air at 200°C for 2 min, the dominant spectral feature in the response of type A cells was the peak at 0.68μm (about 1.8eV) which is probably associated with the band gap of CdSe and indicates that a considerable fraction of the incident light had been absorbed in the CdSe rather than in the Cu_2Se. In addition there was no response from the band at 1.04μm., i.e. from absorption by the Cu_2Se. This is attributed to loss of copper by diffusion into the CdSe. The opposite was observed for Type B cells. While there was no response in the as-made condition, heat treatment in air produced spectra similar to those of as-made type A cells. The minority carrier diffusion lengths were found from EBIC results, (Figure 7.23). The values of diffusion length Ln (in Cu_xSe) and Lp (in CdSe) obtained were 0.45μm and 0.48μm respectively. Both these values are similar in magnitude for values obtained in the related Cu_2S/CdS system. Ideally, larger values would be preferred. It is since layers have a twin related grains structure significant improvement should be possible.

7.7.5 Heat treatment in Argon

The current-voltage (J-V) characteristics of a typical type B cell before and after various periods of heat treatment are shown in Figures 7.24 and 7.25. Comparison with Figures 7.15 and 7.16 show the differences between heating in air and in Argon. After heat treatment in air, the parameters V_{OC}, J_{SC}, FF attain their optimum values at an earlier stage of the heat treatment. This may be attributed to the fact that in air heated devices there are effects of copper diffusion and oxygen adsorption at the interface(6). Both of these acceptor states, which increase band bending and the width of the depletion region in the CdSe which reduces the probability of tunnelling. However, with argon heated cells compensation is by the diffusion of copper only(34,35).

7.7.6 Analysis of CdSe/Cu_2Se junction

The dark current-voltage characteristics at different temperatures in the range from 300K to 85K are given in Figure 7.16. The results showed that the forward current increased exponentially with applied forward voltage V for $V > 3kT/q$ and the barrier heights varied between 0.64 and 0.30eV. This suggests that forward current transport was due to the tunnelling of electrons from the Cu_2Se layer to the CdSe through the interface states(36). TeVelde(37) has suggested variable barrier heights may be caused by changes in the density of charged interface states. The barrier height was found to increase with heating in air at 200°C for

2 min. (see Table 7.3). Capacitance-voltage measurements indicate that there was a decrease in the net donor concentration from 0.68 x 10^{15} to 0.40 x 10^{15} cm^{-3} on heating while the barrier height increased from 0.56 to 0.75eV and the depletion region increased in thickness with heating in air from 0.811 to 1.76 µm. This in a good agreement with other results that have been reported on thin film CdSe/Cu_2Se(5).

7.8 Conclusions

Heterojunction Cu_2Se-CdSe devices have been formed on orientated single crystal substrates by a chemiplating technique. The structure of the Cu_2Se layers was investigated using RHEED and found to take the cubic modification. The layer thickness has been found to follow at a $t^{1/2}$ relationship, where t is the chemiplating time. The current-voltage characteristics of all the devices showed good rectifying characteristics except for heterojunctions formed on very low resistivity (~ 0.2Ωcm) CdSe substrates, where a short heat treatment of 2 minutes in air or 30 minutes in Argon was found to be necessary. The photovoltaic output characteristics have been measured under simulated AMI illumination. Typical values of V_{oc} and J_{sc} were 200mV and 3.8mA cm^{-2} respectively. The spectral dependence of V_{oc} was measured for the devices, and showed that the principal response arose from the Cu_2Se in most cases. Photocapacitance spectra were also measured and used to identify the more important deep levels. The main threshold in the device indicated a dominant level with an activation energy of 1.0 eV with respect to the conduction band in the CdSe.

References

(1) Bonnet, D., (1979), Proc. Photovoltaic Solar energy Conf. W. Berlin, 387.

(2) Rickus, E., Bonnet, D., (1980), Proc. 3rd E.C. Photovoltaic Solar energy Conf., Cannes, 871.

(3) Richter, H., Hewig, G.H., (1986), 7th European Photovoltaic Solar energy Conf., Sevilla, Spain, 470.

(4) Komashenko, V.N. and Fedorus, G.A., (1967), Soviet Phys. Semicond. 1, 411.

(5) Sorokin, G.P., Papshev, Yu. M. and Dush, P.T., (1965), Soviet Phys. Solid State 7, 1810.

(6) Ture, I.E., Russell, G.J., and Woods, J., (1985), 6th EEC Photovoltaic Conf., London, 861.

(7) Russell, G.J., Fellows, A.T., Oktik, S., Ture, E., and Woods, J., (1982), J. Mater. Sci. lett., 1, 176.

(8) Durose, K., Fellows, A.T., Brinkman, A.W., Russell, G.J., and Woods, J., (1985), Journal of Materials Science 20, 3783.

(9) Caswell, B.G., (1976), Ph.D. Thesis, University of Durham.

(10) Otkik, S., (1982), Ph.D. Thesis, University of Durham.

(11) Russell, G.J., Oktik, S., and Woods, J., (1983), J. Mater. Sci. Lett. 2, 229.

(12) Stuckes, A.A., and Farrell, G., (1964), J. Phys. Chem., 25, 427.

(13) Paskirikin, A.S., and Sapozhriskov, R.A., (1962), Soviet Phys. Crys. 7, 501.

(14) Shiozowa, L.R., Augustine, F., Sullivan, G.A., Smith, J.M., and Cook, W.R. Jr., (1969), Aerospace Research Laboratories Report ARL 69.

(15) Linquist, P.F., and Bube, R.H., (1972), J. Electrochem. Soc. 119, 7, 936.

(16) Singer, J., and Feath, P.A., (1971), Appl. Phys. Lett., 11, 130.

(17) Buckley, R.W., and Woods, J., (1974), J. Phys. D: Appl. Phys. 7, 663.

(18) Idrichan, G.Z., and Sorokin, G.P., Neorganicheskie Materialy, vol. 11, No. 9,(1967),1693.

(19) Heyding, R.D., (1966), Canadian Journal of Chemistry, 44, 1233.

(20) Efendive, G.A., and Kazinets, M.M., (1960), Izv. Akad, Nauk. Azcrb. SSR, Ser. Fiz. Mat. L. Tekhn, Nauk, No. 5, 91,

(21) Shafizade, R.B., Ivanova, I.V., and Kazinet, M.M., (1976), Thin Solid Films, 35, 169.

(22) Shafizade, R.B., Ivanova, I.V. and Kazinets, M.M., (1978), Thin solid films, 55, 211.

(23) Lindquist, P.F., and Bube, R.H. (1972), J. Appl. Phys. 43, 2839.

(24) Oktik, S., Russell, G.J., and Woods, J., (1983), Solar Energy Materials 9, 77.

(25) Komashchenko, V.N., and Fedorus, G.A., (1967), Soviet Physics - semiconductors, 1, 411.

(26) Komaschenk, V.N. and Fedorus, G.A., (1970), Soviet Phys. Semiconductors, 3, 1001.

(27) Robinson, A.L., and Bube, R.H., (1971), J. Appl. Phys. 42, 5280.

(28) Ture, I.E., Claybourn, M., Brinkman, A.W., and Woods, J., (1985), J. Crystal Growth, 72, 189.

(29) Ture, I.E., Claybourn, M., Brinkman, A.W., and Woods, J., (1986), J. Appl. Phys., 60(5), 1670.

(30) Ture, I.E., Brinkman, A.W., Russell, G.J., and Woods, J., (1987), Phys. State Sol. (a), 100, 681.

(31) Caswell, B.G., Russell, G.J., and Woods, J., (1975), J. Phys. D:Appl. Phys., Vol. 8,1889.

(32) Shea, S.P., Partain, L.D., and Warter, P.J., (1978), Scanning Electron Microscopy, Vol. 1. (SEM inc., AMF, IL:60 666, U.S.A., 435.

(33) Shea, S.P., and Partain, L.D., (1978), 13th IEEE Photovoltaic Spec. Conf. (Washington, D.C.), 393.

(34) Pande, P.C., Russell, G.J., and Woods, J., (1983), J. Phys. D:Appl. Phys., 16, 2307.

(35) Pande, P.C., (1984), Ph.D. Thesis, University of Durham.

(36) Komashchenko, V.N., Lukyah, Chikova, N.B., Fedorus, G.A., and Sheinkman, M.K., (1976), Proc. Int. Conf. Phys. and Chem. Semiconductor Heterojunction Layer Structure, Akademia Kiado, Budapest, 213.

(37) Te Velde, T.S., (1973), Solid State Electron., 16, 1305.

CHAPTER 8

$Zn_xCd_{1-x}Se$ Cu_2Se Photovoltaic Cell

8.1 Introduction

The results to be described in this chapter relate to the use of $Cd_{1-x}Zn_xSe$ as the n-type component in $Cu_2Se/Cd_{1-x}Zn_xSe$ photovoltaic heterojunctions. So far as the author is aware, there has been no previously reported work with this structure, although there have been some reports of work with the related $Cu_2Se/CdSe$ system$^{(1-5)}$. Use of the appropriate zinc concentration should improve the matches between the crystal lattices, and the electron affinities of the heterojunction with Cu_2Se. The results described here are for $Cd_{1-x}Zn_xSe$ /Cu_2Se photovoltaic cells which have been formed on single crystal dice cut from crystal boules with compositions in the range $0 < x < 0.4$. (The properties of the mixed crystal $Cd_{1-x}Zn_xSe$ substrate material are described in Chapters 5 and 6).

8.2 Structure of polished $Zn_xCd_{1-x}Se$ surfaces

The single crystal boules of the ternary alloy $Zn_xCd_{1-x}Se$ were grown from the vapour phase by both the Durham and Piper–Polich techniques$^{(6-8)}$ (see Section 4.2), and the crystal structure and lattice parameters were determined by

X-ray diffractometry (Section 5.4). Briefly, the lattice parameters varied linearly up to the transition from the sphalerite to Wurtzite which occurred at about x = 0.5(9). When a single crystal of $Cd_{0.8}Zn_{0.2}Se$ was polished using alumina powder with a particle size of 1µm, the surface was always found to be polycrystalline. This is illustrated in the reflection electron diffraction (RHEED) pattern of Figure 8.1. The radii of the first three rings in this pattern increased in the sequence $\sqrt{3}$, $\sqrt{8}$, $\sqrt{11}$ and can be indexed as the (111), (220) and (311) reflections of the cubic sphalerite phase of $Cd_{0.8}Zn_{0.2}Se$. However, the bulk crystal structure was hexagonal suggesting either that the polishing procedure had induced a phase change from the hexagonal to the cubic on the surface, or that the polishing damage had led to the extinction or attenuation of some of the rings normally observed from hexagonal material(10). The lattice constant was observed to be 5.95A°, in close agreement with the value of 5.97A° from X-ray diffractometry(9). Similar polycrystalline surface layers are produced when single crystal CdSe(11), CdS(12) and ZnS(13) are mechanically polished. Thus it was necessary to etch all samples in cold HCl to remove the polycrystalline cubic polished layer left by the polishing process.

8.3 $Cd_{1-x}Zn_xse/Cu_2Se$ Solar cell

8.3.1 Preparation of the device

The $Cd_{1-x}Zn_xSe$ crystals were oriented by X-ray back-reflection, and cut into dice with dimensions of 4 x 4 x 2 mm^3 with the basal (0001) plane parallel to the large area faces. The dice were mechanically polished with alumina powder down to a grit size of 1um and then etched in concentrated HCl for 2 min. to remove polishing damage. After rinsing in methanol, indium ohmic contacts were applied to the Cd faces of all dice. The topotaxial layer of copper selenide was grown at 95°C on the opposite freshly etched selenium face, by dipping in the plating solution for 60s as described in section 7.3.

Finally, an evaporated gold dot, 2mm in diameter was deposited on the Cu_2Se layer by vacuum evaporation to complete the device structure.

8.3.2 RHEED investigation

The phases of the Cu_xSe layers grown on the $Cd_{0.8}Zn_{0.2}Se$ single crystals were examined by reflection high energy electron diffraction (Chapter 4). Figures 8.2 and 8.3 show the RHEED patterns obtained from as-formed layers of copper selenide grown on the selenium $(000\bar{1})$ plane of $Cd_{0.8}Zn_{0.2}Se$ where the electron beam was incident along the $[10\bar{1}0]$ and $[11\bar{2}0]$ directions in the CdZnSe respectively. There are polycrystalline rings which pass through some of the more intense spots.

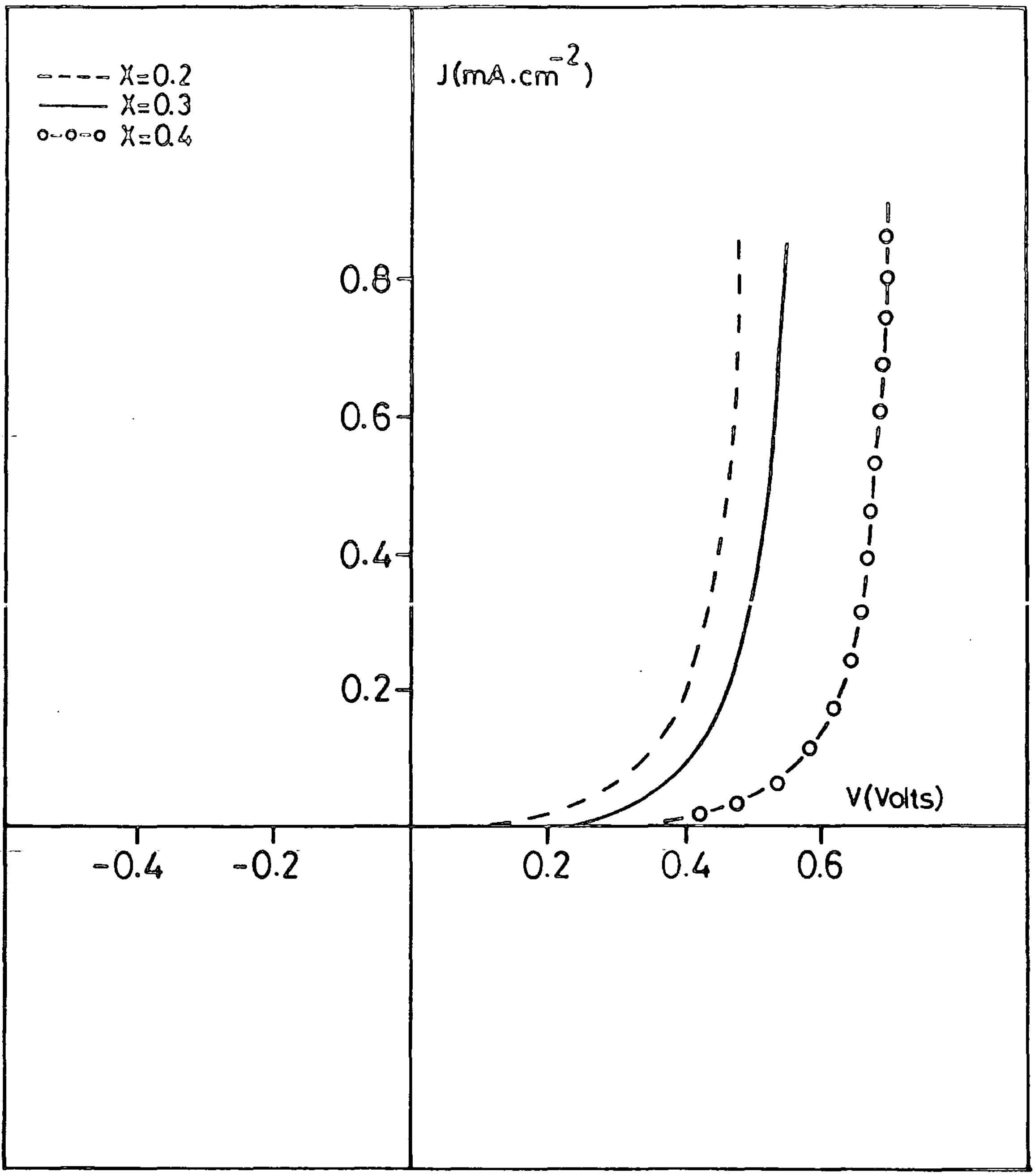

Figure 8.5 Dark current-voltage characteristics for $Cd_{1-x}Zn_xSe/Cu_2Se$ cells.

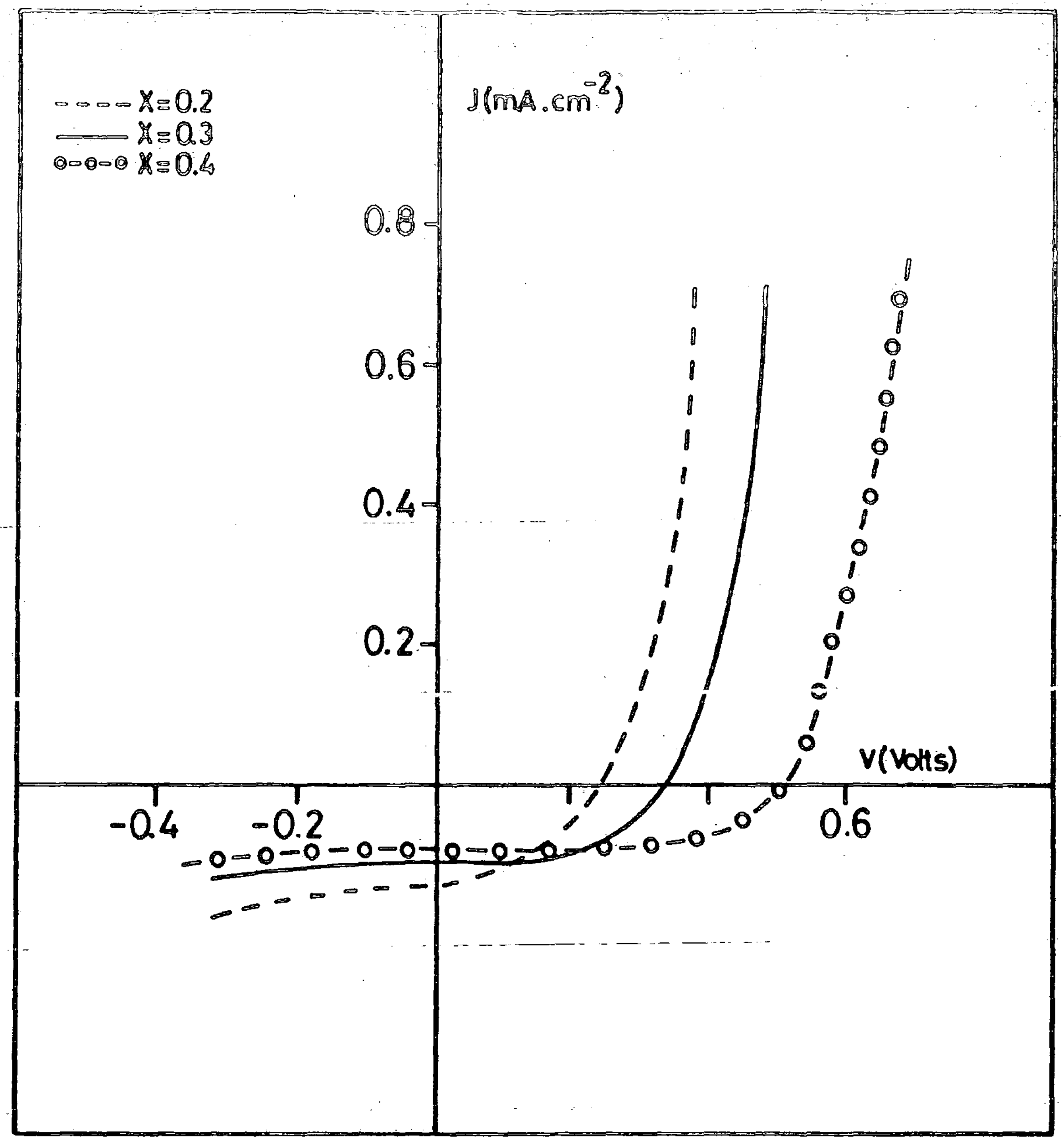

Figure 8.6 Current-voltage characteristics for $Cd_{1-x}Zn_xSe/Cu_2Se$ cells measured under 100 mW cm^{-2} AMI illumination.

8.2.

Parameters	$CdSe/Cu_2Se$	$Cd_{0.8}Zn_{0.2}Se/Cu_2Se$	$Cd_{0.7}Zn_{0.3}Se/Cu_2Se$	$Cd_{0.6}Zn_{0.4}Se/Cu_2Se$
V_{oc}	0.2	0.25	0.34	0.42
I_{sc} mA/cm^2	3.8	1.4	1.1	1.0

Table 8.2 Current-Voltage characteristics for $Zn_xCd_{1-x}Se/Cu_2Se$ cells measured under 100 mW cm^{-2} (AMI) illumination.

The value of V_{oc} increased in proportion to the Zn content from 0.2 volt in $CdSe/Cu_2Se$ cells to 0.42V in $Cd_{0.6}Zn_{0.4}Se/Cu_2Se$ cells (Section 7.4.1). However, there was a simultaneous reduction in J_{sc} from 3.8mA/cm^2 to 1.0mA/cm^2, so that the efficiencies of the mixed crystal devices were always less than those formed on the binary CdSe substrates. In order to determine the optimum annealing time, the current voltage characteristics of a typical device formed on very low resistivity $Cd_{0.8}Zn_{0.2}Se$ were measured after different periods of heat treatment in air at 200°C. These results are summarised in Figures (8.7) and (8.8). The devices which exhibited ohmic behaviour in the as-plated condition, however, rectification effects began to appear after 60 sec of heat treatment, but full rectification did not occur until after 120 sec of heating. Also there was similar improvement in the photovoltaic response, and in general the optimum appeared to be after about 2 min heating in air. The dark current-voltage characteristics of a typical as-made

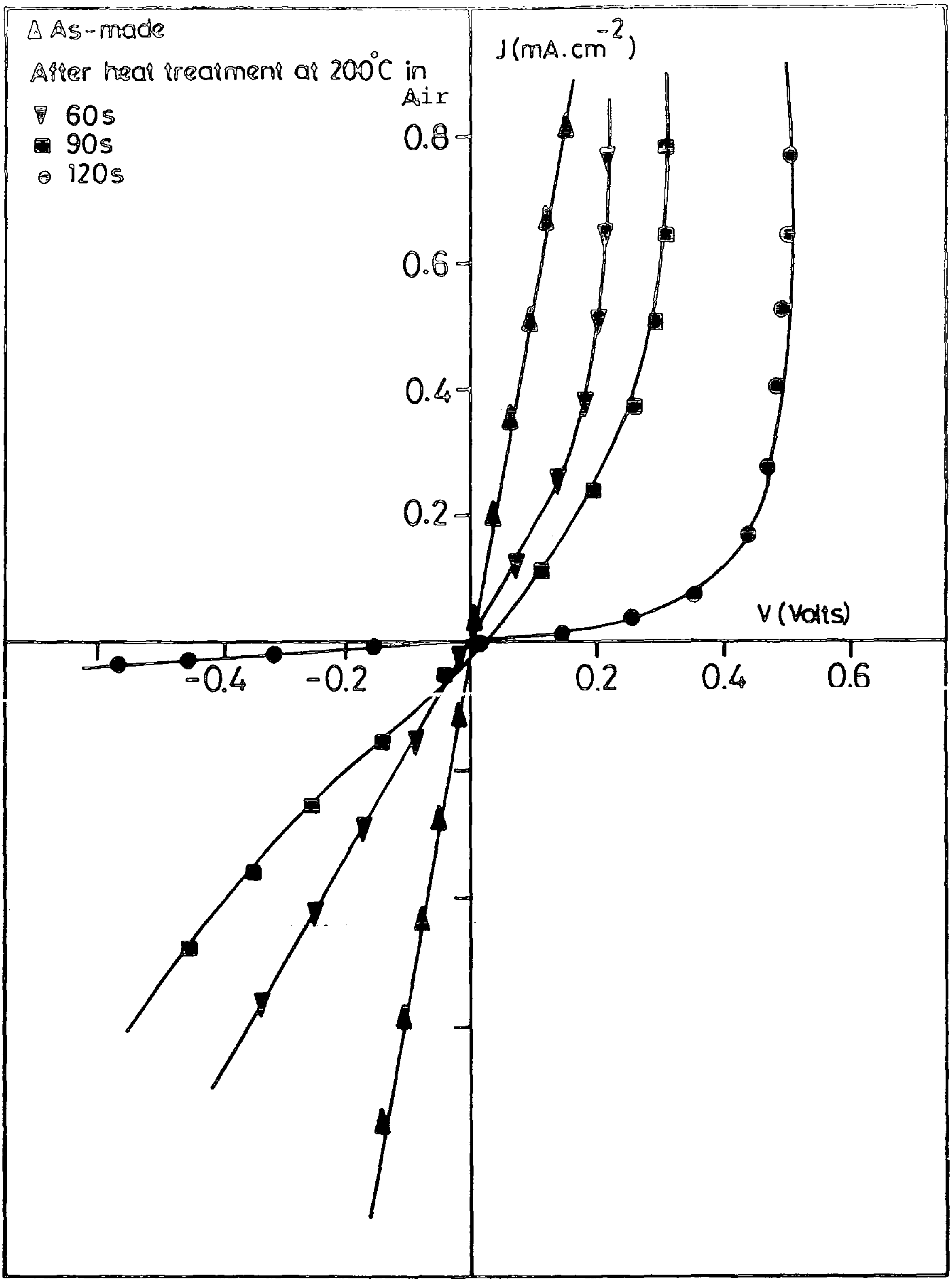

Figure 8.7 Dark (J-V) characteristics of the device formed on very low resistivity $Cd_{0.8}Zn_{0.2}Se$ as a function of air bake time (at 200°C).

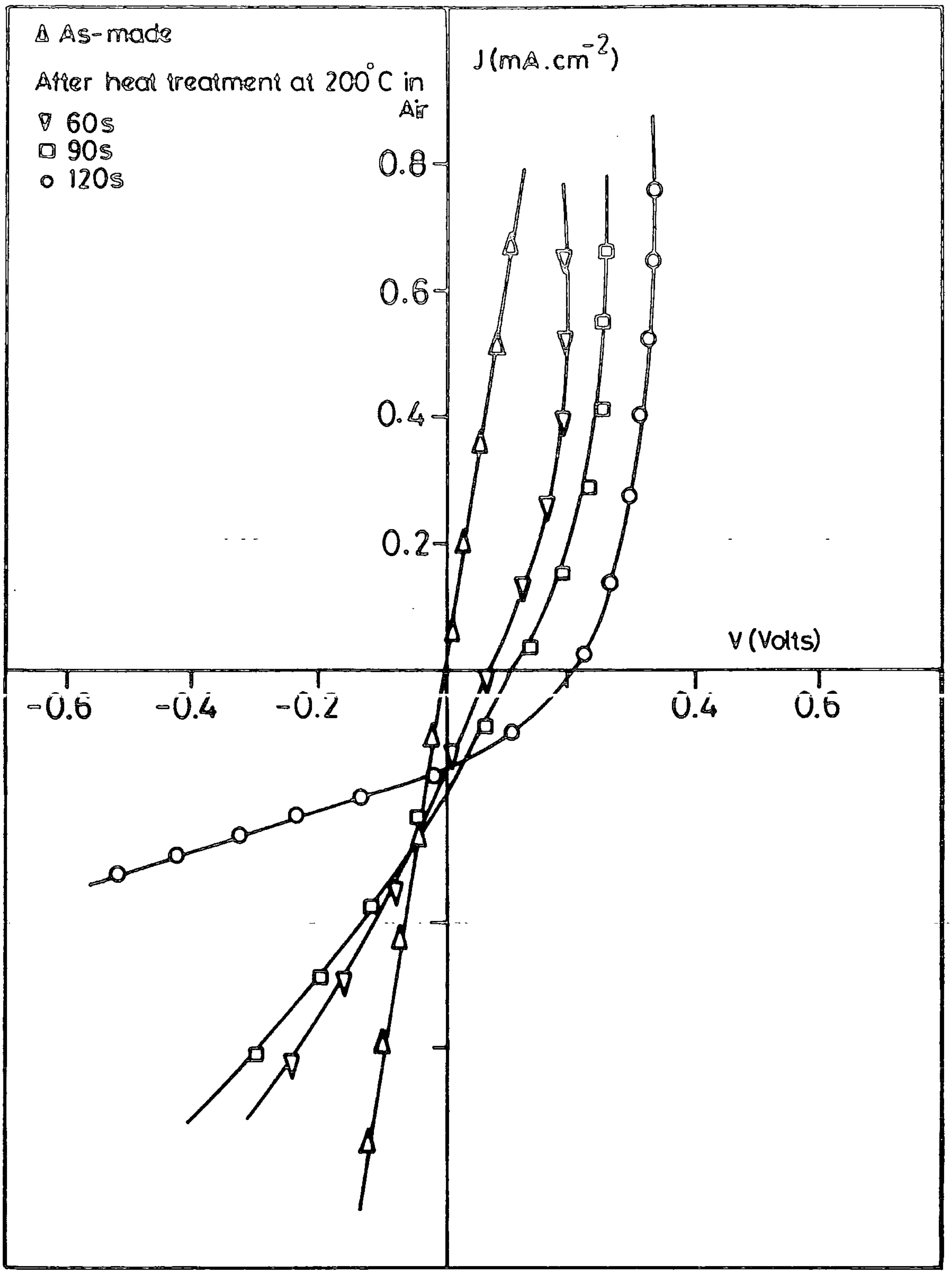

Figure 8.8 Light (J-V) characteristics of the device formed on very low resistivity $Cd_{0.8}Zn_{0.2}Se$ as a function of air bake time (at 200°C).

$Cd_{0.8}Zn_{0.2}Se/cu_2Se$ cell measured at various temperatures between 300K and 143K are shown in Figure 8.9 and the experimentally determined parameters for this device at different temperaturesare given in Table 8.3.

Temperature (K)	diode factor n	$J_o(mA/cm^2)$	$\emptyset_b$ (eV)
300	1.0	1.5×10^{-1}	0.50
213	1.522	8.0×10^{-2}	0.30
143	1.82	1.0×10^{-2}	0.22

Table 8.3. The variation of current and diode parameters with temperature for an as-made cell.

8.3.4 Spectral response

The spectral response at 300K and 90Kof the open circuit-voltage of a typical as-made $Zn_{0.2}Cd_{0.8}Se/Cu_2Se$ device is shown in Figure 8.10. The response at room temperature showed three peaks at wavelengths of 1.04, 0.78 and 0.65µm. The major response occurred at 1.04 µm and corresponds to the band gap in Cu_2 Se at 1.2eV, while the response at 0.65 µm corresponds to the band gap of $Cd_{0.8}Zn_{0.2}Se$ at 1.9eV. The response at 0.7µm (~ 1.59eV) is probably associated with the excitation to the conduction band of electrons from copper levels 0.21eV above the valence band of $Cd_{0.8}Zn_{0.2}Se$. The spectral response at low temperature, also showed three peaks at wavelengths of 1.04, 0.8 and 0.63 µm. The shift in the response to shorter wavelengths is due to the increase in the band gap of $Cd_{0.8}Zn_{0.2}Se$ from 1.9eV to 1.94eV at the reduced temperature.

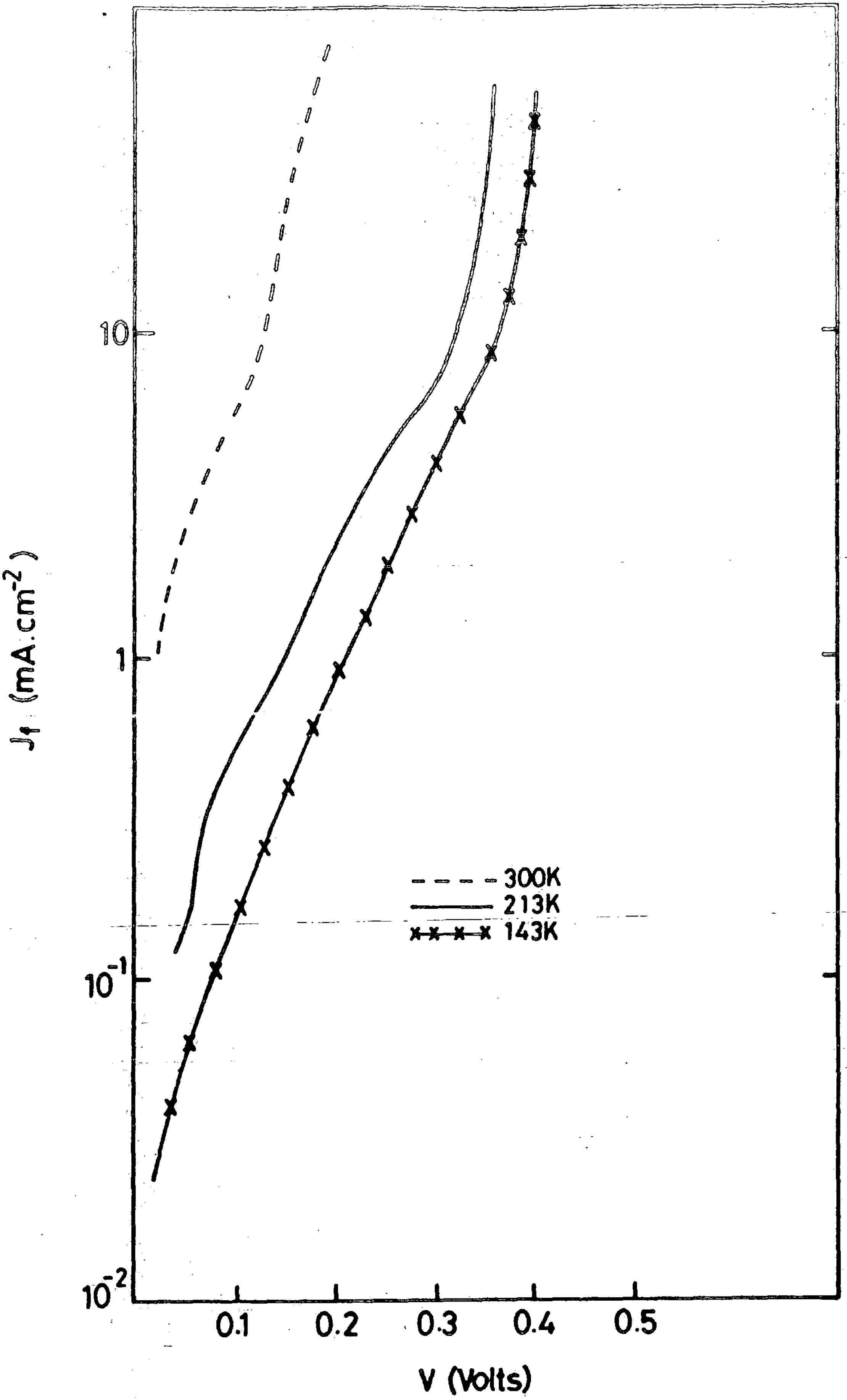

Figure 8.9 Dark current-voltage characteristics as a function of temperature for a cypical $Cd_{0.8}Zn_{0.2}Se/Cu_2Se$ cell.

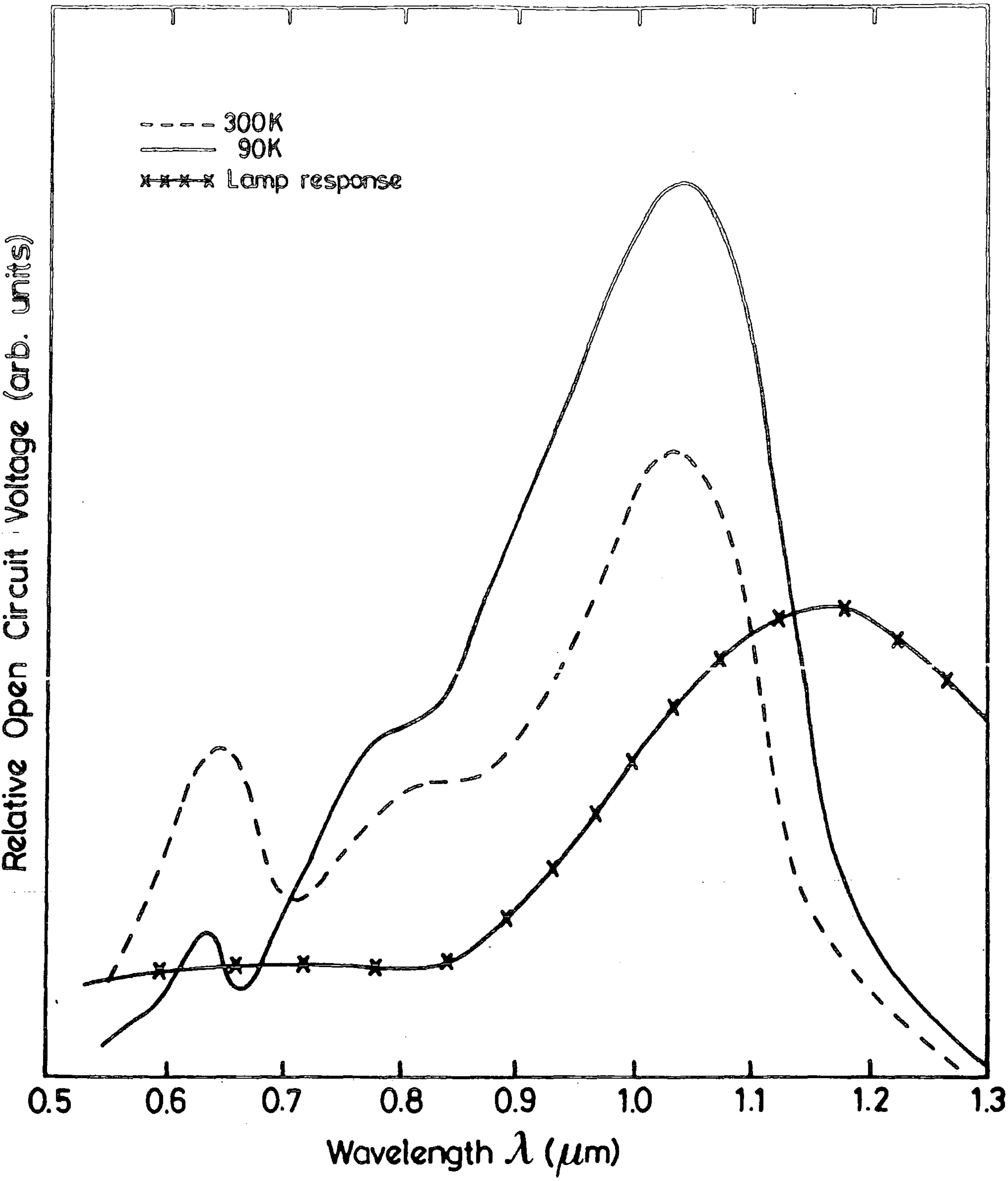

Figure 8.10 Spectral response of V_{oc} for a typical as-made $Zn_{0.2}Cd_{0.8}Se$ cell at 300K and 90K.

The major response, however, was still that at 1.04μm.

The spectral responses of the open circuit-voltage V_{oc} of the $Zn_xCd_{1-x}Se/Cu_2Se$ devices ($0 < x < 0.4$) after a 2 minute heat treatment in air measured at room and liquid nitrogen temperatures are shown in Figures 8.11 and 8.12 respectively. In each case the principal response occurred at ~ 0.55 - 0.68 μm depending on composition, with the peak occurring at shorter wavelengths for material with higher x values. This entire response was related to absorption in the $Cd_{1-x}Zn_xSe$. There was also a smaller response in all of devices at wavelengths of 0.7 - 0.8 μm, again increasing towards shorter wavelengths as the zinc fraction (and hence the band gap) increased. Again this is consistent with the previous assignemnt of this response to Cu centres, located just above (~ 0.2eV) the valence band. More surprising was the attenuation of the response at ~ 1.04 μm. Whereas, this had been the largest peak in the as-made devices (Figure 8.10), it was dramatically reduced in the heat treated cells, and vanished altogether in cells formed on zinc rich ($x = 0.4$) substrates.

Figure 8.12 shows the spectral response at 90K of the open circuit voltage for $Cd_{1-x}Zn_xSe$ devices. The response at low temperature was found to be larger at all wavelengths than at room temperature, with a slight shift of the three principal peaks to shorter wavelengths as expected (see Figure 8.10 for $x = 0.2$).

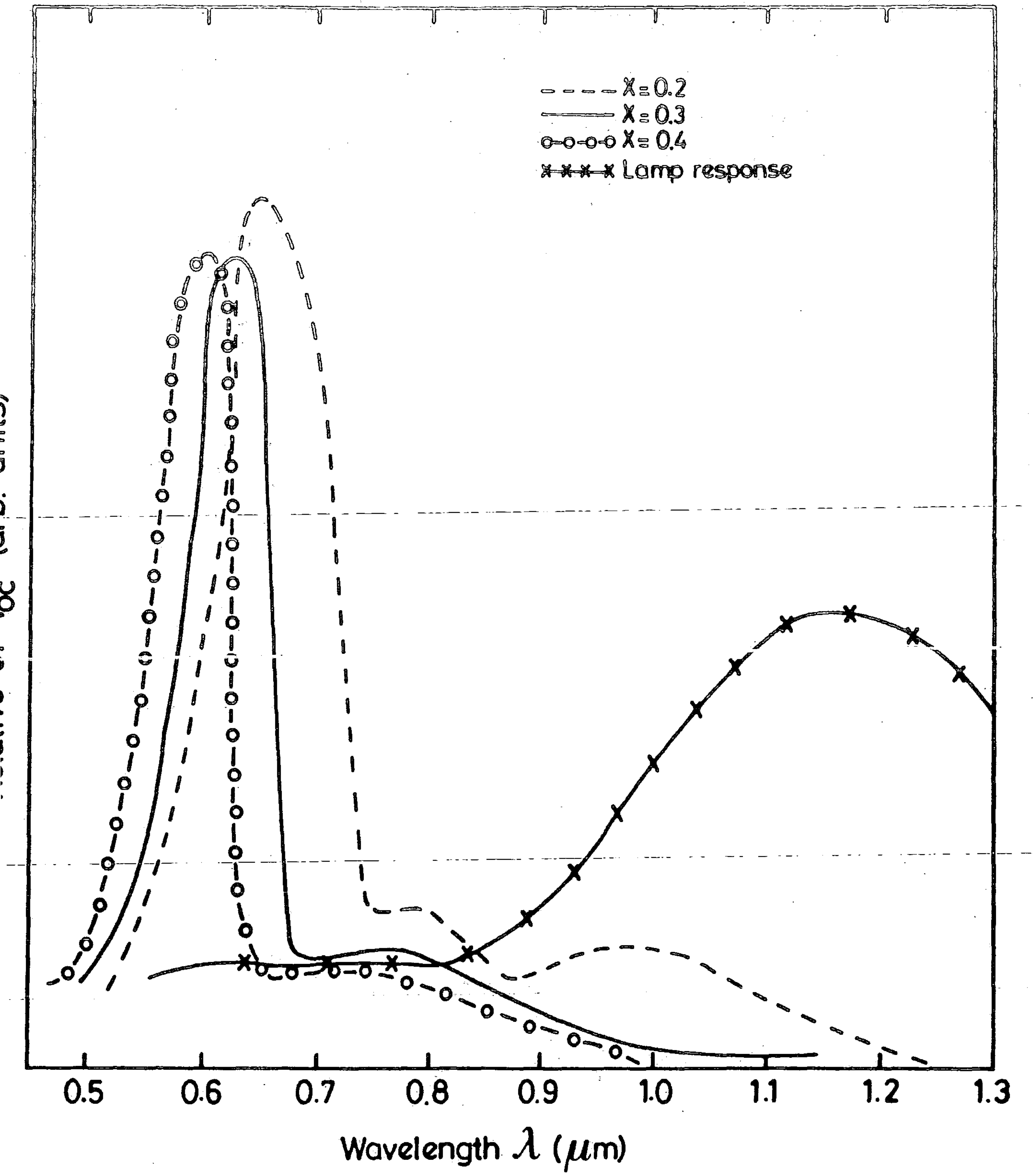

Figure 8.11 Spectral response of V_{OC} after 2 min. heat treatment in air at 200°C for $Cd_{1-x}Zn_xSe/Cu_2Se$ at room temperature.

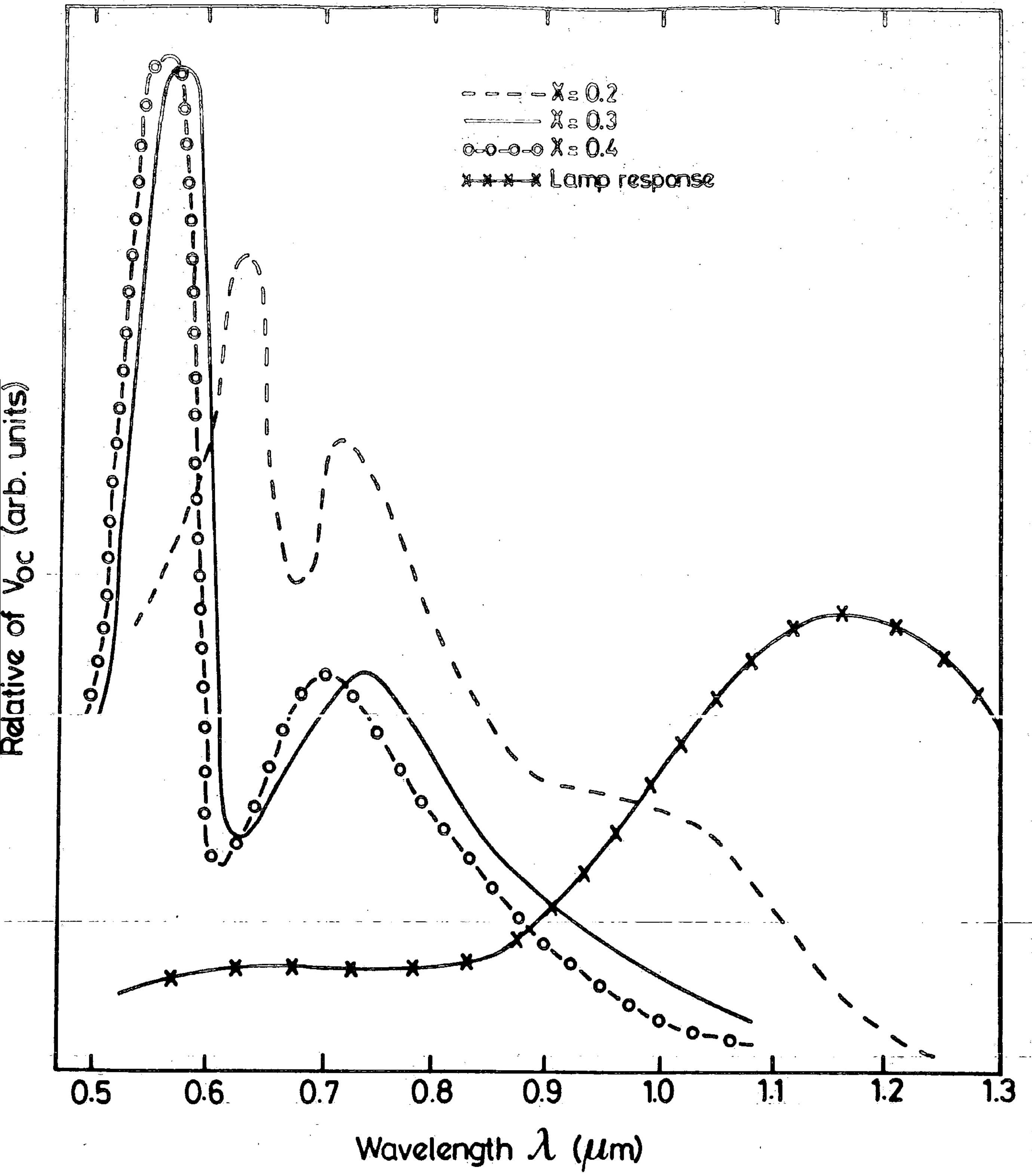

Figure 8.12 Spectral response of V_{OC} after 2 min. heat treatment in air at 200°C for $Cd_{1-x}Zn_xSe/Cu_2Se$ at liquid nitrogen temperature.

8.4 Photocapacitance measurements

The spectral response of steady state photocapacitance (PHCAP) obtained from a typical $Cd_{0.8}Zn_{0.2}Se/Cu_2Se$ device is shown in Figure 8.13 at both room and liquid nitrogen temperatures.

A negative going threshold in PHCAP was observed in the room temperature spectrum at 0.87 eV indicating a level, 0.93eV below the conduction band. This was followed by a positive going threshold at 1.07eV corresponding to a level 0.73eV above the valence band. The 300K spectra also revealed a relatively shallow acceptor level~0.2ev above the valence band corresponding to a photon energy of 1.6eV. The same features were also present in the low temperature spectrum at energies of 0.87eV and 1.18eV corresponding to energy levels of 1.03 and 0.72eV with respect to the valence band. The low temperature curve showed an additional threshold corresponding to a level 0.21eV above the valence band.

The PHCAP spectra for the more zinc rich $Cd_{0.6}Zn_{0.4}Se/Cu_2Se$ heterojunction is shown in Figure 8.14. The principal negative threshold in the PHCAP spectrum at R.T. occurred at 0.91eV indicating a level 1.0eV below the conduction band. A similar threshold was observed at liquid nitrogen at 1.01eV giving a value of 1.02eV for the position of the level relative to the conduction band edge. The room temperature spectrum showed an additional positive going threshold at 1.25eV, indicating a level 0.67eV above the valence band (v.b). The corresponding feature in the low

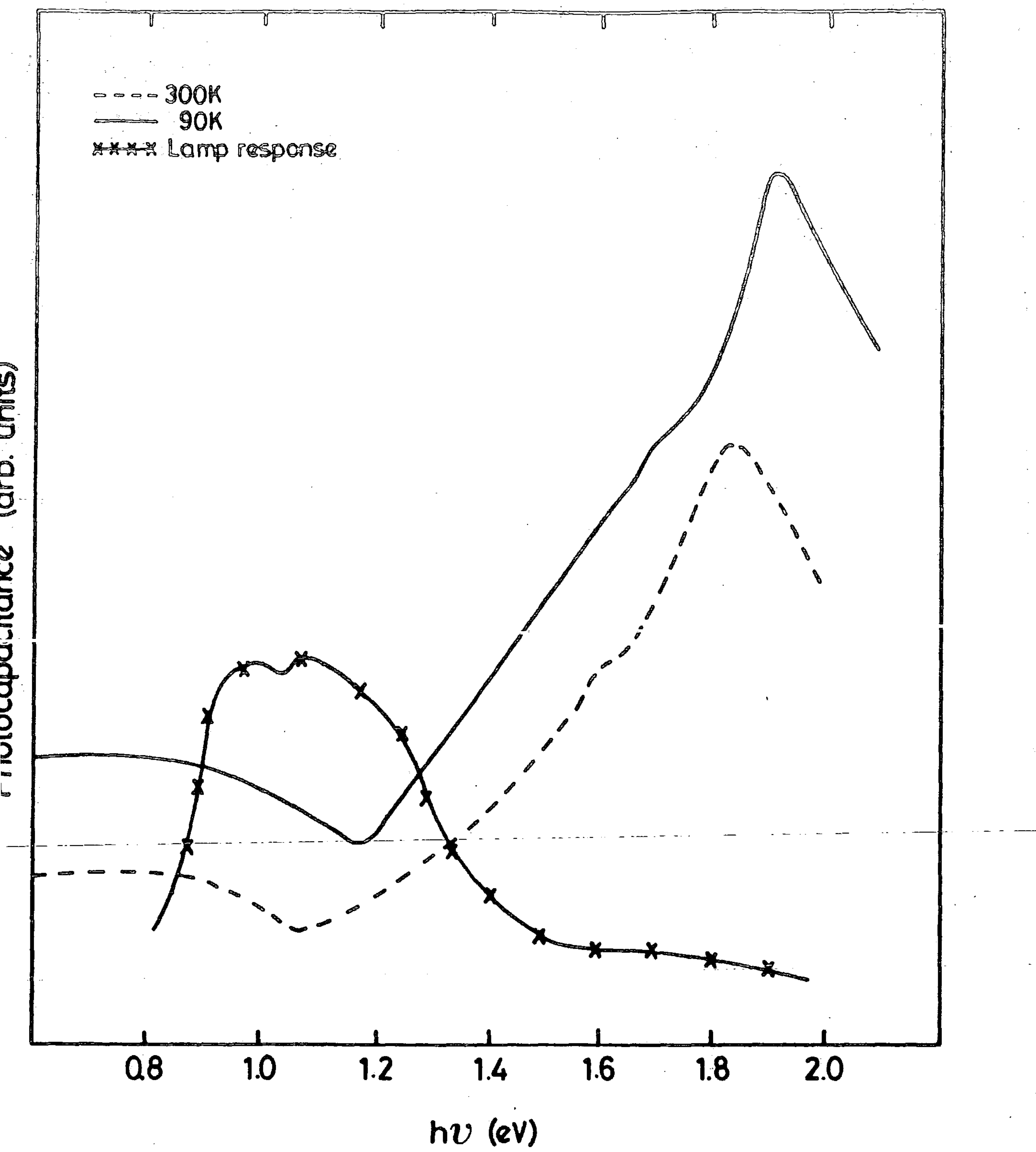

Figure 8.13 Photocapacitance spectra for a typical Zn$_{0.2}$Cd$_{0.8}$SeCu$_2$Se cell at 200K and 90K.

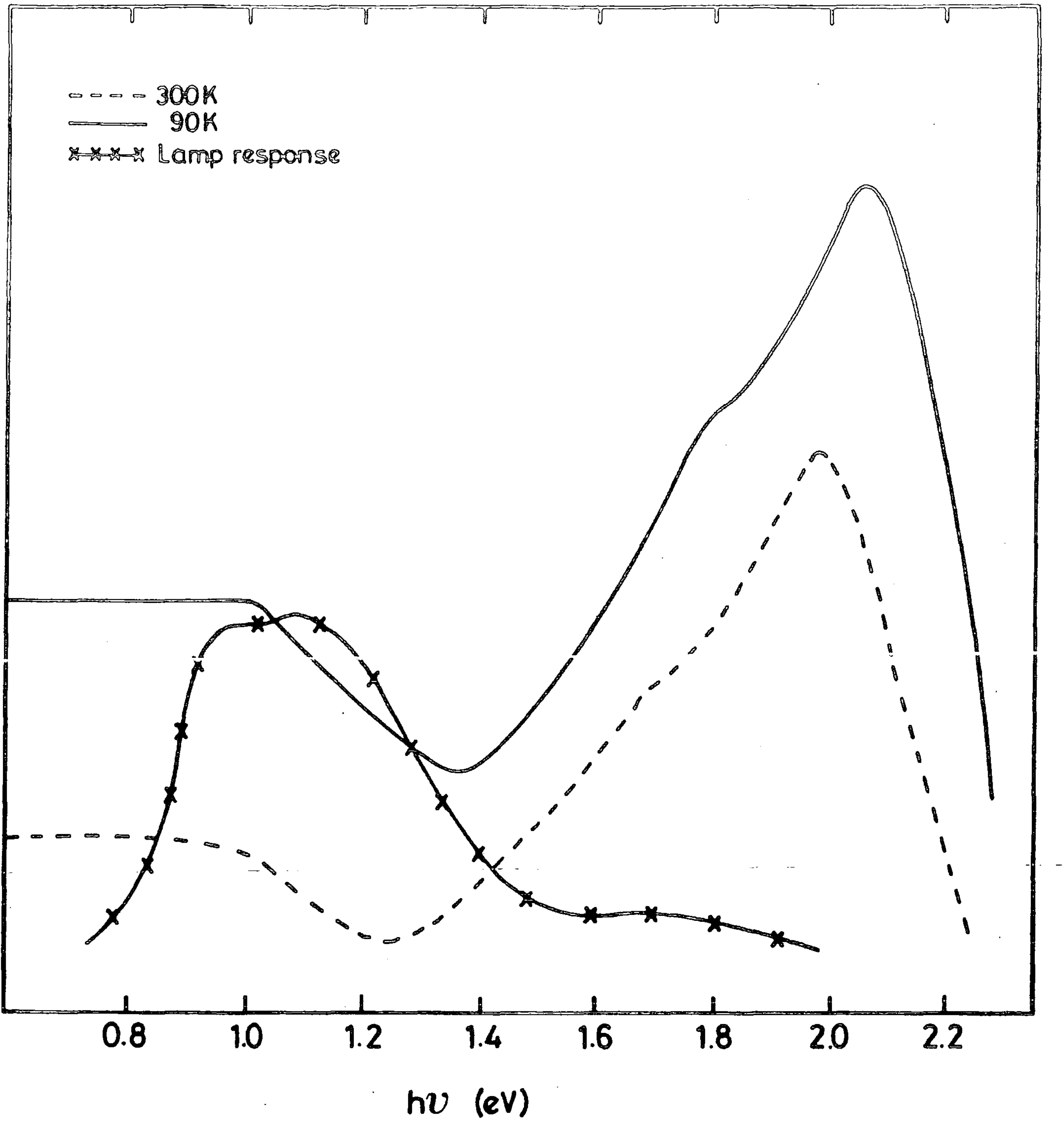

Figure 8.14 Photocapacitance spectra of a typical $Zn_{0.4}Cd_{0.6}Se/Cu_2Se$ cell at 300K and 90K.

temperature spectrum occurred at 1.36eV giving a value of 0.67eV with respect to the valence band. Both the 300K and 90K spectra showed an additional threshold at about 1.7eV, corresponding to a centre situated about 0.21eV above the valence band.

8.5 Capacitance voltage characteristics for $Zn_xCd_{1-x}Se/Cu_2Se$ cells

The capacitance-voltage characteristics of $Cd_{1-x}Zn_xSe/Cu_2Se$ heterojunctions (with x = 0.2, 0.4) were measured in the as-made condition at 1MHz, and the resulting plots of C^{-2} against V are shown in Figure 8.15. Analysis of the C-V plots led to estimates of diffusion potential (Vd), donor density (N_d), Fermi energy, (E_c-E_f), barrier height and the width of the depletion region, which are summarised in Table 8.4.

Composition (x)	Nd($\times10^{15}$) cm^{-3}	(E_c-E_f) eV	Vd(eV)	ϕ_{c-v}(eV)	W_{c-v}(μm) (zero bias)
0.2	2.2	0.16	0.58	0.74	0.731
0.4	0.69	0.19	0.69	0.88	1.34

Table 8.4 Barrier height and carrier densities for as-made cells on substrates of different compositions.

The results show the value of donor density decreased slightly from 2.2 x $10^{15}cm^{-3}$ at x = 0.2 to 0.69 x $10^{15}cm^{-3}$ at

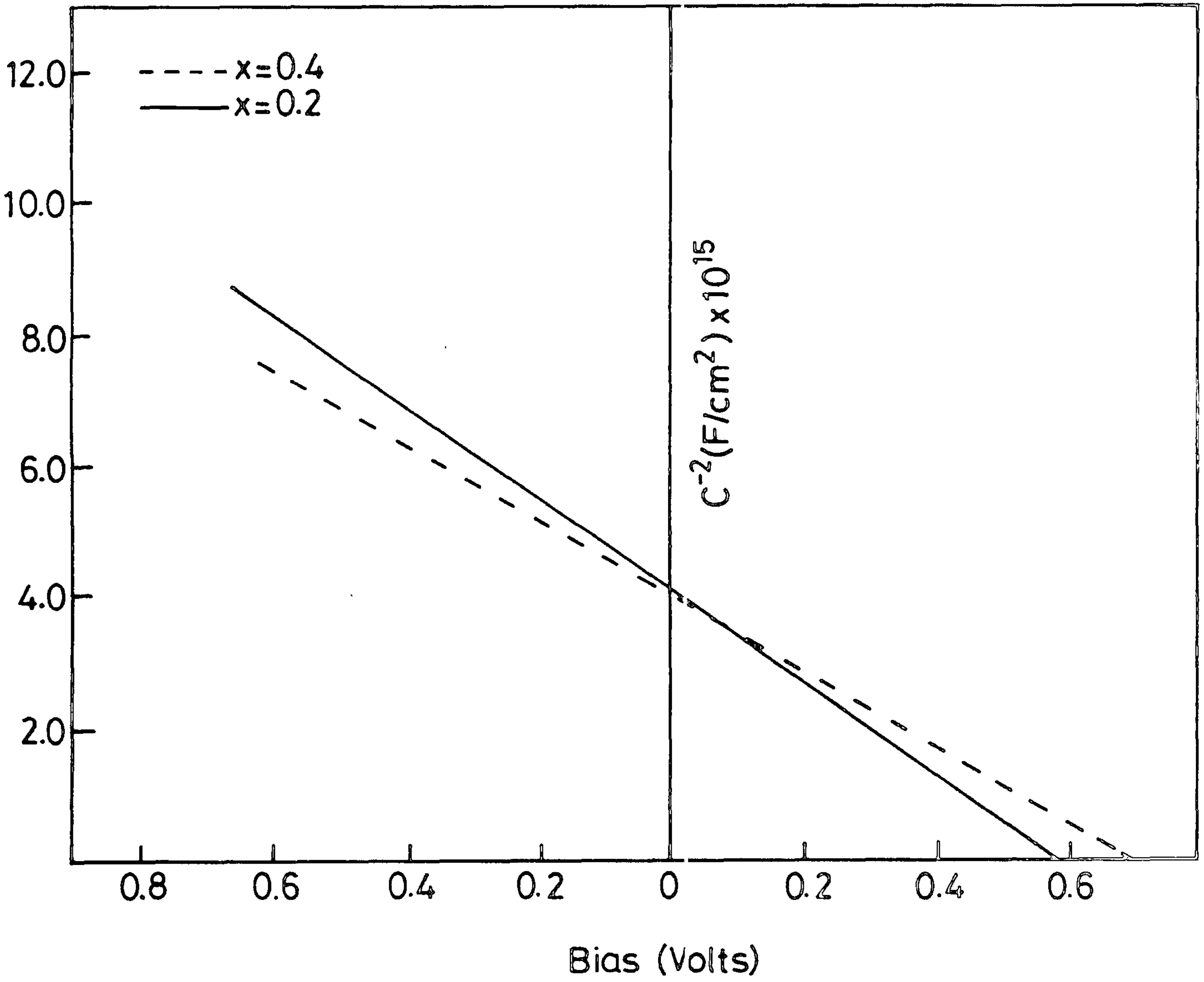

Figure 8.15 C^{-2}-V characteristics for $Zn_xCd_{1-x}Se/Cu_2Se$ (x = 0.4, 0.2) at 300K.

x = 0.4. The corresponding Fermi energy values (E_C-E_f) were calculated and found to increase with increasing x, from 0.16 at x = 0.2 to 0.19 at x = 0.4. The width of the depletion region at zero bias W_{C-V} was found to range between 0.7μm at x = 0.2 to 1.3 μm at x = 0.4. The barrier height also increased with increasing x.

8.6 Barrier height measurements

The barrier heights were also found directly from photothreshold measurements(14) (Section 3.2.5). These results are given in Figure 8.16 in the form of Fowler plots ($J_{sc}^{1/2}$ vs hυ), and Table 8.5, where they are compared with barrier heights determined by other methods.

X	ϕ_{C-V} (eV)	ϕ_{PH} (eV)	ϕ_{I-V} (eV)
0.0	0.56	0.75	0.60
0.2	0.74	0.77	0.50
0.3	0.79	0.91	0.57
0.4	0.88	0.94	0.66

Table 8.5 Barrier height calculated from photothreshold capacitance-voltage and current-voltage.

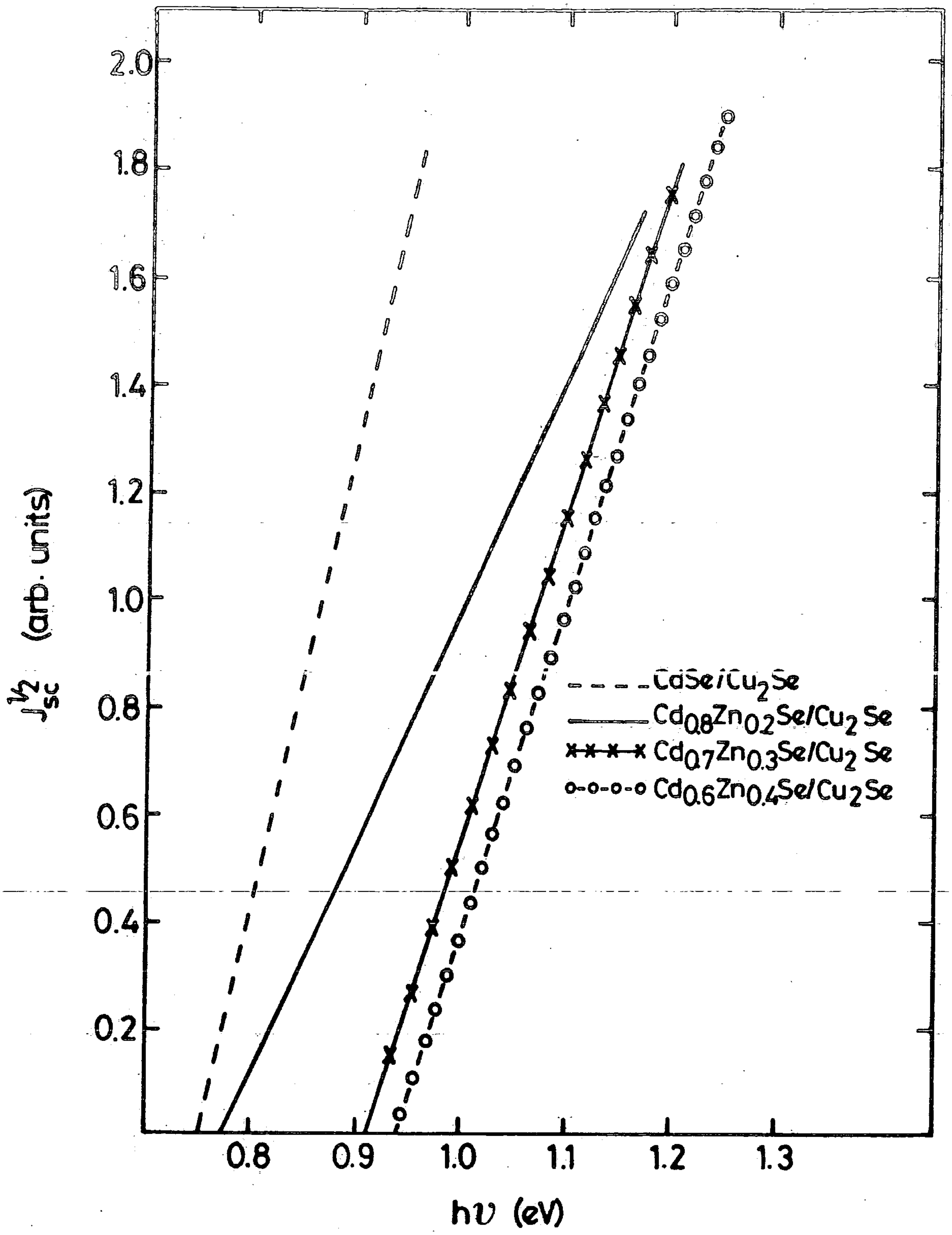

Figure 8.16 Fowler plot of $J_{sc}^{1/2}$ for cells of different composition.

8.7 Discussion

8.7.1 RHEED measurements

The $Cd_{1-x}Zn_xSe/Cu_2Se$ heterojunctions were fabricated by forming layers of p-type Cu_2Se on n-type single crystals of $Cd_{1-x}Zn_xSe$. RHEED patterns from as-formed layers of Cu_2Se (Figures 8.2 and 8.3) which consisted rings and spots, indicated that the layers were mixed deposits of polycrystalline and ordered material. This was similar to the structure of the layers that were produced on single crystals of CdSe (see Chapter 7, Section 3). Measurements of the relative diameters of the rings indicated that the layers had a f.c.c. structure with a lattice parameter of 5.86A^o, in close agreement with the ASTM index value of 5.85A^o for Cu_2Se. This accords with the value of 5.82$\overset{0}{A}$ determined for Cu_2Se layers on CdSe (see Section 7.3.3). Similar results have been reported for the lattice parameter of Cu_2Se by R.H. Hyding(15), G.A. Efendive and M.M. Kazinets(16), Shafizade et al.(17,18), and Ture et al.(5). Idrichan and Sorokin(19) found a study of X-ray diffraction pattern that the lattice parameters of Cu_2Se decreased monotonically from 5.78A^o to 5.66A^o as x increases.

The effect on the structure of the Cu_2Se of heat treatment in air at 200^{o}C for 2 min was demonstrated in the diffraction pattern of Figure 8.4. This showed that while some other spots disappeared after heat treatment, the remaining spot pattern indicated a twinned cubic structure.

This was identical behaviour to that observed with CdSe, i.e. that Cu_2Se grows topotaxially on $Cd_{1-x}Zn_xSe$ in the f.c.c. modification of the grains in twin oriented positions, on the basal plane of the $Cd_{1-x}Zn_xSe$. The orientational relationship appears to be (111) Cu_2Se parallel to (0001) $Cd_{1-x}Zn_xSe$ and [110] Cu_2Se parallel to $[10\bar{1}0]$ $Cd_{1-x}Zn_xSe$(5).

8.7.2 Current-voltage characteristics

The measurements reported here for $Cd_{1-x}Zn_xSe/Cu_2Se$ devices formed on single crystals showed that the open circuit voltage V_{OC} under AM1 illumination increased from 0.2 to 0.42V, while the short circuit current decreased from 3.8mA/cm^2 to 1.0mA/cm^2 as Zn content was increased from 10% to 40% (table 8.2). There was also an increase in the values of photothreshold measured over the same composition range (Table 8.5). These results suggest that the electron affinity of $Zn_xCd_{1-x}Se$ decreased as the zinc concentration was increased (see Section 6.5).

This in a good agreement with other results reported for thin film $Cd_{1-x}Zn_xS/Cu_2S$ devices(20,21). Similar behaviour has been reported for crystals $Cd_{1-x}Zn_xS/Cu_2S$ (23). However, in the latter case, the addition of too much Zn to the CdS lattice, causes the electron affinity to become less than that of Cu_2S. This happens abruptly causing a potential spike to be formed in the conduction band. The increase in V_{OC} observed in $Cu_2Se/Cd_{1-x}Zn_xSe$ cells can be attributed almost entirely to the increase in barrier height. However the higher resistivity of the mixed crystal system, particularly at the higher zinc concentration would lead to a greater series resistance, and thus to the decline in J_{sc} as the zinc content is increased$^{(23)}$.

The current-voltage characteristics of a $Cd_{0.8}Zn_{0.2}Se/Cu_2Se$ cell fabricated on the low resistivity $Cd_{1-x}Zn_xSe$ are shown in Figures 8.7 and 8.8 showed no rectification in the as-made cell. This is because the heterojunction was formed between two highly conducting nearly degenerate semiconductors, with the result that both depletion regions were very narrow so that carriers were able to tunnel easily through the barrier. The improvement in the diode characteristics following the heat treatment can be attributed to the effects of copper diffusion from the Cu_2Se into the $Cd_{1-x}Zn_xSe$ to form an interface layer.

8.7.3 Spectral response

The spectral response curve of the open circuit voltage for an as-made cell on single crystal $Cd_{0.8}Zn_{0.2}Se/Cu_2Se$ is shown in Figure 8.10. The major response occurring at wavelengths of 1.04µm corresponds to the energy band gap in Cu_2Se ~ 1.2eV. Similar results were observed in the $CdSe/Cu_2Se$ (see Section 7.4) case. The second largest response at 0.65µm (~ 1.9eV) was thought to arise from the band gap of the ternary at room temperature, while the response at 0.78µm (~ 1.59eV) is associated with the excitation to the conduction band of electrons from copper levels located 0.21eV above the valence band of $Cd_{0.8}Zn_{0.2}Se$. The spectral response of the open circuit-voltage V_{oc} of the $Zn_xCd_{1-x}Se/Cu_2Se$ heterojunction ($0 < x < 0.4$) was also measured after heat treatment in air at 200°C for 2min. (Figures 8.11 and 8.12). Subsequently heat treatment of these cells in air did not appear to have a beneficial effect on any of the devices formed on mixed crystal samples.

8.7.4 Deep levels

The experimental data obtained from the photocapacitance studies of the $Cd_{1-x}Zn_xSe/Cu_2Se$ heterojunctions showed good agreement with the spectral response measurements. The resulting deep levels are summarised in Table 8.7. The (0.93 - 1.03)eV level was attributed to copper impurity(24-27) by comparison with the photocapacitance measurements made on Cu-$Cd_{1-x}Zn_xSe$ Schottky diodes (see Section 6.3.3) with the data published by Robinson and Bube(25), and Ture et al.(24,26) who reported the main copper impurity level at 1.0eV above the valence band. The level at 0.21eV above the valence band has been attributed to a Cu-related impurity centre(26). A similar level has been found in $CdSe/Cu_2Se$ and doped Au-$Cd_{1-x}Zn_xSe$ Schottky diodes, and is in accord with other results reported by Ture et al.(5) who found from photocapacitance measurements and from optical deep level transient spectroscopy that a transition at 1.52eV is associated with excitation to the conduction band of electrons from copper levels 0.22ev above the valence band. In the present study acceptor levels were also found in the range 0.67 - 0.78eV above the valence band. Lewis et al.(27) suggested that the activation energy of this level is close to that of one widely reported in CdSe(25) at 0.62ev which has been associated with doubly ionised Cd vacancies(25).

This is in good agreement with other results on Au-$Cd_{1-x}Zn_xSe$ Schottky diodes with activation energies in the range 0.55-0.6eV.(28)

Composition (x)	Temperature (K)	Energy gap Eg (eV)	Activation energies		
0.0	300	1.74	0.95(c)	0.78(v)	0.21(v)
0.0	90	1.84	1.0 (v)	-	0.2 (v)
0.2	300	1.8	0.93(c)	0.73(v)	0.2 (v)
0.2	90	1.9	1.03(c)	0.72(v)	0.21(v)
0.4	300	1.92	1.01(c)	0.67(v)	0.22(v)
0.4	90	2.03	1.02(c)	0.67(v)	0.21(v)

Table 8.7 Summary of deep levels observed in $Cd_{1-x}Zn_xSe/Cu_2Se$ heterojunctions by photocapacitance .

8.8 Conclusions

Heterojunction $Cu_2Se/Cd_{1-x}Zn_xSe$ (X < 0.4) cells have been formed on orientated single crystal substrates using a chemiplating technique. The structure of the Cu_2Se layers was investigated using reflection high energy diffraction (RHEED) and found to take the cubic modification.

The photovoltaic output characteristics were measured under simulated AM1 illumination. Cells formed on CdSe were found to have higher short circuit current densities (J_{SC}) and lower open circuit voltages (V_{OC}) than those produced on the mixed $Zn_xCd_{1-x}Se$ crystal substrates.

Typical values of V_{OC} and J_{SC} were 200mV and 3.8mA cm^{-2} for CdSe based devices and 420mV and 1.0mA cm^{-2} for cells formed on, for example $Zn_xCd_{1-x}Se$ ($x = 0.4$). The spectral response of V_{OC} showed that the principal response arose from the Cu_2Se in most cases for as-made cells. Photocapacitance spectra were also obtained and used to identify the more important deep levels. The main threshold in all the devices indicated a dominant level with an activation energy of between 0.93eV and 1.03eV with respect to the conduction band in the $Zn_xCd_{1-x}Se$.

References

(1) Komashchenko, V.N. and Fedorus, G.A., (1968), Ukr, Fiz. Zh., 13, 688, (1968), Ukr. Phys. J., 13, 486.

(2) Komashchenko, V.N. and Fedorus, G.A., (1970), Soviet Physics : Semicon. 3, 8, 1001.

(3) Komashchenko, V.N., Lukyanchikova, N.B., Fedorus, G.A. and Sheinkman, M.K., (1971), Proc. Int. Conf. Phys. and Chem. Semicon. Heterojunction layer Structure Akademia Kiado, Budapest, 213.

(4) Komashchenko, V.N. and Fedorus, G.A., (1967), Soviet Phys. Semicond. I, 411.

(5) Ture, I.E., Russell, G.J. and Woods J., (1985), EEC Photovoltaic Conf., London, 861.

(6) Clark, L. and Woods, J., (1968), J. Crystal Growth 3/4, 126.

(7) Piper, W.W. and Polich, S.J., (1961), J. Appl. Phys. 32, 1278.

(8) Russell,G,J, Thompson, N.F. and Woods, J., (1985), J. Crystal Growth, 71, 621.

(9) Al Bassam, A., Brinkman, A.W., Russell, G.J. and Woods, J., (1985), British Assoc. Crystal Growth Conf., Brighton.

(10) Durose, K., Fellows, A.T., Brinkman, A.W., Russell, G.J., and Woods, J., (1985), J. Mat. Sci. 20, 3783.

(11) Ture,I,E., (1984), Ph.D. Thesis, University of Durham.

(12) Oktik, S., (1982), Ph.D. Thesis, University of Durham.

(13) Russell, G.J., Fellows, A.t., Oktik, S., Ture, E., and Woods, J., (1982), J. Mat. Sci. Lett., 1, 176.

(14) Rideout, V.L., (1978), Thin Solid Films, 48, 261.

(15) Heyding, R.D., (1966), Canadian J. Chem. Volume 44,1233.

(16) Efendiev, G.A., and Kazinets, M.M., (1960) Izv. Akad. Nauk. Azcrb. SSR, SCR. Fiz. Mat. 1 Tekn. Nauk, No. 5, 91,

(17) Shafizade, R.B., Ivanova, I.V., and Kazinets, M.M., (1976), Thin Solid Films, 35, 169.

(18) Shafizade, R.B., Ivanova, I.V., and Kazinets, M.M., (1978), Thin Solid Films, 55, 211.

(19) Idrichan, G.Z., and Sorokin, G.P., Neorganicheskie materialy, 11, (1967), 1693.

(20) Das, S.R., Banergee, A., and Chopra, K.L., (1979), Solid State Electron. 22, 533.

(21) Hall, R.B., Birkmire, R.W., Phillips, J.E., and Menkin, J.D., Appl. Phys. Lett. 38, 925.

(22) Burton, L.C., (1979), Solar Cells, 1, 159.

(23) Oktik, S., Russell, G.J. and Woods, J., (1982), J. Crystal Growth 59, 414.

(24) Ture, I.E., Claybourn, M., Brinkman, A.W. and Woods, J., (1985), J. Crystal Growth, 72, 189.

(25) Robinson, A.L., Bube, R.H., (1971), J. Appl. Phys. 42, 5280.

(26). Ture, I.E., Claybourn, M., Brinkman, A.W., and Woods, J., (1986), J. Appl. Phys., 60(5), 1670.

(27) Lewis, J.E., Ture, I.E., Brinkman, A.W. and Woods, J., (1986), Semicond. Sci. Technol. 1, 213.

(28) Al Bassam, A., Brinkman, A.W., Russell, G.J. and Woods, J., (1987), J. Crystal Growth, 86(1988)667.

CHAPTER 9

Summary and Conclusions

9.1 Summary

The main objective of the work described in this thesis has been to investigate the properties of crystals of $Cd_{1-x}Zn_xSe$ and to assess their potential in $Cd_{1-x}Zn_xSe/Cu_2Se$ ($0 < x < 0.4$) and photovoltaic cells. The material (Cd,Zn)Se was grown from the vapour phase, by two methods; the Durham and the Piper-Polich, both of which yielded boules 1cm in diameter and 3-4cm in length containing typically 3 or 4 crystals. The crystal boules often showed a graded composition along their length and so use was made of EDAX as a rapid and non-destructive technique for the measurement of composition. However, a calibration curve had to be established first; by comparing the EDAX spectra with the absolute composition as determined by atomic absorption spectroscopy (AAS), which, although quantitative, is a destructive technique. Crystal structure and lattice parameters were determined by X-ray diffractometry and showed that for $x < 0.5$ the crystal adopts the hexagonal wurtzite structure, changing to the cubic sphalerite phase for composition with higher concentrations. Lattice parameters were found to vary linearly with composition up to the transition phase point.

Measurements of the band gap energy show that it changes quadratically in x for $x < 0.6$ with bowing parameters of 0.82 and 0.87 at 300K and 90K respectively. Thus Eg has been found to obey an empirical relationship of the form:

$Eg(x) = 1.74 + 0.11x + 0.82\,x^2$, $(x < 0.6)$ at 300K

and $Eg(x) = 1.84 + 0.13x + 0.87\,x^2$, $(x < 0.6)$ at 77K.

The electrical characteristics of Au-$Zn_xCd_{1-x}Se$ diodes prepared on chemically etched surfaces were also examined for $x < 0.45$. The conductivity of as-grown material was found to decrease sharply as the zinc fraction was increased beyond about 40%, which precluded the use of Au-$Zn_xCd_{1-x}Se$ diode structures for material with greater zinc concentrations.

The barrier heights in Au-$Zn_xCd_{1-x}Se$ diodes were determined both from C^{-2}-V and photoelectric characteristics. The measurements showed that the barrier height increased from 0.88 to 1.26eV as x increased from 0 to 0.45. The spectral dependence of steady-state photocapacitance was also measured over the same compositional range and provides a preliminary survey of the electron and hole traps. The most consistent features were two positive going thresholds which corresponded to the emission of electrons from levels which appeared to remain pinned at 0.55 - 0.6eV and 1.14 - 1.16eV above the valence band.

Heterojunctions of Cu_2Se-CdSe and Cu_2Se-$Zn_xCd_{1-x}Se$ $(x < 0.4)$ were formed on orientated single crystal (Cd,Zn)Se substrates by a chemiplating technique. The structure of the resulting Cu_2Se layers was examined using reflection high energy diffraction (RHEED) and found to take the cubic modification, with a lattice parameter of 5.82Å. In the case of the CdSe substrates, the layer thickness was found to follow a $t^{1/2}$ relationship, where t is the chemiplating time.

Cells formed on as-grown low resistivity (~ 0.2Ω cm)CdSe substrates exhibited no rectification. This was because the heterojunction was formed between two highly conducting, degenerate semiconductors, with the result that both depletion regions were very narrow and carriers would have been able to tunnel easily through the barrier. However, good photovoltaic properties were produced by heating the devices at 200°C for 2 min in air or 30 min in Argon. On the other hand when heterojunctions were formed on higher resistivity CdSe, the resultant devices showed a photovoltaic effect without further treatment.

The photovoltaic output characteristics were measured under simulated AM1 illumination. Cells formed on CdSe were found to have higher short circuit current densities (J_{sc}), but lower open circuit voltages (V_{oc}) than those produced on the mixed $Zn_xCd_{1-x}Se$ crystal substrates. Typical values of V_{oc} and J_{sc} were 200mV and 3.8mA cm^{-2} for CdSe based devices and 420mV and 1.0mA cm^{-2} for cells formed on, for example, $Zn_xCd_{1-x}Se$ (x = 0.4). The spectral dependence of V_{oc} was measured for the devices, and showed that the principal response arose from the Cu_2Se in most cases. Photocapacitance spectra were also measured and used to identify the more important deep levels. The main threshold in all the devices indicated a dominant level with an activation energy of between 1.0 and 1.1eV with respect to the conduction band in both CdSe and $Zn_xCd_{1-x}Se$.

9.2 Discussion and Conclusion

Although good single crystals of the ternary compound CdZnSe were grown from the vapour phase using the Durham and the Piper-Polich methods, generally the more controlled Durham method produced crystals that were both larger and of better quality than the Piper-Polich method. However with a 2-3 week growth cycle, the Durham method takes much longer. It was also found to be more difficult to grow good crystals with compositions in the middle of the range, possibly because one crystallographic modification was not so strongly preferred over the other.

The carrier concentration calculated from plots of C^{-2} versus V for Au-$Zn_xCd_{1-x}Se$ diodes was found to be roughly independent of composition over the range $0 < x < 0.28$ and then decreased steeply as x was increased beyond this, and explains why it was not possible to fabricate diodes from crystals with $x > 0.5$.

Heat treatment of CdSe/Cu_2Se and Zn_xCd_{1-x}/Cu_2Se cells in air at 200°C improved the efficiency of type B cells after an optimum baking time of 2 minutes. In contrast the same treatment reduced the efficiency of Type A devices. Thus a heat treatment of these cells for periods of a few minutes had a deleterious effect as copper diffusion led to amore insulating region in the CdSe. The lattice parameters of $Zn_xCd_{1-x}Se$ single crystals were found to vary linearly with composition up to the transition point and a perfect lattice match is expected when copper selenide is grown on $Zn_{0.4}Cd_{0.6}Se$. With this composition the open circuit voltage V_{oc} increased to 0.42V. The increase in V_{oc} with rising zinc content is similar to the increase in the photothreshold values measured over the same composition. It was suggested that the increase in V_{oc} can be directly attributed to an increase in the barrier height due to the improved lattice match between $Zn_xCd_{1-x}Se$ and copper selenide.

9.3 Suggestions for further work

In order to extend the scope of the work described in this thesis, the following suggestions are made:-

(1) Deep level defects in $Zn_xCd_{1-x}Se$ mixed crystal need to be more systematically determined, this would entail a detailed study being carried out using DLTS and optical DLTS.

(2) The viability of Au-ZnSe-$Zn_xCd_{1-x}Se$ (MIS) Structures for photovoltaic applications should also be investigated. This structure could be readily fabricated using thermal evaporation or MOVPE to deposit ZnSe onto $Cd_xZn_{1-x}Se$ substrates.

(3) The fabrication of thin film $Cd_{1-x}Zn_xSe$ based devices should be investigated and resulting structures need to be

fully characterised.